

Characterization of tumor microstructures with diffusion-weighted MRI



Shu Xing

Department of Physics

McGill University

A thesis submitted to McGill University in partial fulfilment of the
degree of

Doctor of philosophy

© Copyright Shu Xing

August 2020

Table of Contents

List of Figures	v
List of Tables	xii
Abbreviations and Notations	xiii
Acknowledgment	xv
Preface	xvii
Contributions of authors	xviii
Other Publications	xix
Abstract	xxi
Résumé	xxiii
Original Contributions	xxv
1 Introduction	1
2 Background	4
2.1 Imaging tissue microstructures	4
2.1.1 Tumor heterogeneity	4
2.1.2 Tumor microstructures	6
2.1.3 Imaging tumor microstructures	8
2.2 Magnetic Resonance Imaging.....	9
2.2.1 The Fundamentals of MRI	10
2.2.2 Signal generation and detection	12

2.2.3	Spatial localization	14
2.3	Diffusion MRI.....	17
2.3.1	Introduction to diffusion and Fick's Law.....	17
2.3.2	Probabilistic description of diffusion	18
2.3.3	Diffusion in free medium	19
2.3.4	Diffusion inside finite boundaries	21
2.3.5	Diffusion contrast.....	22
2.3.6	The Bloch-Torrey equation for diffusion	23
2.3.7	Diffusion contrast at short measurement time.....	24
2.3.8	Diffusion spectrum.....	29
2.3.9	Diffusion encoding sequences.....	31
2.4	Diffusion MRI Modelling.....	35
2.4.1	Apparent diffusion coefficient (ADC)	35
2.4.2	Diffusion Tensor Imaging	36
2.4.3	IVIM model.....	38
2.4.4	Stanisz' model	39
2.4.5	CHARMED Model	40
2.4.6	VERDICT Model	40
2.4.7	IMPULSED Method	42
3	Probabilistic Classification of Tumor Habitats.....	50
3.1	Preface.....	50
3.2	Abstract.....	52
3.3	Introduction.....	53
3.4	Theory	55
3.5	Methods.....	60
3.6	Results.....	64
3.7	Discussion	72
3.8	Conclusion	78
3.9	Supporting Information.....	85
4	Non-invasive apparent cell size mapping with diffusion weighted MRI	87
4.1	Preface.....	87
4.2	Introduction.....	88
4.3	Theory	89

4.3.1	Diffusion modeling	89
4.4	Methods.....	91
4.4.1	Computer simulations	91
4.4.2	Cell preparation	92
4.4.3	<i>In-vitro</i> cell imaging.....	92
4.4.4	Diffusion phantom preparation	93
4.4.5	Diffusion phantom imaging	94
4.4.6	<i>In-vivo</i> volunteer imaging	95
4.4.7	Image processing and analysis	95
4.5	Results.....	96
4.5.1	Computer simulations	96
4.5.2	<i>In-vitro</i> cell imaging.....	98
4.5.3	Ice-water phantom imaging.....	99
4.5.4	<i>In-vivo</i> healthy volunteer imaging.....	100
4.6	Discussion	103
4.7	Conclusion	104
5	Microstructure modeling of tumor with two cell populations	109
5.1	Preface.....	109
5.2	Abstract.....	111
5.3	Introduction.....	112
5.4	Theory	113
5.4.1	One cell population microstructure model (1P-MM).....	113
5.4.2	Two cell population microstructure model (2P-MM).....	115
5.5	Method	117
5.5.1	Diffusion signal simulation	117
5.5.2	Fitting	118
5.5.3	Simulated Influence of SNR	119
5.5.4	Simulated Influence of pre-defined <i>D_{in}</i>	119
5.6	Results.....	120
5.6.1	One population model (1P-MM).....	120
5.6.2	Two population model (2P-MM)	121
5.6.3	Influence of SNR.....	124
5.6.4	Influence of fixing <i>D_{in}</i> in the model fit	127
5.6.5	Comparison of methods	128

5.7	Discussion	129
5.8	Conclusion	131
5.9	Supplementary Information	137
6	Detecting the evolving tumor microenvironment	138
6.1	Preface.....	138
6.2	Abstract.....	140
6.3	Introduction.....	141
6.4	Methods.....	144
6.5	Results.....	147
6.6	Discussion.....	152
6.7	Conclusion	154
7	Conclusion and Future work	159
7.1	Summary	159
7.2	Future directions	161
8	Appendix A.....	165

List of Figures

Figure 2.1 T2-weighted image of myxofibrosarcoma located on the flank demonstrates considerable heterogeneity within the tumor. Data collected as part of a local study[18].	5
Figure 2.2 Myxoid liposarcoma demonstrates a morphological continuum varying the amount of round cell component. Figure adapted from Bone and Soft Tissue Pathology Chapter 4. Angelo Paolo Dei Tos. Adipocytic Tumors, Page 22, © 2010, with permission from Elsevier [23].	6
Figure 2.3 Schematic illustrations of biological processes involved in therapy induced changes in tumors. Figure reprinted by permission from the Springer Nature Customer Service Centre GmbH: Springer Nature, Nature Clinical Practice Oncology, Technology Insight: water diffusion MRI-a potential new biomarker of response to cancer therapy, Daniel M Patterson et al. © 2008 [28]. .	7
Figure 2.4 Schematic illustration of major imaging techniques in the evaluation of tumor microenvironment. Figure reprinted from Insights into imaging 10 (28), Roberto Barcia-Figueiras et al. How clinical imaging can assess cancer biology © 2019 with permission under the Creative Commons CCBY license [4].	9
Figure 2.5 In the absence of an external magnetic field, spins are randomly orientated (a). The spins align in parallel or antiparallel with the direction of \mathbf{B}_0 field, in the presence of an external magnetic field (b).	10
Figure 2.6 In a rotating frame of reference, the net magnetization \mathbf{M} is tipped from the longitudinal plane to the transverse plane with a flip angle of 90° (a). The behavior of the same magnetization rotation is observed to be more complicated in a fixed laboratory frame. Figure reprinted by permission from WILEY: John Wiley and Sons, Magnetic Resonance Imaging: Physical Principle and Sequence design, 2 nd Edition, E. Mark Haacke et al. © 2014 [32].	12
Figure 2.7 Schematic illustration of the spin-echo pulse sequence. After the 90° pulse, the signal decays with T_2^* . Following the 180° pulse, an echo appears at $t = 2\tau$, with amplitude proportional to $e^{-2\tau/T_2}$	14

Figure 2.8 Illustration of the Fick's first Law. The net diffusion flux J is caused by a concentration gradient ∇n	17
Figure 2.9 (a) As diffusion time t increases, the probability distribution of Brownian particles becomes wider (diffusion coefficient $D = 2 \mu\text{m}^2/\text{ms}$). Similarly, increasing the coefficient of diffusion D increases the width of the displacement distribution, shown in (b) (diffusion time $t = 1.5 \text{ ms}$	20
Figure 2.10 Schematic representation of the DW-MR sequence of Stejskal and Tanner. This sequence which uses two lobe gradients is sensitive to Brownian motion of water. The introduction of diffusion weighting illustrated by the green, orange and blue filled circles represents spins at different locations. G represents the strength of the gradient. δ is a measure of the gradient duration. Δ represents the time interval between the two gradient lobes.....	22
Figure 2.11 Qualitative illustration of velocity autocorrelation functions and their corresponding diffusion spectra. Unrestricted water (top) experiencing only Brownian motion exhibits a flat diffusion spectrum, while restriction (bottom) acts to decrease the diffusion spectrum amplitude at lower frequencies. Figure reprinted from Magnetic Resonance Imaging 21 (3-4), Parsons EC et al. Modified oscillating gradient pulses for direct sampling of the diffusion spectrum suitable for imaging sequences, Pages 279-285, © 2003, with permission from Elsevier [52].	30
Figure 2.12 Schematic illustration of the standard pulsed gradient spin echo (PGSE) sequence, the sine-modulated and cosine-modulated oscillating gradient spin echo (OGSE) sequences. The sinusoidal waveform can be replaced with square or trapezoidal waveforms.....	32
Figure 2.13 Schematics of water molecule diffusion in (a) normal tissue: loosely packed cells, (b) cancerous tissue: densely packed cells and (c) fluid or necrosis: close to free diffusion	36
Figure 2.14 The first row demonstrates the isotropic diffusion of water molecules in a hindered environment. The displacement distribution can be described by a Gaussian function with a single ADC. The second row demonstrates diffusion in anisotropic tissues. The diffusion coefficients are direction dependent. The diffusion properties have to be described by a diffusion tensor.	37
Figure 2.15 Illustration of the influence from the IVIM effect on the diffusion signal in liver at lower b -values. A biexponential behavior is clearly observed in the signal with respect to b -values. Figure reprinted from Radiology 249 Luciani A, Vignaud A. et al. Liver Cirrhosis: Intravoxel Incoherent Motion MR Imaging – Pilot Study, Pages 891-899, © 2008, with permission from Radiological Society of North America [57].	38
Figure 2.16 Schematic representations of the prostate tissue and the corresponding VERDICT model. Figure reprinted from Investigative Radiology 50 (4), Panagiotaki et al. Microstructural characterization of normal and malignant human prostate tissue with vascular, extracellular and restricted diffusion for cytometry in tumors magnetic resonance imaging, © 2015, with permission from Wolters Kluwer Health,Inc.[66].....	41

Figure 2.17 Schematic representation of the tissue model used in the IMPULSED method. The cancer cells were modeled as impermeable spheres. The extracellular diffusion was considered as hindered diffusion. 42

Figure 3.1 Plot of the values of simDWI for ranges of T_2 and ADC values with $TE = 88$ ms and $b = 1000$ s/mm². The contour lines from left to right represent simDWI values equal to the 90th percentile (dash-dot), median (solid), and 10th percentile (dash) of the distribution of simDWI in muscle. When both T_2 and ADC are higher in a tumor pixel than in muscle, the value of simDWI serves to differentiate necrosis from high T_2 proteinaceous fluid, like the high b-value DW-MRI in the qualitative approach. 57

Figure 3.2 Workflow of the classification method: A. Image acquisition, B. Parameter calculation, C. Classification. Spin-echo MRIs must be acquired for at least 2 TEs to compute the T_2 map. DWI-MRI must be acquired for at least 2 b-values to produce the ADC map. The T_2 , ADC and simDWI maps are fed to the algorithm to produce classification maps. Reference tissue parameter distributions are shown in Figure 3.3..... 58

Figure 3.3 Regions of interests (ROIs) in muscle are shown as red overlays on T_2 -weighted FSE images acquired prior to radiotherapy: (a) Patient 1: lower thigh, (b) patient 2: lower thigh, (c) patient 3: lower thigh, (d) patient 4: forearm, and (e) patient 5: lower thigh. A representative slice from each patient is shown. Probability density functions of T_2 (f), ADC (g), and simDWI (h) in muscle voxels are also shown. The x-axis of T_2 and simDWI distributions was truncated for better visualization. A 3-term Gaussian model was fitted to each distribution, shown as solid orange lines. 65

Figure 3.4 A representative case of high grade myxofibrosarcoma demonstrates three regions of distinct intensity patterns. These regions were classified as hypercellular (red), proteinaceous fluid (green), and necrosis (blue), respectively, by the classification algorithm. This corresponds to the interpretation in Table 1. Regions I, II, and III are discussed in the text. The ADC map is the same for both the qualitative and quantitative approaches. 66

Figure 3.5 Classification results in all 7 patients (representative slices, column a), FDG-PET images (column b) and histopathological images (column c), from pre-radiotherapy imaging and biopsy samples. Each tumor was classified into 5 possible habitats: hypercellular (red), high T_2 proteinaceous fluid (green), necrosis (blue), collagenous stroma (purple) and fibrosis (yellow). Tumor habitats at pre-radiotherapy generally agreed with pathological observations from biopsy (discussed in the text). Regions of necrosis (blue) from MRI correspond well to the low uptake on FDG-PET. 69

Figure 3.6 Percentage of necrosis estimated by the classification method plotted versus quantitative estimates of necrosis from FDG-PET uptake. A strong correlation was observed at both pre-radiotherapy and post-radiotherapy, with R^2 of 0.97 and 0.96 respectively..... 71

- Figure 3.7** The relative tumor composition from the classification method are reported in all tumors in this study, including myxofibrosarcoma (MFS, P1, P2, P3), round cell/myxoid liposarcoma (RMLS, P4), myxoid liposarcoma (MLS, P5), synovial sarcoma (SS, P6) and fibromyxoid sarcoma (FMS, P7). MRI data were collected and analyzed at 3 time-points: pre-radiotherapy, during the 3rd week of radiotherapy, and after radiotherapy. 72
- Figure 4.1** The standard diffusion phantom used for the characterization of PGSE and OGSE sequences. The phantom consists of 30ml vials of aqueous solutions of polymer at different concentrations (a). The vials are submerged in an ice water bath to maintain 0 °C at the time of the measurement (b)..... 94
- Figure 4.2** The difference between fitted model parameters and the ground truth values for R, vin demonstrates improved accuracy and precision as SNR increases from 20 to 80. Fitted parameters were extracted from fitting Eq.1 to the diffusion signals from 5 microstructures with R=4,5,6,7, 8 μm and $vin = 50\%$. For each box, the central line (red) indicates the median and the edges of the box indicate the 25th and 75th percentiles, respectively. The error bars represent the maximum and minimum values. 97
- Figure 4.3** Representative fits (solid line) to PGSE (orange square) and OGSE (N=1, yellow triangle; N=2 purple circle; N=3, blue hexagon) signals from a single voxel of the MDA-MBA-231 cell pellet are demonstrated. The diffusion signals decay faster as the effective diffusion time decreases. 98
- Figure 4.4** Compare to the T2-weighted image acquired from turbo spin echo sequence (a), the single shot EPI diffusion sequence (b) at $b=0 \text{ s/mm}^2$ demonstrated noticeable geometric distortions. The center vial with deionized water (red circle) was easily visible and used for ADC analysis.99
- Figure 4.5** A representative example image of liver (pointed by red arrow) from a healthy volunteer, acquired with PGSE and OGSE sequences at $b=0 \text{ s/mm}^2$. An example liver ROI was drawn (yellow circles). The average diffusion signals from this ROI were shown in Figure 4.6. 100
- Figure 4.6** A representative example of signals from PGSE and OGSE from a liver ROI demonstrates bi-exponential signal decay as a function of increasing b-values (a). Greater IVIM effect was observed for signals at longer diffusion times. Mono-exponential model was fitted to signals with $b \geq 200 \text{ s/mm}^2$ (b) to reduce the IVIM effect. 101
- Figure 4.7** Average diffusion signal attenuations as a function of increasing b-values for corrected PGSE and OGSE signals from an example ROI in the liver. Markers represent the mean signals with the error bars as the standard deviations. The solid lines are fitted results using Eq.1. 102
- Figure 4.8** Parametric maps of ADC, R and vin overlaid on the PGSE $b=0 \text{ s/mm}^2$ image demonstrated significant heterogeneity within the liver. The estimated range of ADC and R are within the expected values from previous literatures. 103

- Figure 5.1** Simulated diffusion signals over a range of diffusion times Δ_{eff} (for fixed b-value) shows strong dependence on cell radii. Signal from cells of small radii (e.g. 1 – 2 μm) shows little change over diffusion times. For the 2- cell population model, strategic selection of diffusion times removes signal sensitivity to small cells and reduces the number of fitting parameters, producing more stable fits..... 116
- Figure 5.2** Schematic of the diffusion signal simulation and analysis pipeline. The cells are modeled as impermeable spheres of different sizes, where red and grey spheres represent the large and small cell populations, respectively. 117
- Figure 5.3** The 1P-MM was fitted to signals from two sets of microstructures (Table 1): microstructure set 1 (99 microstructures) (a,c) and microstructure set 2 (66 microstructures) (b,d). Plots show the estimated R of a microstructure (circles, panels a and b) where the red to blue color gradient indicates increasing vin, l , and the estimated vin of a microstructure (hexagons, panels c and d) where the green to orange color gradient shows increasing Rl . The black dashed and black dotted lines (a, b) represent the ground truth values of Rl and Rs , respectively. The blue dot-dashed and grey dot-dashed lines (c,d) represent the ground truth values of vin, l and vin, s respectively. The solid line (c,d) indicates the ground truth value of the total % volume fraction $vin, tot = 60\%$ 121
- Figure 5.4** The difference maps of estimated Rl, vin, l, vin, s from the ground truth values demonstrated good estimation accuracy. The model parameters were estimated by fitting the constrained-2P-MM to diffusion signals of microstructure set 1 (99 microstructures). The color brown and blue in the color bar represents overestimation and underestimation respectively. . 122
- Figure 5.5** The difference maps of estimated Rl, Rs, vin, l, vin, s from the ground truth values demonstrated good estimation accuracy for Rl greater than $7\mu\text{m}$. The model parameters were estimated by fitting the constrained-2P-MM to diffusion signals of microstructure set 2 (66 microstructures). The color brown and blue in the color bar represents overestimation and underestimation respectively. 123
- Figure 5.6** Comparison of extracted model parameters Rl, Rs, vin, l, vin, s from 2P-MM (green) and 2-step-2P-MM (pink). The model parameters were extracted by fitting both models to the noisy signal (SNR=50) of 4 microstructures with combinations of $Rl = 7: 1: 10 \mu\text{m}$, $Rs = 4 \mu\text{m}$, $vin, l = 45 \%$ and $vin, s = 15\%$. The difference between fitted model parameters and the ground truth values for Rl, Rs, vin, l, vin, s are plotted. For each box, the central line (red) indicates the median and the edges of the box indicate the 25th and 75th percentiles, respectively. The error bars represent the maximum and minimum values. 124
- Figure 5.7** Influence of noise on fitted model parameters, extracted from fitting the constrained-2P-MM to simulated noisy signals with SNR = 20, 35, 50, and 80, showing the accuracy and

precision of the fitted radius of the large cells (R_l) and of the relative volume fraction for both cell populations (vin, l, vin, s)..... 125

Figure 5.8 Influence of noise on fitted model parameters, extracted from fitting the 2-step-2P-MM to simulated noisy signals with SNR = 30, 50, and 80 , showing the accuracy and precision of fitted radii and the percentage volume fraction for both cell populations..... 126

Figure 5.9 Influence of fixing D_{in} to pre-defined values 0.6, 0.8, 1 (ground truth), 1.2, 1.4 $\mu m^2/ms$ on the estimation accuracy and precision is assessed. The absolute % error of the fitted R_l, R_s, vin, l, vin, s from the ground truth value are plotted for a representative microstructure with combinations of $R_l = 9 \mu m, R_s = 4 \mu m, vin, l = 45 \%$ and $vin, s = 15\%$. For each box, the central line (red) indicates the median and the edges of the box indicates the 25th and 75th percentiles, respectively. The error bars represent the maximum and minimum values..... 127

Figure 5.10 The accuracy and robustness of the 3 models– 2P-MM, 2-step-2P-MM and 2P-MM with fixed D_{in} was evaluated. All three models were fitted to the noisy signal (SNR=50) of 4 microstructures with combinations of $R_l = 7: 1: 10 \mu m, R_s = 4 \mu m, vin, l = 45 \%$ and $vin, s = 15\%$. The boxplots in each panel represents the distribution over 4 microstructures. Fits that were not within 1% of the fit constraints were considered acceptable fits..... 128

Figure 6.1 Schematic illustration of three possible scenarios after immunotherapy including 1) therapy induced necrosis, 2) increased number of cancerous cells due to ineffective therapy, and 3) infiltration of modified T-cells (cell radius $R \sim 4 \mu m$) to the cancerous cells ($R \sim 8-10 \mu m$) in immunotherapy or radiation induced immune-response. The diffusion inside the cells is considered restricted, and the diffusion in the extracellular space (blue background) is modeled as hindered and ascribed a constant diffusion coefficient..... 142

Figure 6.2 Model selection pipeline that choose the most suitable diffusion model among 1P-MM, 2P-MM and ME-ADC in a three-step process. The corrected Akaike information criterion (cAIC) allows the separation between necrosis and cellular tissue. The comparison between fitted radii from 1P-MM and 2P-MM further classifies cellular tissue into tissue with one underlying cell population and tissue with two underlying cell populations..... 146

Figure 6.3 Model selection based on the corrected Akaike information criterion (cAIC) allows the distinction between necrotic and cellular tissue. Example fits of three diffusion models, ME-ADC, 1P-MM and 2P-MM (row 2-4), to diffusion signals from three scenarios simulating tumor microstructures are demonstrated. The noisy signals (SNR=50) were simulated at four diffusion times ($\Delta_{eff} = 5.7, 16.7, 36.7, 66.7 ms$), normalized to signal at $b = 0 ms/\mu m^2$. The cAIC distributions are plotted over 1600 fits to noisy data..... 148

Figure 6.4 A representative example of model selection based on the fitted radii to differentiate cellular tissue with one cell population from tissue (a,c) with two cell populations (b,d). Both 1P-MM and 2P-MM were fitted to the noisy signals (SNR=50) of tissue microstructure with one cell

population ($R = 7,8,9,10\mu\text{m}$, $vin = 45\%$) and microstructure with two cell populations ($Rl = 7,8,9,10\mu\text{m}$, $Rs = 4\mu\text{m}$, $vin, l = 45\%$, $vin, s = 15\%$), where $Rapp$ (gray), Rl (pink) and Rs (blue) were estimated. The dashed and dotted black lines represent the ground truth values for Rl and Rs respectively. For each box, the central red line indicates the median and the edge of the box indicates the 25th and 75th percentiles over 1600 noisy simulations. 150

Figure 6.5 Simulations from the digital “tumor” object mimicking three clinical scenarios over a range of radii and volume fractions. ADC values are similar for multiple regions. The 1P-MM, 2P-MM and ME-ADC are correctly selected for $(72 \pm 5) \%$, $(86 \pm 7) \%$, and $(82 \pm 8) \%$ of the noisy iterations after removal of extreme fit values. The parameter maps (middle row) show results from individual fits and demonstrate the overall viability of the technique in spite of the variability of the parameter estimates. The median parameter maps (bottom row) computed as the median of 1600 noisy fits of SNR =50 showed intra-tumoral heterogeneity in regions identified as cellular tissue. The $Rapp$, vin , app estimated from 1P-MM are displayed in the Rl and vin, l maps. The Rs and vin, s not applicable for the one cell population voxels, are displayed in brown. 151

Figure 7.1 Pipeline of the proposed validation study..... 162

Supporting Figure 3.1 Histograms of ADC (a), T2 (b), and simDWI (c) in muscle across patients yield similar mean values. Each data point is the center value for the histogram bin, and the bin height normalized to the total number of voxels. A Gaussian function is fitted to the histogram from each patient..... 85

Supporting Figure 3.2 Histology sample of (a) myxofibrosarcoma (P2) and (b) round cell/myxoid liposarcoma (P4) shows different morphologies of treatment-related necrosis. Liquefactive necrosis in (a), indicated by the dotted lines, is an acellular geographic area of necrosis with necrotic nuclear debris and viscous consistency. In (b), the myxoid stroma still appears to be retained, but with no cellular component present in treatment-related necrotic areas (dotted lines) reflected by a homogeneous acellular myxoid/hyalinised appearance in the stain. 86

Supporting Figure 5.1 Apparent diffusion coefficient (ADC) of various combinations of large and small cells of different radii. The radius of large cells varies from 7 to 10 μm and the small cells are always of radius = 4 μm . The total % volume of the cells is kept at 60% for all combinations. The grey band indicates ADC value of $(3.00 \pm 0.15) \times 10^{-4} \text{ mm}^2/\text{s}$ 137

List of Tables

Table 2.1 Summary of b-values and effective diffusion time for various waveforms.....	34
Table 3.1 Interpretation of tumor sub-regions from diffusion and T ₂ MRI. The qualitative interpretations were proposed by Patterson et al. [23] and served as the basis for our quantitative method (column 4: “Quantitative”). The habitats are listed in column 5 (“Interpretation”) and colour coded according to the visual representation of the classification result.....	55
Table 3.2 Median parameter values (with interquartile range), for different tissue habitats following the probabilistic classification at pre-, mid- and post-radiotherapy (RT).	67
Table 3.3 Comparison of MRI-based sub-region classification results with FDG-PET and pathological observations.....	70
Table 4.1 Image acquisition parameters with 3T clinical scanner	95
Table 4.2 ADC measurements of deionized water with PGSE and OGSE sequences	99
Table 5.1 Summary of input model parameters for simulated microstructures used in this manuscript. Respectively. The term “microstructure” is used represent tissue model with a single combination of input model parameters.	118
Supporting Table 3.1 The minimum and maximum value of the imaging parameters for patients in this study at pre-radiotherapy are reported.	86

Abbreviations and Notations

B_0	Main magnetic field
B_1	RF Excitation Field
b -value	diffusion gradient weighting
D_{in}	Intracellular diffusion coefficient
D_{exo}	Extracellular diffusion coefficient
δ	Diffusion gradient duration
Δ	Diffusion gradient separation
G_x, G_y, G_z	x-, y-, z-gradient field
R	Cell Radius
T_1	Spin-Lattice Relaxation Time
T_2	Spin-Spin Relaxation Time
v_{in}	Percentage Volume fraction

ADC	Apparent diffusion coefficient
DWI	Diffusion weighted imaging
FID	Free Induction Decay
FOV	Field of view
IMPULSED	Imaging Microstructural Parameters Using Limited Spectrally Edited Diffusion
MR/MRI	Magnetic resonance/magnetic resonance imaging
NIST	National Institute of Standard and Technology
NMR	Nuclear magnetic resonance
OGSE	Oscillating gradient spin echo
PGSE	Pulsed gradient spin echo
RF	Radiofrequency
ROI	Region of interest
SD	Standard deviation
SE	Spin-echo
SNR	Signal-to-noise ratio
TE	Echo time
TR	Repetition time
1P-MM	One-cell-population Microstructure model
2P-MM	Two-cell-population Microstructure model

Acknowledgment

First, I would like to express my sincerest gratitude to my parents for their unweaving support, encouragement and understanding. During my PhD, my mother was diagnosed with gastric cancer, then leukemia shortly after. Even in the worst of times, she had always encouraged me to finish my PhD and believed that someday we would find a cure for cancer. Witnessing her going through countless amount of treatments has served as an inspiration to me to keep bettering cancer treatments. When she passed away, the only comfort that I had was that I did everything that I could. I think all the patients that are fighting cancer and their families deserve to know that their healthcare team has done everything possible for them. In my career after my PhD, I hope to keep pushing the limit for cancer diagnosis and treatment. I do not know if I can “cure” cancer, but I would like to make my honest effort.

I would like to thank my doctoral advisor, Professor Ives Levesque, for taking me on as one of his first graduate students. He has always encouraged me to explore various research topics and listened to my ideas, no matter how crazy they are. His patience and trust allowed me to pursue a research topic that I was truly interested in. Dr. Levesque also offered his help, guidance and encouragement, when I was supporting my mother through cancer. Without his understanding and support, none of this work would have been possible.

It has been an absolute pleasure to spend the past 5 years at the Medical Physics Unit. I would also like to thank our Unit director Dr. Jan Seuntjens. Thank you for all the selfless advice that you have given me, that made me a better researcher, a better medical physicist and a better person. I

could not have had a better mentor than you. You have always put your students first. Your work ethics, care for your patients, and kindness will continue to serve as an inspiration to me.

I also wish to thank my collaborators from the McGill University Health Center, who have kept my PhD project grounded and applicable to the clinic: Dr. Carolyn Freeman, Dr. Robert Turcotte, Dr. Sungmi Jung and Dr. Livia Garcia. Thank you for letting me into the operating room to observe that how pathological evaluation was perform. Thank you for spending hours explaining different pathological signatures of soft-tissue sarcoma. I am infinitely grateful for my colleagues, who contributed to a friendly and simulating work environment: Zaki Ahmed, Veronique Fortier, Mikael Simard, Alex Ensworth, Anastasia Kolokotronis and Dipal Patel. You have really made me feel like home and my PhD journal enjoyable.

Shu Xing

Montreal, April 2020

Preface

The core of this thesis consists of three manuscripts:

1. Shu Xing, Carolyn R. Freeman, Sungmi Jung, Robert Turcotte, Ives R. Levesque. “Probabilistic classification of tumor habitats in soft tissue sarcoma”, published in *NMR in biomedicine*, e4000, 2018
2. Shu Xing, Ives R. Levesque. “A simulation study of cell size and volume mapping for tissue with two underlying cell populations using diffusion weighted MRI”, under review at *Magnetic Resonance in Medicine*
3. Shu Xing, Ives R. Levesque. “Detecting the evolving tumor microenvironment with diffusion microstructure modeling: a simulation study”, to be submitted to *Magnetic Resonance in Medicine*

All of these manuscripts appear in full and in sequence in this thesis.

Contributions of authors

As the first author of all three manuscripts, I designed, implemented and validated all the classification algorithms and microstructure modelling frameworks. I conducted all the simulation experiments, performed data analysis and drafted the papers. The contributions of my co-authors are listed below.

Ives R. Levesque, PhD: As the candidate's supervisor, Professor Levesque provided essential guidance and mentorship throughout the project and reviewed all manuscripts extensively.

Carolyn R. Freeman, MD: For manuscript 1, Dr. Freeman was the principle investigator of the clinical study on the role of functional imaging in the management of soft-tissue sarcoma. She recruited the patients in the study, provided guidance and revision of the manuscript, with respect to the clinical aspects

Sungmi Jung, MD: For manuscript 1, Dr. Jung provided all the figures of patient pathology and written observations of their tumor composition. She provided guidance and revision of the manuscript, with respect to the pathology aspects

Robert Turcotte, MD: For manuscript 1, Dr. Turcotte was the surgeon who performed the biopsy on the patients in the study. He provided guidance regarding the location of biopsy.

Other Publications

The following are additional peer-reviewed journal and conference publications that were produced over the course of this project, which have not been included in this thesis:

- i. Vallieres M, Serban M, Benzyane I, Ahmed Z, Xing S, El Naqa I, Leveque IR, Seuntjens, J, Freeman CR. (2018). Investigating the role of functional imaging in the management of soft-tissue sarcoma of the extremities. *Physics and Imaging in Radiation Oncology* 6, 53-60.
- ii. Xing S, Levesque IR (2020) Detecting the evolving tumor microenvironment with diffusion microstructure modeling: a simulation study. *International Society for Magnetic Resonance in Medicine (ISMRM) Annual Meeting, Sydney*. Accepted.
- iii. Xing S, Levesque IR (2020) A simulation study of the robustness of cell size and volume mapping for tissue with two underlying cell populations using diffusion weighted MRI. *ISMRM Annual Meeting, Sydney*. Accepted.
- iv. Xing S, Levesque IR (2019) Modeling the microstructure of tissue with two cell populations of different sizes using diffusion-weighted MRI. *ISMRM Annual Meeting, Montreal*. Program 3540
- v. Xing S, Levesque IR (2019) Investigation of tumor microstructures with diffusion weighted MRI. *Quebec Bio-Imaging Network 9th Scientific Day*. Montreal.

- vi. Xing S, Levesque IR (2019) Non-invasive apparent cell radius mapping with diffusion weighted MRI. Cancer Research Program Scientific Day. Montreal.
- vii. Xing S, Freeman CR, JungS, Levesque IR (2017) A probabilistic approach to automated classification of tumor habitats in soft-tissue sarcoma. ISMRM Annual Meeting, Honolulu. Program 4507
- viii. Xing S, Freeman CR, JungS, Levesque IR (2016) Automated segmentation of soft tissue sarcoma into distinct pathological regions using diffusion and T2 relaxation. ISMRM Annual Meeting, Singapore. Program 2467
- ix. Xing S, Freeman CR, JungS, Levesque IR (2016) Automated classification of soft tissue sarcoma. International Sarcoma Symposium, Toronto, Canada

Abstract

Cancerous tumors are often heterogenous in their cellular composition and morphology. The tumor subregions can differ in many properties including growth rate, ability to metastasize, immunological characteristics, and sensitivity to therapies. Characterizing the tumor microenvironment could be beneficial for cancer diagnosis and the development of targeted therapy. Diffusion-weighted MRI is a powerful tool for the characterization of tumor microenvironment, due to its sensitivity to the Brownian motion of water molecules. By relating plausible models of the underlying tissue architecture to the acquired diffusion signal, microstructural information such as cell size and volume fraction can be obtained. The overall goal of this thesis was to develop novel DW-MRI based techniques to characterize tumor microenvironment. Our first aim was to characterize heterogeneity in the tumor microenvironment, by identifying different tumor habitats in soft tissue sarcoma. To this end, we developed a novel reference-tissue-based method for probabilistic classification of up to five tumor habitats, using maps of the apparent diffusion coefficient (ADC), T_2 relaxation maps, and a calculated map representing high- b -value diffusion-weighted MRI. The classification method was demonstrated in soft-tissue sarcoma. The classification results were qualitatively consistent with histopathology. The second part of our work focused on further characterization of tumor microenvironment by extracting microstructural information on a cellular level, such as cell size and volume fractions. Building on the existing microstructure imaging framework which assumed a single cell population in the tumor, we developed microstructure mapping with two cell populations co-existing in the same space. It was found that for a minimum difference of $3 \mu m$ in radius between the large and small cell populations and an SNR of 50, the radii and volume fractions of both cell populations could be accurately estimated. To demonstrate the potential application of

microstructure mapping in cancer treatment monitoring, the final component of this thesis focused on differentiating three potential post-treatment tumor microenvironments including necrosis, progression of disease, and infiltration of T-cells, all without a priori knowledge. This was achieved by developing a model selection method that chose the most suitable diffusion model to describe the tumor microenvironment. The method was evaluated with simulated diffusion data. Overall, this thesis introduced three novel DW-MRI based techniques for the characterization of tumor microenvironment.

Résumé

Les tumeurs cancéreuses sont souvent hétérogènes dans leur composition cellulaire et leur morphologie. Les sous-régions tumorales peuvent différer selon de nombreuses propriétés, notamment le taux de croissance, le potentiel de métastase, les caractéristiques immunologiques et la sensibilité aux traitements. La caractérisation du microenvironnement tumoral pourrait être bénéfique pour le diagnostic du cancer et le développement d'une thérapie ciblée. L'imagerie par résonance magnétique (IRM) de diffusion est un outil puissant pour caractériser le microenvironnement tumoral, en raison de sa sensibilité au mouvement brownien des molécules d'eau. En reliant des modèles réalistes de l'architecture sous-jacente des tissus au signal de diffusion, des informations microstructurales telles que la taille des cellules et la fraction volumique peuvent être obtenues. L'objectif général de cette thèse était de développer de nouvelles techniques d'imagerie basées sur l'IRM de diffusion pour caractériser le microenvironnement tumoral. Notre premier objectif était de caractériser l'hétérogénéité dans le microenvironnement tumoral, en identifiant différents habitats tumoraux dans des sarcomes des tissus mous. Nous avons développé une nouvelle méthode basée sur les tissus de référence pour la classification probabiliste d'un maximum de cinq habitats tumoraux, en utilisant le coefficient de diffusion apparente (ADC), la carte de relaxation T2 et une carte calculée représentant une IRM de diffusion avec une valeur b élevée. La méthode de classification a été démontrée dans des sarcome des tissus mous. Les résultats de la classification étaient qualitativement comparables avec l'histopathologie. La deuxième partie de mon travail s'est concentrée sur une caractérisation plus détaillée du microenvironnement tumoral en calculant des informations microstructurales au niveau cellulaire, telles que la taille moyenne des cellules et les fractions de volume cellulaire. En s'appuyant sur des méthodes existantes d'imagerie de la microstructure qui supposent une population de cellules

uniques dans les tumeurs, nous avons développé une approche de cartographie de microstructure avec deux populations de cellules coexistant dans le même espace. Il a été constaté que pour une différence de rayon minimum de 3 μm entre les populations de cellules de grande et petite taille et un rapport signal-sur-bruit de 50, les rayons et les fractions de volume des deux populations cellulaires ont pu être estimés avec précision. Pour démontrer l'application potentielle de la cartographie de la microstructure dans l'évaluation des traitements du cancer, la dernière partie de cette thèse portait sur la différenciation de trois microenvironnements tumoraux plausibles suivant un traitement. Les microenvironnements post-traitement comprenaient la nécrose, la progression de la maladie et l'infiltration des lymphocytes T. Cet objectif a été atteint en développant une méthode de sélection de modèle qui choisit le modèle de diffusion le plus approprié pour décrire le microenvironnement tumoral. La méthode a été évaluée avec des données de diffusion simulées. Dans l'ensemble, cette thèse a introduit trois nouvelles techniques basées sur l'IRM de diffusion pour la caractérisation du microenvironnement tumoral.

Original Contributions

The original scientific contributions of this PhD thesis are:

1. Development of a probabilistic classification algorithm that allows the automated classification of tumor habitats
2. The design, programming and validation of the analysis program, used for microstructure mapping with the one cell population model
3. Contribution to the Microstructure Imaging Sequence Simulation Toolbox by incorporating tissue geometry with two cell populations
4. The design, testing and validation of the two-cell population model.
5. The design, testing and validation of the model selection method which allows the differentiation of three post-treatment scenarios.

Chapter 1

Introduction

Cancer is a group of diseases characterized by the uncontrolled growth and spread of abnormal cells, which has major impacts on the population in Canada and world-wide [1]. It is estimated that approximately one in two Canadians will develop cancer in their lifetime, and one in four Canadians will die from cancer, making cancer the number one cause of death in Canada. In 2019 alone, approximately 220,400 Canadians will be diagnosed with cancer and 82,100 will die from the disease [2].

Most cancerous tumors are not homogenous in their cellular composition and morphology, but are often composed of multiple sub-populations of cancer cells [3]. The sub-populations differ in many properties, including growth rate, ability to metastasize, immunological characteristics and sensitivity to therapeutic modalities [4]. These intra-tumoral variations can in turn create different morphologies for different sub-regions within the tumor. These sub-regions can be termed habitats [5].

Tumor heterogeneity poses challenges for the development of effective therapy. Currently, the most prevalent treatment modalities including surgery, chemotherapy, radiotherapy, and recently immunotherapy, tend to treat the tumor as a homogenous entity. For example, in radiotherapy, the

same amount of radiation is often prescribed to the entire tumor. As our understanding of tumor biology improves, a considerable amount of evidence has suggested that the cancer cell sub-populations differ in susceptibility to chemotherapy [6]–[8], radiation therapy [9], [10] and immunotherapy [11], [12]. To overcome these limitations, personalized approaches are developed to provide different treatments for each tumor. For instance, dose painting in radiotherapy has been considered to deliver different amounts of radiation to various tumor habitats [9]. Targeted therapies such as anti-HER2 (human epidermal growth receptor 2) therapy has been applied to treat HER2-positive breast cancer, by blocking the function of the HER2 protein [13]. The clinical translation of these personalized treatments could greatly benefit from the ability to accurately map tumor habitats and to characterize the tumor microenvironment at a cellular level. To this end, imaging techniques with capability to characterize the tumor microenvironment are of great interest to clinicians.

Magnetic resonance imaging (MRI) has become a powerful tool for cancer diagnosis, treatment planning, and treatment assessment, because of its superior soft tissue contrast and the absence of ionizing radiation. The non-invasive nature of MRI allows repeated measurements at different time points during the course of treatment to monitor treatment induced changes. Among various MR techniques, diffusion-weighted MRI (DW-MRI) has become an increasingly popular tool for the characterization of tumor microenvironment, due to its sensitivity to the Brownian motion of water. In free water, the water molecular displacements follow a Gaussian distribution. In biological tissue, water diffusion is constrained by the presence of molecular and cellular obstacles. Thus, the displacement distribution is no longer Gaussian. Characterizing MRI signal behavior due to non-Gaussian diffusion can therefore provide valuable information on the tissue microstructure, such as cell size, shape, and volume fractions. This is achieved by developing realistic models of the underlying tissue architecture and relating them to the acquired diffusion signal. A brief overview of essential principles of MRI is presented in Chapter 2. In addition, a more comprehensive review of DW-MRI and diffusion modeling including microstructure modeling is provided in Chapter 2.

The overall goal of this thesis is to develop DW-MRI based imaging techniques to characterize tumor microenvironment. The first aim was to characterize heterogeneity in the tumor microenvironment, by identifying different tumor habitats in soft tissue sarcoma. To this end, we

proposed a method, allowing automated classification of five distinct tumor habitats. This work is presented in Chapter 3. The second objective of this thesis was to further characterize tumor habitat by extracting microstructural information on a cellular level, such as cell size and volume fractions. Concrete and careful steps were taken to ensure accurate and robust estimations of these microstructural parameters through computer simulations, in vitro and in vivo experiments. These steps are summarized in Chapter 4. While studying tumor microstructures, a type of soft tissue tumor with two cancer cell populations co-existing in the same space caught our attention. The existing microstructure imaging techniques assume that the tumor only contains a single cell population. To address this limitation, a computational proof-of-concept study was conducted on the feasibility of estimating cell radii and volume fractions of a mixture of two cell populations, when they co-exist in the same MR voxel. The results of this study are presented in Chapter 5. The final aim of this thesis was to differentiate tumor microenvironment with one cell or two cell populations without a priori knowledge. This was achieved by developing a model selection method that chose the most suitable diffusion model to describe the tumor microenvironment. The work is presented in Chapter 6. Lastly, the thesis concludes with summary discussion of major findings and future work in Chapter 7.

Chapter 2

Background

This chapter provides the necessary information to understand the principles of MRI, and more specifically the principles of diffusion weighted MRI and its applications in microstructure imaging. The first section (section 2.1) introduces the motivation of characterizing tumor microenvironment. Section 2.2 provides a brief overview on the basic theory of MRI, including the phenomenon of nuclear magnetic resonance, signal generation, detection and spatial localization. In the following sections 2.3 and 2.4, we discuss in detail the fundamental principles of diffusion, diffusion contrast in free and restricted environments and diffusion microstructure modeling.

2.1 Imaging tissue microstructures

2.1.1 Tumor heterogeneity

Tumors are commonly heterogeneous populations of cancer cells that experience uncontrollable growth. Among patients with the same type of cancer, there is a variety of tumor morphology, such as tumor shape and size. Heterogeneity is seen within the tumor for the same patient over the course of time, where the biological characteristics of a tumor can vary remarkably at different

stages of progression. Recent imaging studies have shown that some tumors are heterogenous at the time of diagnosis, with multiple distinct subregions, namely habitats, present within the tumor (Figure 2.1) [14]. Histological examination of a tumor specimen often reveals considerable differences in the morphology of cancer cells in different areas of the same lesion. Depending on the tumor size and grade, necrosis may be present as well as alterations in vasculature distributions, leading to differences in oxygenation [3].

Tumor heterogeneity presents challenges and opportunities for the development of effective therapy. Habitats of varying characteristics may differ in susceptibility to chemotherapy, radiotherapy or immunotherapy. For example, it has been demonstrated that poorly oxygenated tumor regions (i.e. hypoxia) are associated with greater risk of metastasis and are more resistant to radio- and chemotherapies [15], [16]. In addition, the presence of high cellularity regions in pancreatic cancer has been shown to relate to worse prognosis [17]. To overcome these limitations, strategies such as dose painting in radiotherapy have been considered to deliver different amounts of radiation to various habitats. This strategy aims to provide a radiation dose boost to the hypoxic volume and regions of high cellularity, while minimizing excess dose to the surrounding healthy tissue [18]. The clinical translation of dose painting relies in part on the ability to accurately map radioresistant regions. To this end, imaging techniques with the capability to characterize various tumor habitats are of great interest to clinicians.

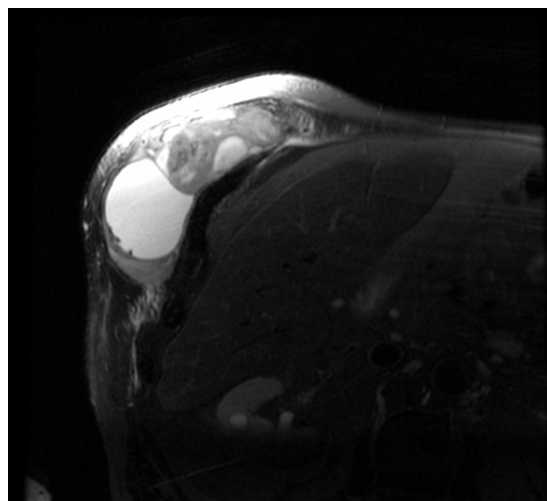


Figure 2.1 T2-weighted image of myxofibrosarcoma located on the flank demonstrates considerable heterogeneity within the tumor. Data collected as part of a local study[18].

2.1.2 Tumor microstructures

Looking beyond the tumor habitats on a macroscopic scale, the fundamental abnormality causing the development of cancer is the continual unregulated proliferation of cancer cells [19]. Microstructural features on a micron scale such as cell size and cellularity have been found to play an important role in cell proliferation and tumor growth [20]. For cancer diagnosis and prognosis, cell size and volume fraction (i.e. % volume occupied by cells) have reportedly been linked to cancer types and grade [21], [22]. For example, tumor cell size is one of the key histological characteristics differentiating large cell neuroendocrine carcinoma and small cell lung carcinoma [21]. In the following paragraph, I further exemplify how cell size helps the grading of myxoid liposarcoma, which is an application of interest that motivates the current work.

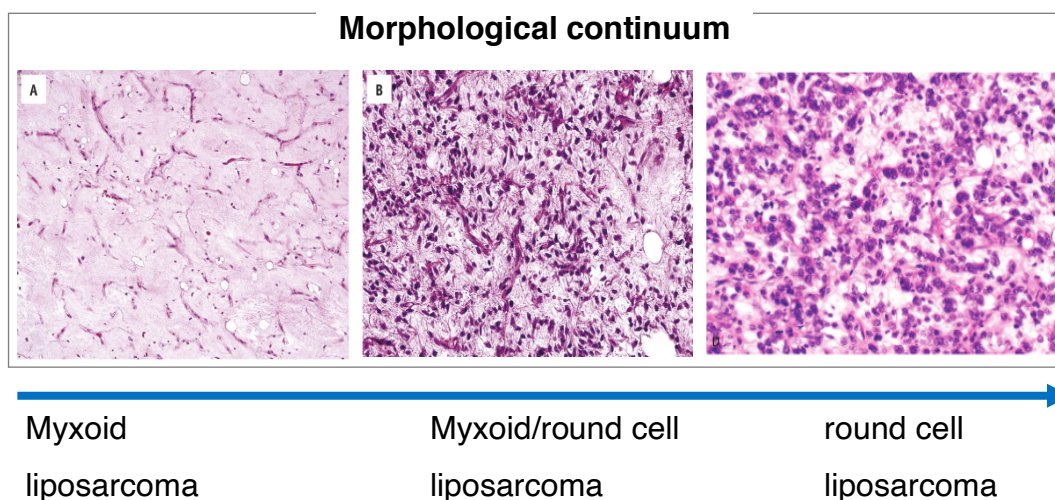


Figure 2.2 Myxoid liposarcoma demonstrates a morphological continuum varying the amount of round cell component. Figure adapted from Bone and Soft Tissue Pathology Chapter 4. Angelo Paolo Dei Tos. Adipocytic Tumors, Page 22, © 2010, with permission from Elsevier [23].

Myxoid liposarcoma is a type of soft-tissue sarcoma which accounts for 30% -35% of all liposarcomas. Myxoid liposarcoma forms a morphological continuum that includes a hypercellular neoplasm composed of oval to round neoplastic cells, known as round cells [23], [24] (Figure 2.2). Pure myxoid liposarcomas are well differentiated tumors with cell sizes 5-10 μm in diameter, whereas their hypercellular round cell counterparts are poorly differentiated tumors with cell sizes 15-20 μm in diameter [24]. The amount of round cell component in a myxoid liposarcoma is

directly related to tumor grade, metastasis, and patient survival [25]. Lesions with less than 5% round cell component are classified by clinicians as low grade lesions, and lesions with greater than 5% round cell component are classified as high grade [26]. The amount of round cell component is also linked to metastatic potential. Kilpatrick *et al.* found that 58% of the patients with > 25% of round cell component developed metastasis, whereas only 23% of patients with < 5% round cell component developed metastasis [27].

In addition to cancer diagnosis, variations in cell size and volume fraction have important implications for monitoring treatment response (Figure. 2.3). During therapy, cells may undergo a transient cell-swelling phase, which could be an indication of chemotherapy- or radiotherapy-induced cell injury, before going through apoptosis [27]. Cell shrinkage is a hallmark of morphologic features associated with apoptosis or necrosis, which is a common indicator for successful anti-cancer therapies [28].

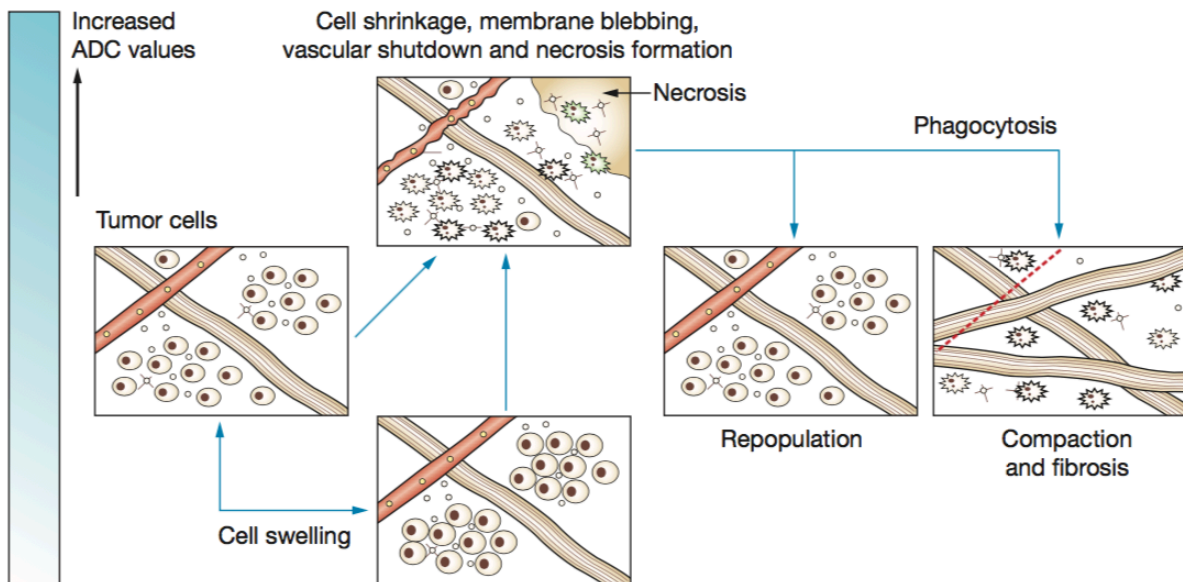


Figure 2.3 Schematic illustrations of biological processes involved in therapy induced changes in tumors. Figure reprinted by permission from the Springer Nature Customer Service Centre GmbH: Springer Nature, Nature Clinical Practice Oncology, Technology Insight: water diffusion MRI-a potential new biomarker of response to cancer therapy, Daniel M Patterson et al. © 2008 [28].

2.1.3 Imaging tumor microstructures

Currently, both cellular and subcellular information is obtained by means of invasive biopsy, which is the gold standard for tumor diagnosis and grading. Direct visual observation of cancerous cells provides an intuitive understanding of the tumor microenvironment; staining leads to high specificity to pathological observations [25]. However, biopsy only captures the characteristics of a limited sample of the tumor. The invasive nature of biopsy may cause clinical complications, including pain, hemorrhage and infections, making it unfeasible for repeated measurements. Therefore, a non-invasive imaging technique with the capability of detecting tissue microstructural information on the cellular scale would be of great interest to clinicians. Such technique could become a complementary tool to biopsy, allowing better characterization of the tumor microenvironment for the application of cancer diagnosis and treatment monitoring.

Different imaging techniques have been developed for the characterization of tumor microenvironment (Figure 2.4). For instance, dynamic contrast-enhanced MRI (DCE-MRI) has been used to assess tumor blood supply. Tumor hypoxia have been characterized by blood oxygenation level-dependent MR imaging (BOLD-MRI). Among these valuable techniques, diffusion-weighted MRI (DW-MRI) has become an increasingly popular tool that allows the characterization of multiple features in the tumor microenvironment due to its sensitivity to the Brownian motion of water. These features include heterogeneity, cellular density, proliferation, apoptosis/necrosis and tumor microenvironment (Figure 2.4). The principles of DW-MRI are discussed in detail in section 2.3.

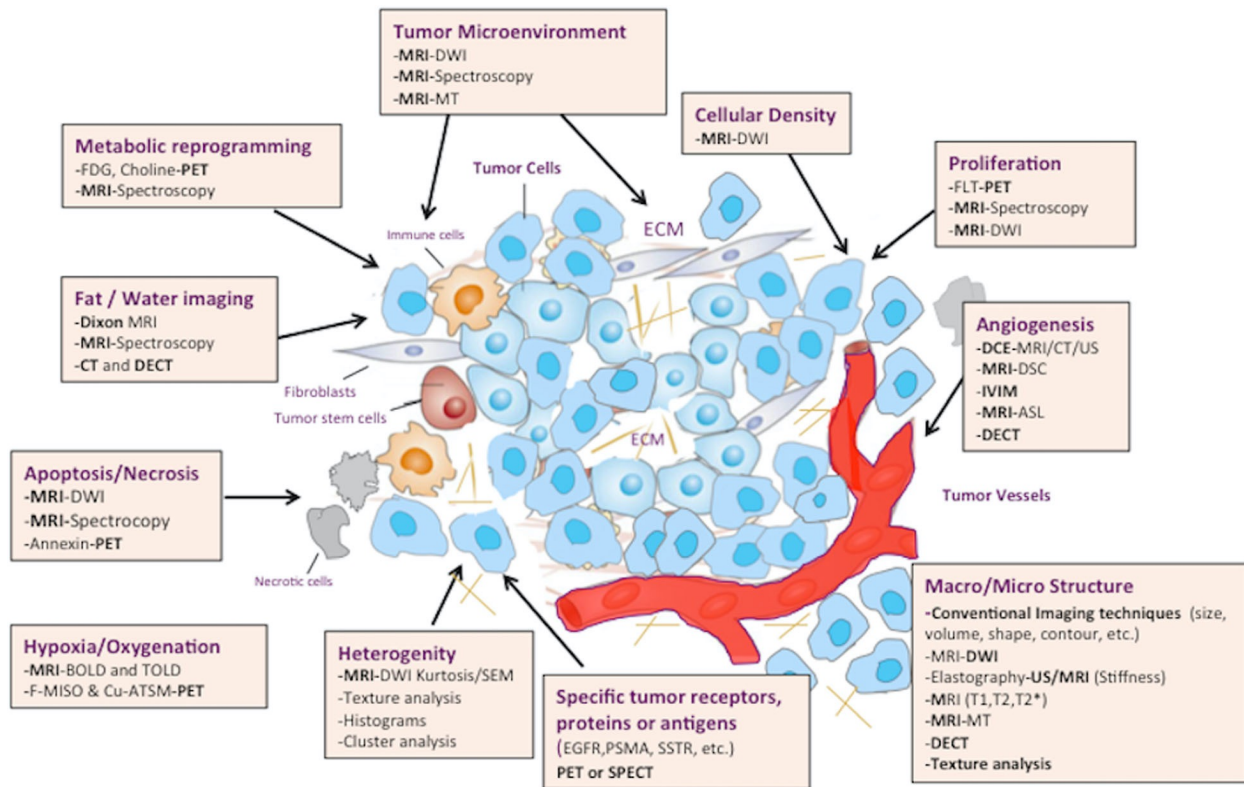


Figure 2.4 Schematic illustration of major imaging techniques in the evaluation of tumor microenvironment. Figure reprinted from Insights into imaging 10 (28), Roberto Barcia-Figueiras et al. How clinical imaging can assess cancer biology © 2019 with permission under the Creative Commons CCBY license [4].

2.2 Magnetic Resonance Imaging

Magnetic resonance imaging (MRI) is a powerful noninvasive imaging modality that has widespread applications in research and clinical medicine. The origin of NMR in condensed matter can be tracked back to 1930's, when Isidor Isaac Rabi found that certain nuclei could be induced to flip their principal magnetic orientation by an oscillating magnetic field. Their work was awarded the Nobel Prize in Physics in 1944 and is the essence of MRI today. This section provides a brief overview of the fundamental principles of MRI. The concepts described here are based on the book written by Dwight G. Nishimura [29].

2.2.1 The Fundamentals of MRI

The phenomenon of nuclear magnetic resonance (NMR) is based upon the interaction between nuclei with non-zero intrinsic angular momentum (i.e. spin) and a magnetic field. Several nuclei with non-zero net spins, including ^1H , ^{13}C , ^{15}N , ^{17}O , ^{19}F , ^{23}Na and ^{31}P , are most suitable for detection by magnetic resonance, and are thus referred to as MR active nuclei [30]. The hydrogen nucleus ^1H is the MR active nucleus most commonly used in biomedical imaging with MRI, because of its abundance in the human body (in H_2O and lipids).

The spin angular momentum is a vector quantity expressed as:

$$\mathbf{S} = \hbar \mathbf{I} \quad (1)$$

where \hbar is the Planck's constant divided by 2π and I is the spin quantum number. For nuclei with a net spin of $\frac{1}{2}$, I has two allowed discrete values. As a result, the magnitude of spin angular momentum is quantized. Associated with \mathbf{S} is a magnetic moment $\boldsymbol{\mu}$, which can be expressed as

$$\boldsymbol{\mu} = \gamma \mathbf{S} = \gamma \hbar \mathbf{I} \quad (2)$$

where γ is the gyromagnetic ratio, a constant unique for different nuclear species. The gyromagnetic ratio for ^1H is $2.675 \times 10^8 \text{ rad s}^{-1} \text{ T}^{-1}$ [29].

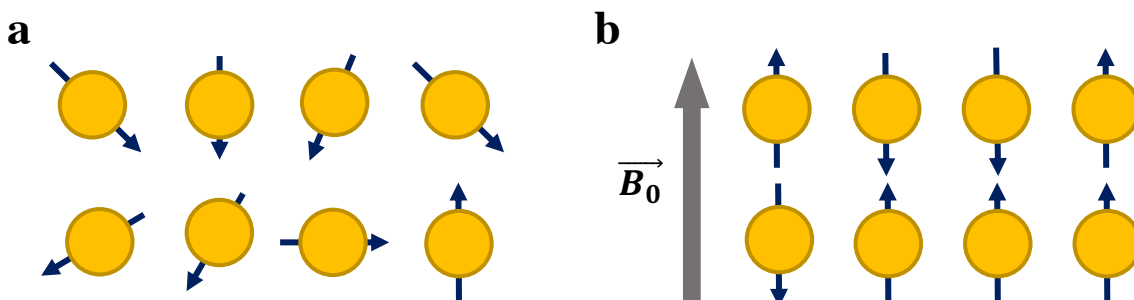


Figure 2.5 In the absence of an external magnetic field, spins are randomly orientated (a). The spins align in parallel or antiparallel with the direction of \mathbf{B}_0 field, in the presence of an external magnetic field (b).

In the presence of an external magnetic field \mathbf{B}_0 , the magnetic moment $\boldsymbol{\mu}$ tends to align in parallel or antiparallel with the direction of the \mathbf{B}_0 field (Figure 2.5), creating two possible energy states separated by:

$$\Delta E = \gamma \hbar B_0 \quad (3)$$

The spins aligned parallel to \mathbf{B}_0 are considered to be in a lower energy state, while spins aligned antiparallel are in a higher energy state. The ratio of the number of spins in each state is determined by the thermal energy of the spin system, which can be described by the Boltzmann distribution:

$$\frac{n_-}{n_+} = \exp\left(-\frac{\Delta E}{kT}\right) \quad (4)$$

where n_+ and n_- represent number of spins in the low and high energy states, respectively. k is Boltzmann's constant and T is the absolute temperature. Macroscopically, the excess number of parallel spins creates a net magnetization $\mathbf{M} = \sum \boldsymbol{\mu}$ in the same direction as \mathbf{B}_0 .

When the net magnetization \mathbf{M} is tipped away from the direction of \mathbf{B}_0 , the magnetic field imposes a torque on the magnetic moment, inducing a precession of the magnetic moment about the applied field \mathbf{B}_0 . The precessions of individual magnetic moments cause a precession in the net magnetization around the \mathbf{B}_0 field, which can be expressed as:

$$\frac{d\mathbf{M}}{dt} = \mathbf{M} \times \gamma \mathbf{B} \quad (5)$$

The solution to Eq. 5 provides the expression of the precession resonance frequency, termed the Larmor frequency. Since γ is a unique constant for each nuclide with a nuclear magnetic moment, for a given nuclide, the Larmor frequency only depends on the strength of the magnetic field:

$$\omega = \gamma B \quad (6)$$

2.2.2 Signal generation and detection

To induce a MR signal, an oscillating radiofrequency (RF) magnetic field \mathbf{B}_1 perpendicular to the \mathbf{B}_0 field and tuned to the resonance frequency of the spins is applied. The \mathbf{B}_1 field causes some spins to absorb sufficient energy to move to a higher energy state. As a result, this process is often referred to as excitation. This causes the net magnetization \mathbf{M} to rotate away from the direction of the \mathbf{B}_0 field in an amount proportional to the duration t and magnitude B_1 of the RF pulse. The amount of rotation is often referred to as the flip angle, expressed as $\theta = \gamma B_1 t$. The common flip angles are 90° and 180° corresponding to complete net magnetization transfer to the transverse plane and magnetization inversion respectively. For example, if the \mathbf{B}_0 field is along the z -direction, a \mathbf{B}_1 field with flip angle 90° would rotate \mathbf{M} into the x - y plane (Figure 2.6) in a rotating frame of reference.

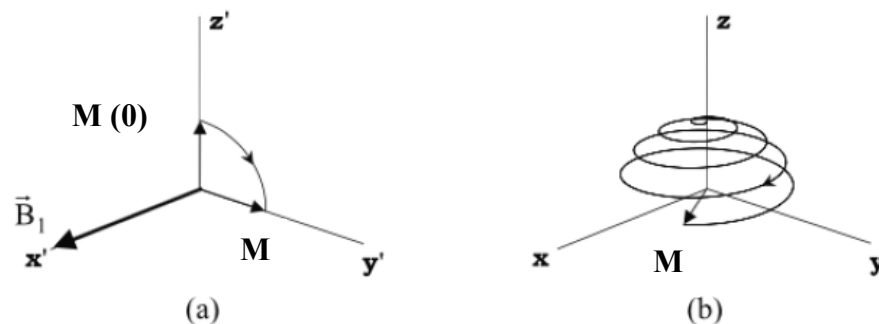


Figure 2.6 In a rotating frame of reference, the net magnetization \mathbf{M} is tipped from the longitudinal plane to the transverse plane with a flip angle of 90° (a). The behavior of the same magnetization rotation is observed to be more complicated in a fixed laboratory frame (b). Figure reprinted by permission from WILEY: John Wiley and Sons, *Magnetic Resonance Imaging: Physical Principle and Sequence design*, 2nd Edition, E. Mark Haacke et al. © 2014 [32].

After the \mathbf{B}_1 field is turned off, the net magnetization \mathbf{M} continues to precess in the transverse plane and returns to re-align with the \mathbf{B}_0 field and to restore its original magnitude. This phenomenon is associated with the loss of stored energy from spins to the surrounding lattice, thus termed spin-lattice relaxation or longitudinal T_1 recovery. The rate of recovery of the longitudinal magnetization is characterized by:

$$\frac{dM_z}{dt} = -\frac{M_z - M_0}{T_1} \quad (7)$$

where T_1 represents the spin-lattice relaxation time, characterizing the return of \mathbf{M} to its equilibrium state along the z-axis. Taking $M_z(t_0)$ as the initial magnetization, Eq. 7 has the solution:

$$M_z(t) = M_0 - [M_0 - M_z(t_0)] \exp\left(-\frac{t - t_0}{T_1}\right) \quad (8)$$

At the same time, spin-spin interactions also contribute to relaxation. The interaction of neighboring spins with each other causes the loss of phase coherence (dephasing) of the transverse magnetization. This behavior is therefore called spin-spin relaxation or transverse T_2 decay, with characteristic time T_2 . The rate of the relaxation can be described as:

$$M_{xy}(t) = M_{xy}(t_0) \exp\left(-\frac{t - t_0}{T_2}\right) \quad (9)$$

The dephasing of spins is further increased by local magnetic field inhomogeneities. The actual decay time T_2^* is therefore shorter than T_2 , accounting for the additional decay time T_2' due to field inhomogeneities.

$$\frac{1}{T_2^*} = \frac{1}{T_2} + \frac{1}{T_2'} \quad (10)$$

For a MR experiment, signal detection occurs after the RF excitation pulse is turned off. The magnetization continues to precess in the transverse plane with the Larmor frequency of the spins. A precessing magnetic moment generates a rotating magnetic field, which in turn produces an electromotive force (EMF), according to Faraday's law of induction. The same RF coil used to generate the RF excitation pulse is used to detect the EMF. The resulting basic MR signal is called the free induction decay (FID). It is important to realize that the receiver coil only detects signal generated from the transverse magnetization. As T_1 and T_2 relaxation effects take place, the signal amplitude decreases. FID is thereby a time dependent signal, which decays with T_2^* . To measure signal decay due to T_2 relaxation, the T_2' effect can be corrected by applying an additional 180°

pulse. The 180° pulse inverts the spin precession direction and creates an echo of the original FID signal at a moment called echo time (2τ). The amplitude of the signal at 2τ decays according to T_2 relaxation. The combination of 90° and 180° pulses is referred to as the spin-echo sequence (Figure 2.7).

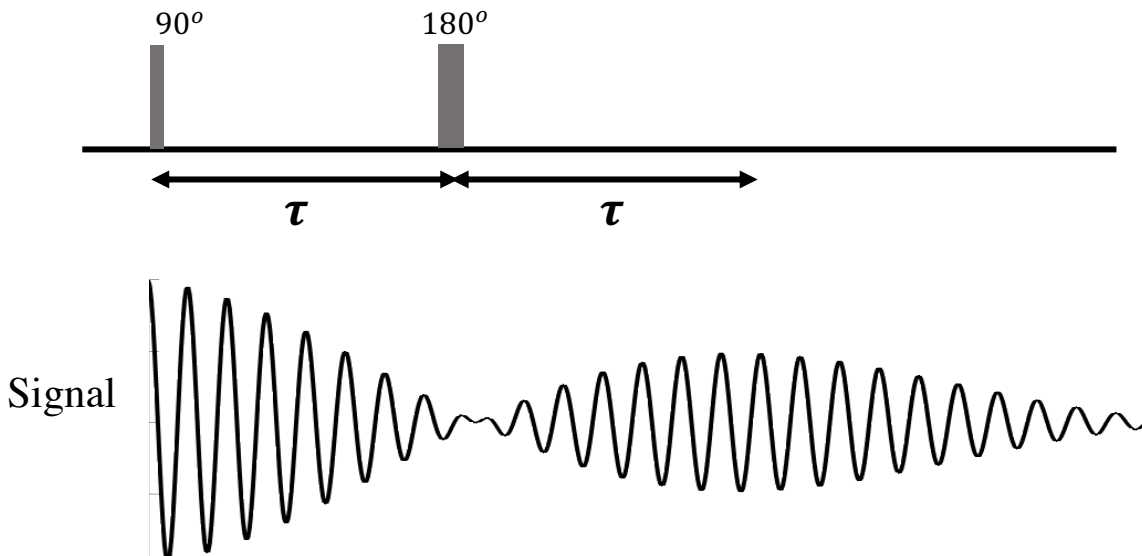


Figure 2.7 Schematic illustration of the spin-echo pulse sequence. After the 90° pulse, the signal decays with T_2^* . Following the 180° pulse, an echo appears at $t = 2\tau$, with amplitude proportional to $e^{-2\tau/T_2}$.

2.2.3 Spatial localization

The signal acquisition described in section 2.2.2 provides an average signal for the entire sample of interest. In order to distinguish signal from different spatial locations, a gradient field $\mathbf{G} = (G_x, G_y, G_z)$ that provides field strength variation on the \mathbf{B}_0 field is often applied in three steps: 1) slice selection 2) frequency encoding and 3) phase encoding.

Slice selection is realized by applying a gradient field usually along the z-direction, which introduces a linear variation of the resonance frequency as a function of location along the z-axis. A RF pulse with a limited range of frequencies (i.e. bandwidth) is then applied, affecting only the slice that has the same resonance frequencies.

After a slice has been selectively excited, the signal coming from the slice must be located along both axes of the image. Frequency encoding is used to provide information about position along the x-axis. When the frequency encoding gradient G_x is on, the magnitude of the magnetic field in the z-direction now has a position dependence on x . As a result, the precession frequency of the spins varies linearly with position x , mathematically expressed in Eq. 11.

$$\omega(x) = \gamma(B_0 + G_x x) = \omega_0 + \gamma G_x x \quad (11)$$

The signal generated from spins at point x in an infinitesimal interval dx is:

$$S(x, t)dx = \rho(x)e^{-i(\omega_0 + \gamma G_x x t)} dx \quad (12)$$

where $\rho(x)$ accounts for spin density, T_1 and T_2 relaxation and flip angles. After demodulation (i.e. removal of the $e^{-i\omega_0 t}$ term), the signal from the entire object becomes:

$$S(t) = \int_{-\infty}^{\infty} S(x, t)dx = \int_{-\infty}^{\infty} \rho(x)e^{-i\gamma G_x x t} dx \quad (13)$$

Phase encoding is applied between excitation and frequency encoding to provide spatial information along the y-axis. Similar to frequency encoding, G_y is applied to alter the magnitude of the external magnetic field and therefore the precessional frequency as a function of y . As the precession frequency changes, the accumulated phase of the magnetic moment also changes. The phase dependence on the location of y provides the spatial location of the signal along y-axis.

The FID signal generated from spins in an infinitesimal interval dy at point y is:

$$S(y, t)dy = \rho(y)e^{-i(\omega_0 + \gamma G_y y t)} dy \quad (14)$$

The phase encoded signal after demodulation is:

$$S(t) = \int_{-\infty}^{\infty} S(y, t) dy = \int_{-\infty}^{\infty} \rho(y) e^{-i\gamma G_y y t} dy \quad (15)$$

Frequency and phase encoding can then be used to localize the signal in a 2D plane, with the total signal of:

$$S(t) = \iint I(x, y) e^{-i\gamma G_x x T_{FE}} e^{-i\gamma G_y y T_{PE}} dx dy \quad (16)$$

where T_{FE} and T_{PE} represent the frequency encoding and phase encoding interval. Eq. 16 can be re-written by substituting the spatial frequencies (Eq.17).

$$\begin{aligned} k_x &= \frac{1}{2\pi} \gamma G_x x T_{FE} \\ k_y &= \frac{1}{2\pi} \gamma G_y y T_{PE} \end{aligned} \quad (17)$$

We obtain:

$$S(k_x, k_y) = \iint I(x, y) e^{-2\pi i k_x x} e^{-2\pi i k_y y} dx dy \quad (18)$$

The Fourier relationship between the image function $I(x, y)$ and the signal in k-space $S(k_x, k_y)$ demonstrated in Eq. 18 is an important concept in image acquisition. This means by measuring signal in k-space, we can recover the image function, which is the quantity of interest. The k-space can be traversed by manipulating the frequency and phase encoding gradients G_x and G_y ; various sampling schemes including linear, radial and spiral can be used to cover the entire k-space of interest.

The reconstruction of the image function $I(x, y)$ can be achieved by applying a two-dimensional inverse Fourier transform for each slice. The resulting image function is complex, which is used to create both the magnitude and phase images.

2.3 Diffusion MRI

2.3.1 Introduction to diffusion and Fick's Law

Diffusion is a naturally occurring mass transport process, which results in particle mixing without bulk motion. Macroscopically, diffusion describes the random motion of particles from a region of high concentration to a region of low concentration. Imagine carefully introducing a drop of fluorescent dye into a glass of lukewarm water. Initially, the dye appears to remain concentrated at the point of release, but over time it spreads radially until it is uniformly distributed throughout the water. The mixing process takes place without stirring or other bulk fluid motion.

Adolf Fick, a German physicist, proposed a mathematical description of this phenomenon in 1855, which relates the flux of particles to the concentration gradient with Eq. 19. This relationship is known as Fick's first law and is illustrated in Figure 2.8.

$$\mathbf{J}(\mathbf{r}, t) = -D\nabla n(\mathbf{r}, t) \quad (19)$$

where $\mathbf{J}(\mathbf{r}, t)$ represents the particle flux, D is the diffusion coefficient and $n(\mathbf{r}, t)$ is the particle concentration. Intuitively, the minus sign in this equation describes that the direction of flow is from high to low concentrations [35].

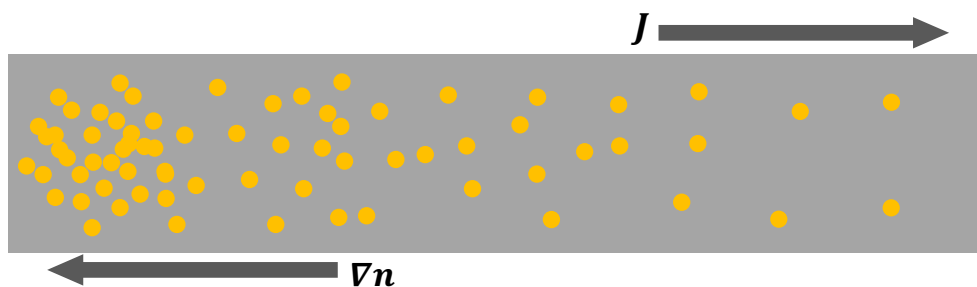


Figure 2.8 Illustration of the Fick's first Law. The net diffusion flux \mathbf{J} is caused by a concentration gradient ∇n .

In addition, the conservation of particles requires that the rate of change of particle concentration is related to the change of flux

$$-\nabla \cdot \mathbf{J} = \frac{\partial n}{\partial t} \quad (20)$$

Combining Equation 19 and 20, we arrive at Fick's second law of diffusion:

$$\frac{\partial n(\mathbf{r}, t)}{\partial t} = D \nabla^2 n(\mathbf{r}, t) \quad (21)$$

which is also known to as the diffusion equation [36].

2.3.2 Probabilistic description of diffusion

Fick's law was originally developed to describe the behavior of solute molecules drifting from higher to lower concentration to equalize the concentration gradient. In the absence of a macroscopic concentration gradient, however, random molecular motion still exists. This phenomenon has its origins in the observation of Scottish botanist Robert Brown, who first reported the random migrations of pollen grains suspended in water without any apparent cause in 1827, while studying them under the microscope. This random motion was thereafter named the Brownian motion [37].

In the early part of the twentieth century, Albert Einstein recognized that Brownian motion was associated with diffusion through a process known as self-diffusion, where molecules undergo diffusion arising from local concentration fluctuations. Self-diffusion is driven by the random motions associated with thermal energy. Einstein showed that while the macroscopic particle concentration $n(\mathbf{r}, t)$ may be uniform, the probability density function $p(\mathbf{r}, t)$ for the position of particles still obeys Fick's law in the same manner as $n(\mathbf{r}, t)$ [38]. This important insight from Einstein enabled the quantification of the displacement distribution of particles, which is the fundamental concept that allows diffusion weighted MR to be sensitive to microstructural features. The mathematical theories in this section are based on the book "Translational dynamics and magnetic resonance : principles of pulsed gradient spin echo NMR", by Callaghan et al [35].

In order to describe the dynamics of Brownian motion, it is crucial to know the probabilities associated with the various possible paths of Brownian particle displacement $x(t)$ as time advances. This can be represented by the conditional probability that a Brownian particle starts at x_0 at t_0 , and would be found between x_1 and $x_1 + dx_1$ at time t_1 :

$$P(x_1, t_1 | x_0, t_0) dx_1 = \frac{P(x_0, t_0; x_1, t_1) dx_1}{p(x_0, t_0)} \quad (22)$$

where $P(x_0, t_0; x_1, t_1)$ represents the joint probability that $x_0 \leq x_0(t) \leq x_0 + dx_0$ while $x_1 \leq x_1(t) \leq x_1 + dx_1$.

Since the conditional probability $P(x, t | x_0, t_0)$ also obeys Fick's law, Fick's second law (Eq. 21) can then be expressed in terms of the conditional probability as:

$$\frac{\partial P(x, t | x_0, t_0)}{\partial t} = D \nabla^2 P(x, t | x_0, t_0) \quad (23)$$

2.3.3 Diffusion in free medium

The one-dimensional, time-dependent diffusion equation (Eq. 23) can be solved for specific initial and boundary conditions. For diffusion in homogeneous and free medium (*i.e.* fluid of infinite extent), the boundary condition becomes $P(x, t | x_0, t_0) \rightarrow 0$ when $x \rightarrow \infty$, with initial condition of $\delta(x - x_0)$ at $t = 0$. The solution to Eq. 23 has previously been reported [39]:

$$P(x, t | x_0, t_0) = \frac{1}{\sqrt{4\pi D(t - t_0)}} e^{-\frac{(x-x_0)^2}{4D(t-t_0)}} \quad (24)$$

where $P(x, t | x_0, t_0)$ represents the conditional probability of finding a Brownian particle at x at time t , given it started at x_0 at time t_0 .

For 3-dimensional diffusion along x , y and z directions, the conditional probability of the particle displacements can be written as

$$P(\mathbf{r}, t | \mathbf{r}_0, t_0) = (4\pi D(t - t_0))^{-\frac{3}{2}} \exp\left(-\frac{(\mathbf{r} - \mathbf{r}_0)^2}{4D(t - t_0)}\right) \quad (25)$$

The expressions of conditional probability shown in Equation 24 and 25 demonstrate that the distribution of particle displacements takes a Gaussian form in a free medium. The displacement distribution depends on both the diffusion time t and the diffusion coefficient D . As the diffusion time increases, Brownian particles travel a greater distance for a given diffusion coefficient D , leading to wider distributions (Fig.2.9 (a)). Similarly, increasing the coefficient of diffusion also increases the width of the distribution for a given diffusion time (Fig. 2.9 (b)). The Gaussian nature of the distribution allows us to characterize the average squared displacement of particles from their starting point over time t :

$$\langle (\mathbf{r} - \mathbf{r}_0)^2 \rangle = \int_{-\infty}^{\infty} (\mathbf{r} - \mathbf{r}_0)^2 P(\mathbf{r}, t | \mathbf{r}_0, t_0) d\mathbf{r}_0 d\mathbf{r} = nD(t - t_0) \quad (26)$$

where $n=2, 4, 6$ for one, two and three dimensions respectively. e.g. $\langle (x - x_0)^2 \rangle = 2D(t - t_0)$.

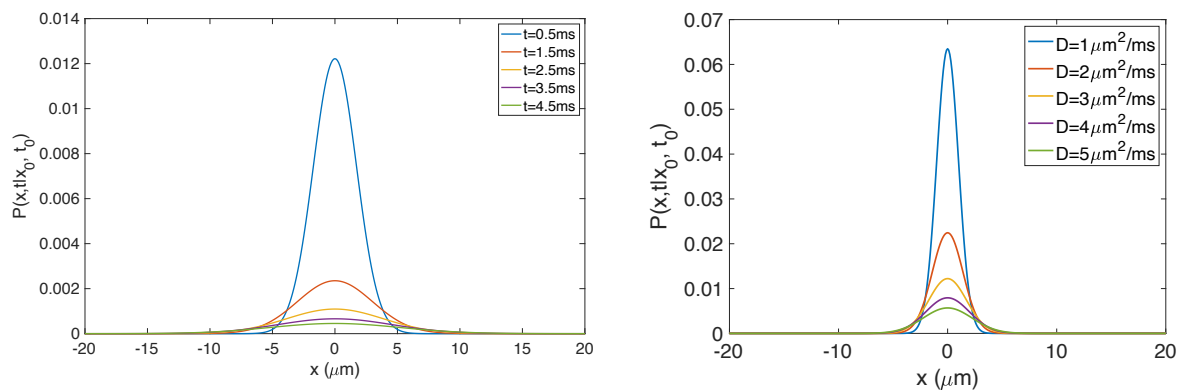


Figure 2.9 (a) As diffusion time t increases, the probability distribution of Brownian particles becomes wider (diffusion coefficient $D = 2 \mu\text{m}^2/\text{ms}$). Similarly, increasing the coefficient of diffusion D increases the width of the displacement distribution, shown in (b) (diffusion time $t = 1.5 \text{ ms}$).

This relationship (Eq. 26) referred to as ‘‘Einstein’s equation’’ has important significance in diffusion-weighted MR imaging. For a body of water at body temperature ($37^{\circ}C$), the diffusion coefficient of water is approximately $3 \times 10^{-3} mm^2 s^{-1}$. Thus, if we observe water molecules for 30 ms, they will have displaced over a mean distance of $25 \mu m$ in all directions. If the measured mean distance is much smaller compared to $25 \mu m$, finite structures might be present causing water molecules to slow down. This property has been applied to differentiate cancerous cells from normal tissue, based on the assumption that cancer cells are more densely packed. For cases where the mean distance measured is smaller in two out of three directions, this could be indicative of structure shape. Water could be diffusing in a cylindrical, ellipsoidal or rectangular structure.

2.3.4 Diffusion inside finite boundaries

In the previous section (2.3.3), we have discussed the solution to Fick’s law in the case of free diffusion in an infinite medium with the initial condition of $P(\mathbf{r}, 0 | \mathbf{r}_0, 0) = \delta(\mathbf{r} - \mathbf{r}_0)$. For real life applications in biology, water molecules are often trapped inside structures, such as cells. The diffusion of water molecules is slowed by the dimensions of the obstructions. Therefore, it is important to obtain a solution of the conditional probability of particle displacement $P(\mathbf{r}, t | \mathbf{r}_0, t_0)$ for diffusion inside finite boundaries. This type of diffusion is referred to as restricted diffusion.

The diffusion equation in terms of $P(\mathbf{r}, t | \mathbf{r}_0, t_0)$ (Eq. 21) can be solved using separation of variables. $P(\mathbf{r}, t | \mathbf{r}_0, t_0)$ is expressed as a product of functions $u(\mathbf{r})$ and $v(t)$, where u and v are functions of \mathbf{r} and t , respectively. The general solution may be written as the linear superposition of eigenmodes [35]:

$$P(\mathbf{r}, t | \mathbf{r}_0, t_0) = \sum_{n=0}^{\infty} u_n^*(\mathbf{r}) u_n(\mathbf{r}_0) e^{-D\lambda_n(t-t_0)} \quad (27)$$

where $u_n(\mathbf{r})$ are the eigenfunctions of the diffusion equation parameterized by the eigenvalues λ_n . The function u_n depends on the boundary conditions of specific structures, in which Brownian particles are enclosed in.

2.3.5 Diffusion contrast

This section explains how MR measurements can be sensitive to molecular displacements. When the external magnetic field B_0 is homogeneous, the cumulative phase of individual spins is $\phi(t) = \omega_0 \cdot t = \gamma B_0 t$. When a spatially dependent gradient field $G(t)$ is applied, the cumulative phase becomes:

$$\phi(t) = \int_0^t (\omega_0 + \gamma G(t')r(t'))dt' = \omega_0 t + \gamma \int_0^t G(t')r(t')dt' \quad (28)$$

In 1965, Stejskal and Tanner introduced an MR sequence sensitive to the Brownian motion of water as illustrated in Figure 2.10 [40]. The 90° RF excitation pulse brings the net magnetization into the transverse plane. The first gradient causes spins from hydrogen nuclei in water molecules to de-phase depending on the combined external field they experience. After the gradient is turned off, the spins evolve freely. Static spins stay in the same position while diffusing spins change their relative positions. A 180° RF pulse then flips the phase of all spins to the opposite direction. Another identical gradient is used to rephase the spins. The static spins restore their phase coherence. The diffusing spins, however, do not recover their phase coherence completely, leading to a signal attenuation. This sequence is commonly known as “pulsed gradient spin-echo” (PGSE).

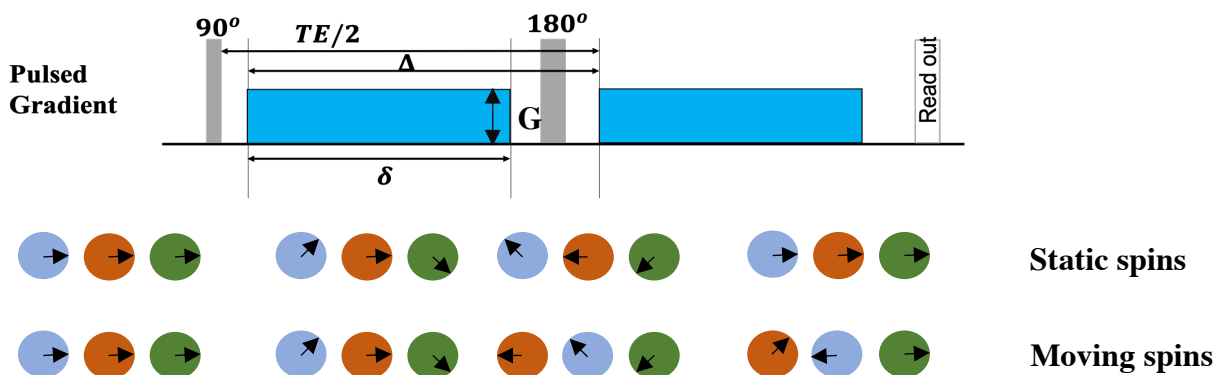


Figure 2.10 Schematic representation of the DW-MR sequence of Stejskal and Tanner. The introduction of diffusion weighting illustrated by the green, orange and blue filled circles represents spins at different locations. G represents the strength of the gradient. δ is a measure of the gradient duration. Δ represents the time interval between the two gradient lobes.

2.3.6 The Bloch-Torrey equation for diffusion

The mathematical formulations relating the signal attenuation to diffusion were first introduced by H.C. Torrey, by adding an additional term (red in Eq. 29) to the Bloch equations, accounting for the effect of molecular self-diffusion [41]. The self-diffusion is represented as a “transport of magnetization” [35]. The transverse magnetization M_+ in the rotating frame is therefore:

$$\frac{\partial M_+}{\partial t} = -i\gamma\mathbf{r} \cdot \mathbf{G}^*(t)M_+ - \frac{M_+}{T_2} + D\nabla^2 M_+ \quad (29)$$

where $M_+ = M_x + iM_y$ and $\mathbf{G}^*(t)$ is the effective gradient, which is the equivalent total gradient accounting for the effect of the 180° RF pulse.

If we consider the part of Eq. 29 that accounts for diffusion separately from the rest, we can write down a solution for M_+ .

$$M_+ = E(t) \cdot \exp\left(-i\gamma\mathbf{r} \cdot \int_0^t \mathbf{G}^*(t')dt'\right) \cdot \exp\left(-\frac{t}{T_2}\right) \quad (30)$$

where $E(t)$ here represents the signal attenuation due to diffusion. If we substitute Eq. 30 into Eq. 29 and compute the expression for both sides of Eq. 29, an expression for $E(t)$ can be obtained:

$$\begin{aligned} \frac{\partial E(t)}{\partial t} &= -D\gamma^2 \left[\int_0^t \mathbf{G}^*(t')dt' \right]^2 E(t) \\ E(t) &= \exp\left(-D\gamma^2 \int_0^t \left[\int_0^{t'} \mathbf{G}^*(t'')dt'' \right]^2 dt'\right) \end{aligned} \quad (31)$$

Note that the signal attenuation due to diffusion is often expressed as $E(t) = \exp(-bD)$, where the gradient terms are gathered in a “ b -value” [42]. This quantity named by the French scientist Denis Le Bihan is frequently used to quantify the diffusion weighting [42].

$$b = \gamma^2 \int_0^t \left[\int_0^{t'} \mathbf{G}^*(t'') dt'' \right]^2 dt' \quad (32)$$

For a typical PGSE sequence (Figure 2.10), the signal attenuation due to diffusion can be calculated by integrating Eq. 31 from 0 to the echo time TE:

$$E(t) = \exp\left(-D\gamma^2 G^2 \delta^2 \left(\Delta - \frac{\delta}{3}\right)\right)$$

This mathematical formalism is commonly used for mapping of the isotropic apparent diffusion coefficient (ADC) or the diffusion tensors.

2.3.7 Diffusion contrast at short measurement time

The Bloch-Torrey equation describes the analytical relationship between signal attenuation and diffusion coefficient for free diffusion on a macroscopic scale. In the case of restricted diffusion inside of finite structures, this macroscopic approach becomes mathematically intractable. As a result, a variety of different approximations have been introduced to find analytical formulations of signal attenuation, accounting for the diffusion coefficient, boundary and experimental conditions [43]. Two common approximations have been developed, the short pulse gradient (SPG) approximation and the Gaussian phase distribution (GPD) approximation. In this section, we are going to discuss the theory behind both approximations [35].

Short pulse gradient (SPG) approximation

The SPG approximation is the basis of the diffusion signal simulation code - Microstructure imaging sequence simulation toolbox (MISST), used in this manuscript. The restricted diffusion under general gradient waveforms were handled by breaking the gradient pulse into successive narrow intervals and writing a propagator for each stage of the evolution. These evolutions were expressed in terms of a product of matrix operators [43]. Hence, this method was referred to as

the matrix method. The detailed formulations and validations can be found in multiple published studies [44], [45].

The underlying principle of the short pulse gradient (SPG) approximation is that gradient field pulses must be sufficiently narrow so that we may neglect molecular motion over the gradient pulse duration, *i.e.* $\delta \ll \Delta$. This way, the effect of the first gradient field pulse is merely to impart a phase shift $\gamma\delta\mathbf{G} \cdot \mathbf{r}_0$. This effect is subsequently inverted by the 180° RF pulse. After the second gradient field pulse, the net phase shift $\Delta\phi$ is $\gamma\delta\mathbf{G} \cdot (\mathbf{r}_1 - \mathbf{r}_0)$. If the spins are stationary, a perfectly refocused echo will occur. If the spins have moved, the net phase shift will contribute to the loss of signal in the echo.

The signal attenuation due to diffusion can be written as $\langle \exp(i\Delta\phi) \rangle = \langle \exp(i\gamma\delta\mathbf{G} \cdot (\mathbf{r}_1 - \mathbf{r}_0)) \rangle$. If we neglect the relaxation effects and consider the initial distribution of particles $\rho(\mathbf{r}_0)$, the total echo signal is given by the ensemble average of the phase term $\int \rho(\mathbf{r}_0) \cdot \langle \exp(i\gamma\delta\mathbf{G} \cdot (\mathbf{r}_1 - \mathbf{r}_0)) \rangle$. Therefore, the ensemble average accounting for the probability that a particle moves from position \mathbf{r}_0 to \mathbf{r}_1 in the time interval Δ is:

$$E(\mathbf{G}, \Delta) = \int \int \rho(\mathbf{r}_0) P(\mathbf{r}_0 | \mathbf{r}_1, \Delta) \exp(i\gamma\delta\mathbf{G} \cdot (\mathbf{r}_1 - \mathbf{r}_0)) d\mathbf{r}_0 d\mathbf{r}_1 \quad (33)$$

We can then define a reciprocal space $\mathbf{q} = \frac{1}{2\pi} \gamma\delta\mathbf{G}$. $E(\mathbf{G}, \Delta)$ is therefore,

$$E(\mathbf{q}, \Delta) = \int \int \rho(\mathbf{r}_0) P(\mathbf{r}_0 | \mathbf{r}_1, \Delta) \exp(2\pi i \mathbf{q} \cdot (\mathbf{r}_1 - \mathbf{r}_0)) d\mathbf{r}_0 d\mathbf{r}_1 \quad (34)$$

Since the integrand is only displacement dependent, we can define $\mathbf{r}_1 = \mathbf{r}_0 + \mathbf{R}$ and the average propagator as $\bar{P}(\mathbf{R}, \Delta) = \int \rho(\mathbf{r}_0) P(\mathbf{r}_0 | \mathbf{r}_0 + \mathbf{R}, \Delta) d\mathbf{r}_0$. Therefore, Equation 33 can be simplified to:

$$E(\mathbf{q}, \Delta) = \int \bar{P}(\mathbf{R}, \Delta) \exp(2\pi i \mathbf{q} \cdot \mathbf{R}) d\mathbf{R} \quad (35)$$

Note that there is a Fourier relationship between $E(\mathbf{G}, \Delta)$ and $\bar{P}(\mathbf{R}, t)$. Using the SPG approximation, acquiring the signal in q-space allows the estimation of $\bar{P}(\mathbf{R}, t)$.

Gaussian phase distribution approximation (GPD)

The SPG approximation requires a sufficiently narrow gradient pulse. However, due to hardware limitations of the clinical MR scanner, such a requirement is difficult to meet. An analytical expression of the restricted diffusion signal can be constructed assuming the displacement of the spins and their phases follow a Gaussian distribution [46], [47]. The signal equation is derived here. The significance of the Gaussian phase distribution will become apparent in the derivation.

Recall the net phase shift after the second RF pulse $\Delta\phi = \gamma\delta\mathbf{G} \cdot (\mathbf{r}_1 - \mathbf{r}_0)$. In a more general form,

$$\Delta\phi = \gamma \int_0^t \mathbf{G}^*(t') \cdot [(\mathbf{r}_1(t') - \mathbf{r}_0)] dt' \quad (36)$$

Using integration by parts,

$$\begin{aligned} a &= [(\mathbf{r}_1(t') - \mathbf{r}_0)] & l &= \gamma \int_0^t \mathbf{G}^*(t') dt' \\ \frac{da}{dt} &= \mathbf{v}_1(t') & \frac{dl}{dt} &= \gamma \mathbf{G}^*(t') \end{aligned}$$

where \mathbf{v}_1 here signifies the particle velocity. The expression of $\Delta\phi$ then becomes:

$$\Delta\phi = [(\mathbf{r}_1(t') - \mathbf{r}_0)] \gamma \int_0^t \mathbf{G}^*(t') dt' - \int_0^t \mathbf{v}_1(t') dt' \gamma \int_0^t \mathbf{G}^*(t') dt'$$

To simplify this equation further,

$$\mathbf{F}(t) = \gamma \int_0^t \mathbf{G}^*(t') dt' \quad (37)$$

And

$$\Delta\phi = [(\mathbf{r}_1(t') - \mathbf{r}_0)] \gamma \int_0^t G^*(t') dt' - \int_0^t \mathbf{v}_1(t') \mathbf{F}(t) dt'$$

At the point of echo formation, $\int_0^{TE} \mathbf{G}^*(t') dt' = 0$, thus,

$$\Delta\phi = - \int_0^t \mathbf{v}_1(t') \mathbf{F}(t') dt' \quad (38)$$

As mentioned previously, the signal attenuation due to diffusion can be written as the ensemble average of spin shifts as:

$$\langle \exp(i\Delta\phi) \rangle = \langle \exp(-i \int_0^t \mathbf{v}(t') \mathbf{F}(t') dt') \rangle$$

The total echo signal has contribution from the initial spin distribution, hence,

$$S = S_0 \langle \exp(i\Delta\phi) \rangle$$

Let the normalized signal $E(t) = \langle \exp(i\Delta\phi) \rangle$, and applying the cumulant expansion theorem,

$$E(t) = \langle \exp(i\Delta\phi) \rangle = \exp(i\langle \Delta\phi \rangle - \frac{1}{2}(\langle \Delta\phi^2 \rangle - \langle \Delta\phi \rangle^2) + \text{higher order terms})$$

Because of the stochastic nature of the interaction, we can assume that the particle velocity changes in small independent steps. In this case, the central-limit theorem allows a Gaussian approximation of the modulation distribution function. This means that one can neglect all higher correlations but the second term [46].

$$E(t) = \exp(i\langle \Delta\phi \rangle - \frac{1}{2}(\langle \Delta\phi^2 \rangle - \langle \Delta\phi \rangle^2)) = \exp(i\alpha(t) - \beta(t))$$

where,

$$\begin{aligned}\alpha(t) &= \Delta\phi = - \int_0^t \langle \mathbf{v}(t') \rangle \mathbf{F}(t') dt' \\ \beta(t) &= \frac{1}{2} \left(\left\langle \left[\int_0^t \langle \mathbf{v}(t') \rangle \mathbf{F}(t') dt' \right]^2 \right\rangle - \left[\int_0^t \langle \mathbf{v}(t') \rangle \mathbf{F}(t') dt' \right]^2 \right) \\ &= \frac{1}{2} \int_0^t \int_0^t \mathbf{F}(t') \langle \mathbf{v}(t') \mathbf{v}(t'') \rangle \mathbf{F}(t'') dt' dt''\end{aligned}\quad (39)$$

The α term represents the phase change due to flow drift and the β term represents the phase change because of random particle migration, namely diffusion. Notice that there is a velocity autocorrelation function in Eq. 39, which describes the correlation between particle velocity at a time point with its velocity at a later time.

We can also re-write Equation 39 in terms of the particle-particle correlation $\langle r(t_1)r(t_2) \rangle$:

$$\beta(t) = \frac{\gamma^2}{2} \int_0^t \int_0^t \mathbf{G}^*(t_1) \langle r_1(t_1)r_2(t_2) \rangle \mathbf{G}^*(t_2) dt_1 dt_2 \quad (40)$$

In the case of restricted diffusion,

$$\beta(t) = \frac{\gamma^2}{2} \int_0^t \int_0^t \rho(\mathbf{r}_1) \int_V \int_V \mathbf{r}_1 P(\mathbf{r}_1, t_1 | \mathbf{r}_2, t_2) \mathbf{r}_2 d\mathbf{r}_1 d\mathbf{r}_2 \mathbf{G}^*(t_1) \mathbf{G}^*(t_2) dt_1 dt_2 \quad (41)$$

Using the general solution of conditional probability for bounded medium (Eq. 27):

$P(\mathbf{r}_1, t_1 | \mathbf{r}_2, t_2) = \sum_{n=0}^{\infty} u_n^*(\mathbf{r}_2) u_n(\mathbf{r}_1) e^{-D\lambda_n(t_2-t_1)}$, Equation 41 becomes:

$$\beta(t) = \frac{\gamma^2}{2} \int_0^t \int_0^t \rho(\mathbf{r}_1) \int_V \int_V \mathbf{r}_1 \sum_{n=0}^{\infty} u_n^*(\mathbf{r}_2) u_n(\mathbf{r}_1) e^{-D\lambda_n(t_2-t_1)} \mathbf{r}_2 d\mathbf{r}_1 d\mathbf{r}_2 \mathbf{G}^*(t_1) \mathbf{G}^*(t_2) dt_1 dt_2 \quad (42)$$

Let $B_n = \frac{1}{\rho} \int_V d\mathbf{r}_1 \int_V \mathbf{r}_1 \mathbf{r}_2 u_n^*(\mathbf{r}_2) u_n(\mathbf{r}_1) d\mathbf{r}_2$, Equation 41 then becomes:

$$\beta(t) = \frac{\gamma^2}{2} \sum_{k=0}^{\infty} B_k \int_0^t \int_0^t e^{-D\lambda_n(t_2-t_1)} \cdot \mathbf{G}^*(t_1)\mathbf{G}^*(t_2) dt_1 dt_2 \quad (43)$$

Here, B_n, λ_n are geometry dependent factors, which have analytical expressions for simple geometries including impermeable parallel planes, cylinders, spheres and spherical shells [46], [48], [49].

Under the GPD approximation, the signal due to diffusion becomes:

$$E(t) = \exp(-\beta(t)) = \exp\left(-\frac{\gamma^2}{2} \sum_{k=0}^{\infty} B_k \int_0^t \int_0^t e^{-D\lambda_n(t_2-t_1)} \cdot \mathbf{G}^*(t_1)\mathbf{G}^*(t_2) dt_1 dt_2\right) \quad (44)$$

2.3.8 Diffusion spectrum

The PGSE sequences are widely used for diffusion weighted imaging to capture the average diffusion properties in tissue. Narrow pulses are necessary to provide the short diffusion times required to probe the dimensions of cellular structures. Short pulses are often challenging to fulfill, partly due to the limitation on the gradient system hardware. A different approach was proposed in the 1980s by Stepisnik et al., in which the use of gradients to measure motion is described in the frequency domain. This method is termed temporal diffusion spectroscopy [50].

The diffusion spectrum can be expressed as the Fourier transform of the velocity autocorrelation function [50]:

$$D(\omega) = \int_0^{\infty} \langle v(t')v(0) \rangle \exp(i\omega t') dt' \quad (45)$$

The velocity autocorrelation function $\langle v(t')v(0) \rangle$ indicates the dependence of the particle velocity at time t' on the velocity at $t = 0$. For free diffusion, the particle velocity is independent of its previous state. As a result, $\langle v(t')v(0) \rangle$ resembles a delta function, leading to a flat spectrum of

$D(\omega)$ (Figure 2.11). When diffusion is restricted, $D(\omega)$ is no longer flat. There is a negative velocity autocorrelation caused by the reflection on the boundaries. The diffusion spectrum is frequency dependent and exhibits a dip at low frequencies [51]. The manner in which $D(\omega)$ disperses with frequency can provide unique information on the structure of the medium.

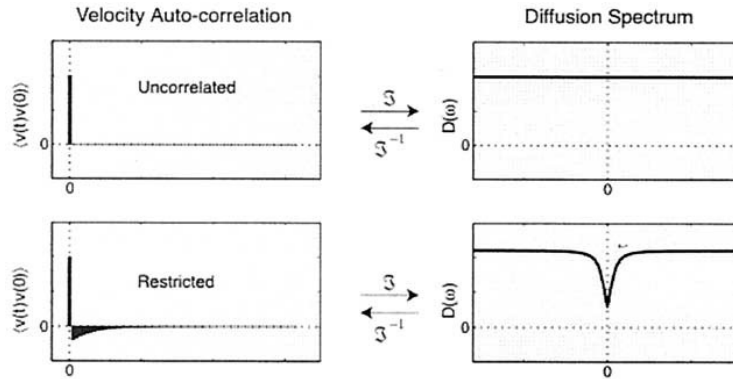


Figure 2.11 Qualitative illustration of velocity autocorrelation functions and their corresponding diffusion spectra. Unrestricted water (top) experiencing only Brownian motion exhibits a flat diffusion spectrum, while restriction (bottom) acts to decrease the diffusion spectrum amplitude at lower frequencies. Figure reprinted from Magnetic Resonance Imaging 21 (3-4), Parsons EC et al. Modified oscillating gradient pulses for direct sampling of the diffusion spectrum suitable for imaging sequences, Pages 279-285, © 2003, with permission from Elsevier [52].

The velocity autocorrelation function can also be expressed in terms of the diffusion spectrum $D(\omega)$ by applying the inverse Fourier transform:

$$\langle v(t_1)v(t_2) \rangle = \frac{1}{\pi} \int_{-\infty}^{\infty} D(\omega) \exp(-i\omega(t_1 - t_2)) d\omega \quad (46)$$

Substituting Eq. 46 to Eq. 39, $\beta(t)$ can be expressed in terms of the frequency spectrum as:

$$\begin{aligned}
\beta(t) &= \frac{1}{2} \int_0^t \int_0^t F(t_1) \langle v(t_1) v(t_2) \rangle F(t_2) dt_1 dt_2 \\
&= \frac{1}{2} \int_0^t \int_0^t F(t_1) \frac{1}{\pi} \int_{-\infty}^{\infty} D(\omega) \exp(-i\omega(t_1 - t_2)) d\omega F(t_2) dt_1 dt_2 \\
&= \frac{1}{2\pi} \int_0^t F(t_1) \exp(-i\omega t_1) dt_1 \int_0^t F(t_2) \exp(i\omega t_2) dt_2 \int_{-\infty}^{\infty} D(\omega) d\omega \\
&= \frac{1}{2\pi} \int_{-\infty}^{\infty} F(-\omega) D(\omega) F(\omega) d\omega
\end{aligned} \tag{47}$$

where,

$$F(\omega) = \int_0^t \exp(i\omega t) F(t') dt' \tag{48}$$

The signal attenuation due to diffusion expressed in the frequency domain is thus:

$$E(t) = \exp(-\beta(t)) = \exp\left(-\frac{1}{2\pi} \int_0^{\infty} F(\omega) D(\omega) F(-\omega) d\omega\right) \tag{49}$$

Equation 49 has important implications that the signal attenuation depends on the shape and the frequency of the gradient waveforms. This is particularly useful when studying the effect of an oscillating gradient waveform on the measurement of diffusion coefficients.

2.3.9 Diffusion encoding sequences

The standard diffusion encoding PGSE sequence uses gradient field pulses in the shape of a rectangle (assuming infinite slew rate), with relatively long diffusion intervals and gradient pulses of finite width (Figure 2.12). In light of the development in temporal diffusion spectroscopy (described in section 2.3.7), alternative gradient waveforms can be used to improve the sensitivity of the diffusion signal to tissue characteristics on a cellular level. For example, oscillating gradient spin echo (OGSE) sequences replace the rectangular gradient with oscillating gradients, such as sine, cosine, square or trapezoidal waveforms (Figure 2.12). The OGSE sequences allow us to probe shorter diffusion times, with more relaxed requirements on the gradient coil hardware.

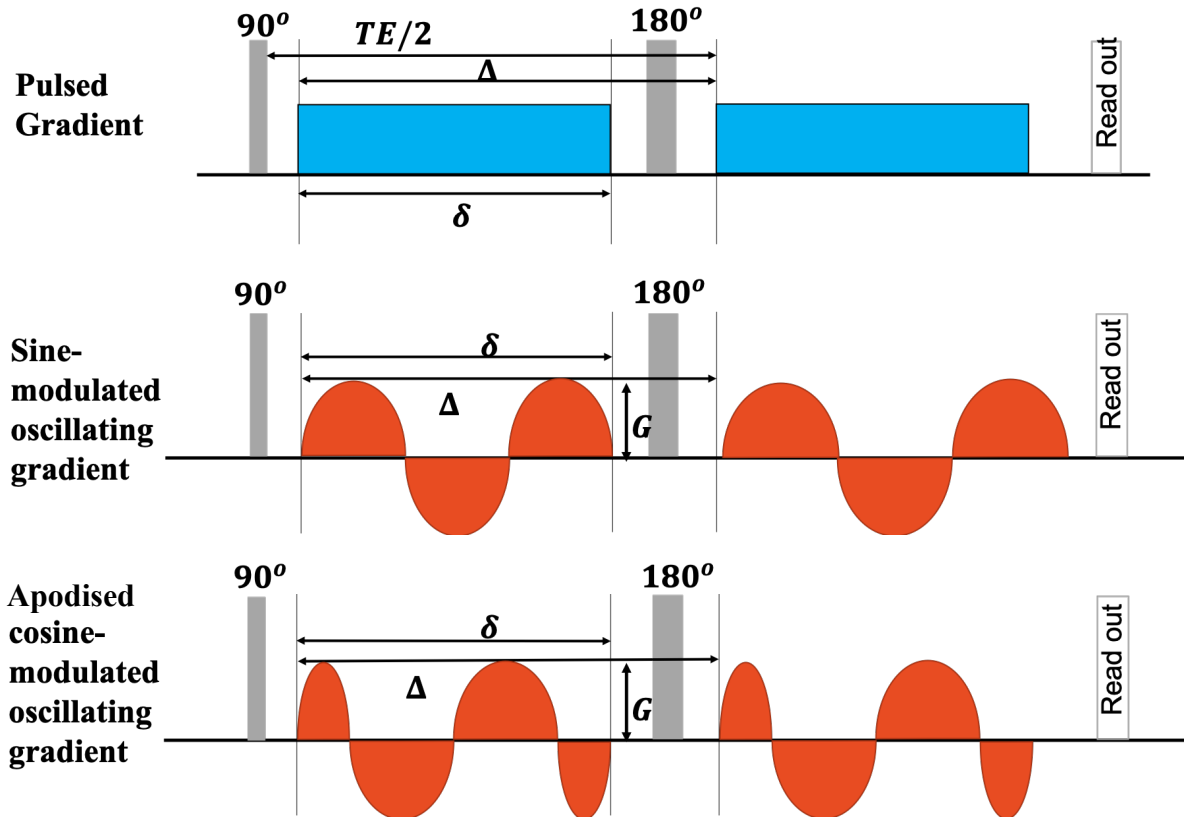


Figure 2.12 Schematic illustration of the standard pulsed gradient spin echo (PGSE) sequence, the sine-modulated and cosine-modulated oscillating gradient spin echo (OGSE) sequences. The sinusoidal waveform can be replaced with square or trapezoidal waveforms.

It is worth noting that the cosine-OGSE poses the challenge of a sharp initial pulse edge. Experimentally, we need to smooth the initial transient by replacing the first quarter cycle cosine with a half cycle sine-lobe at twice the frequency (Figure 2.12). This sequence is often referred to as the apodised cosine-OGSE [52].

For PGSE sequences, the diffusion weighting imparted by the gradient is represented by the b -value (discussed in section 2.3.6) as:

$$b = \int_0^t dt \left[\gamma \int_0^{t'} G(t'') dt'' \right]^2 = \gamma^2 G^2 \delta^2 \left(\Delta - \frac{\delta}{3} \right)$$

For OGSE sequences, the b -values can be derived in a similar fashion, by replacing the gradient pulses of a constant amplitude with the oscillating gradient waveforms. For example, the b -value of a sine-modulated gradient waveform is expressed as

$$b = \int_0^t dt \left[\gamma \int_0^{t'} G(t'') dt'' \right]^2 = \int_0^{2\tau} dt \left[\gamma \int_0^{t'} G \sin(\omega t'') dt'' \right]^2 \quad (50)$$

where τ represents the echo time, ω as the modulation frequency of the gradient waveform $\omega = \frac{2\pi}{T}$ and T as the period of the oscillation. The total duration of the gradient contains N periods, hence $\delta = NT$. Solving the integral in Eq. 50 gives us an expression for the b -value for a sine-modulated gradient waveform:

$$b = \int_0^{2\tau} dt \left[\gamma G \left(\frac{-\cos(\omega t')}{\omega} + \frac{1}{\omega} \right) \right]^2 = \frac{3}{4} \left(\frac{\gamma G}{\pi N} \right)^2 \delta^3 \quad (51)$$

Similarly, the b -value for the apodised-cosine-modulated waveform can be computed using Eq.32 in a piecewise manner. The first and last gradient lobes have twice the oscillating frequency.

$$G(t) = \begin{cases} G \sin(2\omega t), & 0 \leq t < \frac{T}{4} \\ G \cos(\omega t), & \frac{T}{4} \leq t < \delta - \frac{T}{4} \\ G \sin(2\omega t), & \delta - \frac{T}{4} \leq t < \delta \end{cases}$$

The expression for the b -value of the apodised cosine modulated gradient waveform is derived as:

$$\begin{aligned} b &= 2 \left(\int_0^{\frac{T}{4}} dt \left[\gamma \int_0^{t'} G \sin(2\omega t'') dt'' \right]^2 + \int_{\frac{T}{4}}^{\delta - \frac{T}{4}} dt \left[\gamma \int_0^{t'} G \cos(\omega t'') dt'' \right]^2 + \int_{\delta - \frac{T}{4}}^{\delta} dt \left[\gamma \int_0^{t'} G \sin(2\omega t'') dt'' \right]^2 \right) \\ &= \frac{1}{4} \left(\frac{\gamma G}{\pi N} \right)^2 \delta^3 \left(1 - \frac{1}{8N} \right) \end{aligned} \quad (52)$$

The effective diffusion time (Δ_{eff}) provides an intuitive sense of the time scale of the diffusion measurement and can be computed for OGSE by comparison to the Δ_{eff} calculation of PGSE. For a PGSE sequence, $b = \gamma^2 G^2 \delta^2 \left(\Delta - \frac{\delta}{3} \right)$, where $G\delta$ is the area of the rectangular gradient pulse and $\left(\Delta - \frac{\delta}{3} \right)$ is defined as Δ_{eff} [53]. For a sine-modulated waveform of period τ , the area under one lobe is $\int_0^\pi G \sin(\omega t) dt = \frac{G\tau}{\pi}$. Rewriting the b-value expression for sine-modulated waveform (Eq. 51):

$$b = \frac{3}{4} \left(\frac{\gamma G}{\pi N} \right)^2 \delta^3 = N \gamma^2 \left(\frac{G\tau}{\pi} \right)^2 \left(\frac{3\delta}{4N} \right) \quad (53)$$

where the effective diffusion time $\Delta_{eff} = \frac{3\delta}{4N}$. The leading term N in Eq. 46 reflects the repeated gradient periods. Similarly, the Δ_{eff} can be computed for other waveforms (Table 2.1). As the Δ_{eff} is inversely dependent on the number of oscillations N , a shorter Δ_{eff} (< 10 ms) could be achieved by increasing N for the same gradient duration time. Reaching shorter diffusion times greatly improves the sensitivity of the diffusion signal to tissue microstructure characteristics, such as cell size and volume fractions. As a result, OGSE sequences are widely used to study the tumor microenvironment and their changes during cancer therapy.

Table 2.1 Summary of b-values and effective diffusion time for various waveforms

Pulse shape	b-values	Effective diffusion time Δ_{eff}
PGSE	$\gamma^2 G^2 \delta^2 \left(\Delta - \frac{\delta}{3} \right)$	$\left(\Delta - \frac{\delta}{3} \right)$
OGSE-sine	$\frac{3}{4} \left(\frac{\gamma G}{\pi N} \right)^2 \delta^3$	$\frac{3\delta}{4N}$
OGSE-cosine	$\frac{1}{4} \left(\frac{\gamma G}{\pi N} \right)^2 \delta^3$	$\frac{\delta}{4N}$
OGSE- apodised cosine	$\frac{1}{4} \left(\frac{\gamma G}{\pi N} \right)^2 \delta^3 \left(1 - \frac{1}{8N} \right)$	$\frac{\delta}{4N}$

2.4 Diffusion MRI Modelling

In order to extract physically or biologically meaningful information from the diffusion signals, various diffusion models were proposed. Depending on the complexity of the diffusion measurements, different models can be applied to infer a wide range of parameters representing tissue characteristics. Here, we present several of the most commonly used models, starting with the simplest mono-exponential model.

2.4.1 Apparent diffusion coefficient (ADC)

In a free medium, the conditional probability distribution of diffusion follows a Gaussian distribution. The diffusion signal can be written as $S = S_0 e^{-b \cdot D}$ (discussed in section 2.3.6). This means that if we assume free diffusion in an isotropic, homogeneous environment, such as water, the MR signal follows a mono-exponential decay. A linear fit to the log of the measured signal at different b-values would allow us to estimate the diffusion coefficient D of water.

In more complex media, e.g. biological tissues, the water molecules are slowed down by various barriers, such as cell membranes and macromolecules. If we assume that we have no prior knowledge of the media, we can perform the same measurement as if it was done in free water. However, the negative slope of the linear fit no longer represents the true water diffusion coefficient. It characterizes the water diffusion coefficient modulated by inhomogeneities, namely the apparent diffusion coefficient (ADC).

$$ADC = -\frac{\log\left(\frac{S}{S_0}\right)}{b} \quad (54)$$

ADC is of particular interest for cancer applications because it is related to cellularity. In general, malignant tumors have more densely packed cells than normal tissue, leading to lower ADCs (Figure 2.13 (a)-(b)). Liquefactive necrosis (i.e. cell death) with an ADC close to free water occasionally occurs in advanced tumors and in response to successful treatment (Figure 2.13 (c)).

Therefore, ADC has been used as a clinical biomarker to aid cancer diagnosis and treatment assessment [54].

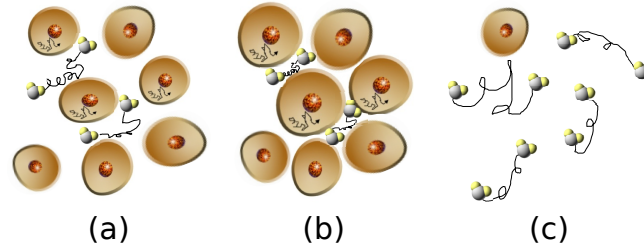


Figure 2.13 Schematics of water molecule diffusion in (a) normal tissue: loosely packed cells, (b) cancerous tissue: densely packed cells and (c) fluid or necrosis: close to free diffusion

2.4.2 Diffusion Tensor Imaging

Pure water is known to have isotropic diffusion properties, meaning that the molecules are equally likely to displace in any direction. This implies that the diffusion can be measured in any physical direction and the effect on the MR signal would be identical. Diffusion in cancer cells is assumed to be isotropic, where a single ADC is sufficient to characterize the behavior of the water molecules in a restricted environment (Figure 2.14 (a)).

For anisotropic tissues, such as neurons in the white matter of the brain, the magnitude of the diffusion coefficient is direction dependent. As demonstrated Figure 2.14 (b), water diffusion along the cylinder would experience faster diffusion compared to the water diffusion perpendicular to the cylinder, *i.e.* $D_{xx} = D_{yy} \ll D_{zz}$. The diffusion properties can be described mathematically by a diffusion tensor with diffusion coefficients along 9 different directions:

$$[D] = \begin{bmatrix} D_{xx} & D_{xy} & D_{xz} \\ D_{yx} & D_{yy} & D_{yz} \\ D_{zx} & D_{zy} & D_{zz} \end{bmatrix} \quad (55)$$

The diffusion tensor is symmetric (*i.e.* $D_{xy} = D_{yx}$), thus it contains only 6 unique values (marked in blue, Eq. 55). For the special case of isotropic diffusion, the off-diagonal elements are all zero

and the diagonal elements are the same and equal to a single value, $D_{xx} = D_{yy} = D_{zz} = ADC$. For anisotropic diffusion, however, the diagonal elements are no longer the same and the off-diagonal elements are not negligible. To make a full measurement of ADC in anisotropic tissue, diffusion images in 6 directions and a $b = 0$ unweighted image are required.

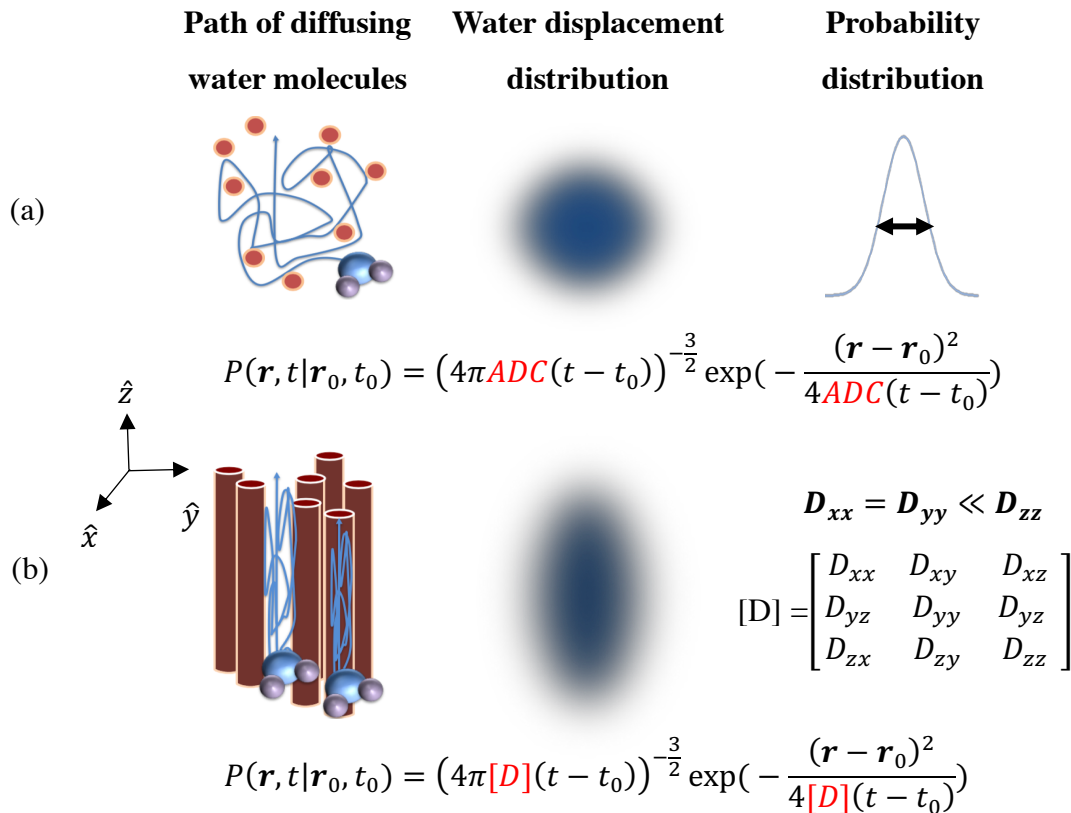


Figure 2.14 The first row demonstrates the isotropic diffusion of water molecules in a hindered environment. The displacement distribution can be described by a Gaussian function with a single ADC. The second row demonstrates diffusion in anisotropic tissues. The diffusion coefficients are direction dependent. The diffusion properties have to be described by a diffusion tensor.

2.4.3 IVIM model

When the diffusion measurement is performed in well-perfused body tissues, such as liver, prostate or brain, the signal attenuation at low b -values ($< 200 \text{ s/mm}^2$) arises not only from diffusion, but also from the microcirculation within the normal capillary network [55]. This phenomenon is termed the intravoxel incoherent motion (IVIM) effect [56], which leads to a much faster signal decay at low b -values (Figure 2.15). As a result, a mono-exponential model is unable to fit the signal properly.

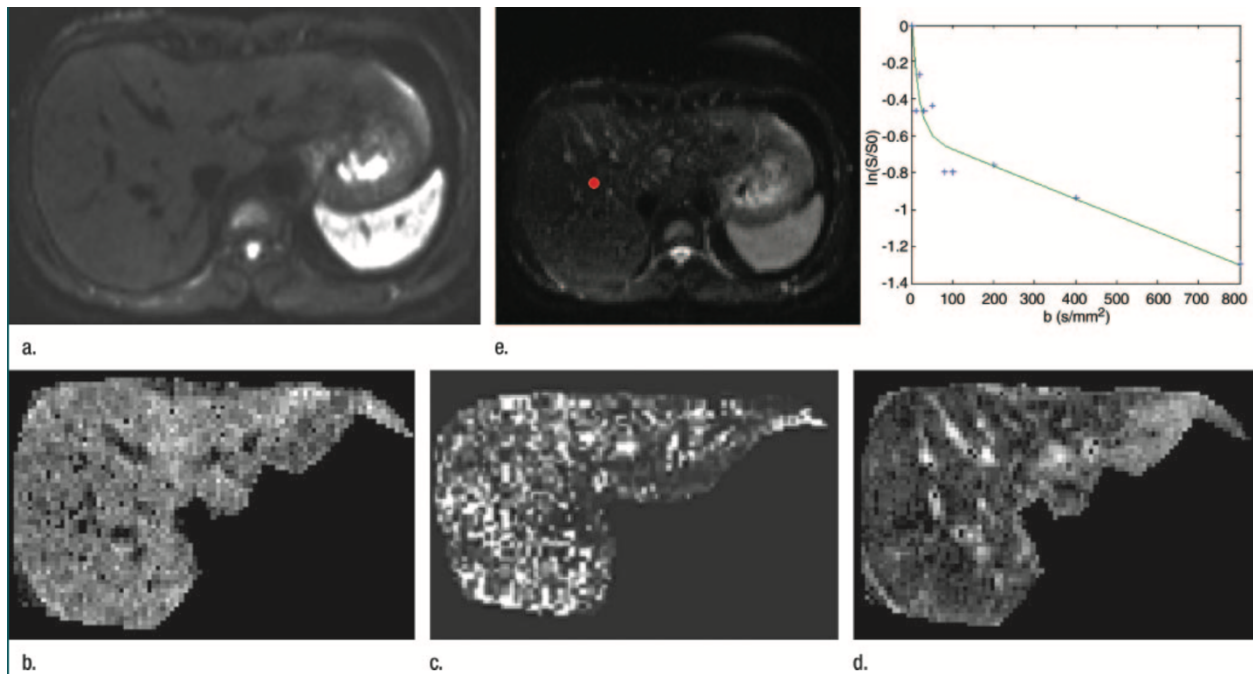


Figure 2.15 Illustration of the influence from the IVIM effect on the diffusion signal in liver at lower b -values. A biexponential behavior is clearly observed in the signal with respect to b -values. Figure reprinted from Radiology 249 Luciani A, Vignaud A. et al. Liver Cirrhosis: Intravoxel Incoherent Motion MR Imaging – Pilot Study, Pages 891-899, © 2008, with permission from Radiological Society of North America [57].

Le Bihan et al. have proposed a bi-exponential model to describe the IVIM effect [56]:

$$S = S_0 [(1 - f)e^{-bD} + fe^{-b(D^*)}] \quad (56)$$

where signal is composed of slow and fast diffusion compartments. D and D^* represent the slow and fast diffusion coefficients respectively, and f represents the fraction of signal decay from the fast compartment due to microcirculatory perfusion. Microcirculatory perfusion has no specific orientation and therefore can be considered as a type of “pseudo diffusion” with coefficient D^* .

The bi-exponential model provides a more appropriate description of the signal attenuation in well-perfused body tissues. For studies that are solely interested in the diffusion characteristics, the IVIM effect can be reduced by fitting the mono-exponential model to signals from higher b -values ($> 200 \text{ s/mm}^2$) only.

2.4.4 Stanisz’ model

In the previous decades, extensive research has been done on improving the image quality of ADC mapping (section 2.3) and diffusion tensor imaging (section 2.4). These techniques have been gradually integrated into the clinical workflow. One downfall of these techniques is that they can only provide information above the nominal resolution of clinical MRI, which is constrained to the millimeter level. Unwilling to settle for the resolution limitation, the diffusion MR community started to explore the feasibility of mapping cellular-level biophysics parameters, such as cell size, % cell volume and membrane permeability [58].

One of the first biophysical models was proposed by Stanisz et al., which described restricted diffusion signal in bovine optic nerves [59]. The study represented the tissue using three compartments: prolate ellipsoids for axons, spheres for glial cells and hindered diffusion for the extracellular space. The short pulse gradient (SPG) approximation was applied to compute the analytical expression for the restricted diffusion signal in the axons and glial cells. Fitting the analytical equation to the measured signals allowed the estimation of the average axon diameter and length, the radius of glial cells and the intra-/extra-cellular diffusivities. While this study pioneered the development of microstructure imaging, the signal-to-noise ratio (SNR) requirement (>1000) makes the clinical translation of this model unfeasible.

2.4.5 CHARMED Model

A simpler version of the multi-compartment model for the characterization of axons was introduced by Assaf et al.[60], where tissue was represented with two compartments. The intra-axonal space was modeled as a distribution of cylinders, the extracellular space was represented as hindered diffusion with a cylindrically symmetric diffusion tensor [61]. This is referred to as the composite hindered and restricted model of diffusion (CHARMED). It is worth noting that hindered diffusion differs from restricted diffusion. Hindered diffusion refers to the delay of passage of water molecules as they navigate around cellular obstacles, such as in the extracellular space. On the other hand, restricted diffusion is used to describe the trapping of water molecules within an enclosed compartment, such as within cell membranes. The CHARMED model estimated axon orientation, intracellular diffusivity parallel to the axons, extracellular diffusivity and the relative volume fraction of each compartment, while keeping the axon diameters fixed to a pre-defined value.

Building on their own CHARMED model, Assaf et al. later developed a technique, AxCaliber, which allowed the estimation of axon diameters, assuming a known axon orientation and a Gamma distribution for the axon diameters [62]. AxCaliber was then validated with ex-vivo experiments using porcine optic and sciatic nerves. The estimated axon diameter distributions from MRI showed agreement with the axon diameter distribution derived from electron microscopy measurements.

CHARMED and AxCaliber models served as a foundation for the development of *in-vivo* microstructure imaging in the brain. Other techniques including ActiveAx [63], high angular resolution diffusion imaging (HARDI) [64] and neurite orientation dispersion and density imaging (NODDI) [65] built on the existing framework and tried to address some of their limitations.

2.4.6 VERDICT Model

The majority of the early microstructure imaging work, such as CHARMED, was developed for neurological applications. As MRI became increasingly popular for the diagnosis of cancerous

tumors, the use of biophysical models was extended for microstructure imaging in tumors. Vascular, extracellular and restricted diffusion for cytometry in tumors (VERDICT) was one of the first models to describe diffusion in the tumor microenvironment. The diffusion signal from tumor tissue was represented by the linear combination of signal from three compartments: 1) restricted diffusion inside the cell, modeled as impermeable spheres, 2) hindered diffusion outside the cells and blood vessels, and 3) pseudo-diffusion inside the blood vessels (Figure 2.16). The VERDICT model contained 6 variables including the cell radius R , the intracellular and extracellular diffusivity D_{ic} and D_{ees} , the pseudo-diffusivity D_p and the intra- and extra-cellular volume fraction f_{ic} and f_{ees} . The vascular volume fraction f_{vas} was calculated as $1 - f_{ic} - f_{ees}$. This technique was demonstrated in prostate cancer patients, where the estimated model parameters clearly differentiated benign from cancerous tumor subregions.

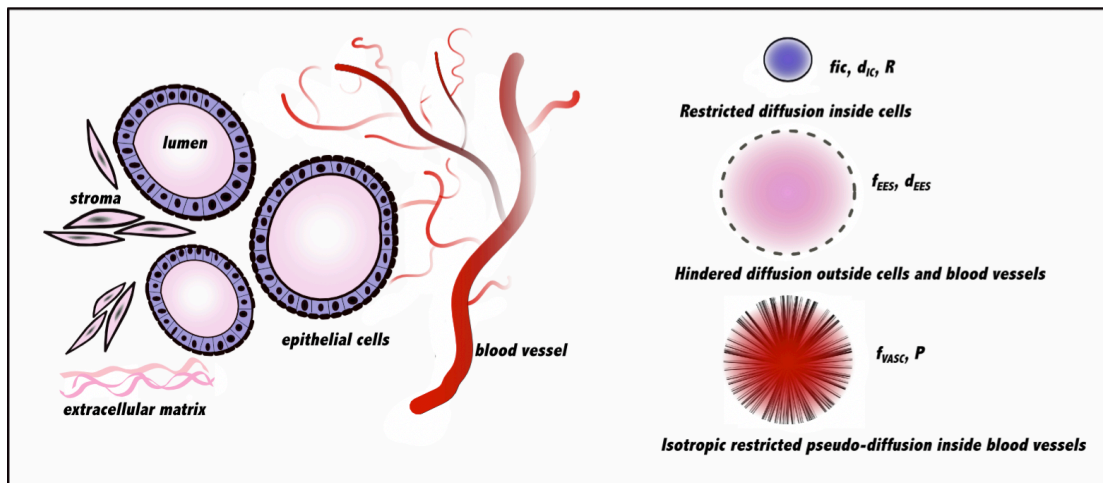


Figure 2.16 Schematic representations of the prostate tissue and the corresponding VERDICT model. Figure reprinted from *Investigative Radiology* 50 (4), Panagiotaki et al. Microstructural characterization of normal and malignant human prostate tissue with vascular, extracellular and restricted diffusion for cytometry in tumors magnetic resonance imaging, © 2015, with permission from Wolters Kluwer Health, Inc.[66].

While the VERDICT framework has the potential for clinical translation, it also has several limitations. For example, the diffusion signals were acquired using PGSE sequences with narrow gradient to reach short diffusion time and high b -values ($= 3000s/mm^2$). This requires high-performance gradient coils, which are not readily available in the clinic. In addition, due to the

complexity of the VERDICT model, some of the variables (D_{ic} , D_{ees} , D_p) were often fixed to improve the stability of the fitting.

2.4.7 IMPULSED Method

To overcome the limitation of the VERDICT model, the imaging microstructural parameters using limited spectrally edited diffusion (IMPULSED) method was proposed. The IMPULSED method used a combination of diffusion signals from the conventional PGSE sequence and OGSE sequences, where OGSE sequences could reach short diffusion times with a lower requirement on the maximum gradient strength [49]. Instead of the three-compartment model in VERDICT, the tumor tissue was described by two compartments (Figure 2.17): the restricted diffusion inside the cell, model as impermeable spheres, and the hindered diffusion outside of the cell.

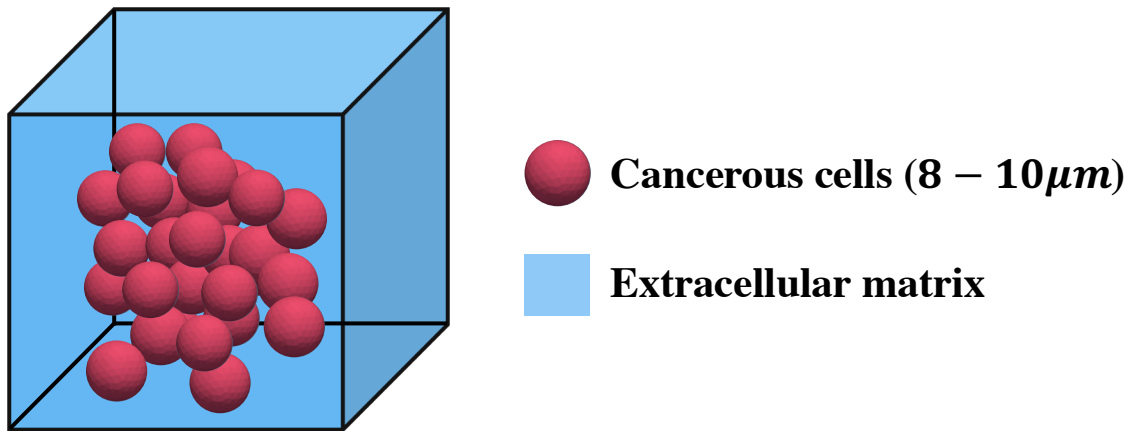


Figure 2.17 Schematic representation of the tissue model used in the IMPULSED method. The cancer cells were modeled as impermeable spheres. The extracellular diffusion was considered as hindered diffusion.

The normalized diffusion MR signal was modeled with an analytical expression combining the signal of intracellular restricted diffusion S_{in} , with the signal from hindered extracellular diffusion S_{exo} (Eq. 57).

$$S/S_0 = v_{in} S_{in}(R, D_{in}) + (1 - v_{in}) S_{exo}(D_{exo}) \quad (57)$$

Four variables in Eq. 57 were estimated including v_{in} , representing the percentage volume occupied by cells, referred to as the intracellular volume fraction, the cell radius R , and D_{in}/D_{exo} representing the intra- and extra-cellular diffusion coefficient, respectively.

The IMPULSED method was tested with in-vitro [49] and in-vivo experiments [67], where the cell radius extracted from the diffusion signal demonstrated good agreement with cell radius measured from histological slides viewed under the light microscope.

References

- [1] D. Hanahan and R. A. Weinberg, “Hallmarks of cancer: The next generation,” *Cell*. 2011.
- [2] Canadian Cancer Statistics Advisory Committee, *Canadian Cancer Statistics 2019*. 2019.
- [3] G. H. Heppner and B. E. Miller, “Tumor heterogeneity: biological implications and therapeutic consequences,” 1983.
- [4] R. García-Figueiras *et al.*, “How clinical imaging can assess cancer biology,” *Insights Imaging*, vol. 10, no. 1, p. 28, Dec. 2019.
- [5] R. J. Gillies, P. E. Kinahan, and H. Hricak, “Radiomics : Images Are More than Pictures, They Are Data,” vol. 278, no. 2, 2016.
- [6] J. Siracký, “An approach to the problem of heterogeneity of human tumor-cell populations,” *Br. J. Cancer*, vol. 39, no. 5, pp. 570–577, 1979.
- [7] D. L. Dexter, T. DeNucci, F. R. Miller, and P. Calabresi, “Heterogeneity in Drug Sensitivity among Tumor Cell Subpopulations of a Single Mammary Tumor,” *Cancer Res.*, vol. 38, pp. 3758–3763, Nov. 1978.
- [8] L. Håkansson and C. Tropé, “ON THE PRESENCE WITHIN TUMORS OF CLONES THAT DIFFER IN SENSITIVITY TO CYTOSTATIC DRUGS,” *Acta Pathol. Microbiol. Scand. Sect. A Pathol.*, vol. 82 A, no. 1, pp. 35–40, 1974.
- [9] F. Meric-Bernstam, C. Farhangfar, J. Mendelsohn, and G. B. Mills, “Building a personalized medicine infrastructure at a major cancer center,” *Journal of Clinical Oncology*, vol. 31, no. 15. American Society of Clinical Oncology, pp. 1849–1857, 20-May-2013.
- [10] J. T. Leith, L. A. Gaskins, D. L. Dexter, P. Calabresi, and A. S. Glicksman, “Alteration of the Survival Response of Two Human Colon Carcinoma Subpopulations to X-Irradiation by N,N-Dimethylformamide,” *Cancer Res.*, vol. 42, no. 1, pp. 30–34, Jan. 1982.
- [11] A. Pelin, S. Boulton, L. A. Tamming, J. C. Bell, and R. Singaravelu, “Engineering vaccinia virus as an immunotherapeutic battleship to overcome tumor heterogeneity,” *Expert Opin. Biol. Ther.*, Apr. 2020.
- [12] L. Annaratone *et al.*, “The Multifaceted Nature of Tumor Microenvironment in Breast Carcinomas,” *Pathobiology*, pp. 1–18, 2020.

- [13] E. H. Romond *et al.*, “Trastuzumab plus adjuvant chemotherapy for operable HER2-positive breast cancer,” *N. Engl. J. Med.*, vol. 353, no. 16, pp. 1673–1684, Oct. 2005.
- [14] S. Xing, C. R. Freeman, S. Jung, R. Turcotte, and I. R. Levesque, “Probabilistic classification of tumor habitats in soft tissue sarcoma,” *NMR Biomed.*, no. June, p. e4000, 2018.
- [15] B. V. Jardim-Perassi *et al.*, “Multiparametric MRI and coregistered histology identify tumor habitats in breast cancer mouse models,” *Cancer Res.*, vol. 79, no. 15, pp. 3952–3964, Aug. 2019.
- [16] J. M. Brown, “Tumor Hypoxia in Cancer Therapy,” *Methods in Enzymology*, vol. 435, 2007.
- [17] I. Heid *et al.*, “Co-clinical assessment of tumor cellularity in pancreatic cancer,” *Clin. Cancer Res.*, vol. 23, no. 6, pp. 1461–1470, Mar. 2017.
- [18] M. Vallières *et al.*, “Investigating the role of functional imaging in the management of soft-tissue sarcomas of the extremities,” 2018.
- [19] G. M. Cooper and R. E. Hausman, *The cell : a molecular approach*. .
- [20] R. Baserga, “Is Cell Size Important ?,” *Cell*, vol. 6, 2007.
- [21] L. Sun, S. Sakurai, T. Sano, M. Hironaka, O. Kawashima, and T. Nakajima, “High-grade neuroendocrine carcinoma of the lung: Comparative clinicopathological study of large cell neuroendocrine carcinoma and small cell lung carcinoma,” *Pathol. Int.*, vol. 59, no. 8, pp. 522–529, Aug. 2009.
- [22] M. F. Akay, “Support vector machines combined with feature selection for breast cancer diagnosis,” *Expert Syst. Appl.*, vol. 36, pp. 3240–3247.
- [23] A. L. Folpe and C. Y. Inwards, *Bone and soft tissue pathology*. Saunders/Elsevier, 2010.
- [24] U. Tateishi, T. Hasegawa, Y. Beppu, A. Kawai, and N. Moriyama, “Prognostic significance of grading (MIB-1 system) in patients with myxoid liposarcoma.” *J. Clin. Pathol.*, vol. 56, no. 8, pp. 579–82, Aug. 2003.
- [25] J. R. Goldblum, A. L. Folpe, S. W. Weiss, F. M. Enzinger, and S. W. Weiss, *Enzinger and Weiss’s soft tissue tumors*. .
- [26] F. Willeke *et al.*, “Analysis of FUS-CHOP fusion transcripts in different types of soft tissue liposarcoma and their diagnostic implications,” *Clin. Cancer Res.*, vol. 4, no. 7, pp. 1779–84, Jul. 1998.

- [27] S. E. Kilpatrick, J. Doyon, P. F. M. Choong, F. H. Sim, and A. G. Nascimento, "The clinicopathologic spectrum of myxoid and round cell liposarcoma: A study of 95 cases," *Cancer*, vol. 77, no. 8, pp. 1450–1458, Apr. 1996.
- [28] D. M. Patterson, A. R. Padhani, and D. J. Collins, "Technology insight: water diffusion MRI--a potential new biomarker of response to cancer therapy.," *Nat. Clin. Pract. Oncol.*, vol. 5, no. 4, pp. 220–233, 2008.
- [29] D. G. Nishimura, *Principles of magnetic resonance imaging*. Stanford Univ., 2010.
- [30] C. Westbrook and C. K. Roth, *MRI in Practice*. John Wiley & Sons, 2011.
- [31] M. Seufert, "PhD thesis," *ACM SIGMultimedia Rec.*, vol. 10, no. 3, pp. 13–13, 2018.
- [32] M. E. Haacke, R. W. Brown, M. R. Thompson, and R. Venkatesen, *Magnetic Resonance Imaging: Physical Principles and Sequence Design*. 1999.
- [33] M. E. Mercredi, "Probing Tissue Microstructure Using Oscillating Spin Echo Gradients," 2018.
- [34] A. R. Luna, R. Ribes, and J. A. Soto, *Diffusion MRI Outside the Brain*. Verlag Berlin Heidelberg: Springer Berlin Heidelberg, 2012.
- [35] P. T. Callaghan, *Translational dynamics and magnetic resonance : principles of pulsed gradient spin echo NMR*. Oxford University Press, 2011.
- [36] D. K. Jones, *Diffusion MRI : theory, methods, and applications*. Oxford University Press, 2011.
- [37] R. Brown, "XXVII. *A brief account of microscopical observations made in the months of June, July and August 1827, on the particles contained in the pollen of plants; and on the general existence of active molecules in organic and inorganic bodies,*" *Philos. Mag.*, vol. 4, no. 21, pp. 161–173, Sep. 1828.
- [38] A. Einstein, "UN THE MOVEMENT OF SMALL PARTICLES SUSPENDED IN STATIONARY LIQUIDS REQUIRED BY THE MOLECULAR-KINETIC THEORY OF HEAT," 1905.
- [39] W. Price, "Pulsed-field gradient nuclear magnetic resonance as a tool for studying translational diffusion: Part 1. Basic theory," *Concepts Magn. Reson.*, vol. 9, pp. 299–336, 1997.
- [40] E. O. Stejskal and J. E. Tanner, "Spin diffusion measurements: spin echoes in the presence of a time-dependent field gradient," *J. Chem. Phys.*, vol. 42, no. 1, pp. 288–292, 1965.
- [41] H. C. Torrev, "Bloch Equations with Diffusion Teriris*," 1956.

- [42] D. Le Bihan and E. Breton, “Imagerie de diffusion in-vivo par résonance magnétique nucléaire,” *Comptes-Rendus l’Académie des Sci.*, vol. 93, no. 5, pp. 27–34, 1985.
- [43] P. T. Callaghan, “A Simple Matrix Formalism for Spin Echo Analysis of Restricted Diffusion under Generalized Gradient Waveforms,” *J. Magn. Reson.*, vol. 129, pp. 74–84, 1997.
- [44] I. Drobnjak, H. Zhang, M. G. Hall, and D. C. Alexander, “The matrix formalism for generalised gradients with time-varying orientation in diffusion NMR,” *J. Magn. Reson.*, vol. 210, no. 1, pp. 151–157, May 2011.
- [45] P. T. Callaghan, “A Simple Matrix Formalism for Spin Echo Analysis of Restricted Diffusion under Generalized Gradient Waveforms,” *J. Magn. Reson.*, vol. 129, no. 1, pp. 74–84, Nov. 1997.
- [46] J. Stepihik, “PYSICA I8 Time-dependent self-diffusion by NMR spin-echo,” *Phys. B*, vol. 183, pp. 343–350, 1993.
- [47] J. Stepišnik, A. S. Mohoriš, and A. Duh, “Diffusion and flow in a porous structure by the gradient spin echo spectral analysis,” *Phys. B*, vol. 307, pp. 158–168, 2001.
- [48] J. C. Gore, J. Xu, D. C. Colvin, T. E. Yankeelov, E. C. Parsons, and M. D. Does, “Characterization of tissue structure at varying length scales using temporal diffusion spectroscopy,” *NMR Biomed.*, vol. 23, no. 7, pp. 745–56, Aug. 2010.
- [49] X. Jiang *et al.*, “In vivo imaging of cancer cell size and cellularity using temporal diffusion spectroscopy,” *Magn. Reson. Med.*, vol. 00, no. June, pp. 1–9, 2016.
- [50] J. Stepišnik, “Analysis of NMR self-diffusion measurements by a density matrix calculation,” *Phys. B+C*, vol. 104, no. 3, pp. 350–364, Apr. 1981.
- [51] A. S. Ianu, “Advanced Diffusion MRI for Microstructure Imaging: Theoretical Developments,” 2016.
- [52] E. C. Parsons, M. D. Does, and J. C. Gore, “Modified oscillating gradient pulses for direct sampling of the diffusion spectrum suitable for imaging sequences,” *Magn. Reson. Imaging*, vol. 21, no. 3–4, pp. 279–285, 2003.
- [53] M. D. Does, E. C. Parsons, and J. C. Gore, “Oscillating gradient measurements of water diffusion in normal and globally ischemic rat brain,” *Magn. Reson. Med.*, vol. 49, no. 2, pp. 206–215, Feb. 2003.

- [54] V. Vandecaveye *et al.*, “Detection of head and neck squamous cell carcinoma with diffusion weighted MRI after (chemo)radiotherapy: Correlation between radiologic and histopathologic findings,” *Int. J. Radiat. Oncol. Biol. Phys.*, vol. 67, no. 4, pp. 960–971, 2007.
- [55] Y.-C. Hu *et al.*, “Intravoxel incoherent motion diffusion-weighted MR imaging of gliomas: efficacy in preoperative grading,” *Sci. Rep.*, vol. 4, no. 16, p. 7208, 2014.
- [56] D. Le Bihan, E. Breton, D. Lallemand, M. L. Aubin, J. Vignaud, and M. Laval-Jeantet, “Separation of diffusion and perfusion in intravoxel incoherent motion MR imaging.,” *Radiology*, vol. 168, no. 2, pp. 497–505, Aug. 1988.
- [57] D. M. Koh, D. J. Collins, and M. R. Orton, “Intravoxel incoherent motion in body diffusion-weighted MRI: Reality and challenges,” *Am. J. Roentgenol.*, vol. 196, no. 6, pp. 1351–1361, 2011.
- [58] D. S. Novikov, V. G. Kiselev, and S. N. Jespersen, “On modeling,” *Magn. Reson. Med.*, vol. 79, no. 6, pp. 3172–3193, Jun. 2018.
- [59] G. J. Stanisz, A. Szafer, G. A. Wright, and R. M. Henkelman, “An analytical model of restricted diffusion in bovine optic nerve.,” *Magn. Reson. Med.*, vol. 37, no. 1, pp. 103–111, 1997.
- [60] Y. Assaf, R. Z. Freidlin, G. K. Rohde, and P. J. Basser, “New modeling and experimental framework to characterize hindered and restricted water diffusion in brain white matter,” *Magn. Reson. Med.*, vol. 52, no. 5, pp. 965–978, 2004.
- [61] E. Panagiotaki, T. Schneider, B. Siow, M. G. Hall, M. F. Lythgoe, and D. C. Alexander, “Compartment models of the diffusion MR signal in brain white matter: A taxonomy and comparison,” *Neuroimage*, vol. 59, no. 3, pp. 2241–2254, 2012.
- [62] Y. Assaf, T. Blumenfeld-Katzir, Y. Yovel, and P. J. Basser, “AxCaliber: A method for measuring axon diameter distribution from diffusion MRI,” *Magn. Reson. Med.*, vol. 59, no. 6, pp. 1347–1354, 2008.
- [63] D. C. Alexander *et al.*, “Orientationally invariant indices of axon diameter and density from diffusion MRI,” *Neuroimage*, vol. 52, no. 4, pp. 1374–1389, 2010.
- [64] L. R. Frank, “Anisotropy in high angular resolution diffusion-weighted MRI,” *Magn. Reson. Med.*, vol. 45, no. 6, pp. 935–939, Jun. 2001.
- [65] H. Zhang, T. Schneider, C. A. Wheeler-Kingshott, and D. C. Alexander, “NODDI: Practical in vivo neurite orientation dispersion and density imaging of the human brain,” *Neuroimage*, vol. 61, no. 4, pp. 1000–1016, Jul. 2012.

[66] E. Panagiotaki *et al.*, “Microstructural Characterisation of Normal and Malignant Human Prostate Tissue with VERDICT MRI,” vol. 3, p. 46410, 2014.

[67] J. Xu *et al.*, “Magnetic resonance imaging of mean cell size in human breast tumors,” *Magn. Reson. Med.*, p. mrm.28056, Nov. 2019.

Chapter 3

Probabilistic Classification of Tumor Habitats

3.1 Preface

As discussed in Chapter 2, characterization of tumor heterogeneity has important clinical applications for designing effective radiotherapy, where dose boost can be provided to regions of high cellularity. Various tumor habitats (*i.e.* sub-regions) have different imaging signatures that can be recognized by visual inspection. However, this is both time consuming and error prone. In this chapter, we propose a method to characterize tumor heterogeneity via MRI, using probabilistic classification based on a reference tissue. This method emulates the thought process of radiologists by automating the habitat classification process. Using maps of the apparent diffusion coefficient (ADC), T_2 relaxation, and a calculated map representing high- b -value diffusion-weighted MRI (denoted *simDWI*), up to five habitats can be identified, including hypercellular tumor, high T_2 proteinaceous fluid, necrosis, collagenous stroma, and fibrosis. The feasibility of the proposed method was demonstrated in 7 patients with biopsy-confirmed soft tissue sarcoma, and results were qualitatively consistent with histopathology.

Probabilistic Classification of Tumor Habitats in Soft Tissue Sarcoma

Shu Xing, MSc^{1,2}, Carolyn R. Freeman, MD³, Sungmi Jung, MD⁴, Ives R. Levesque, PhD^{1,2,5}

¹ Medical Physics Unit, McGill University, Montreal, Canada,

² Department of Physics, McGill University, Montreal, Canada

³ Radiation Oncology, McGill University Health Centre, Montreal, Canada

⁴ Department of Pathology, McGill University Health Centre, Montreal, Canada

⁵ Research Institute of the McGill University Health Centre, Montreal, Canada

Published in *NMR in biomedicine*, e4000, 2018

Corresponding author: Shu Xing, MSc
Cedars Cancer Centre, Glen Site, room DS1.7141
1001 Boul. Décarie
Montreal, QC, Canada, H3A 3J1
shu.xing@mail.mcgill.ca

Running title: Habitats in soft tissue sarcoma

Keywords: tumor; diffusion; probabilistic classification; soft tissue sarcoma

3.2 Abstract

Purpose: To propose a method to characterize tumor heterogeneity on magnetic resonance imaging (MRI), using probabilistic classification based on a reference tissue. The method uses maps of the apparent diffusion coefficient (ADC), T_2 relaxation, and a calculated map representing high- b -value diffusion-weighted MRI (denoted *simDWI*), to identify up to five habitats (*i.e.* sub-regions) of tumors.

Theory: In this classification method, the parameter values (ADC, T_2 , and *simDWI*) from each tumor voxel are compared against the corresponding parameter probability distributions in a reference tissue. The probability that a tumor voxel belongs to a specific habitat is the joint probability for all parameters. The classification can be visualized using a custom color scheme.

Methods: The proposed method was applied to data from seven patients with biopsy-confirmed soft tissue sarcoma, at three times-points over the course of pre-operative radiotherapy. Fast-spin-echo images with two different echo times and diffusion MRI with three b -values were obtained and used as inputs to the method. Imaging findings were compared to pathology reports from pre-radiotherapy biopsy and post-surgical resection.

Results: Regions of hypercellularity, high T_2 proteinaceous fluid, necrosis, collagenous stroma, and fibrosis were identified within soft tissue sarcoma. The classifications were qualitatively consistent with pathological observations. The percentage of necrosis on imaging correlated strongly with necrosis estimated from FDG-PET, at pre-radiotherapy ($R^2 = 0.97$) and post-radiotherapy ($R^2 = 0.96$).

Conclusion: The probabilistic classification method identifies realistic habitats and reflects the complex microenvironment of tumors, as demonstrated in soft tissue sarcoma.

3.3 Introduction

Magnetic resonance imaging (MRI) is the modality of choice for diagnosis, staging, and follow-up of soft tissue sarcoma (STS) [13]. Conventional T₁- and T₂-weighted fast spin-echo (FSE) MRI allow the differentiation of STS from surrounding normal tissues and gross characterization of tumor properties[14]. Many STS present heterogeneous composition, with several compartments of viable tumor and of necrotic tissue [15], reflecting a complex histological composition [16], [17].

Diffusion-weighted MRI (DW-MRI) can be added to conventional MRI to refine diagnosis and soft tissue tumor characterization [18]–[20]. Water diffusion is dependent on tissue constituents; for example, the dense cellular environment of tumors generally results in restricted diffusion and high signal intensity on high *b*-value DW-MRI. Thus, DW-MRI offers qualitative visual assessment of cellularity, which has been reported to help with tumor delineation and differentiation between benign and malignant lesions [21]–[23]. The average diffusion of water molecules can be quantified by the apparent diffusion coefficient (ADC). ADC analysis has been used to characterize various types of STS and to differentiate malignant from benign STS [23]–[25].

Studies using DW-MRI in combination with T₂-weighted MRI have demonstrated that the addition of DW-MRI to standard protocols improves diagnostic accuracy for soft tissue tumors. For instance, visual comparison of tumor signal intensity to surrounding muscles on DW-MRI (*b* = 1400 s/mm²) revealed that hyperintensity relative to muscle was more frequent in malignant soft tissue tumors [26]. In soft tissue tumors that are hyperintense on T₂-weighted MRI, the ratio between minimum tumor ADC and average muscle ADC can differentiate benign and malignant tumors with 90 % sensitivity and 96.4 % specificity [15].

Prior studies have mainly characterized STS based on minimum or average diffusion properties (DW-MRI and/or ADC); however, tumor characterization based on whole-tumor ADC metrics does not capture tumor sub-region heterogeneity. Genetic heterogeneity within individual tumors, which is likely reflected on imaging, is one of the major problems limiting the efficacy of targeted

therapies [27], [28]. Therefore, further understanding of intra-tumoral heterogeneity has important implications for personalized medicine. The term “habitat” is used to describe the sub-regions within tumors [29].

Recent preclinical studies have reported that the multispectral analysis of ADC, T_2 , and proton density parameter maps with k -means clustering algorithms can aid the differentiation between viable and necrotic tumor, and the identification of multiple compartments within necrotic tissue [30]–[32]. A similar approach using k -means clustering and Gaussian mixture modeling of ADC and positron emission tomography with fluorodeoxyglucose (FDG-PET) differentiated two types of viable tissue and necrosis tissue in xenograft tumors [33]. While these are promising methods to study intra-tumor heterogeneity, k -means clustering partitions voxels into mutually exclusive clusters. This imposes that a tumor voxel can only belong to a single habitat, which might not reflect the complex microenvironment in a voxel, especially at the border of two habitats.

To address the limitations of qualitative analysis and data-driven clustering methods, we propose a novel reference-tissue-based method for probabilistic classification of tumor habitats. The main contribution of this work is to emulate the thought process of the radiologists by automating the habitat classification process. The method is based on prior qualitative work used to describe tumor habitats by visual inspection (Table 3.1) [13], [34], [35]. Analysis of parametric maps of T_2 , ADC, and a quantitative surrogate for high- b -value diffusion weighted MRI (called *simDWT*) was employed to distinguish tumor habitats. The proposed approach calculates the probability that a voxel belongs to each habitat and allows the co-existence of different habitats in the same voxel. These habitats include hypercellular tumor, high T_2 proteinaceous fluid, necrosis, collagenous stroma, and fibrosis. The term “necrosis” is used here to specify necrosis identified on imaging. The distinction from pathological necrosis will be discussed. The method was demonstrated on 7 patients with confirmed high-grade soft tissue sarcoma. Habitats were compared across multiple exams during the course of neo-adjuvant radiation therapy. Observations were compared with histology.

3.4 Theory

Quantitative MRI Inputs

Prior work has identified habitats by comparing the tumor signal intensity on T₂-weighted images, high *b*-value DW-MRIs, and ADC maps to a reference tissue [13]. The signal intensity pattern from all three images was used to interpret the habitats as described in the *Qualitative* classification of Table 3.1.

Table 3.1 Interpretation of tumor sub-regions from diffusion and T₂ MRI. The qualitative interpretations were proposed by Patterson et al. [23] and served as the basis for our quantitative method (column 4: “Quantitative”). The habitats are listed in column 5 (“Interpretation”) and colour coded according to the visual representation of the classification result.

Qualitative			Quantitative	Interpretation
T ₂ -w	DWI	ADC	Joint probability of a habitat ¹	
High	High	High	$F(T_2)F(ADC)F(SimDWI)$	T ₂ shine-through, high T ₂ content, often proteinaceous fluid
High	High	Low	$F(T_2)F(ADC)[1 - F(SimDWI)]$	Tumor of high cellularity
High	Low	High	$F(T_2)[1 - F(ADC)]F(SimDWI)$	Fluid, necrosis, lower cellularity
				Collagenous tissue ²
Low	Low	Low	$[1 - F(T_2)][1 - F(ADC)][1 - F(SimDWI)]$	Fibrous tissue with low water content

$${}^1F(x_t) = \int_0^{x_t} p_r(x)dx, \text{ where } x \equiv ADC, T_2 \text{ or } simDWI$$

²This habitat was not included in the interpretations proposed by Patterson *et al.*

The signal values in T₂-weighted and DW-MRI have an arbitrary scaling that depends on factors such as the field strength, receive coil sensitivity, pulse sequence, actual flip angle, receive gain, and analog-to-digital conversion. As a result, these signal values have no absolute meaning. The ADC, however, is a quantitative parameter that can be used in reference tissue comparison. To

automate the reference-based analysis process, we must first identify comparable quantitative spaces for T_2 -weighted and high b -value DW-MRI.

T_2 -weighted MRI reflects the T_2 relaxation time of tissue. Quantitative T_2 mapping is therefore a natural choice to represent T_2 -weighted images. Selecting a quantitative parameter to represent DW-MRI seems more challenging. In the pulsed-gradient spin-echo pulse sequence, the signal at the echo time (TE) reflects the loss of phase coherence in the transverse magnetization due to the combination of the spin-spin relaxation process, proportional to $\exp(-TE/T_2)$, and the additional spin-echo amplitude attenuation due to the diffusion process, which can be modelled as $\exp(-b \cdot ADC)$. The theoretical signal for DW-MRI can be expressed as [6]:

$$S_{SE}(TE, b) = S_{SE}(TE = 0, b = 0) \exp\left(-\frac{TE}{T_2}\right) \exp(-b \cdot ADC) \quad (1)$$

where $S_{SE}(TE = 0, b = 0)$ is the theoretical signal with negligible T_2 and diffusion weighting, which reflects proton density and incomplete T_1 relaxation and is constant for a given voxel and pulse sequence. Therefore, the major physical characteristics of DW-MRI can be captured by the product of the two exponential terms in Equation 1, which can be used to construct a surrogate map. We refer to this surrogate map as “simulated DW-MRI” or *simDWI*, calculated with Equation 2. *simDWI* ranges from 0 to 1 and reflects the relative contribution of T_2 relaxation and diffusion to DW-MRI signal attenuation. When both T_2 and ADC of the tumor are greater than for the reference tissue, *simDWI* serves to differentiate necrosis from high T_2 proteinaceous fluid. *simDWI* varies predictably as a function of T_2 and ADC (Figure 3.1) and will be discussed further.

$$\text{simDWI} = \exp\left(-\frac{TE_{DWI_b}}{T_2}\right) \cdot \exp(-b \cdot ADC) \quad (2)$$

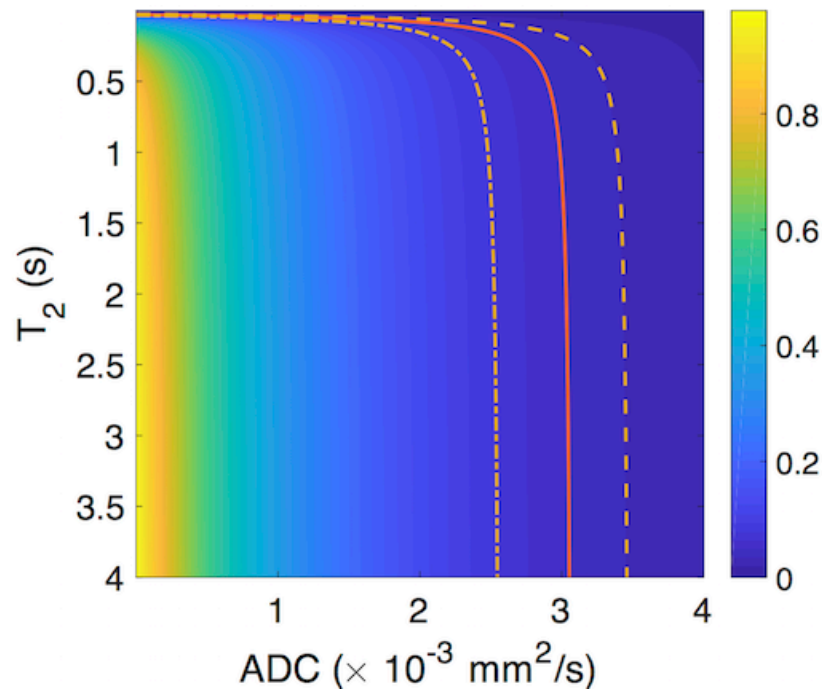


Figure 3.1 Plot of the values of simDWI for ranges of T_2 and ADC values with $TE= 88$ ms and $b = 1000$ s/mm². The contour lines from left to right represent simDWI values equal to the 90th percentile (dash-dot), median (solid), and 10th percentile (dash) of the distribution of simDWI in muscle. When both T_2 and ADC are higher in a tumor pixel than in muscle, the value of simDWI serves to differentiate necrosis from high T_2 proteinaceous fluid, like the high b-value DW-MRI in the qualitative approach.

The T_2 , ADC, and simDWI maps can then be used as inputs to the probabilistic classification. The workflow of the reference-region based probabilistic classification is summarized in Figure 3.2.

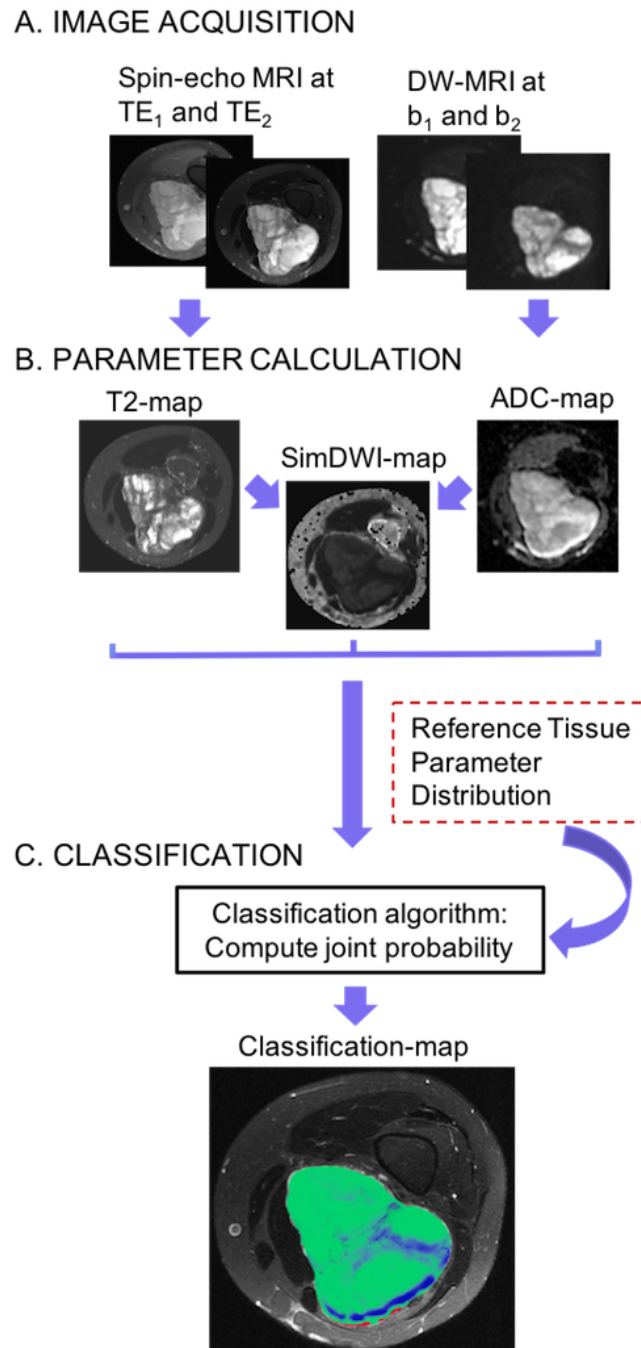


Figure 3.2 Workflow of the classification method: A. Image acquisition, B. Parameter calculation, C. Classification. Spin-echo MRIs must be acquired for at least 2 TEs to compute the T_2 map. DWI-MRI must be acquired for at least 2 b-values to produce the ADC map. The T_2 , ADC and simDWI maps are fed to the algorithm to produce classification maps. Reference tissue parameter distributions are shown in Figure 3.3

Habitat Classification

Prior to the classification, a reference tissue is selected. The distribution of parameter values in the reference tissue is used to define probability density functions $p_r(x)$ for each parameter, where x represents ADC, T_2 , or simDWI. The parameter values from each tumor voxel are compared against the parameter distributions of the reference tissue in a 3-step process:

1. The probability for a parameter in a tumor voxel, denoted x_t (where $x_t = \text{ADC}, T_2$, or simDWI in the tumor), of being greater than in the reference tissue is computed by integrating the probability density function $p_r(x)$ from 0 to x_t . This is equivalent to the cumulative distribution function $F(x)$ of the reference tissue, evaluated at x_t :

$$F(x_t) = \int_0^{x_t} p_r(x) dx \quad (3)$$

$F(x_t)$ ranges from 0 to 1, with $F(x_t) = 1$ when $x_t \gg \max(x)$ of the reference tissue.

2. The probability that x_t is smaller than the reference is $1 - F(x_t)$.
3. The probability that a voxel belongs to a specific habitat is the joint probability for all parameters (ADC, T_2 , and simDWI) according to the expressions in Table 3.1 (*Quantitative* column).

The output of the classification can be visualized by representing each habitat with a different color (green, red, blue, purple, and yellow), overlaid on a conventional image for anatomical reference. The color transparency reflects the magnitude of the probability, between 0 (full transparency) and 1 (fully opaque), controlled by the alpha channel. Voxels with negative or non-physical T_2 or ADC values are classified as “artifact” and are marked black. Voxels with realistic parameter values not assigned a habitat—*i.e.* those that do not fall in any of the classes in Table 3.1—are labeled as “other” and are ignored in the visualization.

During this study, a habitat with similar imaging signatures to necrosis was identified, but with T_2 considerably lower (median $T_2 \approx 60$ ms) than for necrosis (median $T_2 > 300$ ms) (Table 3.1). Also, FDG-PET images showed high uptake for this habitat, in contrast to the conventional understanding of necrosis. In our approach, this habitat was separated from necrosis based on T_2

values compared to the T_2 distribution of muscle. This habitat is suspected to be collagenous stroma based on pathological observations from resected tumors, as presented in the Results. It also shares a similar imaging signature with collagenous stroma as reported in the literature: hypointense on T1-weighted, iso-/hypointense on T2-weighted, and enhancing on post-contrast T1-weighted MRI [36]. Necrosis was assigned when T_2 was much larger than that of muscle (*i.e.* when $F(T_2) = 1$); collagenous stroma if T_2 was closer to but still larger than T_2 of muscle ($F(T_2) < 1$). The probability of either habitat was computed by $F(T_2)[1 - F(ADC)]F(\text{SimDWI})$.

3.5 Methods

Patients

The study was approved by the local Research Ethics Board and written informed consent was obtained from each patient. Eighteen patients with pathologically confirmed STS were recruited to participate in a prospective study on multi-modality imaging in STS treated with surgery and neo-adjuvant radiotherapy. Recruited patients satisfied the following criteria: (a) biopsy performed within 8 weeks prior to registration, (b) surgically resectable tumor, (c) patient was fit for surgery, (d) patient at least 18 years old, (e) for females with childbearing potential, a serum β HCG had to be done within 2 weeks prior to registration and the patient had to practice adequate contraception. Patients with rhabdomyosarcoma, Ewing sarcoma, osteosarcoma, or Kaposi sarcoma were excluded from this study. Patients with contraindications to MRI, prior radiotherapy, or excisional biopsy leading to the removal of the majority of the tumor were also excluded.

Seven of the 18 patients (5 females and 2 males; age range 48-81) had complete imaging data acquired at pre-, mid- and post-radiotherapy, with the exception of P5 who was missing the FDG-PET scan at post-radiotherapy. Tumor types for these patients were: myxofibrosarcoma (P1: thigh; P2: flank; P3: thigh), round cell/myxoid liposarcoma (P4: thigh), myxoid liposarcoma (P5: thigh), synovial sarcoma (P6: forearm), and fibromyxoid sarcoma (P7: thigh).

All patients underwent diagnostic and therapeutic procedures according to our institutional standards. Diagnosis was confirmed by needle biopsy performed by a surgeon or an interventional

radiologist. Radiotherapy was administered with a minimum dose of 50 gray in 25 fractions to cover at least 95% of the tumor (defined as the planning target volume). The tumor was resected following radiotherapy. The median time interval between the last radiation fraction and surgery in this patient cohort was 26 days (ranging 22-41 days). The median time interval between the post-radiotherapy imaging and surgery was 8 days (ranging 6-9 days for 5/7 patients, 13 days for P6, and 27 days for P2). After formalin fixation of the resected specimen, representative sections of the tumor were taken and stained (haematoxylin and eosin, or H&E) for histopathological evaluation.

Image Acquisition

Axial multi-slice two-dimensional DW-MRI and FSE images with fat saturation were acquired on a 1.5 T scanner (GE Healthcare, Waukesha, WI, USA). Imaging was performed at three time-points: one week prior to the start of radiotherapy, at the mid-point of the treatment course (week 3), and post-radiotherapy in the week leading up to surgery. DW-MRI were acquired with $b = 0$, 100, and 800 s/mm², and TR/TE = 5000/88 ms (Fig. 3.2A). FSE images were acquired twice, using a short TE of 9 to 12 ms (PD-weighted) and a long TE of 64 to 83 ms (T₂-weighted), to be used in T₂ mapping (Fig. 3.2A). For FSE images, the TR ranged between 3.95 s and 6.65 s and was held constant for both scans for a given patient. The echo train length was 9. The field-of-view, number of slices, and slice thickness were adapted for each patient (Sup. Table S1).

FDG-PET was performed on a PET/CT scanner (Discovery ST, GE Healthcare, Waukesha, WI, USA). Patients were required to fast for at least six hours before their appointment. Blood glucose levels were recorded immediately prior to FDG administration, allowing a maximum serum glucose level of 11.1 mmol/L. Barium sulfate oral contrast (400 mL) was administered and FDG was injected intravenously (370 to 500 MBq). Sixty minutes after the FDG injection, PET/CT images were acquired from the base of the skull to the upper thighs, with additional images acquired as needed for the STS location.

Quantitative Image Processing

The gross tumor volumes were identified on T₂-weighted axial fat-suppressed FSE images by an experienced radiation oncologist and used to restrict habitat classification.

ADC and T₂ maps were computed using MATLAB (The Mathworks Inc., Natick MA USA). The ADC was computed from images with $b = 100$ and 800 s/mm² (Fig. 3.2B), using the expression

$$\text{ADC} = \frac{1}{(b_{100} - b_{800})} \ln \left(\frac{S_{800}}{S_{100}} \right) \quad (4)$$

S_{100} and S_{800} represent the signal intensity with $b = 100$ and 800 s/mm² respectively. The signal from $b = 0$ s/mm² was not used in the calculation of ADC to avoid the effect of perfusion. DW-MRIs were registered to the image with $b = 0$ s/mm² prior to ADC calculation, via rigid registration (MIMVista, MIM Software Inc., Cleveland OH USA).

The apparent T₂ (Fig. 3.2B) was computed using a 2-parameter model applied to the logarithm of the FSE signal:

$$T_2 = \frac{(TE_2 - TE_1)}{\ln(S_{TE1}/S_{TE2})} \quad (5)$$

where S_{TE1} and S_{TE2} represent the signal intensity of the FSE images.

Voxels with negative, non-physical values of ADC or T₂ were likely due to image noise, artifacts, or imperfect image registration (between the various b -values or TE images). These were replaced with values based on their neighbouring voxels, using a Laplacian filter [37].

ADC and T₂ values were used to generate simDWI maps (Fig. 3.2B). In this calculation, the TE of the DW-MRI sequence was used (88 ms) and the b -value was set to 1000 s/mm². ADC maps were rigidly registered to the T₂-weighted FSE images, and therefore, to the T₂ maps, prior to simDWI calculation.

Reference Tissue Values and Habitat Segmentation

Muscle was used as the reference tissue. Regions-of-interest (ROIs) were manually identified in muscle on the pre-treatment T₂-weighted FSE images, for each patient. These ROIs were then copied onto the ADC, T₂, and simDWI maps, and parameter values were extracted. For each parameter, the probability distributions from all patients were combined (to include all muscle voxels). Each of the distributions was then fitted with a 3-term Gaussian model to produce an analytical form for subsequent integration (per Equation 3) resulting in the cumulative distribution function. The 3-term Gaussian model was chosen to provide very close fits to the data (*i.e.* $R^2 > 0.999$) and hence accurate analytical representations of the probability density functions. The 3-term Gaussian distributions are not believed to represent specific physical characteristics of the distribution. The fitted functions were then used as the reference probability density functions $p_r(x)$, $x \equiv ADC, T_2, simDWI$. Using the reference probability density functions, the classification method was applied to classify voxels in the gross tumor volume of each patient.

FDG-PET was used for the independent assessment of necrosis. The mean and standard deviation of muscle standard uptake values (SUV) were calculated for individual patients. The CT images from the combined PET/CT acquisition were rigidly registered and resampled to the T₂-weighted FSE images, in MIMVista. By extension, FDG-PET images were also spatially aligned to T₂-weighted FSE images and to the habitat maps. The muscle ROIs were defined on T₂-weighted images and copied to the registered PET images. Tumor regions with an SUV two standard deviations below the mean in muscle were defined as low uptake and interpreted as necrosis [38]. The accuracy of this approach to automated identification of low FDG uptake regions was assessed visually prior to proceeding.

Longitudinal analysis

The classification method allowed the longitudinal comparison of tumor composition over the course of radiotherapy. Each voxel was added to a histogram according to the habitat with the highest probability, on a per-patient basis. For instance, a voxel with probabilities of [0.93 proteinaceous fluid; 0.02 hypercellular tissue; 0.05 necrosis] was counted as proteinaceous fluid.

3.6 Results

Reference Tissue Analysis

Parameter distributions were calculated in the reference tissue and used to define the probability density functions. Representative muscle ROIs from five patients are shown in Figure 3.3 (a-e), with the probability density functions for the ADC, T_2 , and simDWI in muscle from all patients (f-h). The ADC in muscle was normally distributed, in individual patients (Sup. Fig. 3.S1) and for all patients combined (Fig. 3.3g). The mean and mode ADC were both $1.0 \times 10^{-3} \text{ mm}^2/\text{s}$, with a standard deviation of $0.2 \times 10^{-3} \text{ mm}^2/\text{s}$. Muscle T_2 skewed positively for individual patients and for the combined distribution (Fig. 3.3 (f)). The mean T_2 (= 45 ms) of muscle was slightly higher than the mode T_2 (= 41 ms), with a standard deviation of 31 ms and skewness of 117. The simDWI of muscle had a mean of 0.05, mode of 0.04, standard deviation of 0.02, and positive skewness of 3 (Fig. 3.3 (h)). The Gaussian models provided good fits to the muscle ADC, T_2 , and simDWI distributions, with R^2 of 0.9994, 0.9995, and 0.9994, respectively. Patient P2, with myxofibrosarcoma in the flank, was excluded from this part of the analysis due to the absence of identifiable muscle in the images.

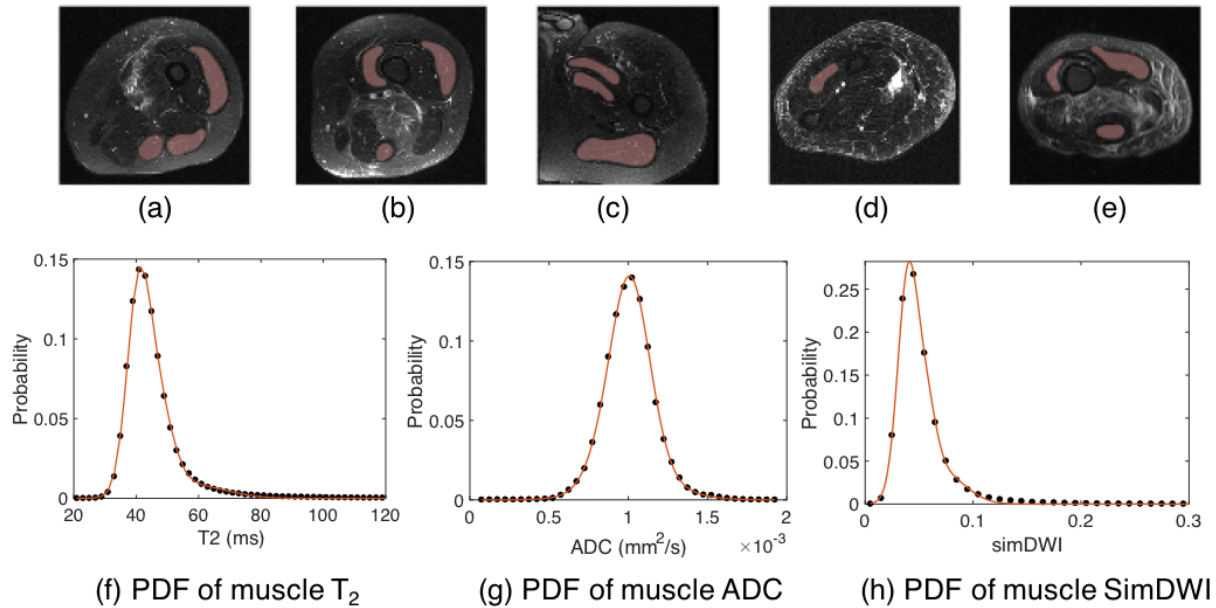


Figure 3.3 Regions of interests (ROIs) in muscle are shown as red overlays on T₂-weighted FSE images acquired prior to radiotherapy: (a) Patient 1: lower thigh, (b) patient 2: lower thigh, (c) patient 3: lower thigh, (d) patient 4: forearm, and (e) patient 5: lower thigh. A representative slice from each patient is shown. Probability density functions of T₂ (f), ADC (g), and simDWI (h) in muscle voxels are also shown. The x-axis of T₂ and simDWI distributions was truncated for better visualization. A 3-term Gaussian model was fitted to each distribution, shown as solid orange lines.

Tumor Habitats

The probabilistic classification was applied to all seven datasets at all time points. As an illustrative example, the case of high-grade myxofibrosarcoma in the flank (P2) featured regions of high T₂ proteinaceous fluid, tissue of hypercellularity, and necrosis (Figure 3.4). This tumor was heterogeneous in all images, qualitative or quantitative. The classification identified three distinct regions (identified in the figure as I, II, and III) with high probability of being hypercellular, high T₂ proteinaceous fluid, and necrosis, respectively. Region I was hyperintense on T₂-weighted MRI and DW-MRI ($b=800$ s/mm²), had higher T₂ and simDWI, and lower ADC, than the reference tissue. Region II was hyperintense on T₂-weighted MRI and DW-MRI, and had high T₂, simDWI, and ADC values. Region III was hyperintense on T₂-weighted MRI but hypointense on DW-MRI, had high T₂ and ADC, and low simDWI. In the visualization, color mixtures were observed in region III and at the transition between habitats.

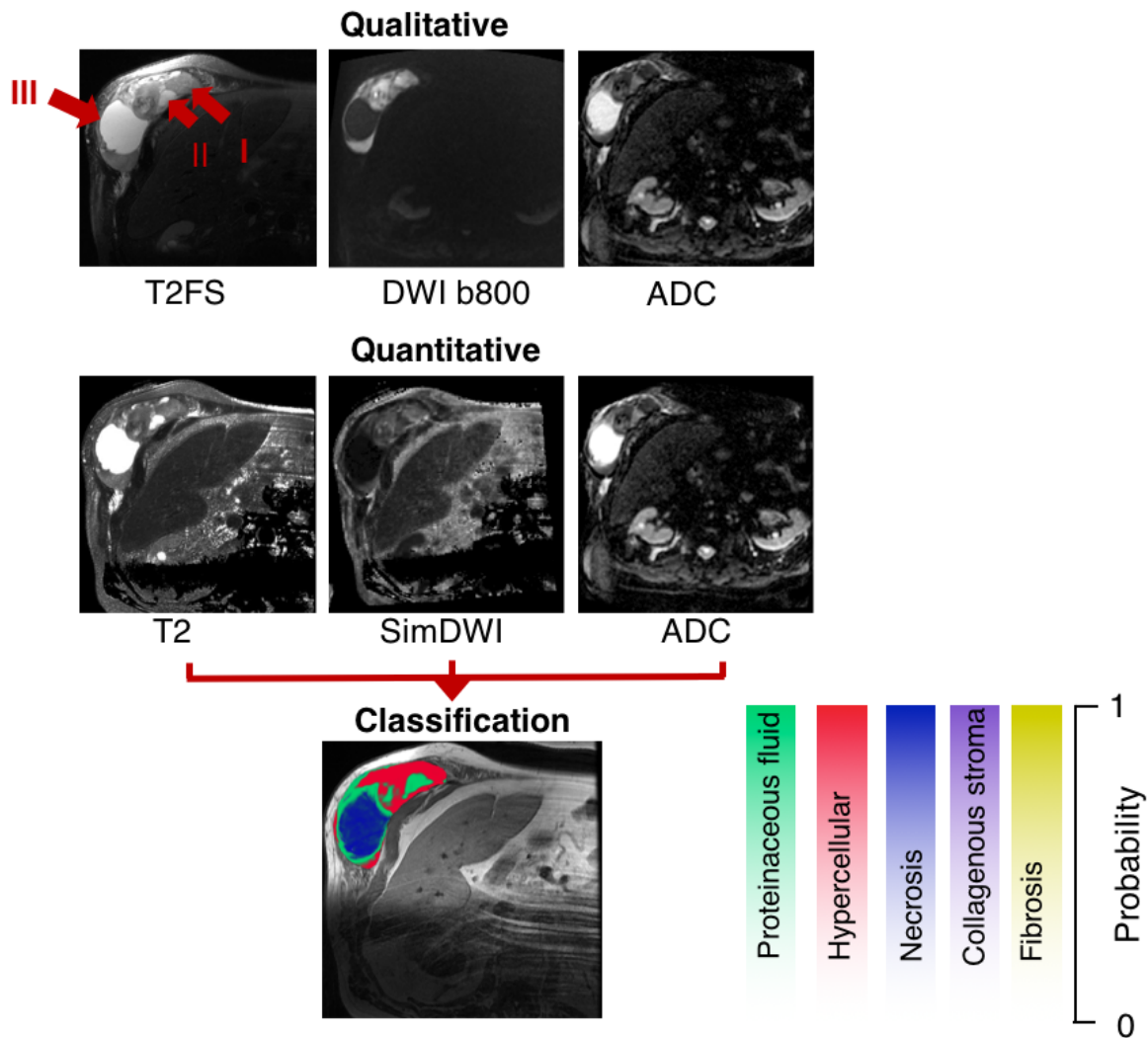


Figure 3.4 A representative case of high grade myxofibrosarcoma demonstrates three regions of distinct intensity patterns. These regions were classified as hypercellular (red), proteinaceous fluid (green), and necrosis (blue), respectively, by the classification algorithm. This corresponds to the interpretation in Table 1. Regions I, II, and III are discussed in the text. The ADC map is the same for both the qualitative and quantitative approaches.

The parameter values (median and interquartile range) at pre-, mid-, and post-radiotherapy show variations between habitats (Table 3.2). Necrosis and collagenous stroma regions both had high ADC and low simDWI, but different T₂ by definition (long for necrosis and shorter for collagenous stroma). Hypercellular tissue had lower ADC and T₂ values than proteinaceous fluid. Fibrosis had low ADC, T₂, and simDWI values.

Table 3.2 Median parameter values (with interquartile range), for different tissue habitats following the probabilistic classification at pre-, mid- and post-radiotherapy (RT).

Visit	Tissue Class	ADC		T ₂		simDWI	
		($\times 10^{-3}$ mm ² s ⁻¹)	(ms)	(ms)	(ms)		
	Muscle (reference)	1.00	(0.19)	43	(8)	0.046	(0.021)
Pre-RT	Hypercellular	0.78	(0.22)	93	(37)	0.174	(0.082)
	Proteinaceous Fluid	1.76	(0.62)	231	(212)	0.110	(0.053)
	Necrosis	3.10	(0.54)	379	(956)	0.036	(0.010)
	Collagenous stroma	1.95	(0.54)	61	(20)	0.034	(0.012)
	Fibrosis	0.79	(0.25)	33	(5)	0.031	(0.013)
Mid-RT	Hypercellular	0.80	(0.32)	98	(78)	0.184	(0.136)
	Proteinaceous Fluid	1.91	(0.84)	217	(240)	0.087	(0.054)
	Necrosis	3.10	(0.43)	535	(1703)	0.037	(0.010)
	Collagenous stroma	2.13	(0.66)	66	(24)	0.032	(0.010)
	Fibrosis	0.70	(0.30)	33	(5)	0.034	(0.012)
Post-RT	Hypercellular	0.85	(0.24)	107	(69)	0.192	(0.116)
	Proteinaceous Fluid	1.86	(0.76)	178	(149)	0.079	(0.053)
	Necrosis	2.99	(0.40)	352	(832)	0.039	(0.008)
	Collagenous stroma	1.92	(0.36)	63	(16)	0.037	(0.011)
	Fibrosis	0.77	(0.24)	33	(5)	0.033	(0.012)

Tumor composition from the classification method at pre- and post-radiotherapy was compared with the histopathological assessment from the pre-radiotherapy biopsy and post-surgical specimen, respectively. FDG-PET was used to identify necrosis. Tumor habitats identified on pre-radiotherapy images agreed with pathological observations from biopsy (Fig. 3.5 columns a and c, and Table 3.3). High T₂ proteinaceous fluid dominated tumors from P1, P3, P4, and P5 (>90%), consistent with histopathology showing large areas of myxoid stroma. One of the myxofibrosarcomas (P2) had markedly different composition, with 16% necrosis. No necrosis was observed in the other myxofibrosarcomas. The tumor from P4 was a round cell/myxoid liposarcoma, a particular type of myxoid tumor that combines low-grade myxoid and high-grade

round cells. Image analysis showed 93% high T₂ proteinaceous fluid and 2% hypercellular tissue. This was qualitatively consistent with histopathological observations from biopsy (Fig. 3.5 column c), which showed large areas of low-grade myxoid area (proteinaceous fluid) and less than 5% high grade round cells (hypercellular). A small area of necrosis (left lower edge in Fig. 3.5 column a, P4) was possibly misclassified. This may have originated from the bright band on the ADC map, a possible artifact due to imperfect rigid registration among DW-MRIs of different *b*-values. The synovial sarcoma (P6) was identified to be primarily hypercellular (75%). Histopathology from the biopsy of this tumor showed predominantly densely packed cells. Post-radiotherapy, tumor composition agreed qualitatively with pathological observations from the resected specimen (Table 3.3). There were discrepancies on the percentage of necrosis between imaging and pathological findings. Pathological evidence suggested two types of treatment-related necrosis were present: liquefactive and treatment-related necrosis with intact stroma (Sup. Fig. 3.S2).

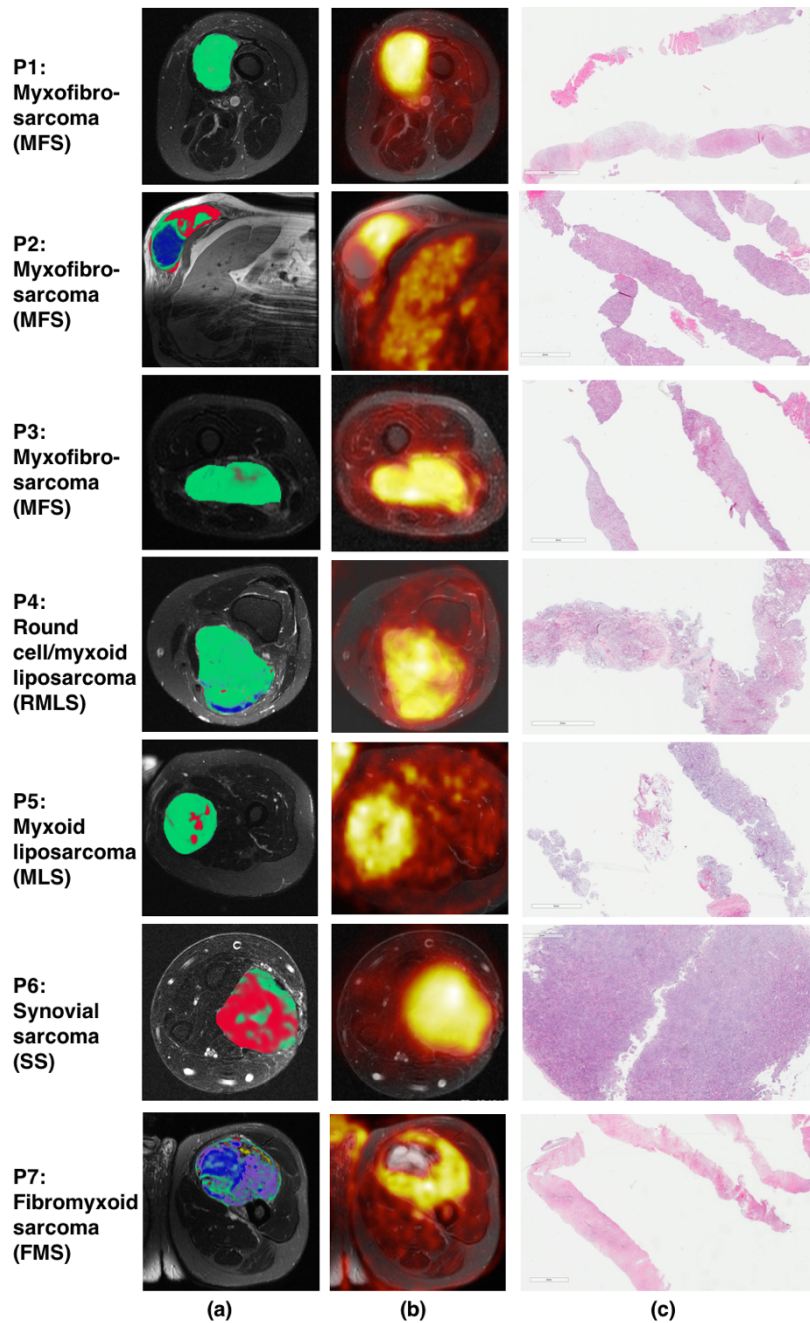


Figure 3.5 Classification results in all 7 patients (representative slices, column a), FDG-PET images (column b) and histopathological images (column c), from pre-radiotherapy imaging and biopsy samples. Each tumor was classified into 5 possible habitats: hypercellular (red), high T2 proteinaceous fluid (green), necrosis (blue), collagenous stroma (purple) and fibrosis (yellow). Tumor habitats at pre-radiotherapy generally agreed with pathological observations from biopsy (discussed in the text). Regions of necrosis (blue) from MRI correspond well to the low uptake on FDG-PET.

Table 3.3 Comparison of MRI-based sub-region classification results with FDG-PET and pathological observations

Tumor	Pre-radiotherapy observations			Post-radiotherapy observations		
	MRI classification	FDG-PET	Biopsy	MRI classification	FDG-PET	Post-surgical resection
P1 Myxofibro-sarcoma	99% high T2. Small regions of high cellularity (1%). No necrosis (0%)	No obvious necrosis	High cellularity pleomorphic spindle cell neoplasm with moderately myxoid areas. No necrosis.	91% high T2. No high cellularity tissue. Small regions of necrosis or very low cellularity (4%)	No obvious necrosis	Low cellular mostly myxoid (> 95%).
P2 Myxofibro-sarcoma	69% high T2. Obvious high cellularity (14%). Necrosis (16%)	Necrosis (18%)	High cellularity pleomorphic spindle cell neoplasm with no obvious myxoid area. No obvious necrosis.	Mostly high T2 tissue (83%). High cellularity regions (7%). Necrosis (10%)	Necrosis (11%)	High cellularity pleomorphic spindle cell neoplasm with mildly to moderately myxoid area. Treatment-related necrosis with liquefactive necrosis (70%).
P3 Myxofibro-sarcoma	99% high T2. Small regions of high cellularity (1%). No necrosis (0%)	No obvious necrosis	Moderately cellular pleomorphic spindle cell neoplasm in diffusely and moderately myxoid stroma. No necrosis.	97% high T2 tissue. Small regions of high cellularity tissue (3%). Minimal necrosis (0.1%)	Minimal necrosis (<1%)	Moderately cellular pleomorphic spindle cell neoplasm in a diffusely and moderately myxoid stroma. Treatment-related necrosis (15%).
P4 Round cell/myxoid liposarcoma	93% high T2. Small regions of high cellularity (2%). Necrosis (5%)	Necrosis (6%)	Moderately cellular neoplasm in diffusely and moderately myxoid stroma. Minimal high grade (< 5%) component. No necrosis.	Mostly high T2 tissue (90%). Minimal regions of high cellularity tissue (1%). Necrosis (7%)	Necrosis (12%)	Low cellular mostly myxoid neoplasm (80% of viable tumor). No definite high grade/round cell component. Treatment-related necrosis (70%).
P5 Myxoid liposarcoma	94% high T2. Small regions of high cellularity (5%). No necrosis (0%)	No obvious necrosis	Moderately cellular neoplasm in diffusely and moderately myxoid stroma. No <u>high grade</u> component or necrosis.	97% high T2. Minimal regions of high cellularity (2%). Minimal necrosis (0.2%)	<i>Not available</i>	Low to moderately cellular neoplasm in diffusely myxoid stroma (>90% of viable tumor). No definite high grade/round cell. Treatment-related necrosis (80%)
P6 Synovial sarcoma	75% high cellularity. Moderate areas of high T2 (25%). No necrosis (0%)	No obvious necrosis	High cellularity spindle cell neoplasm in a collagenous stroma. No necrosis	57% high T2. Minimal high cellularity and necrosis (0.3%). 39% possibly collagenous.	Minimal necrosis (2%)	Low to moderately cellular spindle cell neoplasm in densely collagenous stroma and scattered calcification. Treatment-related necrosis (20-30%).
P7 Fibro-myxoid sarcoma	31% high T2. High cellularity (4%). Necrosis (23%). 39% collagenous stroma.	Necrosis (24%)	Low cellular neoplasm in mostly collagenous stroma, but focal mildly myxoid changes. Observable necrosis.	46% high T2. Small regions of high cellularity (5%). Necrosis (25%). 16% collagenous stroma.	Necrosis (31%)	Low cellular neoplasm in alternating collagenous and mildly myxoid area. Treatment-related necrosis (40%).

Necrosis observed in tumors of P2 and P7 was confirmed by low FDG uptake in the necrotic area, shown overlaid on T₂-weighted MRI (Fig. 3.5 column b). The fraction of necrosis identified by the classification correlated strongly with low uptake on FDG-PET at both pre- and post-radiotherapy with R² of 0.97 and 0.96, respectively (Fig. 3.6). FDG uptake was high for the other habitats. In the fibromyxoid sarcoma (P7), 39% of the lesion was identified as collagenous stroma (purple), which is similar to necrosis on MRI but with a lower T₂. The high FDG uptake of this habitat suggests that it might not be necrotic. Collagenous stroma also appeared in the synovial sarcoma (P6) post-radiotherapy. According to pathology, both tumors (P6 post-radiotherapy and P7 pre- and post-radiotherapy) presented high percentages of collagenous stroma.

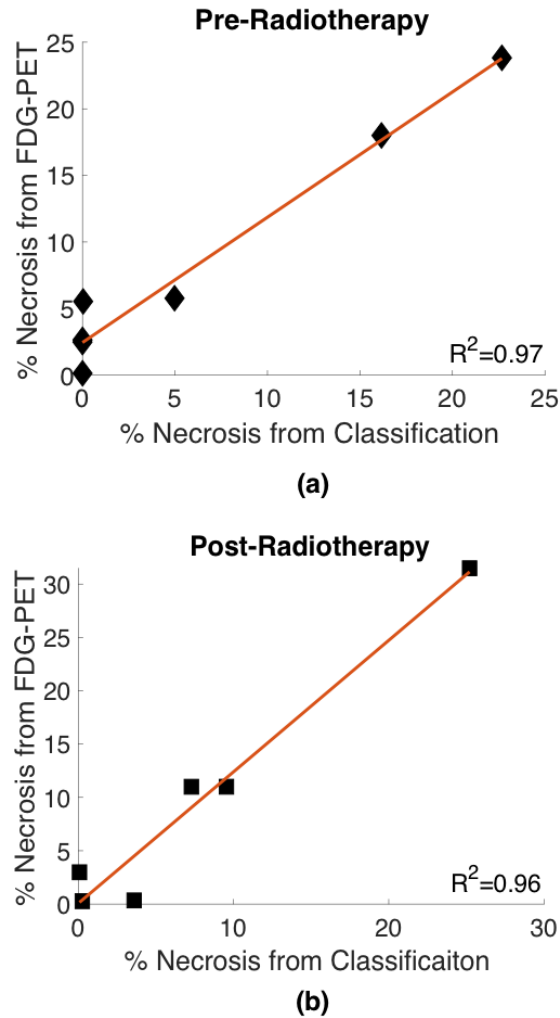


Figure 3.6 Percentage of necrosis estimated by the classification method plotted versus quantitative estimates of necrosis from FDG-PET uptake. A strong correlation was observed at both pre-radiotherapy and post-radiotherapy, with R^2 of 0.97 and 0.96 respectively.

The relative composition varied between tumors and treatment time points (Fig. 3.7). The longitudinal analysis revealed a decrease in hypercellular tissue in 4 of 7 tumors (P2, P3, P5, and P6) from pre- to post-radiotherapy. In this cohort, 99.9% of the tumor voxels from each patient were characterized by one habitat with probability greater than 50%.

Voxels with non-physical T_2 or ADC (negative or zero) remaining after Laplacian filtering were categorized as artifact. This constituted less than 0.2% of voxels for all cases except one—the second myxofibrosarcoma (P2) at visit 1, with 1.5 % artifact. In all cases, artifacts were located

near the tumor edges and were likely due to imperfect rigid image registration among DW-MRI images of different b -values. Voxels classified as “other” were less than 0.3% in all cases, with the exception of the fibromyxoid sarcoma (P7), with 10% of voxels as “other”.

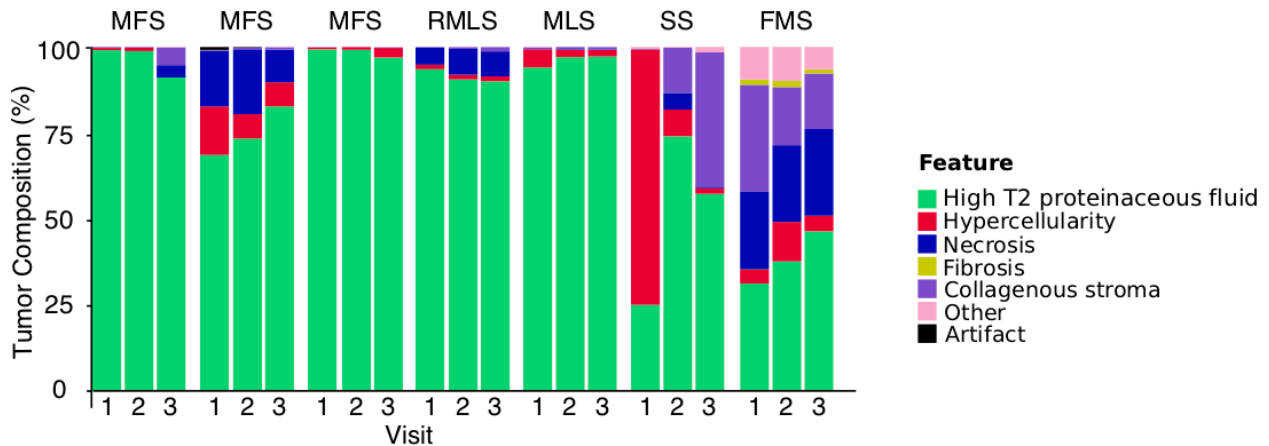


Figure 3.7 The relative tumor composition from the classification method are reported in all tumors in this study, including myxofibrosarcoma (MFS, P1, P2, P3), round cell/myxoid liposarcoma (RMLS, P4), myxoid liposarcoma (MLS, P5), synovial sarcoma (SS, P6) and fibromyxoid sarcoma (FMS, P7). MRI data were collected and analyzed at 3 time-points: pre-radiotherapy, during the 3rd week of radiotherapy, and after radiotherapy.

3.7 Discussion

We have proposed a method to assess tumor heterogeneity in STS on MRI, using maps of the ADC and T_2 to identify tumor habitats: high T_2 proteinaceous fluid, hypercellular tumor, necrosis, collagenous stroma, and fibrosis. Our quantitative approach exploits the intrinsic properties of tumor tissue and is theoretically independent of acquisition parameters. The probabilistic method allows the co-existence of multiple habitats within the same voxel. Habitats can be visualized as a mixture of colors with different degrees of transparency, based on the probability of the voxel being in that habitat.

Probability density functions of the ADC, T_2 and simDWI were computed for a reference tissue: muscle was used in this study. This approach can classify any image including those without

identifiable muscle, using data from other patients. In our work, the case of high-grade myxofibrosarcoma located in the flank (P2) had minimal muscle volume, and our classification distinguished tumor habitats nonetheless. The reference value distributions could be re-used to perform tissue classifications in future cases. Muscle contouring is not necessary in every patient.

In addition to the use of T_2 mapping, our approach innovates by representing high b-value DW-MRI with a quantitative surrogate, namely simDWI (Eq. 2). Either exponential term can dominate simDWI, depending on the T_2 and ADC. For a given ADC, the value of simDWI increases quickly with T_2 for low T_2 values and very slowly for high T_2 values. For a given T_2 , simDWI decreases with increasing ADC (Fig. 3.1). For larger T_2 values, ADC has an increasing impact on simDWI, superseding T_2 as the main effect in simDWI. In the proposed method, simDWI is crucial to distinguish necrosis from high T_2 proteinaceous fluid, by analogy to high-b-value DW-MRI. Necrosis and high T_2 proteinaceous fluid both have high ADC and high T_2 , but simDWI is lower for necrosis and it appears darker than muscle on the simDWI map. Specifically, outside of the 10th and 90th percentile contour lines (Fig. 3.1, dash and dash-dot lines respectively), the probability is highest for necrosis or high T_2 proteinaceous fluid, respectively. When the tumor simDWI falls within the contour lines, the differentiation is less clear and the voxel is labeled as a mixture of necrosis and high T_2 proteinaceous fluid.

The simDWI can be computed for any b-value. Necrosis and high-ADC tumor regions have previously been differentiated using DW-MRI with $b = 1000 \text{ s/mm}^2$ [39], [40] and $b = 925 \text{ s/mm}^2$ [41], but only partial differentiation for $b < 800 \text{ s/mm}^2$ [13], [42], [43]. In this study, data were acquired using $b = 800 \text{ s/mm}^2$ prior to the refinement of the proposed algorithm. We observed that necrosis and proteinaceous fluid were better differentiated using simDWI computed at $b = 1000 \text{ s/mm}^2$, consistent with the literature on DWI. Only partial differentiation was observed when using simDWI calculated with $b = 800 \text{ s/mm}^2$ (data not shown).

The five habitats identified by our method (hypercellular tissue, high T_2 proteinaceous fluid, necrosis, collagenous stroma, and fibrosis) were compared with the habitats obtained by other investigators using clustering algorithms. Four compartments were identified in prior studies of colon cancer xenografts using k-means clustering algorithms, including two types of viable tumors

and two types of necrosis [31], [32]. Connective tissue, viable tumor, and necrosis were distinguished based on FDG-PET and ADC in lung cancer xenografts [33]. Our hypercellular tumor habitat likely corresponds to the viable tumor reported in literature, extremely cell-dense and presumably well-oxygenated with low ADC and T_2 [31]–[33]. Necrosis featuring long T_2 and high ADC resembles that reported in the literature, generally acellular and similar to bulk water [31]–[33]. The collagenous stroma habitat is new and warrants further investigation. An alternative interpretation of this habitat could be severe necrosis with accumulation of blood products, which has been previously described [32], [44]. Blood products would reduce T_2 . If this is the case, the observation of FDG uptake in a necrotic habitat would require an explanation. Voxels classified as “other” in our work (especially in P7) had combinations of physically realistic parameters that did not fit the pre-defined habitats of Table 1, and do not yet have a straightforward interpretation.

The proposed method can characterize the entire tumor non-invasively. Pre-radiotherapy tumor composition identified myxoid and non-myxoid containing lesions. The proteinaceous myxoid forms an amorphous extracellular matrix which contains abundant free water [45]. In this study, all myxoid-containing lesions except the fibromyxoid sarcoma (P7) were classified as mostly high T_2 proteinaceous fluid, consistent with the characteristics of water-abundant myxoid. On biopsy, the fibromyxoid sarcoma had collagenous stroma and focal mildly myxoid stroma, in qualitative agreement with our segmentation result (31% high T_2 and 39% collagenous stroma). Interestingly, most tumors in this study presented only two of the five habitats, and not always the same two. Only two presented more than two habitats prior to radiotherapy (P2, with 3 habitats, and P7, with 5 habitats). This reflects the intra-tumoral and inter-patient heterogeneity in soft-tissue sarcoma.

Pre-treatment tumor necrosis has been shown to be an important prognostic factor for disease recurrence and survival rate in STS [46]. FDG-PET and dynamic contrast enhanced (DCE)-MRI have been proposed to detect necrosis [46]–[48]. Both require intravenous injection of contrast agents, and the former uses ionizing radiation. Our classification method provides a non-invasive tool for identification of necrosis without a contrast agent. It correctly identified the necrosis in the high-grade myxofibrosarcoma (P2), round cell/myxoid liposarcoma (P3), and fibromyxoid sarcoma (P7), at pre- and post-radiotherapy, corroborated by low uptake on FDG-PET. None of the other tumors had obvious regions of necrosis based on FDG-PET. Discrepancies in the

observation of necrosis at pre-radiotherapy could be due to biopsy sampling from non-necrotic areas.

Pathological observations from resection (Table 3) indicated substantial percentage of treatment-related necrosis for 6 out of 7 tumors, with greater percentage than the necrosis identified on imaging. For instance, in round cell/myxoid liposaroma (P4), the classification method identified 7% necrosis with 90% of high T₂ proteinaceous fluid (Table 3), whereas pathology estimated 70% of the tumor as treatment-related necrosis. It has been suggested that radiology and pathology do not correlate well when evaluating complete tumor necrosis [49], [50]. This can be related to differences between necrosis identified on imaging and treatment-related necrosis from pathology. Treatment-related necrosis includes different types of necrosis with distinctive morphological patterns [51]. We speculate that two types of necrosis were present in this study (Sup. Fig. 3.S2): liquefactive necrosis, characterized by liquid viscous mass and the absence of stroma, most obvious in one myxofibrosarcoma (P2), and coagulative necrosis, where tumor cells are destroyed by radiation leaving the stroma intact (P2-P7). Necrosis on MRI refers to regions of high fluid content, and therefore likely reflects a subcategory of necrosis. For the tumor in P4, the tumor cells were destroyed by radiation in the regions of treatment-related necrosis. Nevertheless, the myxoid stroma was still intact to various degrees. Myxoid was associated to the high T₂ proteinaceous fluid habitat, and treatment-related necrosis was likely classified as such. In the synovial sarcoma (P6), therapy-related necrosis was characterized by intact collagenous stroma.

Radiotherapy effects on tumor composition were quantitatively evaluated. In 4 of 7 patients in the study, the percentage of hypercellular tissue decreased from pre- to post-radiotherapy, a likely effect of radiotherapy. Our findings are consistent with reports of effective therapy response resulting in tumor lysis, loss of cell membrane integrity, and increase of extracellular space [35]. The probabilistic nature of this approach allows the co-existence of different habitats in the same voxel, providing a more realistic reflection of the complex microenvironment, especially at habitat boundaries. The identification of these habitats can provide valuable information about tumor composition and its changes during radiotherapy. This classification technique provides information about sub-regions that could be targeted by radiation dose painting, for use of systemic agents that target more resistant tumor components, or in the assessment of treatment response.

Other clinical studies have classified soft tissue sarcoma habitats using Otsu segmentation methods applied to the signal intensity of post-contrast T1-weighted[52] or to the combination of pre-contrast T1-weighted, post-contrast T1-weighted, and T2-weighted images[53], [54]. These studies showed that texture analysis within each distinctive habitat improved the accuracy for the prediction of metastatic and necrotic tumor. It is also possible to envision an approach building on the proposed method where the surrounding normal tissue would be analyzed and used to assess the infiltrative nature of the tumor.

Limitations

The accuracy of the classification relies on the accuracy of reference ADC and T_2 distributions in tumor and muscle. The T_2 and ADC are intrinsic properties of the tissue but the choice of measurement technique, acquisition parameters, receive coil, and field strength could impact the estimation of these parameters [55], [56]. The most notable impact of variations in the quantitative parameters might be the re-use of reference data in studies where the new data are acquired with different parameters, which could be resolved by standardization of the acquisition parameters.

The use of probability distributions of ADC and T_2 from selected muscles in a small group of patients assumes that this sample is representative of muscle in the population and independent of anatomic location. Variations of ADC and T_2 in muscle could lead to inaccurate classification of tumor sub-regions. The ADC and T_2 from the forearm had slightly higher means than other regions, resulting in skewed sample distributions (Sup. Fig. 3.S1). Anatomical variations in the ADC of skeletal muscle have been reported [57]. Literature on ADC and T_2 in muscle is focused on limited anatomical locations [39] or to changes under specific conditions [58], [59]. A systematic study of ADC and T_2 in muscle in a larger group of participants, possibly including patients and healthy individuals, would be of interest for this method.

The classification depends on the registration and resampling of DW-MRI and T_2 maps to compensate for differences in field-of-view and voxel dimensions, and for patient motion. We used rigid registration in this proof-of-principle study, which left discrepancies due to patient motion. Attempts at non-linear registration with the “VoxAlign” algorithm (available in MIMvista

software) did not improve the results and in some cases produced unusable quantitative maps. More advanced non-linear registration methods could be used to improve the registration [60]. Laplacian filtering [37] was applied to ADC and T_2 maps to replace non-physical negative values in certain voxels (due to image artifacts, noise, or imperfect image registration) with values interpolated from neighbouring voxels. In certain cases of imperfect registration, non-physical values spanned multi-voxel regions and Laplacian interpolation became ineffective. Overall, the ADC values in muscle in this study agree with others [15], [26]. However, the ADC measured here in necrosis at pre-treatment (median 3.1×10^{-3} mm²/s, interquartile range 2.8×10^{-3} mm²/s– 3.2×10^{-3} mm²/s) is similar to the accepted diffusion coefficient of water at body temperature (3×10^{-3} mm²/s)[61], and may be higher than expected. Studies have reported similarly high ADC in cerebrospinal fluid (3.0×10^{-3} – 3.4×10^{-3} mm²/s) [62], [63]. This does not affect the quality of the habitat classification in this work.

Biopsy results in this study were obtained retrospectively and were likely to reflect the presence of viable tumor cells, as is the goal of a clinical biopsy. Biopsy procedures were not explicitly recorded; therefore, the location and path of these biopsies were not available. This is a limitation. In this study, a single orthopaedic surgeon (RT) obtained 6 of the 7 biopsies. The biopsy in P6 was collected by a neurosurgeon. Biopsy practice at our institution is largely guided by the tumor position, depth, and morphology, patient considerations, the surgical plan, and surgeon's experience. The physician always aims for soft tissue and to sample viable tumor, avoiding nerves, bones, and joints. In STS, viable tumor is often found at the periphery. The physician reviews available images (cross-sectional imaging on CT or MRI) prior to biopsy. Multiple samples are taken at one puncture position, by angulating the biopsy needle. The biopsy tract is based on the surgical plan and is therefore resected along with the tumor. A typical core is 2.5 cm in length and collected no deeper than the central portion of the tumor, to avoid going beyond the tumor.

Generalizability of the technique to a broader range of STS and to other tumor types remains to be demonstrated. We performed an initial demonstration of the technique in a small cohort of patients with STS of different types, participating in a larger study to validate a model developed by our team that relates imaging findings with the subsequent development of lung metastases [64].

3.8 Conclusion

In conclusion, we have automated the process of identifying pathologically relevant tumor habitats of hypercellularity, high T₂ proteinaceous fluid, necrosis, collagenous stroma, and fibrosis, with a reference-region-based probabilistic classification technique applied to MRI. This technique was demonstrated in 7 patients with biopsy-confirmed soft tissue sarcoma, and results were qualitatively consistent with histopathology.

Acknowledgments

The authors acknowledge the assistance of Laurian Rohoman and the MRI technologists at the Montreal General Hospital in collecting the data. Zaki Ahmed, Véronique Fortier, Tom Powell, and Stephen Salomon, are acknowledged for useful discussion. This study was funded in part by an award from the Montreal General Hospital Foundation, and the Phil Gold Fellowship. S.X. was funded by a scholarship from the *Ministère de la Santé et des Services Sociaux du Québec*, an award from the *Fonds de Recherche Québec – Santé* (FRQS), and the NSERC

References

- [1] D. Le Bihan, “Magnetic Resonance Diffusion Imaging: Introduction and Concepts,” in *Diffusion MRI*, Oxford University Press, 2010, pp. 57–78.
- [2] R. BROOKER, *Principles of biology + connect access card*. MCGRAW-HILL EDUCATION, 2017.
- [3] S. Kondo and T. Miura, “Reaction-diffusion model as a framework for understanding biological pattern formation.,” *Science*, vol. 329, no. 5999, pp. 1616–20, Sep. 2010.
- [4] S. Mori and P. B. Barker, “Diffusion Magnetic Resonance Imaging :,” pp. 102–109, 1999.
- [5] M. P. Marks, A. de Crespigny, D. Lentz, D. R. Enzmann, G. W. Albers, and M. E. Moseley, “Acute and chronic stroke: navigated spin-echo diffusion-weighted MR imaging.,” *Radiology*, vol. 199, no. 2, pp. 403–8, May 1996.
- [6] R. Bammer, “Basic principles of diffusion-weighted imaging.,” *Eur. J. Radiol.*, vol. 45, no. 3, pp. 169–84, Mar. 2003.
- [7] S. Xing, C. R. Freeman, S. Jung, R. Turcotte, and I. R. Levesque, “Probabilistic classification of tumor habitats in soft tissue sarcoma,” *NMR Biomed.*, no. June, p. e4000, 2018.
- [8] G. H. Heppner and B. E. Miller, “Tumor heterogeneity: biological implications and therapeutic consequences,” 1983.
- [9] B. V. Jardim-Perassi *et al.*, “Multiparametric MRI and coregistered histology identify tumor habitats in breast cancer mouse models,” *Cancer Res.*, vol. 79, no. 15, pp. 3952–3964, Aug. 2019.
- [10] J. M. Brown, “Tumor Hypoxia in Cancer Therapy,” *Methods in Enzymology*, vol. 435. 2007.
- [11] I. Heid *et al.*, “Co-clinical assessment of tumor cellularity in pancreatic cancer,” *Clin. Cancer Res.*, vol. 23, no. 6, pp. 1461–1470, Mar. 2017.
- [12] M. Vallières *et al.*, “Investigating the role of functional imaging in the management of soft-tissue sarcomas of the extremities,” 2018.
- [13] M. M. Y. Khoo, P. a. Tyler, A. Saifuddin, and A. R. Padhani, “Diffusion-weighted imaging (DWI) in musculoskeletal MRI: A critical review,” *Skeletal Radiol.*, vol. 40, pp.

- 665–681, 2011.
- [14] R. Stramare *et al.*, “Imaging of soft-tissue tumors,” *J. Magn. Reson. Imaging*, vol. 37, no. 4, pp. 791–804, Apr. 2013.
- [15] P. A. Gondim Teixeira *et al.*, “Diffusion-weighted magnetic resonance imaging for the initial characterization of non-fatty soft tissue tumors: correlation between T2 signal intensity and ADC values,” *Skeletal Radiol.*, vol. 45, no. 2, pp. 263–271, 2016.
- [16] K. Thway, “Pathology of Soft Tissue Sarcomas,” *Clin. Oncol.*, vol. 21, no. 9, pp. 695–705, 2009.
- [17] C. Antonescu, “Round cell sarcomas beyond Ewing: emerging entities,” *Histopathology*, vol. 64, no. 1, pp. 26–37, Jan. 2014.
- [18] J. S. Wu and M. G. Hochman, “Soft-tissue tumors and tumorlike lesions: a systematic imaging approach,” *Radiology*, vol. 253, no. 2, pp. 297–316, 2009.
- [19] O. Dudeck *et al.*, “Diffusion-weighted magnetic resonance imaging allows monitoring of anticancer treatment effects in patients with soft-tissue sarcomas,” *J. Magn. Reson. Imaging*, vol. 27, no. 5, pp. 1109–1113, 2008.
- [20] M. Maeda *et al.*, “Soft-tissue tumors evaluated by line-scan diffusion-weighted imaging: Influence of myxoid matrix on the apparent diffusion coefficient,” *J. Magn. Reson. Imaging*, vol. 25, no. 6, pp. 1199–1204, 2007.
- [21] T. K. Subhawong, M. A. Jacobs, and L. M. Fayad, “Diffusion-weighted MR Imaging for Characterizing Musculoskeletal Lesions,” *RadioGraphics*, vol. 34, no. 5, pp. 1163–1177, Sep. 2014.
- [22] D. M. Koh and D. J. Collins, “Diffusion-weighted MRI in the body: Applications and challenges in oncology,” *Am. J. Roentgenol.*, vol. 188, no. 6, pp. 1622–1635, 2007.
- [23] A. R. Padhani *et al.*, “Diffusion-weighted magnetic resonance imaging as a cancer biomarker: consensus and recommendations,” *Neoplasia*, vol. 11, no. 2, pp. 102–125, 2009.
- [24] K. Oka *et al.*, “Usefulness of Diffusion-Weighted Imaging for Differentiating Between Desmoid Tumors and Malignant Soft Tissue Tumors,” vol. 193, pp. 189–193, 2011.
- [25] C. S. P. Van Rijswijk, P. Kunz, P. C. W. Hogendoorn, A. H. M. Taminiau, J. Doornbos, and J. L. Bloem, “Diffusion-weighted MRI in the characterization of soft-tissue tumors,” *J. Magn. Reson. Imaging*, vol. 15, no. 3, pp. 302–307, 2002.

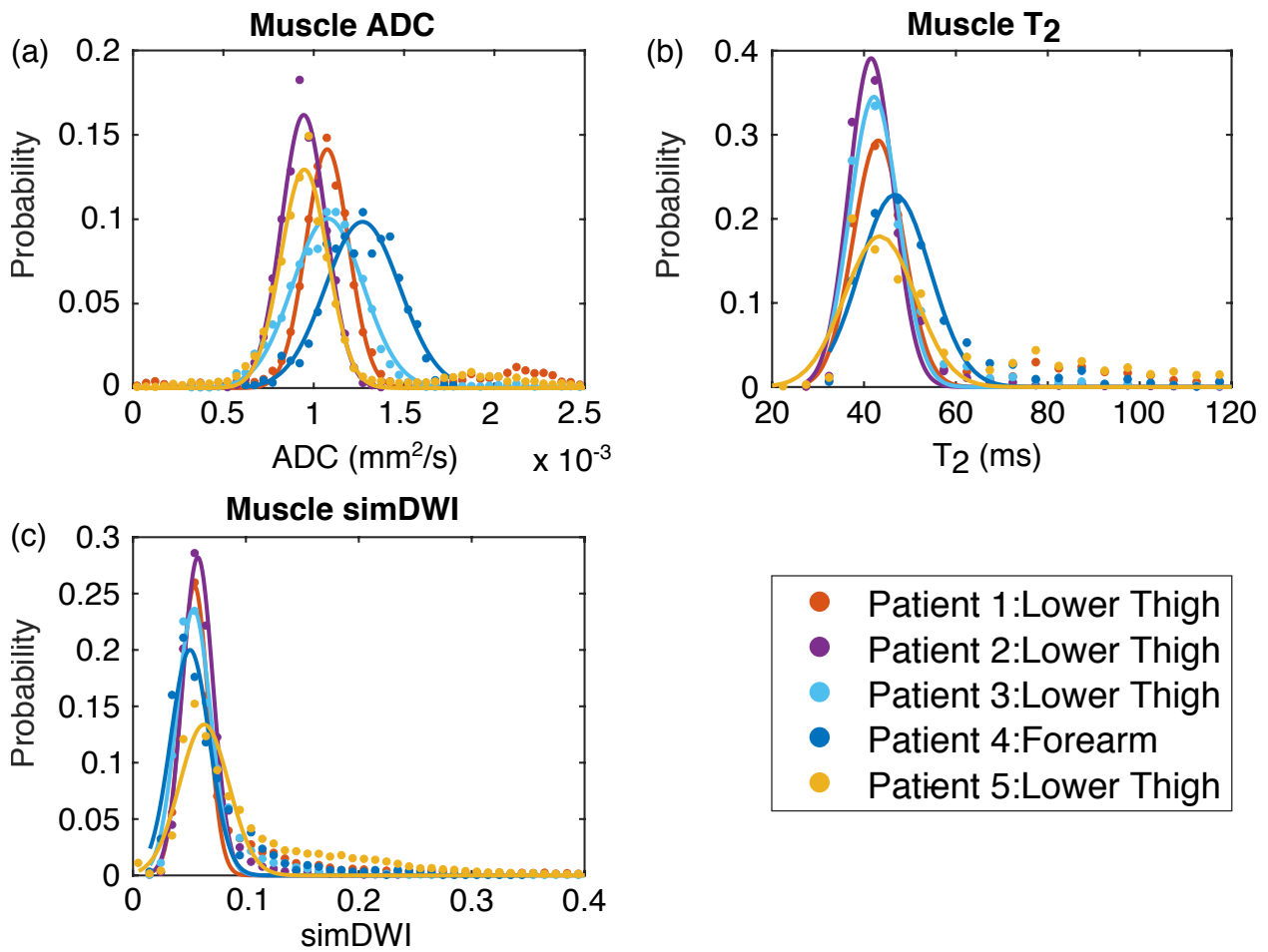
- [26] S.-Y. Lee *et al.*, “Differentiation of malignant from benign soft tissue tumors: use of additive qualitative and quantitative diffusion-weighted MR imaging to standard MR imaging at 3.0 T,” *Eur. Radiol.*, 2015.
- [27] Filip Janku, “Tumor heterogeneity in the clinic: is it a real problem?,” *Ther Adv Med Oncol*, vol. 6, no. 2, pp. 43–51, 2014.
- [28] S. S. F. Yip and H. J. W. L. Aerts, “Applications and limitations of radiomics,” *Phys. Med. Biol.*, vol. 61, no. 13, pp. R150–R166, 2016.
- [29] R. J. Gillies, P. E. Kinahan, and H. Hricak, “Radiomics : Images Are More than Pictures, They Are Data,” vol. 278, no. 2, 2016.
- [30] L. R. Berry *et al.*, “Quantification of viable tumor microvascular characteristics by multispectral analysis,” *Magn. Reson. Med.*, vol. 60, no. 1, pp. 64–72, 2008.
- [31] R. A. D. Carano *et al.*, “Quantification of Tumor Tissue Populations by Multispectral Analysis,” *Magn. Reson. Med.*, vol. 51, no. 3, pp. 542–551, 2004.
- [32] E. C. Henning, C. Azuma, C. H. Sotak, and K. G. Helmer, “Multispectral quantification of tissue types in a RIF-1 tumor model with histological validation. Part I,” *Magn. Reson. Med.*, vol. 57, no. 3, pp. 501–512, 2007.
- [33] M. R. Divine, P. Katiyar, U. Kohlhofer, L. Quintanilla-Martinez, B. J. Pichler, and J. A. Disselhorst, “A Population-Based Gaussian Mixture Model Incorporating 18F-FDG PET and Diffusion-Weighted MRI Quantifies Tumor Tissue Classes,” *J. Nucl. Med.*, vol. 57, no. 3, pp. 473–479, 2016.
- [34] D. M. Koh and H. C. Thoeny, *Diffusion weighted MR Imaging, Applications in the BOdy*. Springer, 2010.
- [35] D. M. Patterson, A. R. Padhani, and D. J. Collins, “Technology insight: water diffusion MRI--a potential new biomarker of response to cancer therapy.,” *Nat. Clin. Pract. Oncol.*, vol. 5, no. 4, pp. 220–233, 2008.
- [36] H. S. Kang, J. Mo, and A. Y. Kang, “Oncologic Imaging Bone Tumors.”
- [37] B. P. F. William H. Press, Saul A. Teukolsky, William T. Vetterling, *Numerical Recipes The Art of Scientific Computing*. 2007.
- [38] M. D. Cheney *et al.*, “[18F]-Fluoromisonidazole positron emission tomography/computed tomography visualization of tumor hypoxia in patients with chordoma of the mobile and sacrococcygeal spine.,” *Int. J. Radiat. Oncol. Biol. Phys.*, vol. 90, no. 5, pp. 1030–6, Dec.

- 2014.
- [39] K. Oka, T. Yakushiji, H. Sato, T. Hirai, Y. Yamashita, and H. Mizuta, "The value of diffusion-weighted imaging for monitoring the chemotherapeutic response of osteosarcoma: a comparison between average apparent diffusion coefficient and minimum apparent diffusion coefficient," *Skeletal Radiol.*, vol. 39, no. 2, pp. 141–146, Feb. 2010.
- [40] V. Vandecaveye *et al.*, "Detection of head and neck squamous cell carcinoma with diffusion weighted MRI after (chemo)radiotherapy: Correlation between radiologic and histopathologic findings," *Int. J. Radiat. Oncol. Biol. Phys.*, vol. 67, no. 4, pp. 960–971, 2007.
- [41] H. Lyng, O. Haraldseth, and E. K. Rofstad, "Measurement of cell density and necrotic fraction in human melanoma xenografts by diffusion weighted magnetic resonance imaging," *Magn. Reson. Med.*, vol. 43, no. 6, pp. 828–836, 2000.
- [42] S. Walker-Samuel, M. Orton, L. D. McPhail, and S. P. Robinson, "Robust estimation of the apparent diffusion coefficient (ADC) in heterogeneous solid tumors," *Magn. Reson. Med.*, vol. 62, pp. 420–429, 2009.
- [43] H. Einarsdóttir, M. Karlsson, J. Wejde, and H. C. F. Bauer, "Diffusion-weighted MRI of soft tissue tumors," *Eur. Radiol.*, vol. 14, no. 6, pp. 959–963, 2004.
- [44] X. Jiang *et al.*, "A Gamma-Knife-Enabled Mouse Model of Cerebral Single-Hemisphere Delayed Radiation Necrosis," *PLoS One*, vol. 10, no. 10, p. e0139596, Oct. 2015.
- [45] M. Maeda *et al.*, "Soft-tissue tumors evaluated by line-scan diffusion-weighted imaging: Influence of myxoid matrix on the apparent diffusion coefficient," *J. Magn. Reson. Imaging*, vol. 25, pp. 1199–1204, 2007.
- [46] R. Rakheja *et al.*, "Necrosis on FDG PET/CT correlates with prognosis and mortality in sarcomas," *Am. J. Roentgenol.*, vol. 201, no. 1, pp. 170–177, 2013.
- [47] T. S. Koh *et al.*, "Assessment of tumor necrotic fraction by dynamic contrast-enhanced MRI: a preclinical study of human tumor xenografts with histopathologic correlation.," *NMR Biomed.*, vol. 27, no. 4, pp. 486–94, Apr. 2014.
- [48] V. A. Larsen, H. J. Simonsen, I. Law, H. B. W. Larsson, and A. E. Hansen, "Evaluation of dynamic contrast-enhanced T1-weighted perfusion MRI in the differentiation of tumor recurrence from radiation necrosis," *Neuroradiology*, vol. 55, no. 3, pp. 361–369, Mar. 2013.

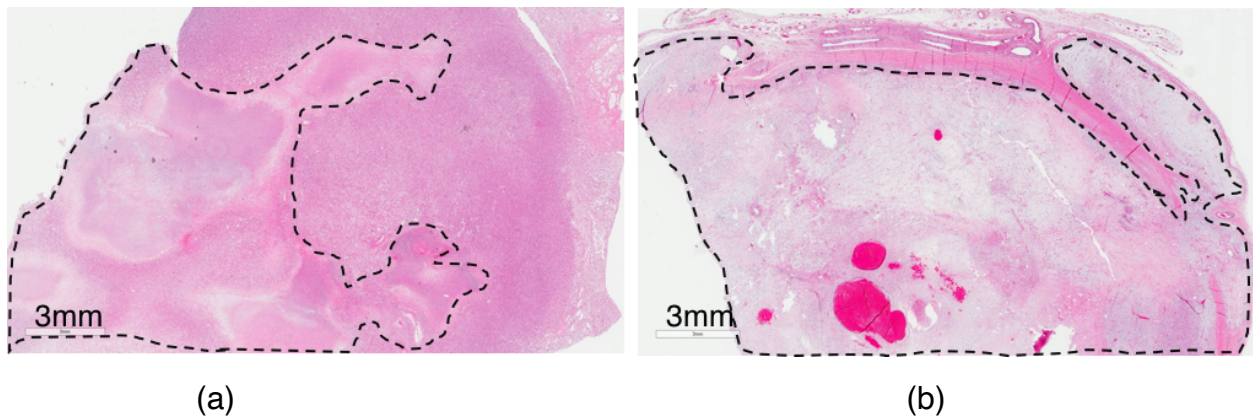
- [49] L. Mannelli, S. Kim, C. H. Hajdu, J. S. Babb, T. W. I. Clark, and B. Taouli, "Assessment of tumor necrosis of hepatocellular carcinoma after chemoembolization: Diffusion-weighted and contrast-enhanced MRI with histopathologic correlation of the explanted liver," *Am. J. Roentgenol.*, vol. 193, no. 4, pp. 1044–1052, 2009.
- [50] H. L. Marin, E. E. Furth, K. Olthoff, A. Shaked, and M. C. Soulen, "Histopathologic outcome of neoadjuvant image-guided therapy of hepatocellular carcinoma," *J. Gastrointest. Liver Dis.*, vol. 18, no. 2, pp. 169–176, 2009.
- [51] J. C. A. Vinay Kumar, Abul K. Abbas, *Robbins & Cotran Pathologic Basis of Disease*. Elsevier Health Sciences, 2014.
- [52] H. Farhidzadeh, M. Zhou, D. B. Goldgof, L. O. Hall, M. Raghavan, and R. A. Gatenby, "Prediction of treatment response and metastatic disease in soft tissue sarcoma," 2014, p. 903518.
- [53] P. Mris, L. O. Hall, J. G. Scott, R. A. Gatenby, R. J. Gillies, and M. Raghavan, "A Quantitative Histogram-based Approach to Predict Treatment Outcome for Soft Tissue Sarcomas Using," pp. 4549–4554, 2016.
- [54] H. Farhidzadeh, D. B. Goldgof, L. O. Hall, R. A. Gatenby, R. J. Gillies, and M. Raghavan, "Texture Feature Analysis to Predict Metastatic and Necrotic Soft Tissue Sarcomas," *2015 IEEE Int. Conf. Syst. Man, Cybern.*, pp. 2798–2802, 2015.
- [55] T. A. G. M. Huisman *et al.*, "Quantitative diffusion tensor MR imaging of the brain: field strength related variance of apparent diffusion coefficient (ADC) and fractional anisotropy (FA) scalars.," *Eur. Radiol.*, vol. 16, no. 8, pp. 1651–8, Aug. 2006.
- [56] B. M. Dale, A. C. Braithwaite, D. T. Boll, and E. M. Merkle, "Field strength and diffusion encoding technique affect the apparent diffusion coefficient measurements in diffusion-weighted imaging of the abdomen.," *Invest. Radiol.*, vol. 45, no. 2, pp. 104–8, Feb. 2010.
- [57] O. Yanagisawa, D. Shima, K. Maruyama, M. Nielsen, T. Irie, and M. Niitsu, "Diffusion-weighted magnetic resonance imaging of human skeletal muscles: gender-, age- and muscle-related differences in apparent diffusion coefficient.," *Magn. Reson. Imaging*, vol. 27, no. 1, pp. 69–78, Jan. 2009.
- [58] L. L. Ploutz-Snyder, S. Nyren, T. G. Cooper, E. J. Potchen, and R. A. Meyer, "Different effects of exercise and edema on T2 relaxation in skeletal muscle," *Magn. Reson. Med.*, vol. 37, no. 5, pp. 676–682, May 1997.

- [59] G. Saab, R. T. Thompson, and G. D. Marsh, "Multicomponent T2 relaxation of in vivo skeletal muscle," *Magn. Reson. Med.*, vol. 42, no. 1, pp. 150–157, Jul. 1999.
- [60] J. Pukala *et al.*, "Benchmarking of five commercial deformable image registration algorithms for head and neck patients," *J. Appl. Clin. Med. Phys.*, vol. 17, no. 3, pp. 25–40, May 2016.
- [61] D. Le Bihan and M. Iima, "Diffusion Magnetic Resonance Imaging: What Water Tells Us about Biological Tissues," *PLOS Biol.*, vol. 13, no. 7, p. e1002203, Jul. 2015.
- [62] L. Annet, T. Duprez, C. Grandin, G. Doms, A. Collard, and G. Cosnard, "Apparent diffusion coefficient measurements within intracranial epidermoid cysts in six patients," *Neuroradiology*, vol. 44, no. 4, pp. 326–328, Apr. 2002.
- [63] R. N. Sener, "Diffusion MRI: apparent diffusion coefficient (ADC) values in the normal brain and a classification of brain disorders based on ADC values," *Comput. Med. Imaging Graph.*, vol. 25, no. 4, pp. 299–326, Jul. 2001.
- [64] M. Vallières, C. R. Freeman, S. R. Skamene, and I. El Naqa, "A radiomics model from joint FDG-PET and MRI texture features for the prediction of lung metastases in soft-tissue sarcomas of the extremities," *Phys. Med. Biol.*, vol. 60, no. 14, pp. 5471–5496, 2015.

3.9 Supporting Information



Supporting Figure 3.1 Histograms of ADC (a), T₂ (b), and simDWI (c) in muscle across patients yield similar mean values. Each data point is the center value for the histogram bin, and the bin height normalized to the total number of voxels. A Gaussian function is fitted to the histogram from each patient.



Supporting Figure 3.2 Histology sample of (a) myxofibrosarcoma (P2) and (b) round cell/myxoid liposarcoma (P4) shows different morphologies of treatment-related necrosis. Liquefactive necrosis in (a), indicated by the dotted lines, is an acellular geographic area of necrosis with necrotic nuclear debris and viscous consistency. In (b), the myxoid stroma still appears to be retained, but with no cellular component present in treatment-related necrotic areas (dotted lines) reflected by a homogeneous acellular myxoid/hyalinised appearance in the stain.

Supporting Table 3.1 The minimum and maximum value of the imaging parameters for patients in this study at pre-radiotherapy are reported.

	Matrix	FOV (mm)	Number of slices	Slice thickness (mm)	Readout bandwidth (Hz/pixel)	TR(ms)	TE (ms)
FSE (longTE)	512× 512	120-400	32-60	4-5	98	3650-5900	76-83
FSE (minTE)	512× 512	120-400	32-60	4-5	98	3650-5900	11-12
DWI $b=100$ s/mm ²	256× 256	300-440	21-52	6	1953	5000	88-91
DWI $b=800$ s/mm ²	256× 256	300-440	21-52	6	1953	5000	88-91

Chapter 4

Non-invasive apparent cell size mapping with diffusion weighted MRI

4.1 Preface

After the automated classification of tumor habitats (Chapter 3), I aim to further characterize each habitat to understand the underlying biophysical structures. A method named Imaging Microstructural Parameters Using Limited Spectrally Edited Diffusion (IMPULSED) has been proposed to map voxel-wise cancer cell size and cellularity non-invasively, by Dr. Gore's group at Vanderbilt University. In the effort to implement the IMPULSED method at the 3T clinical scanner in the McGill University Health Center, I spent a month at Vanderbilt University to learn about the IMPULSED method. This chapter summarizes the three steps that I took to ensure accurate and reproducible estimation of cell size and cell volume fractions. The simulation and experimental work done in this chapter provided me with a thorough understanding of cell size mapping with the IMPULSED method, which served as a starting point for my second and third PhD projects (Chapter 5, 6).

4.2 Introduction

Histopathologic examination of the sample tumor specimen is the current gold standard for clinical tumor diagnosis. Multiple specimens are extracted at different regions of the tumor via biopsy, or obtained from a resected mass, and examined under the microscope by pathologists for abnormal cell size, shape, and arrangement [1]. Direct visual observation of cancerous cells provides an intuitive understanding of the tumor microenvironment; staining leads to high specificity to pathological observations [2]. However, since only a small amount of tumor tissue is obtained by biopsy, the extracted sample might not fully reflect the tumor heterogeneity. In addition, the invasive nature of biopsy can cause significant discomfort to the patients, making it unsuitable for repeated measurements for treatment monitoring and assessment.

Non-invasive imaging techniques such as magnetic resonance imaging (MRI) have been proposed to characterize the tissue microenvironment over the entire tumor. In particular, diffusion-weighted MRI (DW-MRI) provides a non-invasive way to map the diffusion properties of tissue water molecules that are affected by restriction and hindrance to free movement and is thereby able to provide information on tissue microenvironment [3]. For instance, the apparent diffusion coefficient (ADC) calculated from DW-MRI has been shown to inversely correlate with tumor cellularity[4]–[6]. The difference in ADC values has been used to differentiate malignant tumors from benign tumors in multiple cancer types [7]–[9]. The increase in ADC values was reportedly indicative of positive therapy response[10], [11].

In a clinical study of soft-tissue sarcoma conducted at the McGill University Health Centre, we successfully delineated various tumor sub-regions including regions of hypercellularity, necrosis, and proteinaceous fluid, using the combination of T2-weighted images, DWI, and ADC maps [12] (Chapter 3). In addition, we have observed elevated average ADC of the tumor from pre-radiotherapy to post-radiotherapy [13], with increased ADC in the hypercellular and proteinaceous fluid habitats. However, the underlying variations in the biophysical structure of each sub-region and their response to treatment are only partially reflected by ADC. A more specific measurement of tumor microstructure at the cellular level, including cell size and cellular density, could provide valuable information about tumor development and therapeutic response.

The sensitivity to microstructural features generally requires a very powerful gradient coil ($\sim 300\text{mT/s}$), which is beyond the capacity of common clinical scanners ($\sim 60\text{mT/s}$) [14], [15]. An alternative DW-MR technique, developed by Dr. John Gore's group at Vanderbilt University on a 3 T clinical scanner, combines long-diffusion-time pulsed gradient spin echo (PGSE) and low-frequency oscillating gradient spin-echo (OGSE) sequences to provide sensitivity to microstructural features. This method is named Imaging Microstructural Parameters Using Limited Spectrally Edited Diffusion (IMPULSED), and has been proposed to map voxel-wise cancer cell size and cellularity non-invasively [16], [17]. Promising results were shown for both *in-vivo* colon cancer mouse models and human breast tumors [17], [18].

In the effort to implement the IMPULSED method at the 3T clinical scanner in the McGill University Health Center, three steps were taken to ensure accurate and reproducible estimations of cell size and volume fractions. This chapter provides an overview of these steps which include 1) development of analysis tools for the IMPULSED method, validated with simulated diffusion signals at different levels of SNR; 2) cross-site validation of data analysis, comparing estimated microstructural parameters from analysis tools independently developed at Vanderbilt and McGill using a shared *in-vitro* dataset; 3) establishing feasibility of *in-vivo* cell size mapping with IMPULSED. The image acquisition involved in step 3 was completed at Vanderbilt University.

4.3 Theory

4.3.1 Diffusion modeling

In order to quantify tissue parameters below the nominal resolution of MRI, a biophysical model of the underlying cellular geometry and its contribution to the diffusion signal have to be established.

The normalized diffusion MR signal can be modeled with an analytical expression combining the signal of intracellular water undergoing restricted diffusion inside the cells S_{in} , with the signal from extra-cellular water undergoing hindered extracellular diffusion S_{exo} (Eq.1).

$$S/S_0 = v_{in} S_{in}(R, D_{in}) + (1 - v_{in}) S_{exo}(D_{exo}) \quad (1)$$

where v_{in} represents the percentage volume occupied by cells, referred to as the intracellular volume fraction. The cells are modeled as spheres with radius R [19]. D_{in} and D_{exo} are the intra- and extra-cellular diffusion coefficient, respectively. The water exchange between intra- and extracellular spaces is not considered, due to its negligible effect on the estimation of mean cell size [20].

The mathematical expression of S_{in} depends on the pulse sequence, the shape of the diffusion gradient, and the cell shape. The IMPULSED method uses a combination of diffusion signals from the conventional pulsed gradient spin echo (PGSE) sequence and oscillating gradient spin echo (OGSE) sequences[17] (see Chapter 2, Section 2.3.9).

The analytical expression of the intracellular diffusion signal, measured with cosine-modulated gradient waveforms can be expressed as

$$S_{in}(OGSE) = \exp\left(-2(\gamma g)^2 \sum_n \frac{B_n \lambda_n^2 D_{in}^2}{(\lambda_n^2 D_{in}^2 + 4\pi^2 f^2)^2} \left\{ \frac{\lambda_n^2 D_{in}^2 + 4\pi^2 f^2}{\lambda_n D_{in}} \left[\frac{\delta}{2} + \frac{\sin(4\pi f \delta)}{8\pi f} \right] - 1 \right. \right. \\ \left. \left. + \exp(-\lambda_n D_{in} \delta) \right. \right. \\ \left. \left. + \exp(-\lambda_n D_{in} \Delta)(1 - \cosh(\lambda_n D_{in} \delta)) \right\} \right) \quad (2)$$

The expression for the intracellular signal S_{in} contains terms for the gradient pulse: the gradient amplitude g , the gradient pulse duration δ , the separation time between the two diffusion gradients Δ , the oscillation frequency of the gradient f , the geometrical structure dependent parameters λ_n and B_n (e.g. spheres, plane, cylinder) and the intracellular diffusivity D_{in} . The expressions for λ_n and B_n have been reported in published literature [21] as,

$$B_n = \frac{2(R/\mu_n)^2}{\mu_n^2 - 2}, \quad \lambda_n = \frac{\mu_n^2}{R^2}$$

where μ_n is the n^{th} root of the equation $\mu J'_{3/2}(\mu) - \frac{1}{2}J_{3/2}(\mu) = 0$. $J_{3/2}$ is the Bessel function of order 3/2.

Similarly, the diffusion signal measured with PGSE within impermeable spheres can be expressed as,

$$S_{in}(PGSE) = \exp\left(-2\left(\frac{\gamma g}{D_{in}}\right)^2 \sum_n \frac{B_n}{\lambda_n^2} \{\lambda_n D_{in} \delta - 1 + \exp(-\lambda_n D_{in} \delta) + \exp(-\lambda_n D_{in} \Delta)(1 - \cosh(\lambda_n D_{in} \delta))\}\right) \quad (3)$$

The extracellular diffusion is considered hindered, and can be expressed with a mono-exponential function of D_{exo} as:

$$S_{exo} = \exp(-b \cdot D_{exo}) \quad (4)$$

4.4 Methods

4.4.1 Computer simulations

Simulations were performed to explore the performance of model fitting under the influence of noise. The matrix method (Microstructure Imaging Sequence Simulation Toolbox (MISST), UCL) [22] was used to simulate diffusion signals for each tissue microstructure from PGSE and OGSE diffusion sequence [20], [21]. The term “microstructure” represents the tissue model with a single combination of input parameters. The tissue microstructure was characterized in terms of cell radius R , intracellular volume fraction v_{in} , and the intra- and extra-cellular diffusivities D_{in} and D_{exo} . Diffusion signals were generated for 36 tissue microstructures with cell radius $R = 4, 5, 6, 7, 8 \mu\text{m}$ and volume fraction $v_{in} = 25\%, 50\%, 75\%$. D_{in} and D_{exo} were set to be $1 \mu\text{m}^2/\text{ms}$ and $2 \mu\text{m}^2/\text{ms}$ respectively. For each tissue microstructure, PGSE diffusion signals were simulated at effective diffusion time $\Delta_{\text{eff}} = 66.7 \text{ms}$, with diffusion gradient duration $\delta = 10 \text{ms}$ and gradient separation time $\Delta = 70 \text{ms}$. OGSE diffusion signals were simulated at lower $\Delta_{\text{eff}} = 5$ and 10ms ,

with $\delta/\Delta = 40/50.5\text{ms}$. The oscillating frequencies of the gradient waveform were 25 and 50Hz. Nine b -values were simulated from 0 to $2000\text{ ms}/\mu\text{m}^2$ in intervals of $250\text{ ms}/\mu\text{m}^2$. The maximum gradient strength used was 150 mT/m, which is readily achievable for most pre-clinical scanners. 1,500 noisy synthetic signals with SNR = 20, 35, 50 and 80 were generated for each microstructure, with the signal-to-noise-ratio (SNR) defined for the $b = 0\text{ ms}/\mu\text{m}^2$ signal. The SNR was calculated by dividing the signal generated using $b = 0\text{ ms}/\mu\text{m}^2$ by the noise standard deviation.

4.4.2 Cell preparation

The in vitro experiment including cell preparation was conducted by our collaborators at Vanderbilt University. The measured signal data from the in vitro experiment was given to us to test our analysis program. The cell preparation protocol was provided by our collaborators. Human breast cancer MDA-MBA-231 cells were purchased from American Type Culture Collection (ATCC, Manassas, VA). The cells were cultured in Dulbecco's modified eagle medium (DMEM) supplemented with 10% fetal bovine serum (FBS), 50 units/ml penicillin, and 50 $\mu\text{g}/\text{ml}$ streptomycin (Invitrogen, CA) under standard culture conditions in a humidified incubator maintained at 5% CO₂ and 37 °C. Cells were spread every three days by 1:10 dilution and cell density was limited to be no more than 8×10^5 cells/ml. All cell samples were collected, washed with phosphate buffered saline (PBS), and fixed with 4% paraformaldehyde in PBS for over 2 hours. After fixation, the cells were washed, and transferred to 0.65ml Eppendorf tubes. The tubes were centrifuged (Bio-Rad microcentrifuge, Bio-Rad, CA, US) at 1000g centrifugal force for 2 minutes. The medium from the top of the tube was carefully removed, and the residual cell pellets were used for NMR measurements. A total of four sample tubes of MDA-MBA-231 cells were prepared.

4.4.3 *In-vitro* cell imaging

The in-vitro measurements were performed by our collaborator at Vanderbilt University on a 7.0-T, 16-cm bore spectrometer (DirectDrive, Varian Inc., Palo alto, CA, USA). Nine b -values evenly

distributed between 0 and 2000 s/mm² were used for both PGSE and OGSE measurements. For PGSE experiments, the diffusion gradient pulse duration was $\delta=4$ ms, with gradient pulse separation $\Delta=52$ ms. For the OGSE sequence, the gradient waveform oscillation frequencies were at 40, 80, and 120 Hz with $\delta/\Delta=25/30$ ms. The same echo time ($TE=60$ ms) was used for both PGSE and OGSE measurements.

4.4.4 Diffusion phantom preparation

To ensure that the newly implemented OGSE sequence works as expected on a 3T clinical scanner before in-vivo volunteer imaging, the water ADC is measured using the diffusion standard phantom 128 (QalibreMD, Boulder, CO, USA) (Figure 4.1). The phantom consists of ten 30-ml vials of polymer in aqueous solution at different concentrations and 3 vials of deionized water. Since the reference ADC values are provided at temperature 0 °C by the National Institute of Standards and Technology (NIST), the temperature of the phantom has to be kept at approximately 0 °C at the time of image acquisition. To achieve the desired temperature, crushed ice was added to fill the phantom the evening before the measurement. The phantom was placed into a 4 °C sample refrigerator. To ensure that the temperature of the phantom is at 0 °C, more ice is added before the measurement. A thermocouple probe is used to verify that the temperature of the phantom is within 0 ± 0.2 °C.

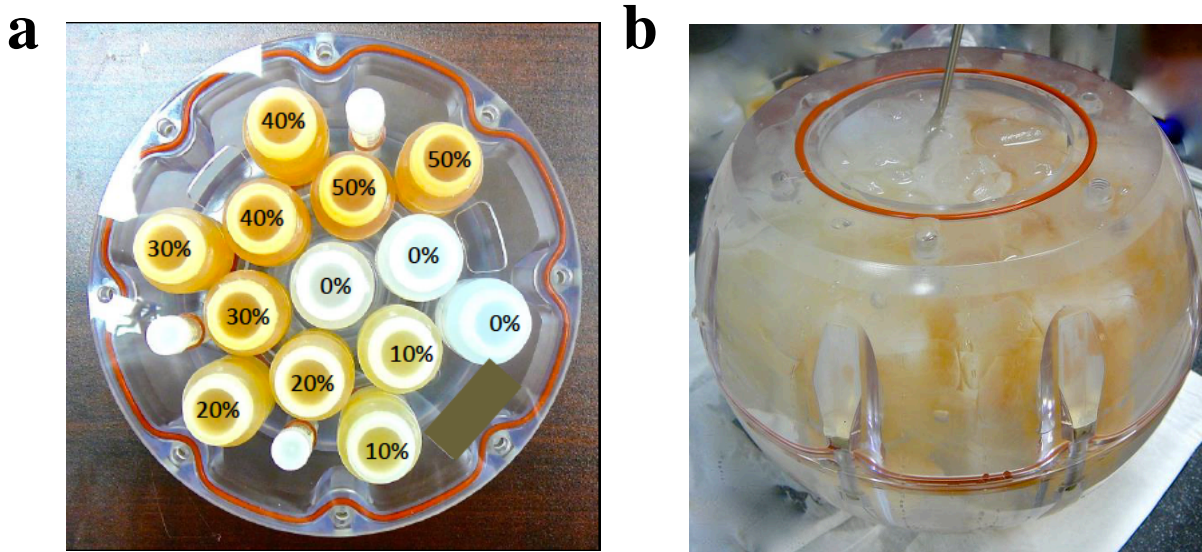


Figure 4.1 The standard diffusion phantom used for the characterization of PGSE and OGSE sequences. The phantom consists of 30ml vials of aqueous solutions of polymer at different concentrations (a). The vials are submerged in an ice water bath to maintain 0 °C at the time of the measurement (b).

4.4.5 Diffusion phantom imaging

The diffusion standard phantom 128 was imaged with a 32-channel head coil in a 3T scanner (Achieva, Philips Healthcare, Eindhoven, NL). DW-MR images were acquired with both PGSE and OGSE sequences for $b = 10, 100, 300, 600, 900 \text{ s/mm}^2$, $T_R/T_E = 6500/107\text{ms}$, field of view (FOV) $224 \times 224 \text{ mm}^2$, 20 slices, voxel size $2 \times 2 \times 2 \text{ mm}^3$ with SENSE factor of 3. The diffusion gradient parameters δ/Δ were 70 ms/12ms for PGSE and 52.4ms /34.8ms for OGSE sequence. To evaluate the accuracy and consistency of the apparent diffusion coefficient (ADC) from PGSE and OGSE, three separate diffusion measurements were performed with the diffusion gradient in x, y and z directions. Geometric diffusion was present on the DW-MR images, acquired with EPI sequences. Turbo spin echo (TSE) images were therefore acquired to visualize the phantom without distortion, using acquisition parameters of $T_R/T_E = 3921/80\text{ms}$ and voxel size $2 \times 2 \times 2 \text{ mm}^3$.

4.4.6 *In-vivo* volunteer imaging

In-vivo data were acquired in the liver of one healthy volunteer with a 32-channel body array, on a 3 T scanner (Achieva, Philips Healthcare, Eindhoven, NL). The volunteer was screened for contraindication of MRI examination and gave informed written consent, under approval from the Research Ethics Board (REB) of the Vanderbilt University Institute of Imaging Science. A single shot echo-planer imaging technique was used with breath-hold to reduce motion artifacts during image acquisition. DW-MR images were acquired with $T_R/T_E=4500/110\text{ms}$, FOV $336 \times 224\text{mm}^2$, number of slices 3, $1.5 \times 1.5 \times 10 \text{ mm}^3$ voxel size, SENSE factor of 3 and fat suppression with spectral attenuated inversion recovery (SPAIR). Three set of DW-MR images were acquired, with the diffusion gradient parameters summarized in Table 4.1. Note that N represents the number of full cycle oscillations of the gradient waveform.

Table 4.1 Image acquisition parameters with 3T clinical scanner

	δ/Δ (ms)	N	f(Hz)	b (s/mm ²)	Δ_{eff}
PGSE	12/74	N/A	0	0,200,400,600,800,1000	70
OGSE	40/56	1	25	0,200,400,600,800,1000	10
		2	50	0,300	5

4.4.7 Image processing and analysis

The PGSE and OGSE diffusion signals from computer simulation, *in-vitro*, phantom and *in-vivo* measurements were normalized to the $b=0 \text{ s/mm}^2$ signal before further analysis. Due to the abundance of blood vessels in the liver, *in-vivo* liver measurements were more likely subject to the intravoxel incoherent motion (IVIM) effect, caused by the microcirculation within the blood vessels. To reduce the IVIM effect on the signal, a linear regression model was fitted to the PGSE and OGSE (N=1) signals with $b \geq 200 \text{ s/mm}^2$, from which the y-intercept was taken as the new $b=0 \text{ s/mm}^2$ signal. The signals with $b \neq 0 \text{ s/mm}^2$ were then re-normalized to the new $b=0 \text{ s/mm}^2$ signal.

The apparent coefficient values (ADC) of the central deionized water vial from the standard diffusion phantom were computed, by fitting a mono-exponential model to the signals at $b= 10, 300, 600, \text{ and } 900 \text{ s/mm}^2$. The average ADC from the water vial was compared with the reference ADC value at 0°C provided from the National Institute of Standards and Technology.

To obtain the desired parameters including cell radius R and intracellular volume fraction v_{in} , Eq. 1 was jointly fitted to the PGSE and OGSE diffusion signals acquired from simulation, in-vitro, or in-vivo experiments. To ensure convergence on the global solution, every fit was performed using a multi-start technique, from one hundred uniformly distributed random starting points. The final parameter estimates were taken as those giving the lowest value of the objective function. The four free parameters from Eq. 1 were constrained to the following ranges: $0.1 \leq R(\mu\text{m}) \leq 25$, $0.01 \leq v_{in} \leq 1$, and $0.1 \leq D_{in}, D_{exo}(\mu\text{m}^2/\text{ms}) \leq 3.0$. Fits within 1% of the fit constraints were excluded from future analysis [23]. All analyses were carried out in MATLAB 2019b, with least squares fitting performed using a Trust-Region reflective algorithm (*Multistart, lsqcurvefit* in MATLAB).

4.5 Results

4.5.1 Computer simulations

The estimation accuracy and precision of the model parameters improved with increased SNR, with greater improvements on the estimation precision. The accuracy and precision metrics were taken as the median and the interquartile range of the difference between the fitted parameters and the ground-truth values, respectively. The median difference of fitted R and v_{in} were within $\pm 1\mu\text{m}, \pm 2\%$, respectively for all SNR levels (Figure 4.2). Another observation from these simulation results was that the estimation precision also depended on the simulated radius. Poorer estimation precision was observed for microstructures with larger radius, consistent with previous simulation results in literature[23]. Similar behavior was exhibited for simulations with microstructures $R=4, 5, 6, 7, \text{ and } 8 \mu\text{m}$ at $v_{in} = 25\%$ and 75% (data not shown).

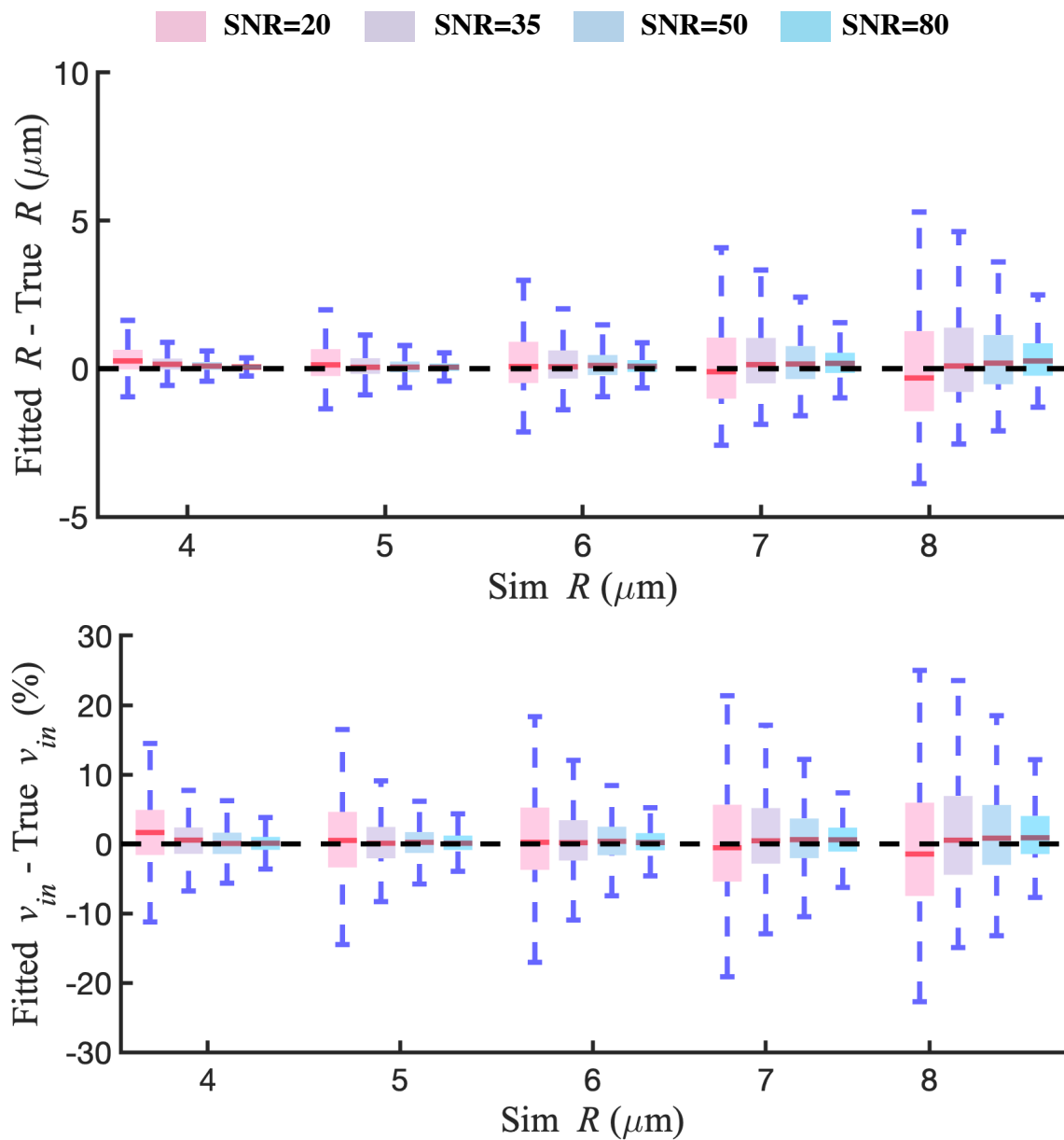


Figure 4.2 The difference between fitted model parameters and the ground truth values for R , v_{in} demonstrates improved accuracy and precision as SNR increases from 20 to 80. Fitted parameters were extracted from fitting Eq.1 to the diffusion signals from 5 microstructures with $R=4,5,6,7,8 \mu\text{m}$ and $v_{in}=50\%$. For each box, the central line (red) indicates the median and the edges of the box indicate the 25th and 75th percentiles, respectively. The error bars represent the maximum and minimum values.

4.5.2 *In-vitro* cell imaging

Identical estimated model parameters were obtained from our in-house analysis program and the analysis program from our collaborators. The estimated cell diameter was comparable to the measured cell diameter using the light microscope. A representative example of PGSE and OGSE signals for a sample of MDA-MBA-231 cell pellet is demonstrated in Figure 4.3. The rate of signal decay increases as the effective diffusion time decreases for the same set of b-values. A total of four parameters D_{in} , R , v_{in} and D_{exo} were estimated from the joint fit of PGSE and OGSE signals. The mean (\pm standard deviation) of the estimated parameters were $1.2 \pm 0.3 \mu\text{m}^2/\text{ms}$, $7.7 \pm 2.6 \mu\text{m}$, 0.4 ± 0.1 , and $0.9 \pm 0.2 \mu\text{m}^2/\text{ms}$, respectively. The same parameter values were obtained using the analysis from our collaborators. The average diameter of approximately 1000 cells were determined as $7.9 \pm 1.8 \mu\text{m}$ from the light microscope images.

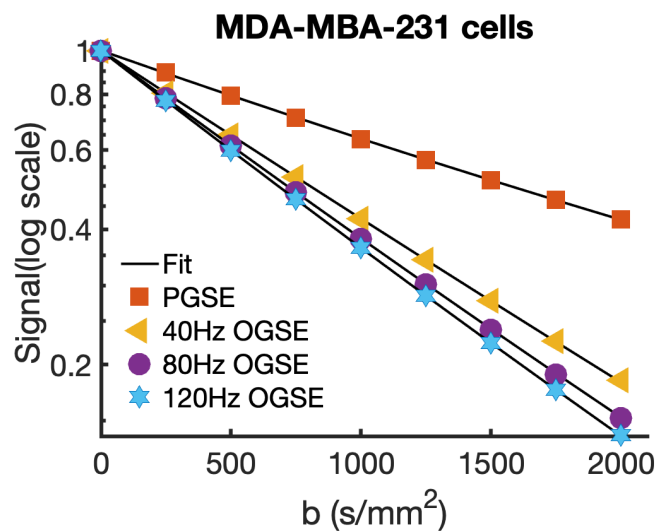


Figure 4.3 Representative fits (solid line) to PGSE (orange square) and OGSE (N=1, yellow triangle; N=2 purple circle; N=3, blue hexagon) signals from a single voxel of the MDA-MBA-231 cell pellet are demonstrated. The diffusion signals decay faster as the effective diffusion time decreases.

4.5.3 Ice-water phantom imaging

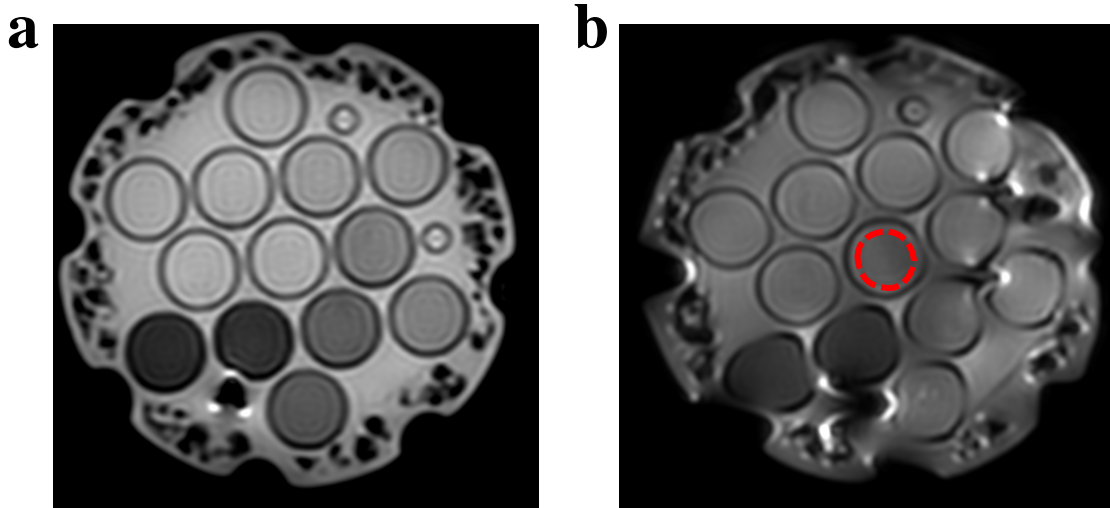


Figure 4.4 Compare to the T2-weighted image acquired from turbo spin echo sequence (a), the single shot EPI diffusion sequence (b) at $b=0$ s/mm² demonstrated noticeable geometric distortions. The center vial with deionized water (red circle) was easily visible and used for ADC analysis.

Accurate and consistent ADC values were obtained from both PGSE and OGSE (N=1) sequences. The acquired diffusion weighted image (Figure 4.4 b) allowed good image quality for vials with deionized water and low polymer concentrations (<30%). The computed mean ADC values of deionized water averaged spatially over the selected region of interest were comparable among three gradient orientations (Table 2). All average ADC values measured at 0 °C were close to the reference ADC = $1.127 \times 10^{-3} \text{mm}^2/\text{s}$, with a maximum discrepancy of $0.05 \times 10^{-3} \text{mm}^2/\text{s}$ along the phase encoding direction (y -direction). The ADC values from the OGSE signals were slightly greater than the ADCs from PGSE signals.

Table 4.2 ADC measurements of deionized water with PGSE and OGSE sequences

	ADC _x ($\times 10^{-3} \text{mm}^2/\text{s}$)	ADC _y ($\times 10^{-3} \text{mm}^2/\text{s}$)	ADC _z ($\times 10^{-3} \text{mm}^2/\text{s}$)	Reference ADC ($\times 10^{-3} \text{mm}^2/\text{s}$)
PGSE	1.10 \pm 0.03	1.12 \pm 0.03	1.10 \pm 0.03	1.127 \pm 0.001
OGSE (N=1)	1.16 \pm 0.04	1.18 \pm 0.07	1.12 \pm 0.03	1.127 \pm 0.001

4.5.4 *In-vivo* healthy volunteer imaging

The liver from a healthy volunteer could be clearly identified in all three DW-MR from PGSE and OGSE sequences (Figure 4.5, red arrow). The SNR in the liver was approximately 30. Example diffusion signals over a range of b-values from a region-of-interest (ROI) (Figure 4.5, yellow circle) in the liver were shown in Figure 4.6.

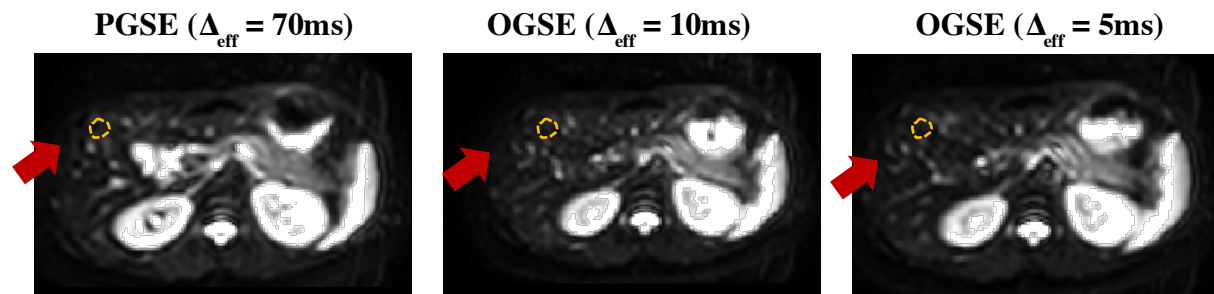


Figure 4.5 A representative example image of liver (pointed by red arrow) from a healthy volunteer, acquired with PGSE and OGSE sequences at $b=0\text{s/mm}^2$. An example liver ROI was drawn (yellow circles). The average diffusion signals from this ROI are shown in Figure 4.6.

Diffusion signals measured at longer diffusion times exhibited bi-exponential signal decay as a function of increasing b-values. The diffusion signal acquired with PGSE sequence at $\Delta_{\text{eff}}=70\text{ms}$ showed a steep slope of attenuation for b-values from $b=0\text{ s/mm}^2$ to $b=200\text{s/mm}^2$, followed by a slower signal decay at higher b-values (Figure 4.6 a). This bi-exponential signal decay behavior is commonly referred to as the IVIM effect, caused by the microcirculatory perfusion of blood within capillaries located in the liver [24]. Contrary to the diffusion signals from MDA-MBA-231 cell pellet (Figure 4.3), the PGSE signals in the liver presented with much faster signal decay across all non-zero b-values, compared to the OGSE signals. This observation suggests that signals at longer diffusion time are subjected to greater IVIM effect. To reduce the IVIM effect, a new $b = 0\text{ s/mm}^2$ signal was calculated by fitting a mono-exponential model to the PGSE and OGSE ($N=1$) signals with $b \geq 200\text{ s/mm}^2$, from which the non-b0 signals were then re-normalized to the new $b = 0\text{ s/mm}^2$ signal.

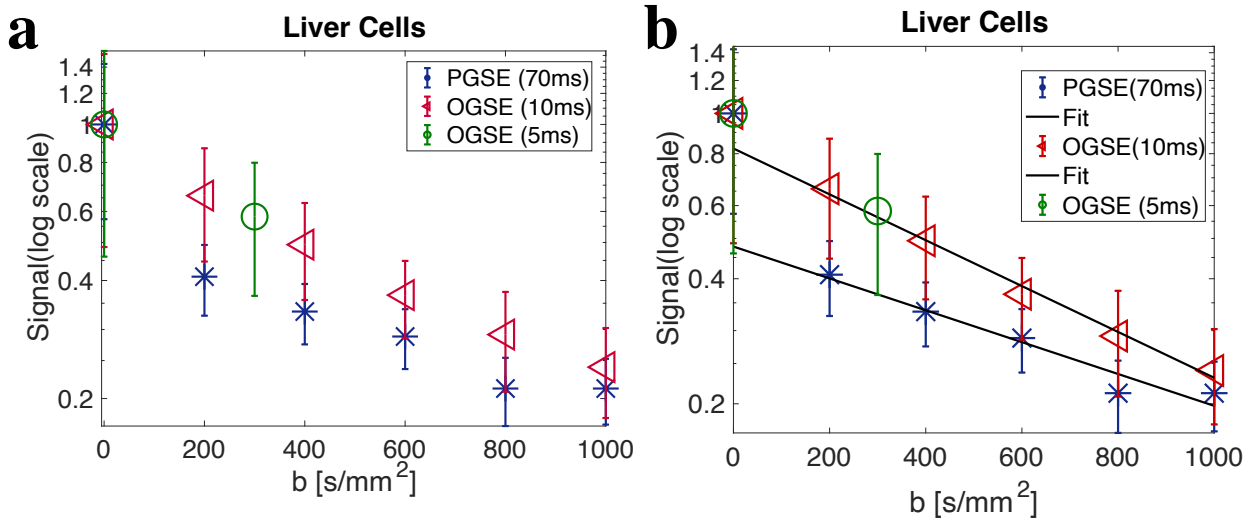


Figure 4.6 A representative example of signals from PGSE and OGSE from a liver ROI demonstrates bi-exponential signal decay as a function of increasing b-values (a). Greater IVIM effect was observed for signals at longer diffusion times. Mono-exponential model was fitted to signals with $b \geq 200 \text{ s/mm}^2$ (b) to reduce the IVIM effect.

The expected signal decay behavior from restricted diffusion was recovered after re-normalization to the synthesized $b = 0 \text{ s/mm}^2$ signal (Figure 4.7). For the same b values, signals acquired with OGSE with an effective diffusion time of 10ms decayed considerably more than those obtained with PGSE at 70 ms. The increase in ADC at shorter diffusion times provides the contrast that enables the measurement of cell size. The two-compartment signal model (Eq.1) was jointly fitted to the PGSE and OGSE signals to extract model parameters R and v_{in} , with $R^2 = 0.99$.

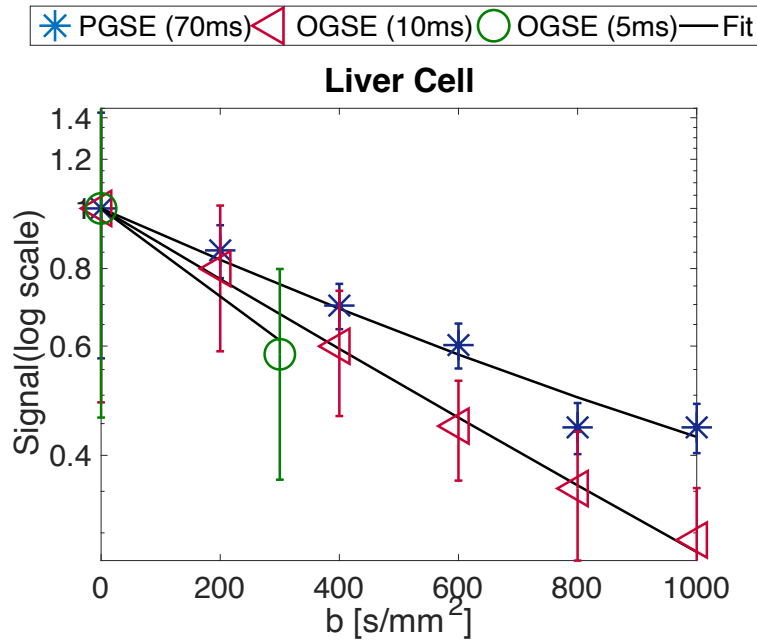


Figure 4.7 Average diffusion signal attenuations as a function of increasing b -values for corrected PGSE and OGSE signals from an example ROI in the liver. Markers represent the mean signals with the error bars as the standard deviations. The solid lines are fitted results using Eq.1.

The parametric R and v_{in} maps (Figure 4.8) overlaid on the PGSE $b = 0$ s/mm² image demonstrated significant heterogeneity within the liver. The mean ADC of the liver, calculated using PGSE signals from $b \geq 200$ s/mm² was determined as $(1.05 \pm 0.28) \times 10^{-3}$ mm²/s, comparable to the ADC values reported in literature of 1.02×10^{-3} mm²/s to 1.25×10^{-3} mm²/s [25]–[27]. The mean estimated radius and volume fraction were 10.1 ± 6.3 μ m and $37\% \pm 24\%$, respectively. The fitted radius is comparable to cell radius reported in literature i.e. ~ 10 – 15 μ m for human hepatic cells [28]. Increased ADC was observed at the center of the liver, with low cell radius and volume fraction, possibly caused by the IVIM effect that are not completely corrected. The T2-weighted image of the same slice (image not shown) acquired with turbo spin echo MR sequence confirms the presence of a major blood vessel, likely the portal vein. Moreover, multiple regions with high percentage cell volume fraction exhibited lower ADC values, consistent with our expectations.

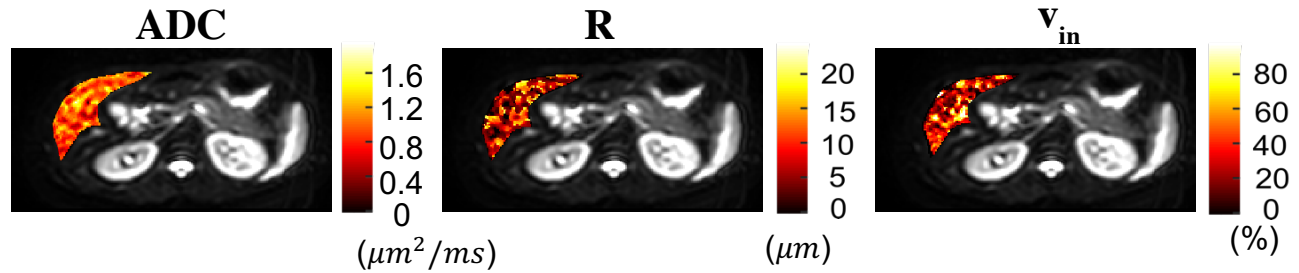


Figure 4.8 Parametric maps of ADC, R and v_{in} overlaid on the PGSE $b=0$ s/mm² image demonstrated significant heterogeneity within the liver. The estimated range of ADC and R are within the expected values from previous literatures.

4.6 Discussion

In this chapter, we have demonstrated through computer simulation, in-vitro and in-vivo experiments that the cell size and volume fraction can be reliably estimated using the IMPULSED method. The accuracy of our in-house analysis program for the joint fitting of PGSE and OGSE signals was cross validated with the one developed by Dr. Gore's group in Vanderbilt. Both programs returned the same estimated parameters. This non-invasive imaging technique capable of characterizing tumor microstructural properties and their changes could help us further characterize tumor habitats in soft-tissue sarcoma and assess changes on a cellular level during radiotherapy. For example, we observed a decreased average ADC value of certain soft tissue sarcoma at the mid-point of the treatment course (week 3), before it increased after the completion of treatment. The decreased ADC could be caused by the swelling of the cells, which is the pre-phase for cell apoptosis, or by increasing cellular density, indicating progression of disease [29]. The IMPULSED method would allow us to differentiate these two scenarios at the mid-point of the treatment, which could impact future treatment.

The estimation accuracy and precision of model parameters depend on both the SNR and the underlying microstructure properties. Our simulation studies have shown that increasing SNR has a greater impact on the precision of the estimated parameters than the accuracy, consistent with previous simulation results [23]. In addition, greater SNR is necessary to maintain the estimation

precision at larger radius. This might be practically important for *in-vivo* imaging with clinical scanners, which could achieve limited SNRs due to the gradient coil strength. For example, at a given SNR, different precision should be expected between imaging cancerous cells ($R \sim 8-10 \mu\text{m}$) and T-cells ($R \sim 4 \mu\text{m}$). Previous studies have demonstrated that using pre-defined D_{in} values could improve fitting stability, leading to better estimation precision at lower SNRs[20]. Techniques such as signal averaging can also be used to improve SNRs at the cost of imaging time.

The parameter maps of radius R and volume fractions v_{in} demonstrated heterogeneity in the liver. The accuracy of the estimated R and v_{in} requires further validation, possibly by examining histological tissue sample under the microscope, which was not possible for healthy volunteers. In addition, *in-vivo* experiment should be repeated on a larger cohort of volunteers to better evaluate the robustness and variability of the measurements.

While the IMPULSED technique has been implemented on a 3T clinical scanner, the clinical translation of this technique still faces several challenges. The protocol used for the *in-vivo* measurements requires a minimum gradient strength of 60 mT/m, which is not readily available for some clinical MRI systems. For example, the 3T clinical scanner at the McGill University Health Center has a maximum gradient strength of 45mT/m. Limited gradient strength can be compensated to reach similar b -values by using a trapezoidal oscillating waveform [30]. In addition, recent development in scanner hardware has introduced more powerful gradient coils, such as the 3T Siemens Prisma ($\sim 80\text{mT/m}$) and the Human Connectome gradient coil ($\sim 300\text{mT/m}$). These advancements can remarkably improve the ability of IMPULSED to probe tumor microstructures. The other limitation lies in the availability of the OGSE sequence. Since OGSE sequence is not used routinely in the clinic, it has to be implemented separately, which often requires a research agreement with the vendor.

4.7 Conclusion

In this chapter, we have demonstrated through computer simulation, *in-vitro* and *in-vivo* experiments that the cell size and volume fraction can be reliably estimated using the IMPULSED

method. The estimated model parameters demonstrated agreement with the ground truth values during the simulation experiment. The estimated cell diameters from in-vitro and in-vivo experiments were comparable to literature values. This non-invasive imaging technique could help us further characterize tumor habitats in soft-tissue sarcoma and assess changes on a cellular level during radiotherapy.

References

- [1] J. S. Wu and M. G. Hochman, “Soft-tissue tumors and tumorlike lesions: a systematic imaging approach,” *Radiology*, vol. 253, no. 2, pp. 297–316, 2009.
- [2] J. R. Goldblum, A. L. Folpe, S. W. Weiss, F. M. Enzinger, and S. W. Weiss, *Enzinger and Weiss’s soft tissue tumors*. .
- [3] M. M. Y. Khoo, P. a. Tyler, A. Saifuddin, and A. R. Padhani, “Diffusion-weighted imaging (DWI) in musculoskeletal MRI: A critical review,” *Skeletal Radiol.*, vol. 40, pp. 665–681, 2011.
- [4] A. R. Padhani *et al.*, “Diffusion-Weighted Magnetic Resonance Imaging as a Cancer Biomarker : Consensus and Recommendations,” vol. 11, no. 2, pp. 102–125, 2009.
- [5] D. M. Koh and D. J. Collins, “Diffusion-weighted MRI in the body: Applications and challenges in oncology,” *Am. J. Roentgenol.*, vol. 188, no. 6, pp. 1622–1635, 2007.
- [6] D. Schnapauff *et al.*, “Diffusion-weighted echo-planar magnetic resonance imaging for the assessment of tumor cellularity in patients with soft-tissue sarcomas,” *J. Magn. Reson. Imaging*, vol. 29, no. 6, pp. 1355–1359, 2009.
- [7] Y. Guo *et al.*, “Differentiation of clinically benign and malignant breast lesions using diffusion-weighted imaging,” *J. Magn. Reson. imaging*, vol. 16, no. 2, pp. 172–178, 2002.
- [8] S.-Y. Lee *et al.*, “Differentiation of malignant from benign soft tissue tumors: use of additive qualitative and quantitative diffusion-weighted MR imaging to standard MR imaging at 3.0 T,” *Eur. Radiol.*, pp. 1–12, 2015.
- [9] Z. Koc, G. Erbay, S. Uluhan, G. Seydaoglu, and F. Aka-Bolat, “Optimization of b value in diffusion-weighted MRI for characterization of benign and malignant gynecological lesions,” *J. Magn. Reson. Imaging*, vol. 35, no. 3, pp. 650–9, Mar. 2012.
- [10] P. W. Hales, Ø. E. Olsen, N. J. Sebire, K. Pritchard-Jones, and C. a. Clark, “A multi-Gaussian model for apparent diffusion coefficient histogram analysis of Wilms’ tumor subtype and response to chemotherapy,” *NMR Biomed.*, no. October 2014, p. n/a-n/a, 2015.
- [11] T. E. Yankeelov *et al.*, “Integration of quantitative DCE-MRI and ADC mapping to monitor treatment response in human breast cancer: initial results,” *Magn. Reson.*

- Imaging*, vol. 25, no. 1, pp. 1–13, Jan. 2007.
- [12] S. Xing, C. R. Freeman, S. Jung, R. Turcotte, and I. R. Levesque, “Probabilistic classification of tumor habitats in soft tissue sarcoma,” *NMR Biomed.*, no. June, p. e4000, 2018.
- [13] M. Vallières *et al.*, “Investigating the role of functional imaging in the management of soft-tissue sarcomas of the extremities,” 2018.
- [14] E. Panagiotaki *et al.*, “Noninvasive Quantification of Solid Tumor Microstructure Using VERDICT MRI,” *Cancer Res.*, vol. 74, no. 7, pp. 1902–1912, Apr. 2014.
- [15] Y. Assaf, T. Blumenfeld-Katzir, Y. Yovel, and P. J. Basser, “AxCaliber: A method for measuring axon diameter distribution from diffusion MRI,” *Magn. Reson. Med.*, vol. 59, no. 6, pp. 1347–1354, 2008.
- [16] E. C. Parsons, M. D. Does, and J. C. Gore, “Temporal diffusion spectroscopy: Theory and implementation in restricted systems using oscillating gradients,” *Magn. Reson. Med.*, vol. 55, no. 1, pp. 75–84, 2006.
- [17] X. Jiang *et al.*, “In vivo imaging of cancer cell size and cellularity using temporal diffusion spectroscopy,” *Magn. Reson. Med.*, vol. 00, no. June, pp. 1–9, 2016.
- [18] J. Xu *et al.*, “Magnetic resonance imaging of mean cell size in human breast tumors.”
- [19] X. Jiang, E. T. McKinley, J. Xie, H. Li, J. Xu, and J. C. Gore, “In vivo magnetic resonance imaging of treatment-induced apoptosis,” *Sci. Rep.*, vol. 9, no. 1, p. 9540, Dec. 2019.
- [20] H. Li, X. Jiang, J. Xie, J. C. Gore, and J. Xu, “Impact of transcytolemmal water exchange on estimates of tissue microstructural properties derived from diffusion MRI,” *Magn. Reson. Med.*, Jun. 2016.
- [21] J. C. Gore, J. Xu, D. C. Colvin, T. E. Yankeelov, E. C. Parsons, and M. D. Does, “Characterization of tissue structure at varying length scales using temporal diffusion spectroscopy.,” *NMR Biomed.*, vol. 23, no. 7, pp. 745–56, Aug. 2010.
- [22] A. S. Ianu, “Advanced Diffusion MRI for Microstructure Imaging : Theoretical Developments,” 2016.
- [23] D. J. McHugh, P. L. Hubbard Cristinacce, J. H. Naish, and G. J. M. Parker, “Towards a ‘resolution limit’ for DW-MRI tumor microstructural models: A simulation study investigating the feasibility of distinguishing between microstructural changes,” *Magn.*

- Reson. Med.*, Oct. 2018.
- [24] D. M. Koh, D. J. Collins, and M. R. Orton, "Intravoxel incoherent motion in body diffusion-weighted MRI: Reality and challenges," *Am. J. Roentgenol.*, vol. 196, no. 6, pp. 1351–1361, 2011.
- [25] T. Kim¹, T. Murakami, S. Takahashi, M. Hon, K. Tsuda, and H. Nakamuna, "Diffusion-Weighted Single-Shot Echo-planar MR Imaging for Liver Disease," 1999.
- [26] M. Bruegel *et al.*, "Diagnosis of Hepatic Metastasis: Comparison of Respiration-Triggered Diffusion-Weighted Echo-Planar MRI and Five T2-Weighted Turbo Spin-Echo Sequences," *Am. J. Roentgenol.*, vol. 191, no. 5, pp. 1421–1429, Nov. 2008.
- [27] S. Gourtsoyianni, N. Papanikolaou, S. Yarmenitis, T. Maris, A. Karantanas, and N. Gourtsoyiannis, "Respiratory gated diffusion-weighted imaging of the liver: Value of apparent diffusion coefficient measurements in the differentiation between most commonly encountered benign and malignant focal liver lesions," *Eur. Radiol.*, vol. 18, no. 3, pp. 486–492, Mar. 2008.
- [28] A. Uzman, H. Lodish, A. Berk, L. Zipursky, and D. Baltimore, "Molecular Cell Biology (4th edition) New York, NY, 2000, ISBN 0-7167-3136-3," *Biochem. Mol. Biol. Educ.*, vol. 29, p. Section 1.2 The Molecules of Life, 2000.
- [29] D. M. Patterson, A. R. Padhani, and D. J. Collins, "Technology insight: water diffusion MRI--a potential new biomarker of response to cancer therapy.," *Nat. Clin. Pract. Oncol.*, vol. 5, no. 4, pp. 220–233, 2008.
- [30] J. Xu *et al.*, "Magnetic resonance imaging of mean cell size in human breast tumors," *Magn. Reson. Med.*, p. mrm.28056, Nov. 2019.

Chapter 5

Microstructure modeling of tumor with two cell populations

5.1 Preface

The non-invasive cell size mapping technique in Chapter 4 assumes that the tumor tissue only contains a single cell population. This assumption may not be valid for tumors where two cell populations co-exist in the same space, such as round cell/myxoid liposarcoma (introduced in section 2.1.2). This chapter presents a proof-of-concept study on the feasibility of estimating cell radii and volume fractions of two cell populations, when they co-exist in the same MR voxel. This is done by fitting the proposed two-cell population microstructure model to simulated diffusion data. Three additional models were proposed to stabilize the fit, which in turn improves the robustness of fitting. We have demonstrated for the first time that the cell radii and volume fractions of both cell populations can be accurately estimated under specific constraints.

A simulation study of cell size and volume mapping for tissue with two underlying cell populations using diffusion weighted MRI

Shu Xing, MSc^{1,2}, Ives R. Levesque, PhD^{1,2,3,4}

¹ Medical Physics Unit, McGill University, Montreal, Canada,

² Department of Physics, McGill University, Montreal, Canada

³ Gerald Bronfman Department of Oncology, McGill University, Montreal, Canada

⁴ Research Institute of the McGill University Health Centre, Montreal, Canada

Under Review at Magnetic Resonance in Medicine

Corresponding author: Shu Xing, MSc
Cedars Cancer Centre, Glen Site, room DS1.7141
1001 Boul. Decarie
Montreal, QC, Canada, H3A 3J1
shu.xing@mail.mcgill.ca

Running title: Microstructure modeling of tumor with two cell populations

Keywords: tumor; diffusion; modelling

5.2 Abstract

Purpose: To propose a method for voxel-wise estimation of cell radii and volume fractions of two cell populations, when they co-exist in the same MR voxel, using the combination of diffusion weighted MRI and microstructural modeling.

Method: The proposed two-cell population microstructure models were validated using simulated diffusion data for a range of microstructures. The effect of noise was investigated for a subset of these microstructures. The accuracy and precision of the estimated model parameters $R_L, R_S, v_{in,L}, v_{in,S}$ were evaluated by comparing the estimates to their ground truth values. The robustness of the fitting was characterized by the percentage of accepted fits.

Results: The estimation accuracy and precision, and thus the ability to robustly distinguish the two cell populations depended on the microstructural properties and SNR. For a SNR of 50, a minimum difference of $3\mu m$ between the radius of the large and small cell populations is required for differentiation. Proposed modifications to the two-cell population model, including constrained fits, improved robustness over brute-force fitting.

Conclusions: In this proof-of-concept study, we have proposed a diffusion MRI-based method for voxel-wise estimation of cell radii and volume fractions of two cell populations, when they co-exist in the same MR voxel. The ability to reliably estimate cell radii and volume fractions for tissue with two cell populations opens exciting avenues of potential applications in both tumor diagnosis and treatment monitoring.

5.3 Introduction

Characterizing complex histological features such as cellular density/volume fraction and cell size is important for an accurate representation of cancerous tumors. Cell size has been reportedly linked to cancer types and grade [1]; and changes in cell size could be a potential early therapeutic biomarker for treatment-induced apoptosis [2], [3]. Invasive biopsy is the currently standard-of-care to assess microstructural information in the cancerous tumor. However, the small specimen size from biopsy might not be representative of the entire tumor, especially in highly heterogeneous tumors[4]. In addition, the invasive nature of biopsy makes repeated assessment during treatment for monitoring therapy-induced changes unfeasible. To this end, a non-invasive imaging technique capable of characterizing tumor microstructural properties and their changes would be of great clinical interest to aid cancer diagnosis and treatment response monitoring.

Diffusion-weighted magnetic resonance imaging (DW-MRI) has been recognized as a potential tool to probe the tumor microenvironment [4], [5], due to its sensitivity to the Brownian motion of water molecules [6]. The mean diffusivity of water molecules can be quantified by the apparent diffusion coefficient (ADC) [7], which is related to cellularity [8]–[10]. As a result, ADC analysis has been applied to characterized various tumor types and to differentiate malignant from benign tumors [4], [11], [12]. The changes in ADC values from pre- to post-treatment have been considered as a probable imaging biomarker for monitoring therapy response [13]. A number of clinical studies have shown that an increased ADC in response to treatment is associated with better clinical outcome [14]–[16]. While ADC measurements might be sensitive to microstructural changes, ADC only represents the overall water diffusion properties, influenced by multiple factors such as cell size, intracellular volume fraction, and intra-/extra-cellular compartment diffusivities[17]–[19]. In order to capture these complex histological features, more advanced imaging techniques are required.

Recent developments in DW-MRI have enabled the quantification of tissue parameters far below the nominal imaging resolution, i.e. microstructural mapping[20]. Advanced DW-MRI methods and analysis frameworks, such as IMPULSED (Imaging Microstructural Parameters Using Limited Spectrally Edited Diffusion) [21], VERDICT (Vascular, Extracellular and Restricted

Diffusion for Cytometry in Tumors) [22] and POMACE (pulsed and oscillating gradient MRI for assessment of cell size and extracellular space) [23] have been proposed to map the average cancer cell radius R and the relative cell volume fraction v_{in} , covering the entire tumor volume. These techniques have been applied to a number of preclinical *in-vitro* and *in-vivo* studies, where the estimated mean cell radius from DW-MRI are comparable with measured cell radius assessed by light microscopy [18], [24]–[26]. Recently, Xu *et al.* have conducted the first clinical study for *in-vivo* imaging of mean tumor cell size of breast cancer patients[27]. These developments allow characterization of the tumor microenvironment and better capture the tumor heterogeneity; however, existing methods assume that tumors feature a single cell population, which is not valid in many applications.

To address the limitation of the single cell population microstructure model, we propose a method for voxel-wise estimation of cell radii and volume fractions of two cell populations, when they co-exist in the same MR voxel. We investigated the robustness of the method under the influence of noise and propose methods to improve the stability of parameter estimation. The ability to reliably estimate cell radii and volume fractions for tissue with 2 cell populations opens exciting avenues of potential applications in tumor diagnosis and treatment monitoring. For instance, round cell/myxoid liposarcoma is composed of high-grade cells ($R \sim 10\mu m$) and low-grade cells ($R \sim 4\mu m$). The amount of the high-grade component is strongly related to tumor grade and changes the course of treatment[28], [29]. In addition, this technique could potentially aid the quantification of the infiltrating T-cells ($R \sim 4\mu m$) to cancerous cells ($R \sim 10\mu m$) during immunotherapy[30].

5.4 Theory

5.4.1 One cell population microstructure model (1P-MM)

Tumor microstructure can be modeled with cancer cells as a single population of impermeable spheres[18], [21], [27], [31]. The normalized diffusion MR signal from a population of uniform cells can be calculated using the one-population microstructure model (1P-MM):

$$S/S_0 = v_{in} S_{in}(R, D_{in}) + (1 - v_{in}) S_{exo}(D_{exo}) \quad (1)$$

where S_{in} and S_{exo} represent the normalized signal from the water inside the cells (restricted diffusion) and the extracellular water (hindered diffusion). D_{in} and D_{exo} are the intra- and extracellular diffusion coefficients. The water exchange between intra- and extracellular spaces is not considered, due to its negligible effect on the estimation of mean cell size [32].

The mathematical expression of the signal S_{in} depends on the pulse sequence, the shape of the diffusion gradient, and the cell shape. The analytical expression for S_{in} within impermeable spheres, measured with pulsed gradient spin-echo (PGSE) [18] with rectangular gradient field pulses is

$$S_{in}(PGSE) = \exp\left(-2\left(\frac{\gamma g}{D_{in}}\right)^2 \sum_n \frac{B_n}{\lambda_n^2} \{\lambda_n D_{in} \delta - 1 + \exp(-\lambda_n D_{in} \delta) + \exp(-\lambda_n D_{in} \Delta)(1 - \cosh(\lambda_n D_{in} \delta))\}\right) \quad (3)$$

The expression for the intracellular signal S_{in} contains terms for the gradient pulse: gradient amplitude g , the gradient pulse duration δ , the separation time between the two diffusion gradients Δ , the structure dependent parameters λ_n and B_n , and the intracellular diffusivity D_{in} . The expressions for λ_n and B_n have been reported in literature [24]:

$$B_n = \frac{2(R/\mu_n)^2}{\mu_n^2 - 2}, \quad \lambda_n = \frac{\mu_n^2}{R^2}$$

where μ_n is the n^{th} root of the equation $\mu J'_{3/2}(\mu) - \frac{1}{2}J_{3/2}(\mu) = 0$. $J_{3/2}$ is the Bessel function of order 3/2.

The extracellular diffusion signal can be expressed with a mono-exponential function of D_{exo} as:

$$S_{exo} = \exp(-b \cdot D_{exo}) \quad (4)$$

5.4.2 Two cell population microstructure model (2P-MM)

The 1P-MM (Eq. 1) can be extended to model tissue with two cell populations of different sizes and percentage volume fractions by including an additional restricted diffusion compartment:

$$S/S_0 = v_{in,l}S_{in,l}(R_l, D_{in}) + v_{in,s}S_{in,s}(R_s, D_{in}) + (1 - v_{in,l} - v_{in,s})S_{exo}(D_{exo}) \quad (5)$$

where the subscripts l and s represent the two cell populations of different sizes, *i.e.* *large* and *small* cell populations. Compared to four free fitting parameters in the 1P-MM $R, v_{in}, D_{in}, D_{exo}$, the two-cell population microstructure model (2P-MM) has two additional fitting parameters from the second cell population : $R_l, v_{in,l}, R_s, v_{in,s}, D_{in}, D_{exo}$. Stabilization of the fitting quickly becomes the primary challenge. Here, we propose two techniques to reduce the number of fitting parameters, thus stabilizing the fit.

Stabilization by suppressing signal dependence on diffusion time from small cell population

The diffusion signal over a range of effective diffusion times Δ_{eff} shows strong dependence on cell radius (Figure 5.1). Signal from cells of $R = 1$ or $2 \mu m$ shows little change with Δ_{eff} . With prior knowledge on the anticipated cell sizes, the set of Δ_{eff} values can be strategically selected for the measurement to remove signal sensitivity to small cells, where $S_{in,s} \approx 1$. The 2P-MM (Eq. 5) can then be simplified to:

$$S/S_0 = v_{in,l}S_{in,l}(R_l, D_{in}) + v_{in,s} \cdot 1 + (1 - v_{in,l} - v_{in,s}) \cdot S_{exo}(D_{exo}) \quad (6)$$

This method, referred to as the *constrained-2P-MM*, reduces the number of fitting parameters and allows the estimation of R_l and $v_{in,l}$ of the large cells and $v_{in,s}$ of the small cells without any sensitivity to R_s .

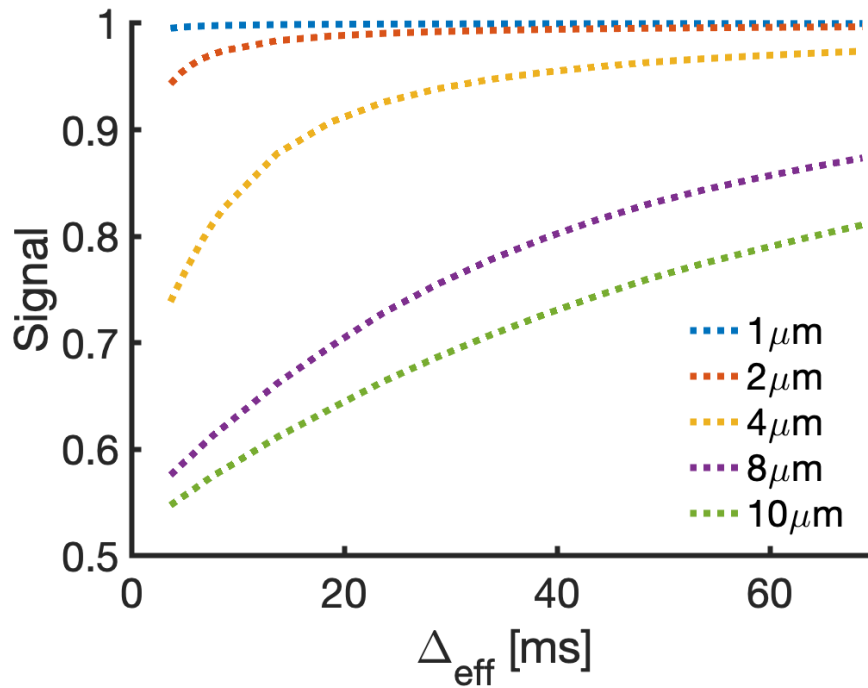


Figure 5.1 Simulated diffusion signals over a range of diffusion times Δ_{eff} (for fixed b-value) shows strong dependence on cell radii. Signal from cells of small radii (e.g. 1 – 2 μm) shows little change over diffusion times. For the 2- cell population model, strategic selection of diffusion times removes signal sensitivity to small cells and reduces the number of fitting parameters, producing more stable fits.

Stabilization by fixing model parameters

For cells of similar radii, the signal can no longer be selectively desensitized during measurement (see Figure 5.1). Simulation results suggest that by fitting the 1P-MM to diffusion signals from tissue with two underlying cell populations, the estimated v_{in} approximately yields the total cell volume which we can denote as $v_{in,tot} = v_{in,l} + v_{in,s}$. This observation holds for multiple combinations of cell populations with different radii and % volumes fractions (see Results section, Figure 5.3), and can be exploited to reduce the number of free parameters by performing two-step fitting process: (1) the diffusion signal is fitted with the 1P-MM to obtain $v_{in,tot}$, and (2) $v_{in,tot}$ is fixed in the 2P-MM fit, as shown in Eq. 7, which is then fitted to the diffusion signals again to obtain the desired parameters.

$$S/S_0 = (v_{in,tot} - v_{in,l}) \cdot S_{in,s}(R_s, D_{in}) + v_{in,l} \cdot S_{in,l}(R_l, D_{in}) + (1 - v_{in,tot}) \cdot S_{exo}(D_{exo}) \quad (7)$$

This technique is referred to as the *2-step-2P-MM* and allows the direct estimation of R_l , R_s , and $v_{in,l}$. The relative volume fraction of the small cell population $v_{in,s}$ can be calculated by subtracting $v_{in,l}$ from $v_{in,tot}$.

5.5 Method

5.5.1 Diffusion signal simulation

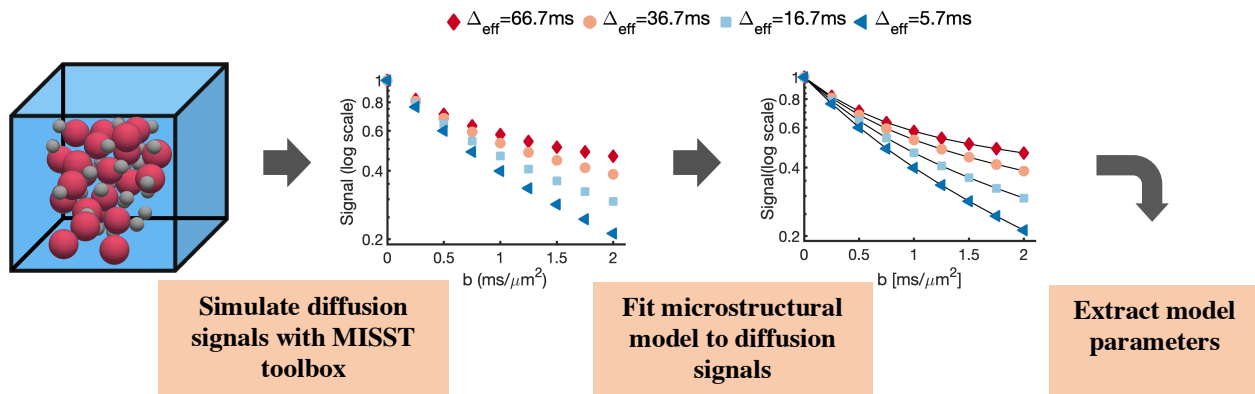


Figure 5.2 Schematic of the diffusion signal simulation and analysis pipeline. The cells are modeled as impermeable spheres of different sizes, where red and grey spheres represent the large and small cell populations, respectively.

The matrix method (Microstructure Imaging Sequence Simulation Toolbox (MISST), UCL) was used to simulate PGSE diffusion signals [34], [35]. Tissue with 2 underlying cell populations was modeled using impermeable spheres of two different radii and volume fractions (Figure 5.2 red and grey spheres). The extracellular matrix is modeled as non-free water tissue with hindered diffusion. The intra- and extra-cellular diffusivities D_{in} and D_{exo} were set to be $\frac{1\mu\text{m}^2}{\text{ms}}$ and $\frac{2\mu\text{m}^2}{\text{ms}}$, respectively. Simulations were performed for two sets of microstructures (Table 5.1). The term “microstructure” is used represent tissue model with a single combination of input model parameters. The first microstructure set contains 99 microstructures with combinations of $R_l =$

2, 3, 4, 5, 6, 7, 8, 9, 10 μm , $R_s = 1 \mu\text{m}$, $v_{in,l} = 5, 10, 15, 20, 25, 30, 35, 40, 45, 50, 55\%$ and $v_{in,s} = 60\% - v_{in,l}$. For each microstructure, signals were simulated at three effective diffusion times $\Delta_{eff} = 5.7, 10.7, 66.7 \text{ ms}$, using b -values from 0 to 2000 $\frac{\text{ms}}{\mu\text{m}^2}$ in intervals of 250 $\frac{\text{ms}}{\mu\text{m}^2}$, gradient duration $\delta = 4 \text{ ms}$, and gradient separation $\Delta = 7, 12, 68 \text{ ms}$. Similarly, for cells of close radii, 66 microstructures (Table 5.1, microstructure set 2) were simulated with combinations of $R_l = 5, 6, 7, 8, 9, 10 \mu\text{m}$, $R_s = 4 \mu\text{m}$, $v_{in,l} = 5, 10, 15, 20, 25, 30, 35, 40, 45, 50, 55\%$ and $v_{in,s} = 60\% - v_{in,l}$. Signals were simulated at four effective diffusion times $\Delta_{eff} = 5.7, 16.7, 36.7, 66.7 \text{ ms}$, with $\delta = 4 \text{ ms}$ and $\Delta = 7, 18, 38, 68 \text{ ms}$.

Table 5.1 Summary of input model parameters for simulated microstructures used in this manuscript. Respectively. The term “microstructure” is used represent tissue model with a single combination of input model parameters.

		R (μm)	v_{in} (%)	D_{in}/D_{exo} ($\mu\text{m}^2/\text{ms}$)	2P Model fitted	Parameter extracted
Microstructure set 1	Large cells	2:1:10	5:5:55	1/2	Constrained- 2P-MM	$R_l, v_{in,l}, v_{in,s}$
	Small cells	1	55: -5:5			
Microstructure set 2	Large cells	5:1:10	5:5:55	1/2	2P-MM,2- step-2P-MM	$R_l, R_s, v_{in,l}, v_{in,s}$
	Small cells	4	55: -5:5			

5.5.2 Fitting

The simulated diffusion signals of each microstructure were fitted with the 1P-MM, the 2P-MM or a simplified version of 2P-MM. To ensure convergence on the global solution, every fit was performed using a multi-start technique, from one hundred random starting points. The final parameter estimates were taken as those giving the lowest value of the objective function. The four free parameters in the 1P-MM were constrained to the following ranges: $0.1 \leq R(\mu\text{m}) \leq 25$, $0.01 \leq v_{in} \leq 1$, and $0.1 \leq D_{in}, D_{exo}(\mu\text{m}^2/\text{ms}) \leq 3.0$. Similarly, for the 2P-MM, six free parameters were constrained to be within plausible limits: $0.1 \leq R_l, R_s(\mu\text{m}) \leq 25$, $0.01 \leq v_{in,l}, v_{in,s} \leq 1$, and $0.1 \leq D_{in}, D_{exo}(\mu\text{m}^2/\text{ms}) \leq 3.0$. Fits within 1% of the fit constraints were excluded from subsequent analysis [31]. The fitting process was repeated for all microstructure combinations and all models, and the estimated radii and volume fractions were compared to the

ground-truth values specified in the simulations. All analyses were carried out in MATLAB 2019b (The MathWorks, Natick, MA, USA), with least squares fitting performed using a Trust-Region reflective algorithm and a multi-start approach for robustness (*lsqcurvefit*, *multistart* in MATLAB).

5.5.3 Simulated Influence of SNR

To evaluate the effect of noise on the accuracy and precision of the fitting, Rician noise was added to the simulated signals of two subsets of microstructures: (1) $R_l = 4, 5, 6, 7, 8, 9, 10 \mu\text{m}$, $R_s = 1 \mu\text{m}$, $v_{in,l} = 45\%$, $v_{in,s} = 15\%$; and (2) $R_l = 7, 8, 9, 10 \mu\text{m}$, $R_s = 4 \mu\text{m}$, $v_{in,l} = 45\%$, $v_{in,s} = 15\%$. 1,500 noisy synthetic signals were generated for each microstructure, with the signal-to-noise-ratio (SNR) defined for the $b = 0 \text{ ms}/\mu\text{m}^2$ signal. The SNR was calculated by dividing the $b = 0 \text{ ms}/\mu\text{m}^2$ signal by the Gaussian noise standard deviation. The *constrained-2P-MM* was fitted to the noisy signals of the first subset of microstructures; both the *2P-MM* and *2-step-2P-MM* were fitted to the noisy signals of the second subset of microstructures. The accuracy and precision of the model parameter estimates were evaluated at four SNRs = 20, 35, 50, 80 for the first subset of signals, and at three SNRs = 30, 50, 80 for the second subset, respectively. The accuracy was assessed using the mean difference between fitted estimates and the ground truth, and precision was assessed using the standard deviation of the fitted values [31].

5.5.4 Simulated Influence of pre-defined D_{in}

In addition to the *constrained-2P-MM* and *2-step-2P-MM* method, the approach of fixing D_{in} to a pre-defined value was investigated as a means of improving fit stability. The *2P-MM* was fitted to the noisy signals (SNR=50) from the microstructures $R_l = 7, 8, 9, 10 \mu\text{m}$, $R_s = 4 \mu\text{m}$, $v_{in,l} = 45\%$, $v_{in,s} = 15\%$, with D_{in} fixed at 0.6, 0.8, 1 (truth), 1.2, and $1.4 \mu\text{m}^2/\text{ms}$. Fitting was repeated for 1,500 noisy signals for each microstructure, following the procedure described in section 3.2 “Fitting”. The resulting model parameter estimates were compared to the estimates from leaving D_{in} as a free parameter. The accuracy metric was taken as the absolute % error between each fitted value and the ground truth for each model parameter estimates.

5.6 Results

Before diving into the more complicated models, the mono-exponential diffusion model was first evaluated for its ability to describe the tumor microstructure with two underlying cell populations. Supplementary Figure S1 shows ADC values from simulated signals in 44 microstructures of large and small cells of different radii and volume fractions. Nine microstructures fall into the narrow grey band that spans ADC value of $(3.00 \pm 0.15) \times 10^{-4} \text{ mm}^2/\text{s}$, which suggests that ADC alone cannot distinguish fundamental variations in the underlying tissue microstructure in the presence of bimodal cell distributions

5.6.1 One population model (1P-MM)

The 1P-MM appeared unfit to describe tissue with 2 underlying cell populations, as it tends to return an apparent radius R between the true radii of large and small cell populations. As $v_{in,l}$ increased, the R estimated from the 1P-MM fit lay between the ground truth of R_l and R_s (Figure 3a). The fitted R latched onto the ground truth values of R_s or R_l when the total cell volume was dominated by the small cells (*i.e.* $v_{in,l}/v_{in,s} = 5\%/55\%$) or large cells (*i.e.* $v_{in,l}/v_{in,s} = 55\%/5\%$), respectively. A similar trend was observed for the other set of 66 microstructures (Figure 3b), where various volumes of large cells were mixed with small cells of $4\mu\text{m}$. The estimated v_{in} from the 1P-MM consistently yielded the total % volume fraction $v_{in,tot}$ (Figures 3c and 3d), even in cases where one population is dominant. The mean v_{in} was approximately 60% for both sets of microstructures, with max/min v_{in} of 64%/57% and 61%/55% respectively.

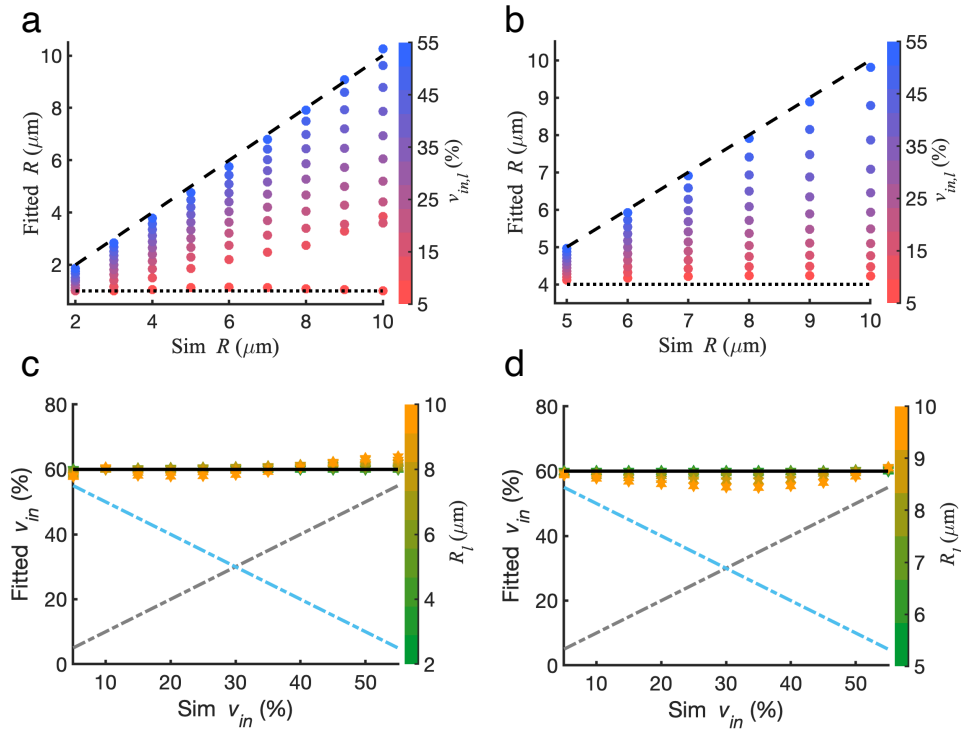


Figure 5.3 The 1P-MM was fitted to signals from two sets of microstructures (Table 1): microstructure set 1 (99 microstructures) (a,c) and microstructure set 2 (66 microstructures) (b,d). Plots show the estimated R of a microstructure (circles, panels a and b) where the red to blue color gradient indicates increasing $v_{in,l}$, and the estimated v_{in} of a microstructure (hexagons, panels c and d) where the green to orange color gradient shows increasing R_l . The black dashed and black dotted lines (a, b) represent the ground truth values of R_l and R_s , respectively. The blue dot-dashed and grey dot-dashed lines (c,d) represent the ground truth values of $v_{in,l}$ and $v_{in,s}$ respectively. The solid line (c,d) indicates the ground truth value of the total % volume fraction $v_{in,tot} = 60\%$

5.6.2 Two population model (2P-MM)

Stabilization by signal suppression from small cell population

Parameters from fits of the *constrained*-2P-MM (Eq. 6), tested with microstructure set 1 (Table 5.1) in a noiseless environment, were accurate. The difference maps between the estimated model parameters R_l , $v_{in,l}$, $v_{in,s}$ and the ground truth values demonstrates improved accuracy, with the

mean/max absolute difference of $0.2 \mu\text{m} / 2 \mu\text{m}$, 1%/9%, 1%/9%, respectively (Figure 5.4). The maximum difference occurred at low $v_{in,l}$ of 5% and R_l of $2 \mu\text{m}$ for all three parameters, where the accuracy is poorer. Both R_l and $v_{in,l}$ tended to be overestimated, as R_l and $v_{in,l}$ increases, where $v_{in,s}$ tends to be underestimated.

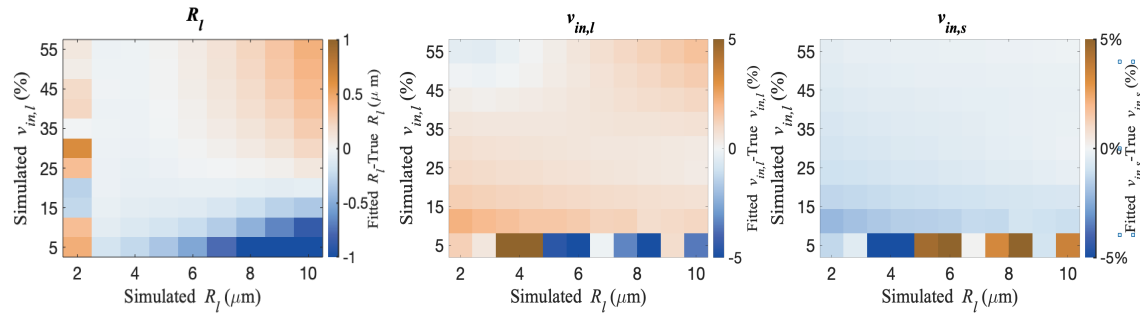


Figure 5.4 The difference maps of estimated R_l , $v_{in,l}$, $v_{in,s}$ from the ground truth values demonstrated good estimation accuracy. The model parameters were estimated by fitting the constrained-2P-MM to diffusion signals of microstructure set 1 (99 microstructures). The color brown and blue in the color bar represents overestimation and underestimation respectively.

Brute force fitting with 2P-MM

The model parameters R_l , R_s , $v_{in,l}$, $v_{in,s}$ can be accurately estimated for microstructure set 2, when $R_l > 7 \mu\text{m}$. The difference maps between the estimated model parameters and the ground truth values illustrate poor estimation accuracy, especially when cells of $R_l = 5, 6 \mu\text{m}$ are mixed with cells of $R_s = 4 \mu\text{m}$ at various volume fractions (Figure 5.5). This observation suggests that when the radii of two cell populations are too similar, the 2P-MM is unable to properly characterize their radii or volume fractions even in the noiseless environment. As a result, the cell mixtures of $R_l = 5, 6 \mu\text{m}$ with $R_s = 4 \mu\text{m}$ were removed from future analysis. Improved estimation accuracy was observed for R_l greater than $7 \mu\text{m}$, with the mean/max absolute difference for R_l , R_s , $v_{in,l}$, $v_{in,s}$ of $0.2 \mu\text{m} / 2 \mu\text{m}$, $0.3 \mu\text{m} / 1 \mu\text{m}$, 0.9%/5%, and 0.9%/5%, respectively. Similar to previous observations, the maximum absolute difference for R_l , $v_{in,l}$, $v_{in,s}$ tended to occur at low $v_{in,l}$ and R_l . For the additional parameter R_s , the accuracy worsened as the $v_{in,l}$ increased, with the maximum absolute difference observed at the highest $v_{in,l}$.

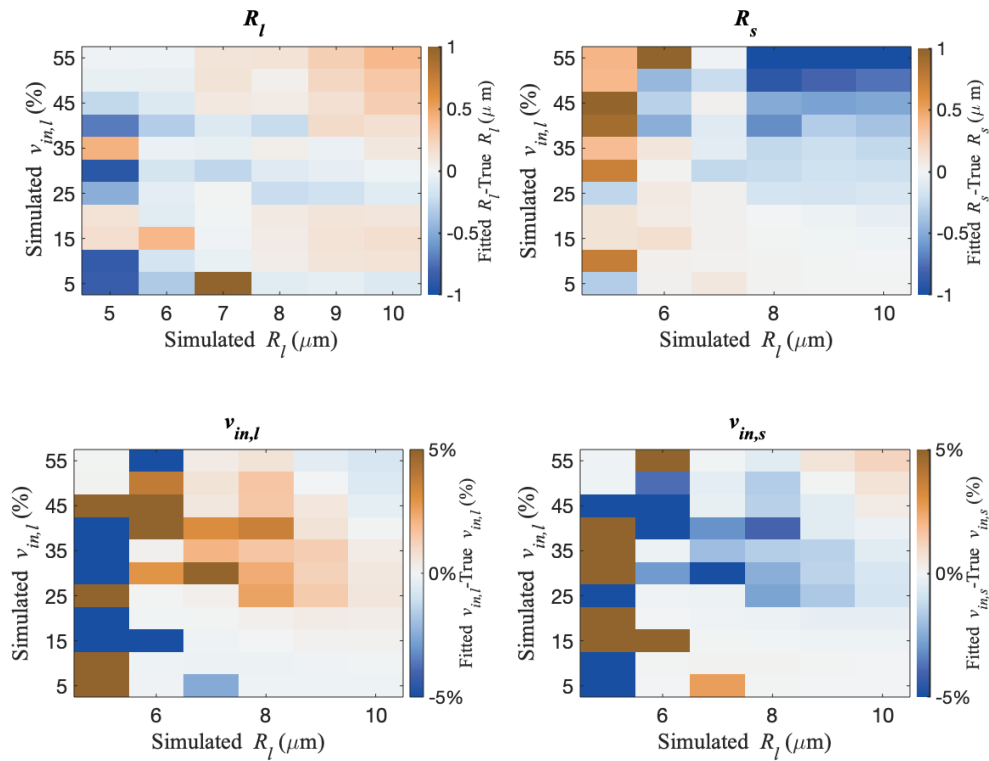


Figure 5.5 The difference maps of estimated R_l , R_s , $v_{in,l}$, $v_{in,s}$ from the ground truth values demonstrated good estimation accuracy for R_l greater than $7\mu\text{m}$. The model parameters were estimated by fitting the constrained-2P-MM to diffusion signals of microstructure set 2 (66 microstructures). The color brown and blue in the color bar represents overestimation and underestimation respectively.

Stabilization by fixing fitting parameters

The precision of parameter estimation was improved by the proposed *2-step-2P-MM*. Fitting with the *2-step-2P-MM* to noiseless diffusion signals from microstructure set 2 showed little improvement, similar to results in Figure 5.5, and are therefore not shown here. Figure 5.6 shows a representative example of a subset of 4 microstructures ($R_l = 7, 8, 9, 10\ \mu\text{m}$, $R_s = 4\ \mu\text{m}$, $v_{in,l} = 45\%$, $v_{in,s} = 15\%$), where both models were fitted to the noisy signals (SNR=50) of these 4 microstructures. Both the 2P-MM and *2-step-2P-MM* yielded similar median difference between the fitted parameters and the ground truth values. However, the interquartile range of the estimated R_l , R_s , $v_{in,s}$ from *2-step-2P-MM* was considerably smaller compared to 2P-MM.

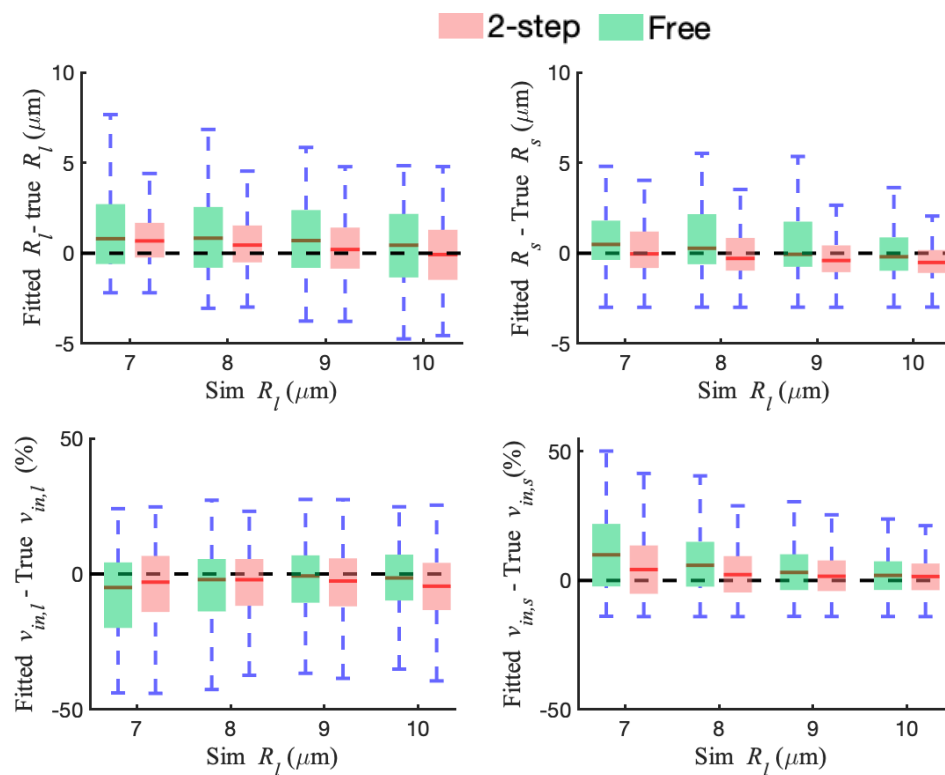


Figure 5.6 Comparison of extracted model parameters R_l , R_s , $v_{in,l}$, $v_{in,s}$ from 2P-MM (green) and 2-step-2P-MM (pink). The model parameters were extracted by fitting both models to the noisy signal (SNR=50) of 4 microstructures with combinations of $R_l = 7: 1: 10 \mu\text{m}$, $R_s = 4 \mu\text{m}$, $v_{in,l} = 45 \%$ and $v_{in,s} = 15\%$. The difference between fitted model parameters and the ground truth values for R_l , R_s , $v_{in,l}$, $v_{in,s}$ are plotted. For each box, the central line (red) indicates the median and the edges of the box indicate the 25th and 75th percentiles, respectively. The error bars represent the maximum and minimum values.

5.6.3 Influence of SNR

The parameter estimation accuracy and precision both depended on the level of noise for the *constrained-2P-MM* (Figure 5.7) and the *2-step-2P-MM* (Figure 5.8). The accuracy and the precision improved as the SNR increased. At an SNR of 35, the mean difference of fitted R_l , $v_{in,l}$ and $v_{in,s}$ were within $\pm 1\mu\text{m}$, $\pm 5\%$ and $\pm 5\%$ respectively (Figure 5.7). Nevertheless, an SNR of

50 is necessary to keep the standard deviations under $2\mu\text{m}$, 10%, and 10%. For the second set of microstructures, a similar SNR was needed to keep the mean difference of fitted R_l , R_s , $v_{in,l}$ and $v_{in,s}$ within $\pm 1\mu\text{m}$, $\pm 1\mu\text{m}$, $\pm 5\%$ and $\pm 5\%$ respectively. At SNR=50, the standard deviation of R_l , R_s , $v_{in,l}$ and $v_{in,s}$ was within $2\mu\text{m}$, $2\mu\text{m}$, 17%, and 16%.

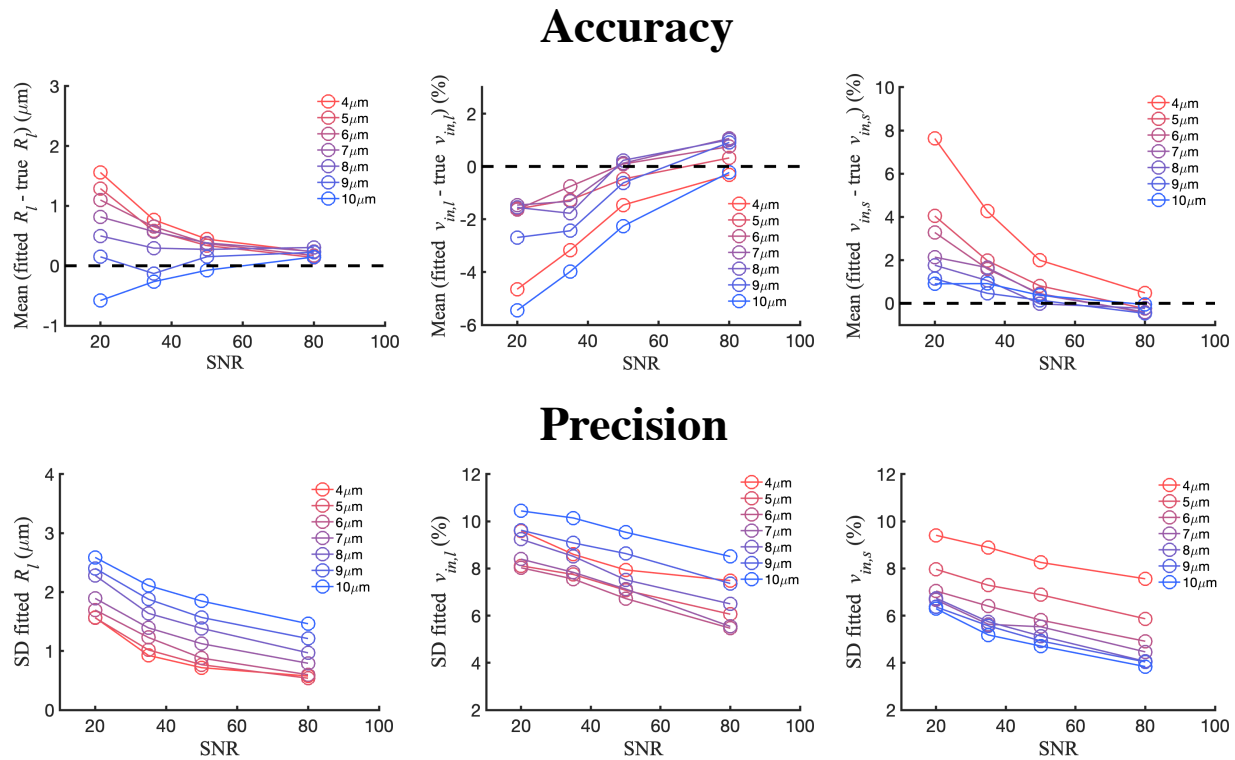
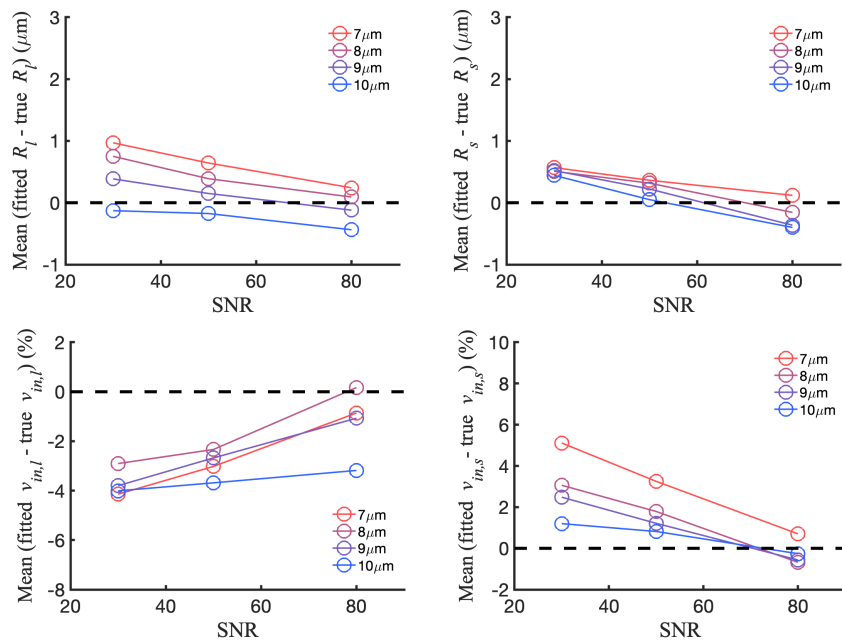


Figure 5.7 Influence of noise on fitted model parameters, extracted from fitting the constrained-2P-MM to simulated noisy signals with SNR = 20, 35, 50, and 80, showing the accuracy and precision of the fitted radius of the large cells (R_l) and of the relative volume fraction for both cell populations ($v_{in,l}$, $v_{in,s}$).

Accuracy



Precision

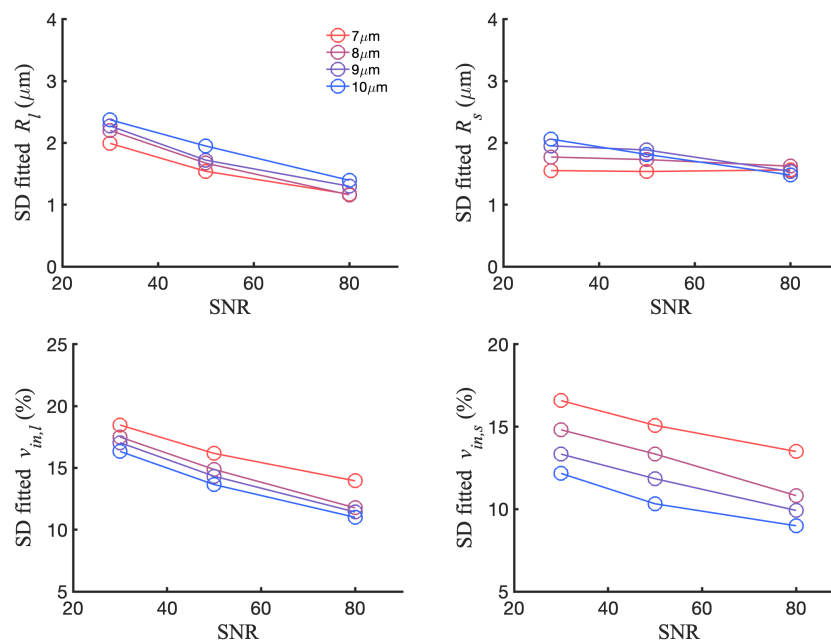


Figure 5.8 Influence of noise on fitted model parameters, extracted from fitting the 2-step-2P-MM to simulated noisy signals with SNR = 30, 50, and 80, showing the accuracy and precision of fitted radii and the percentage volume fraction for both cell populations.

5.6.4 Influence of fixing D_{in} in the model fit

When fitting with a fixed D_{in} , the choice of pre-defined D_{in} influences the estimation accuracy and precision. Greater percentage errors were observed when $D_{in} < 1 \mu\text{m}^2/\text{ms}$ for all 4 estimated model parameters (Figure 5.9). However, the accuracy of the fitted model parameters using all other fixed D_{in} s greater than $1 \mu\text{m}^2/\text{ms}$ was not significantly affected by the choices of D_{in} used in the data analysis. The median and interquartile range of the absolute % errors for fixed $D_{in} \geq 1 \mu\text{m}^2/\text{ms}$ were comparable or slightly lower than that of leaving D_{in} as a free parameter.

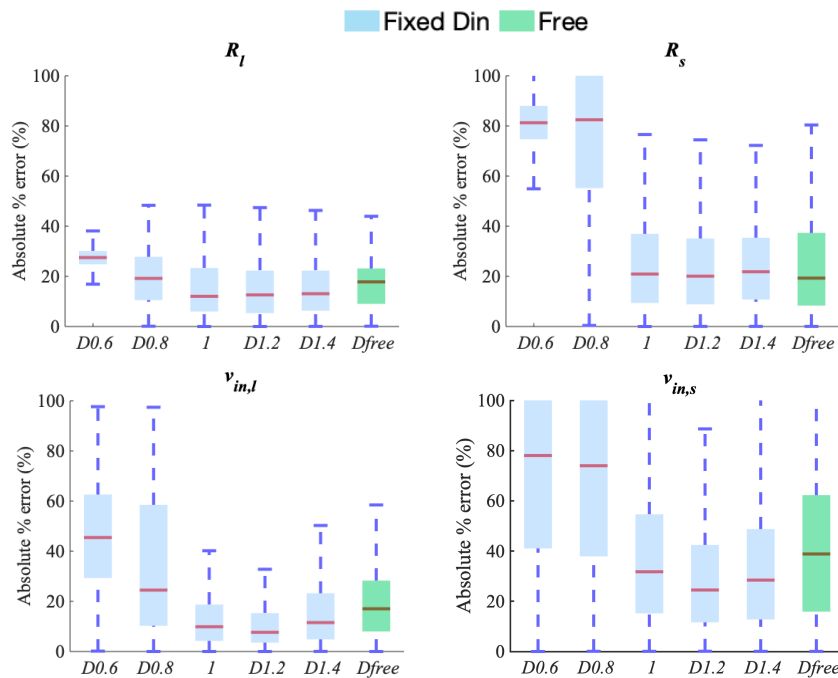


Figure 5.9 Influence of fixing D_{in} to pre-defined values 0.6, 0.8, 1 (ground truth), 1.2, 1.4 $\mu\text{m}^2/\text{ms}$ on the estimation accuracy and precision is assessed. The absolute % error of the fitted R_l , R_s , $v_{in,l}$, $v_{in,s}$ from the ground truth value are plotted for a representative microstructure with combinations of $R_l = 9 \mu\text{m}$, $R_s = 4 \mu\text{m}$, $v_{in,l} = 45 \%$ and $v_{in,s} = 15\%$. For each box, the central line (red) indicates the median and the edges of the box indicates the 25th and 75th percentiles, respectively. The error bars represent the maximum and minimum values.

5.6.5 Comparison of methods

Both *2-step-2P-MM* and 2P-MM with fixed D_{in} demonstrated improved fitting robustness, while maintaining comparable estimation accuracy and precision to the 2P-MM. Figure 5.10 compares the accuracy (Figure 5.10a) and the robustness (Figure 5.10b) of the model parameter estimates from 2P-MM, *2-step-2P-MM* and 2P-MM with fixed D_{in} ($=1, 1.2$ and $1.4 \mu m^2/ms$). The accuracy metric was taken as the median absolute percentage difference between fit result and the ground truth, with the boxplots in each panel representing the distribution over 4 microstructures. The accuracy improved for both *2-step-2P-MM* and 2P-MM with fixed D_{in} . In addition, both the *2-step-2P-MM* and 2P-MM with fixed D_{in} tended to result in a much higher percentage of acceptable fits, suggesting higher degree of robustness than the 2P-MM.

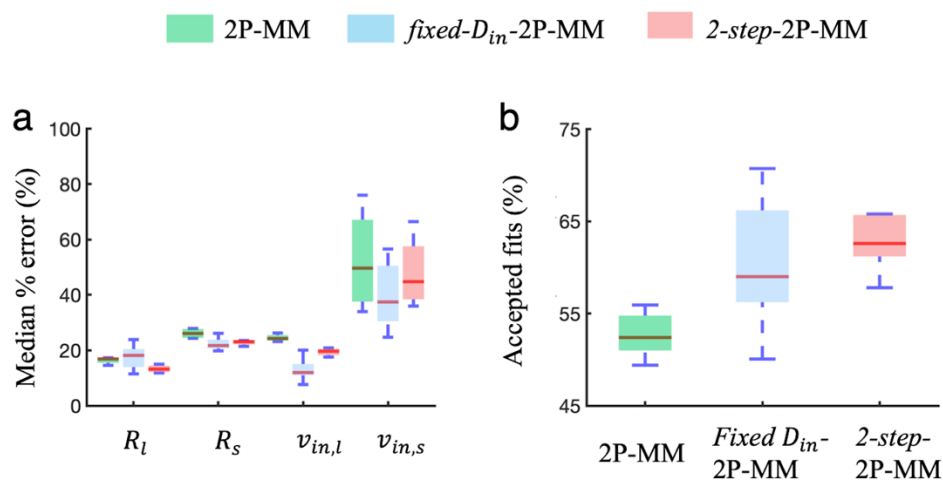


Figure 5.10 The accuracy and robustness of the 3 models— 2P-MM, *2-step-2P-MM* and 2P-MM with fixed D_{in} was evaluated. All three models were fitted to the noisy signal (SNR=50) of 4 microstructures with combinations of $R_l = 7: 1: 10 \mu m$, $R_s = 4 \mu m$, $v_{in,l} = 45 \%$ and $v_{in,s} = 15\%$. The boxplots in each panel represents the distribution over 4 microstructures. Fits that were not within 1% of the fit constraints were considered acceptable fits.

5.7 Discussion

This manuscript introduced a method to characterize the tumor microenvironment when two cell populations of different sizes and volume fractions co-exist in the same space. This development could be useful for applications in diagnosis of complex tumors and assessment of treatment-induced changes. For example, myxoid liposarcoma is a type of soft-tissue sarcoma characterized by a morphological continuum that includes well-differentiated liposarcoma cells ($R \sim 3 - 5 \mu m$) and a hypercellular neoplasm composed of poorly differentiated round cells ($R \sim 8-10 \mu m$)[36], [37]. The amount of round cell component is directly related to tumor grading, metastasis, and survival time[38]. Compared to tumors with less than 5% round cells, tumors with more than 25% round cells have 3 times the probability of developing metastasis, which is often treated with neoadjuvant radiotherapy before surgery[28]. In addition, as emerging immunotherapy becomes a potent treatment for multiple cancers [39]–[41], efforts have been made to visualize and quantify immune cell therapy *in vivo*. Fluorine-19 MRI paired with cell labeling has enabled T-cell imaging and quantification up to 3 weeks post-transfer [42]. While Fluorine-19 MRI is a technique with much merit, it requires specialized hardware not commonly available in most MRI centres[43]. Our proposed method based on diffusion-weighted MRI is both non-invasive and uses proton MRI, more suitable for clinical translation.

The *constrained-2P-MM*, *2P-MM* and *2-step-2P-MM* demonstrated substantial improvement in the estimation accuracy of R_l , R_s , $v_{in,l}$, and $v_{in,s}$ for various microstructures with different radii and volume fractions in a noiseless environment. For microstructure set 1, the *constrained-2P-MM* yielded mean errors of $0.2 \mu m$, 1%, and 1% between model parameter estimates R_l , $v_{in,l}$ and $v_{in,s}$ and the ground truth, respectively. Similarly, mean errors of $0.2 \mu m$, $0.3 \mu m$, 0.9%, and 0.9% for model parameters R_l , R_s , $v_{in,l}$ and $v_{in,s}$ were found for microstructure mixture 2. The imperfect model parameter estimates without the influence of noise originates from the discrepancy between the simulated diffusion signal with MISST and the ideal signal generated by the analytical equation used for fitting. Fitting to signal generated using an independent simulation tool is a more realistic simulation of the actual data acquisition and analysis, rather than using the signal calculated using the analytical signal equation.

The estimation accuracy of the proposed fitting model is limited, even in a noiseless environment, for the following two scenarios: 1) R_l close to R_s , and 2) $v_{in,l} \gg v_{in,s}$ or $v_{in,s} \gg v_{in,l}$. When R_l is too close to R_s , the signal dependence on diffusion times (Figure 5.1) becomes too similar to detect the subtle difference in radii. On the other hand, the similarity in volume fractions between two cell populations has little effect on accuracy. The fit is poorer when one of the cell populations has low volume fraction. This behavior is consistent with previous reports of poorer accuracy and precision of model parameters at low volume fractions in 1P-MM [31]. These results could be of practical importance in determining the appropriate applications and in longitudinal studies. For example, if $v_{in,l}$ is large before treatment and decreases to 5% after treatment, the ability to accurately measure R_l would also decrease.

The estimation accuracy and precision of the fitting models depend on the level of noise. As a result, the ability to differentiate two cell populations is also SNR dependent. While decent accuracy was observed for an SNR of 30 (Figure 5.7, 5.8), an SNR of 50 or greater provides better estimation precision. The stability of the fit at different SNRs was also considered. The stability was quantified by calculating the percentage of acceptable fits where only cases with greater than 50% acceptable fits were considered stable [31], [44]. For microstructure subset 1 (Method section-simulated influence of SNR), more than 50% fits were acceptable for $R_l \geq 5\mu m$ (with $R_s = 1\mu m$) at an SNR of 35, and for $R_l \geq 4\mu m$ (with $R_s = 1\mu m$) at an SNR ≥ 50 . For microstructure subset 2, an SNR of 50 or above was needed to generate stable fits for $R_l \geq 7\mu m$ (with $R_s = 4\mu m$). This means that for an SNR of 50, the difference between R_l and R_s has to be greater $\geq 3\mu m$ for us to robustly differentiate these two cell populations. To determine the extract resolution limit of minimal radii difference between two cell populations, a systematic study of multiple $\Delta R = R_l - R_s$ at various volume fractions and SNRs would be of interest for this method. Signal averaging could be considered to increase the SNR of higher b -value signals, thus reducing the overall SNR requirement [45].

Both the 2-step-2P-MM and 2P-MM with fixed D_{in} improved the estimation accuracy and resulted in much higher percentage of acceptable fits, due to their decreased number of fitted parameters. Fixing D_{in} has been previously studied for both PGSE and IMPULSED acquisitions [32], [33]. It was found that the sensitivity to the intracellular diffusivity is reduced for longer diffusion times

(> 1 ms), thus it could not be reliably estimated. As a result, it is possible to fix D_{in} in fitting to PGSE and IMPULSED data to increase the stability. In this work, fixing D_{in} led to little effect on estimation accuracy for fixed $D_{in} \geq 1 \mu\text{m}^2/\text{ms}$, whereas large estimation errors were obtained for fixed D_{in} below its ground truth value ($1 \mu\text{m}^2/\text{ms}$). This result is consistent with previous studies, which recommend choosing a relatively larger D_{in} than the ground-truth value to maintain the estimation accuracy. [32], [33]

Our simulation experiment showed promising results for the characterization of tissue with two cell populations. However, *in vitro* and *in vivo* validation of the proposed model is still required before it can become a robust tool in the research or clinical setting. The requirement of the gradient coil strength is an important factor to consider during *in vitro* and *in vivo* experiments. For a PGSE sequence, a gradient strength of approximately 300 mT/m is needed to reach the maximum b -value of $2000 \text{ s}/\text{mm}^2$ at the lowest diffusion time of 5.7 ms. A gradient system with maximum gradient amplitude > 300 mT/m in a single direction is available for most pre-clinical MR scanners[21] [44], which makes *in vitro* and *in vivo* experiments using the proposed method feasible. Measures could be taken to adapt the current method for clinical applications, to accommodate for the limited gradient strength (60-80 mT/m). The cosine-modulated oscillating gradient diffusion sequence (OGSE) could be adopted to reach similar b -values with half of the gradient strength required for PGSE[3], [21]. Recently, Xu et al. have proposed a trapezoidal OGSE sequence, which further reduces the requirement of maximum gradient strength [33]. With OGSE sequences, a diffusion time down to 5 ms has been achieved using a human whole-body 3 T MRI system with a gradient strength < 60 mT/m[33], for limited range of b -values. Further investigation is needed to determine the appropriate protocol for clinical applications.

5.8 Conclusion

In this proof-of-concept study, we have proposed a diffusion MRI-based method for voxel-wise estimation of cell radii and volume fractions of two cell populations, when they co-exist in the same MR voxel. We evaluated their feasibility and robustness through simulation experiments. For a minimum difference of $3 \mu\text{m}$ in radius between the large and small cell populations and an SNR of 50, the radii and volume fractions of both cell populations can be accurately estimated.

Three techniques were proposed to improve the stability of the fit, including the *constrained-2P-MM*, *2-step-2P-MM* and *2P-MM* with fixed D_{in} . The ability to reliably estimate cell radii and volume fractions for tissue with two cell populations opens exciting avenues of potential applications in both tumor diagnosis and treatment monitoring.

DATA AVAILABILITY STATEMENT

Code for this study is available online at <https://gitlab.com/MPUmri/dmm>.

Acknowledgement

The authors acknowledge Dr. Junzhong Xu, Dr. Xiaoyu Jiang, Zaki Ahmed, and Véronique Fortier for valuable discussions. This work was supported by Medical Physics Research Training Network Grant of the Natural sciences and Engineering Research Council (Grant number: 432290), and the *Fonds de Recherche en Santé du Quebec*.

References

- [1] L. Sun, S. Sakurai, T. Sano, M. Hironaka, O. Kawashima, and T. Nakajima, “High-grade neuroendocrine carcinoma of the lung: Comparative clinicopathological study of large cell neuroendocrine carcinoma and small cell lung carcinoma in 2402 cases,” 2009.
- [2] X. Jiang, E. T. McKinley, J. Xie, H. Li, J. Xu, and J. C. Gore, “In vivo magnetic resonance imaging of treatment-induced apoptosis,” *Sci. Rep.*, vol. 9, no. 1, p. 9540, Dec. 2019.
- [3] X. Jiang, J. Xu, and J. C. Gore, “Quantitative temporal diffusion spectroscopy as an early imaging biomarker of radiation therapeutic response in gliomas: A preclinical proof of concept,” *Adv. Radiat. Oncol.*, vol. 4, no. 2, pp. 367–376, Apr. 2019.
- [4] A. R. Padhani *et al.*, “Diffusion-weighted magnetic resonance imaging as a cancer biomarker: consensus and recommendations,” *Neoplasia*, vol. 11, no. 2, pp. 102–125, 2009.
- [5] D. M. Patterson, A. R. Padhani, and D. J. Collins, “Technology insight: water diffusion MRI—a potential new biomarker of response to cancer therapy,” *Nat. Clin. Pract. Oncol.*, vol. 5, no. 4, pp. 220–233, 2008.
- [6] R. Bammer, “Basic principles of diffusion-weighted imaging,” *Eur. J. Radiol.*, vol. 45, no. 3, pp. 169–84, Mar. 2003.
- [7] A. B. Rosenkrantz *et al.*, “Body diffusion kurtosis imaging: Basic principles, applications, and considerations for clinical practice,” *J. Magn. Reson. Imaging*, p. n/a-n/a, 2015.
- [8] D. M. Koh and D. J. Collins, “Diffusion-weighted MRI in the body: Applications and challenges in oncology,” *Am. J. Roentgenol.*, vol. 188, no. 6, pp. 1622–1635, 2007.
- [9] D. Schnapauff *et al.*, “Diffusion-weighted echo-planar magnetic resonance imaging for the assessment of tumor cellularity in patients with soft-tissue sarcomas,” *J. Magn. Reson. Imaging*, vol. 29, no. 6, pp. 1355–1359, 2009.
- [10] C. Tsien, Y. Cao, and T. Chenevert, “Clinical Applications for Diffusion Magnetic Resonance Imaging in Radiotherapy,” *Semin. Radiat. Oncol.*, vol. 24, no. 3, pp. 218–226, Jul. 2014.
- [11] K. Oka *et al.*, “Usefulness of Diffusion-Weighted Imaging for Differentiating Between

- Desmoid Tumors and Malignant Soft Tissue Tumors,” vol. 193, pp. 189–193, 2011.
- [12] H. Einarsdóttir, M. Karlsson, J. Wejde, and H. C. F. Bauer, “Diffusion-weighted MRI of soft tissue tumors,” *Eur. Radiol.*, vol. 14, no. 6, pp. 959–963, 2004.
- [13] O. Dudeck *et al.*, “Diffusion-weighted magnetic resonance imaging allows monitoring of anticancer treatment effects in patients with soft-tissue sarcomas,” *J. Magn. Reson. Imaging*, vol. 27, no. 5, pp. 1109–1113, 2008.
- [14] M. M. Y. Khoo, P. a. Tyler, A. Saifuddin, and A. R. Padhani, “Diffusion-weighted imaging (DWI) in musculoskeletal MRI: A critical review,” *Skeletal Radiol.*, vol. 40, pp. 665–681, 2011.
- [15] P. W. Hales, Ø. E. Olsen, N. J. Sebire, K. Pritchard-Jones, and C. a. Clark, “A multi-Gaussian model for apparent diffusion coefficient histogram analysis of Wilms’ tumor subtype and response to chemotherapy,” *NMR Biomed.*, no. October 2014, p. n/a-n/a, 2015.
- [16] N. Just, “Improving tumor heterogeneity MRI assessment with histograms,” *Br. J. Cancer*, vol. 111, no. 12, pp. 2205–2213, 2014.
- [17] E. Panagiotaki *et al.*, “Microstructural Characterisation of Normal and Malignant Human Prostate Tissue with VERDICT MRI,” vol. 3, p. 46410, 2014.
- [18] X. Jiang, H. Li, J. Xie, P. Zhao, J. C. Gore, and J. Xu, “Quantification of cell size using temporal diffusion spectroscopy,” *Magn. Reson. Med.*, vol. 75, no. 3, pp. 1076–1085, Mar. 2016.
- [19] O. Reynaud, “Time-Dependent Diffusion MRI in Cancer: Tissue Modeling and Applications,” *Front. Phys.*, vol. 5, p. 58, Nov. 2017.
- [20] D. S. Novikov, V. G. Kiselev, and S. N. Jespersen, “On modeling,” *Magn. Reson. Med.*, vol. 79, no. 6, pp. 3172–3193, Jun. 2018.
- [21] X. Jiang *et al.*, “In vivo imaging of cancer cell size and cellularity using temporal diffusion spectroscopy,” *Magn. Reson. Med.*, vol. 00, no. June, pp. 1–9, 2016.
- [22] E. Panagiotaki *et al.*, “Noninvasive Quantification of Solid Tumor Microstructure Using VERDICT MRI,” *Cancer Res.*, vol. 74, no. 7, pp. 1902–1912, Apr. 2014.
- [23] O. Reynaud, K. V. Winters, D. M. Hoang, Y. Z. Wadghiri, D. S. Novikov, and S. G. Kim, “Pulsed and oscillating gradient MRI for assessment of cell size and extracellular space (POMACE) in mouse gliomas,” *NMR Biomed.*, no. January, 2016, 29(10):1350-63.

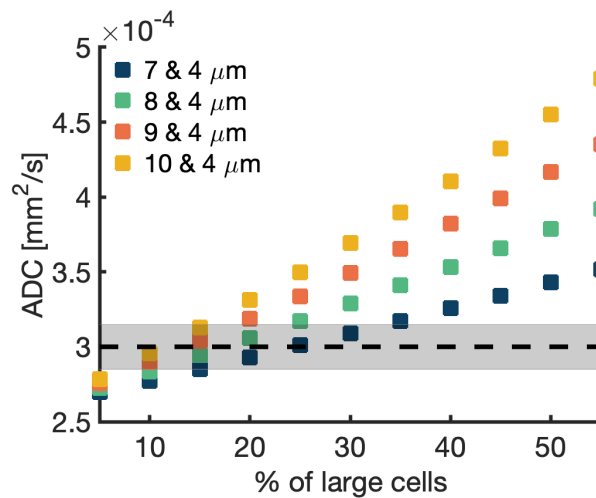
- [24] J. C. Gore, J. Xu, D. C. Colvin, T. E. Yankeelov, E. C. Parsons, and M. D. Does, "Characterization of tissue structure at varying length scales using temporal diffusion spectroscopy.," *NMR Biomed.*, vol. 23, no. 7, pp. 745–56, Aug. 2010.
- [25] D. Barazany, P. J. Basser, and Y. Assaf, "In vivo measurement of axon diameter distribution in the corpus callosum of rat brain," *Brain*, vol. 132, no. 5, pp. 1210–1220, 2009.
- [26] M. D. Does, E. C. Parsons, and J. C. Gore, "Oscillating gradient measurements of water diffusion in normal and globally ischemic rat brain," *Magn. Reson. Med.*, vol. 49, no. 2, pp. 206–215, Feb. 2003.
- [27] J. Xu *et al.*, "Magnetic resonance imaging of mean cell size in human breast tumors."
- [28] S. E. Kilpatrick, J. Doyon, P. F. M. Choong, F. H. Sim, and A. G. Nascimento, "The clinicopathologic spectrum of myxoid and round cell liposarcoma: A study of 95 cases," *Cancer*, vol. 77, no. 8, pp. 1450–1458, Apr. 1996.
- [29] E. Orvieto, A. Furlanetto, L. Laurino, and A. P. Dei Tos, "Myxoid and round cell liposarcoma: a spectrum of myxoid adipocytic neoplasia.," *Semin. Diagn. Pathol.*, vol. 18, no. 4, pp. 267–73, Nov. 2001.
- [30] F. Chapelin, C. M. Capitini, and E. T. Ahrens, "Fluorine-19 MRI for detection and quantification of immune cell therapy for cancer," *J. Immunother. Cancer*, vol. 6, no. 1, p. 105, Dec. 2018.
- [31] D. J. McHugh, P. L. Hubbard Cristinacce, J. H. Naish, and G. J. M. Parker, "Towards a 'resolution limit' for DW-MRI tumor microstructural models: A simulation study investigating the feasibility of distinguishing between microstructural changes," *Magn. Reson. Med.*, Oct. 2018.
- [32] H. Li, X. Jiang, J. Xie, J. C. Gore, and J. Xu, "Impact of transcytolemmal water exchange on estimates of tissue microstructural properties derived from diffusion MRI," *Magn. Reson. Med.*, Jun. 2016.
- [33] J. Xu *et al.*, "Magnetic resonance imaging of mean cell size in human breast tumors," *Magn. Reson. Med.*, p. mrm.28056, Nov. 2019.
- [34] I. Drobnjak, H. Zhang, M. G. Hall, and D. C. Alexander, "The matrix formalism for generalised gradients with time-varying orientation in diffusion NMR," *J. Magn. Reson.*, vol. 210, no. 1, pp. 151–157, May 2011.

- [35] A. Ianus β , B. Siow, I. Drobnjak, H. Zhang, and D. C. Alexander, “Gaussian phase distribution approximations for oscillating gradient spin echo diffusion MRI,” 2013.
- [36] A. L. Folpe and C. Y. Inwards, *Bone and soft tissue pathology*. Saunders/Elsevier, 2010.
- [37] U. Tateishi, T. Hasegawa, Y. Beppu, A. Kawai, and N. Moriyama, “Prognostic significance of grading (MIB-1 system) in patients with myxoid liposarcoma.,” *J. Clin. Pathol.*, vol. 56, no. 8, pp. 579–82, Aug. 2003.
- [38] J. R. Goldblum, A. L. Folpe, S. W. Weiss, F. M. Enzinger, and S. W. Weiss, *Enzinger and Weiss’s soft tissue tumors*. .
- [39] W. Wang *et al.*, “CD8+ T cells regulate tumor ferroptosis during cancer immunotherapy,” *Nature*, vol. 569, no. 7755, pp. 270–274, May 2019.
- [40] R. S. Riley, C. H. June, R. Langer, and M. J. Mitchell, “Delivery technologies for cancer immunotherapy.,” *Nat. Rev. Drug Discov.*, vol. 18, no. 3, pp. 175–196, 2019.
- [41] S. K. Wculek, F. J. Cueto, A. M. Mujal, I. Melero, M. F. Krummel, and D. Sancho, “Dendritic cells in cancer immunology and immunotherapy,” *Nat. Rev. Immunol.*, vol. 20, no. 1, pp. 7–24, Jan. 2020.
- [42] M. Srinivas, M. S. Turner, J. M. Janjic, P. A. Morel, D. H. Laidlaw, and E. T. Ahrens, “In vivo cytometry of antigen-specific t cells using ^{19}F MRI,” *Magn. Reson. Med.*, vol. 62, no. 3, pp. 747–753, Sep. 2009.
- [43] U. Flogel, E. Ahrens, and E. Ahrens, *Fluorine Magnetic Resonance Imaging*. Jenny Stanford Publishing, 2016.
- [44] D. J. Mchugh *et al.*, “Diffusion model comparison identifies distinct tumor sub-regions and tracks treatment response,” no. October 2019, pp. 1–14, 2020.
- [45] C. Eichner *et al.*, “Real diffusion-weighted MRI enabling true signal averaging and increased diffusion contrast,” *Neuroimage*, vol. 122, pp. 373–384, Nov. 2015.

5.9 Supplementary Information

ADC sensitivity to the volume fraction of cells

The apparent diffusion coefficient (ADC) calculated from signals simulated for various combinations of large and small cells of different radii shows increasing ADC as the percentage of large cells increases. This simulation also shows that individual a specific ADC can confoundingly reflect multiple combinations of cells. The narrow grey band indicates an ADC of $(3.00 \pm 0.15) \times 10^{-4} \text{ mm}^2/\text{s}$, within which we find the ADC from 9 microstructures of the simulated 2 cell populations.



Supporting Figure 5.1 Apparent diffusion coefficient (ADC) of various combinations of large and small cells of different radii. The radius of large cells varies from 7 to 10 μm and the small cells are always of radius = 4 μm. The total % volume of the cells is kept at 60% for all combinations. The grey band indicates ADC value of $(3.00 \pm 0.15) \times 10^{-4} \text{ mm}^2/\text{s}$.

Chapter 6

Detecting the evolving tumor microenvironment

6.1 Preface

Cancer therapy can lead to multiple underlying microstructural variations that yield similar ADC values. For example, infiltration of T-cells and tumor progression can both lead to decreased ADC. Acellular necrosis can lead to increased ADC. With the proposed two-cell population model (Chapter 5), all three scenarios can now be characterized by the appropriate diffusion model. However, at the time of image acquisition, the underlying tissue microstructure of a given voxel is usually a “black box”. Differentiating the above three post-treatment scenarios remains a challenge. In this chapter, we propose a voxel-wise model selection method that chooses the most suitable diffusion model among ME-ADC, 1P-MM, and 2P-MM within tumors. Understanding the suitability of the models may provide information about qualitatively different tumor microenvironments, allowing the differentiation of the three post-treatment scenarios.

Detecting the evolving tumor microenvironment with diffusion microstructure modeling: a simulation study

Shu Xing, MSc^{1,2}, Ives R. Levesque, PhD^{1,2,3,4}

¹ Medical Physics Unit, McGill University, Montreal, Canada,

² Department of Physics, McGill University, Montreal, Canada

³ Gerald Bronfman Department of Oncology, McGill University, Montreal, Canada

⁴ Research Institute of the McGill University Health Centre, Montreal, Canada

In preparation for submission to Magnetic Resonance in Medicine

Corresponding author: Shu Xing, MSc
Cedars Cancer Centre, Glen Site, room DS1.7141
1001 Boul. Decarie
Montreal, QC, Canada, H3A 3J1
shu.xing@mail.mcgill.ca

Running title: Detecting evolving tumor microenvironment

Keywords: tumor; diffusion; modelling

6.2 Abstract

Purpose: Cancer therapy can lead to multiple underlying microstructural variations that yield similar ADC values. For example, infiltration of T-cells and tumor progression can both lead to decreased ADC. Acellular necrosis can lead to increased ADC. To differentiate these scenarios, we propose a voxel-wise model selection method that chooses the most suitable diffusion model among the monoexponential ADC (ME-ADC) model, one population microstructure model (1P-MM) and two population microstructure model (2P-MM) within tumors. Understanding the suitability of the models may provide information about qualitatively different tumor microenvironments, allowing the differentiation of the three post-treatment scenarios.

Method: The proposed model selection method was tested using simulated diffusion data with SNR=50 for a range of microstructures which represents the acellular necrotic tissue, cellular tissue with one underlying cell population and cellular tissue with two underlying cell populations. The accuracy of the model selection method was evaluated by comparing the classification from our proposed method to the ground truth. The accuracy and variability of the estimated model parameters were also investigated.

Results: The proposed model selection method demonstrates decent classification accuracy, with $(72\pm 5)\%$, $(86\pm 7)\%$, and $(82\pm 8)\%$ of the noisy iterations correctly classified for the scenarios of one-cell populations, two-cell populations and necrosis, respectively. The parameter maps of cell radii and volume fractions demonstrated expected intra-tumoral heterogeneity.

Conclusion: The combination of corrected Akaike information criterion (cAIC) and estimated radii was able to differentiate among models of acellular tissue, cellular tissue with one cell population, and cellular tissue with two cell populations. This could be used to characterize tumors on a voxel level. This technique potentially allows the differentiation of a variety of clinical outcomes during therapy including necrosis, T-cell infiltration, and tumor advancement (failure of therapy).

6.3 Introduction

Quantitative imaging biomarkers extracted from various non-invasive imaging modalities have become increasingly important in monitoring tumor progression and assessing therapeutic tumor response [1]–[3]. Non-invasive diffusion weighted magnetic resonance imaging (DW-MRI), and more specifically the quantitative apparent diffusion coefficient (ADC), have been used to detect changes in the tumor microenvironment during cancer treatment, such as radio-, chemo- and recently immune therapy[4]–[7]. Therapy induced increases in ADC are often related to the reduction of cellularity or cell apoptosis, which is associated with positive clinical outcomes[8], [9].

The ADC characterizes the overall water diffusion properties, which could be influenced by a number of factors such as cell size, intracellular volume fraction and intra-/extra-cellular compartment diffusivities[10], [11]. As a result, multiple underlying microstructural variations can lead to similar changes in ADC [12]. For example, cancer therapy could lead to several scenarios including (Figure 6.1) 1) therapy induced necrosis, 2) increased number of cancerous cells due to ineffective therapy, and 3) infiltration of modified T-cells (cell radius $R \sim 4\mu m$) among the cancerous cells ($R \sim 8-10\mu m$) in immunotherapy or radiation induced immune-response [13]. The last two scenarios are opposed in terms of clinical response, but both cause the ADC to decrease. ADC alone cannot distinguish them. A more sophisticated method is required to characterize the complex tumor microenvironment.

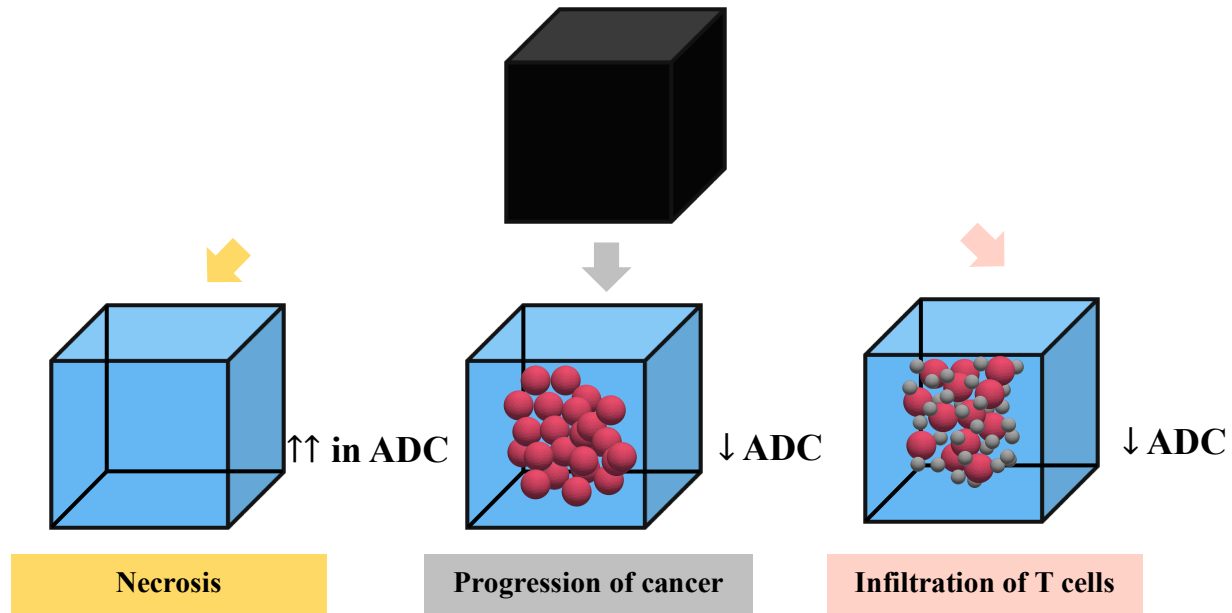


Figure 6.1 Schematic illustration of three possible scenarios after immunotherapy including 1) therapy induced necrosis, 2) increased number of cancerous cells due to ineffective therapy, and 3) infiltration of modified T-cells (cell radius $R \sim 4\mu m$) to the cancerous cells ($R \sim 8-10\mu m$) in immunotherapy or radiation induced immune-response. The diffusion inside the cells is considered restricted, and the diffusion in the extracellular space (blue background) is modeled as hindered and ascribed a constant diffusion coefficient.

Advanced DW-MRI methods and analysis frameworks have been proposed to describe the three scenarios of tumor microenvironment. The mono-exponential ADC model (ME-ADC) is commonly used to characterize diffusion, and is most mathematically appropriate to quantify acellular tissue [14]. This model can be applied to any DW-MRI dataset to characterize the average diffusion properties. Any change in cellular content can affect the ADC. The ME-ADC is unable to capture the underlying tissue microstructures. Multiple DW-MRI analysis techniques assume that tumors can be represented by a single type of cell and use the one-cell population diffusion microstructural model (1P-MM) to map the average cell radius R and percentage volume occupied by cells v_{in} . These include IMPULSED (Imaging Microstructural Parameters Using Limited Spectrally Edited Diffusion) [15], VERDICT (Vascular, Extracellular and Restricted Diffusion for Cytometry in Tumors) [16] and POMACE (pulsed and oscillating gradient MRI for assessment of cell size and extracellular space) [17]. In addition, a previous study has proposed a two-cell population diffusion microstructural model (2P-MM) for voxel-wise estimation of cell radii and

volume fractions of two cell populations, when they co-exist in the same MR voxel [18]. When the underlying tissue microstructure is known, these models can be applied to estimate complex histological parameters. However, at the time of image acquisition, the underlying tissue microstructure of a given voxel is usually a “black box”. Differentiating the above three post-treatment scenarios remains a challenge.

Analysis of model suitability can be used to distinguish between tissue. Model selection techniques have been developed and applied to different diffusion models to determine their applicability, which could infer various tumor microenvironments. For example, a comparison between a microstructural model and the monoexponential ADC model has been used to distinguish viable tissue in gliomas from necrotic or oedematous regions [19]. Recently, McHugh *et al.* proposed a diffusion model comparison technique to differentiate cellular tissue from necrosis in colon carcinoma and to track changes in tissue composition during radiotherapy [20]. While these existing techniques allow us to recognize necrosis from cellular tissue, it provides little information about whether the cellular tissue contains one or two cell populations.

In this work, we propose a voxel-wise model selection method that chooses the most suitable diffusion model among ME-ADC, 1P-MM and 2P-MM within tumors. Understanding the suitability of the models may provide information about qualitatively different tumor microenvironments. We hypothesize that model selection based on the quality of model fit, and constraints based on model parameter values, can be used in the differentiation of the three post-treatment scenarios (Figure 6.1) and become a valuable tool to detect therapy-induced changes. The effects of variations in the underlying tissue properties on different fitted microstructural parameters are also studied. This technique could potentially serve as a non-invasive imaging biomarker capable of quantifying T-cells at the tumor site during immunotherapy, thus predicting therapeutic response following immunotherapy.

6.4 Methods

Simulations were performed to explore the performance of model fitting, and the proposed model selection approach. The matrix method (Microstructure Imaging Sequence Simulation Toolbox (MISST), UCL) [21] was used to simulate diffusion signals for each tissue microstructure from a pulsed gradient spin-echo (PGSE) diffusion MRI sequence [22], [23]. The tissue microstructure was characterized in terms of cell radius R , intracellular volume fraction v_{in} , and the intra- and extra-cellular diffusivities D_{in} and D_{exo} .

Diffusion signals were generated for three sets of tissue microstructures (22 microstructures in total) with various radii and percentage volume fractions. The cells were modeled as impermeable spheres with restricted diffusion; and the extracellular compartment is modeled as non-water tissue with hindered diffusion [22]. Microstructures included 1) ten microstructures with a single underlying cell population $R = 10\mu\text{m}$, $v_{in} = 50\%$, 60% , and 70% ; $R = 9\mu\text{m}$, $v_{in} = 50\%$, 60% , $R = 7, 8\mu\text{m}$, $v_{in} = 50\%$, and $R = 7, 8, 9, 10\mu\text{m}$, $v_{in} = 45\%$, 2) ten microstructures with two cell populations $R_l = 10\mu\text{m}$, $R_s = 4\mu\text{m}$, $v_{in,l} = 35\%$, 40% , 45% , 50% , $v_{in,s} = 25\%$, 20% , 15% , 10% ; $R_l = 8, 9\mu\text{m}$, $R_s = 4\mu\text{m}$, $v_{in,l} = 50\%$, $v_{in,s} = 10\%$, and $R_l = 7, 8, 9\mu\text{m}$, $R_s = 4\mu\text{m}$, $v_{in,l} = 45\%$, $v_{in,s} = 15\%$, and 3) two acellular tissues (*i.e.* necrosis) with different diffusivity $D_{exo} = 2\mu\text{m}^2/\text{ms}$ and $D_{exo} = 2.2\mu\text{m}^2/\text{ms}$. For cellular tissues (*i.e.* microstructure set 1 and 2), D_{in} and D_{exo} were set to be $1\mu\text{m}^2/\text{ms}$ and $2\mu\text{m}^2/\text{ms}$ respectively. For each tissue microstructure, PGSE signals were simulated at four effective diffusion times ($\Delta_{\text{eff}} = 5.7, 16.7, 36.7$, and 66.7ms), using a gradient pulse with duration $\delta = 4\text{ms}$ and gradient separation time $\Delta = 7, 18, 38$, and 68ms . Nine b -values were simulated from 0 to $2000\frac{\text{ms}}{\mu\text{m}^2}$, in intervals of $250\frac{\text{ms}}{\mu\text{m}^2}$. 1,600 noisy synthetic signals with SNR of 50 were generated for each tissue microstructure with the signal-to-noise-ratio (SNR) defined for the $b = 0\text{ms}/\mu\text{m}^2$ signal. The SNR was calculated by dividing the $b = 0\text{ms}/\mu\text{m}^2$ signal by the noise standard deviation. The choice of SNR here was based on the lowest SNR that gave robust fitting results for the 2P-MM, empirically demonstrated in Chapter 5.

The three diffusion models (ME-ADC, 1P-MM, and 2P-MM) and were separately fitted to the signals for each microstructure. The apparent cell radius R_{app} and volume fraction $v_{in,app}$ were

estimated from 1P-MM [15]. The radius and volume fraction of the large and small cells R_l , R_s , $v_{in,l}$ and $v_{in,s}$ were obtained from the 2P-MM [18]. A mono-exponential function was fitted to the same data, yielding the ADC. To ensure convergence on the global solution, every fit was performed using a multi-start technique, from one hundred random starting points. The final parameter estimates were taken as those giving the lowest value of the objective function. The model parameters were constrained to the following ranges: $0.1 \leq R_{app}, R_l, R_s (\mu m) \leq 25$, $0.01 \leq v_{in,app}, v_{in,l}, v_{in,s} \leq 1$ and $0.1 \leq D_{in}, D_{exo} (\mu m^2/ms) \leq 3.0$. Fits within 1% of the fit constraints were considered extreme fits and excluded from subsequent analysis [12]. The D_{in} value was fixed to $1 \mu m^2/ms$ for the 2P-MM to stabilize the fit. All analyses were carried out in MATLAB 2019b (The MathWorks, Natick, MA, USA), with least squares fitting performed using a Trust-Region Reflective algorithm (*lsqcurvefit* and *multistart* in MATLAB).

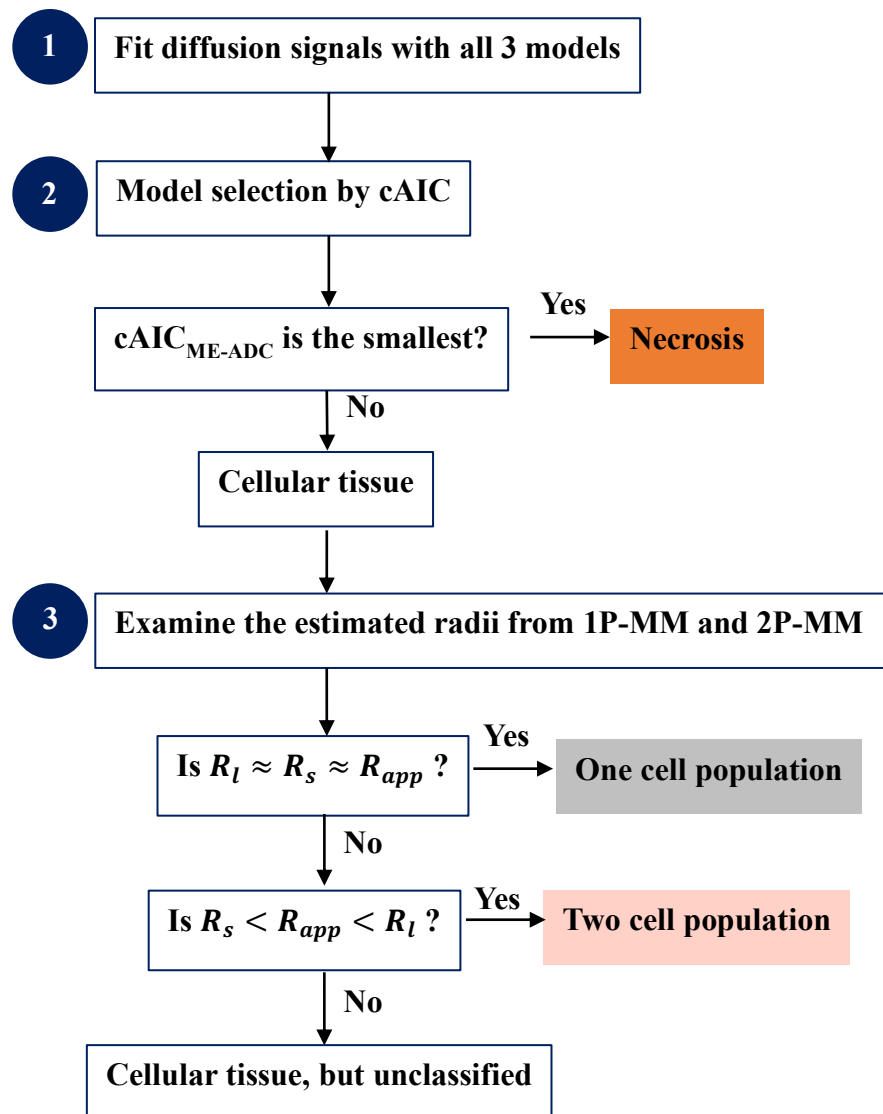


Figure 6.2 Model selection pipeline that choose the most suitable diffusion model among 1P-MM, 2P-MM and ME-ADC in a three-step process. The corrected Akaike information criterion (cAIC) allows the separation between necrosis and cellular tissue. The comparison between fitted radii from 1P-MM and 2P-MM further classifies cellular tissue into tissue with one underlying cell population and tissue with two underlying cell populations.

The proposed model selection method combined an assessment of the fit quality and of fit parameter values in a two-step process (Figure 6.2). First, the corrected Akaike Information Criterion (cAIC) was computed to differentiate necrosis from cellular tissue [20], [24]. The model that produced the lowest cAIC was preferred. Subsequently, to further characterize cellular tissue,

R_l and R_s were compared with R_{app} , based on the interpercentile range (IPR) between the 5th and 95th percentiles of R_{app} estimated by fitting 1P-MM to 1,600 noisy signals. The 1P-MM was preferred when $R_l - R_s \leq \text{IPR of } R_{app}$, suggesting a single underlying cell population. On the other hand, the 2P-MM was selected if $R_l - R_s > \text{IPR of } R_{app}$, suggesting an underlying combination of two cell populations.

To evaluate the accuracy of the model selection method, a digital object mimicking a tumor was created encompassing 16 microstructures covering a range of radii and volume fractions. We generated the diffusion “image” for $b = 1000 \text{ s/mm}^2$, the ADC map, the model selection map, and the R_l , R_s , $v_{in,l}$ and $v_{in,s}$ maps. Each “voxel” in the maps contained estimated model parameters from 1,600 noisy iterations. The median of the estimated parameters was also calculated.

6.5 Results

Separating necrosis from cellular tissue

The quality of the model fit to simulated data, quantified by the cAIC, differentiated between necrosis and cellular tissue models, but was unable to distinguish cellular tissue microstructures with single-cell and two-cell populations. This is visible in the distributions of the cAIC over the 1600 noisy fits (Figure 6.3, bottom row). For the necrotic tissue (Figure 6.3 left column), all three models appear to fit the diffusion signals well (row 2-4). The $\text{cAIC}_{\text{ME_ADC}}$ distribution shifted towards a lower value compared to the $\text{cAIC}_{\text{1P-MM}}$ and $\text{cAIC}_{\text{2P-MM}}$ distributions (Figure 6.3, bottom row). For tissue microstructure with a single cell population (Figure 6.3 Middle column), the example fits to the diffusion signal (row 2-4) demonstrated visually better fit using the 1P-MM and 2P-MM than ME-ADC. The distribution of cAIC from 1P-MM fit ($\text{cAIC}_{\text{1P-MM}}$) overlapped with the cAIC distribution from 2P-MM fit ($\text{cAIC}_{\text{2P-MM}}$). The cAIC distribution from the ME-ADC fit ($\text{cAIC}_{\text{ME_ADC}}$), however, was centered around a considerably greater value. The same trend was observed for tissue microstructure with two cell populations (Figure 6.3 right column).

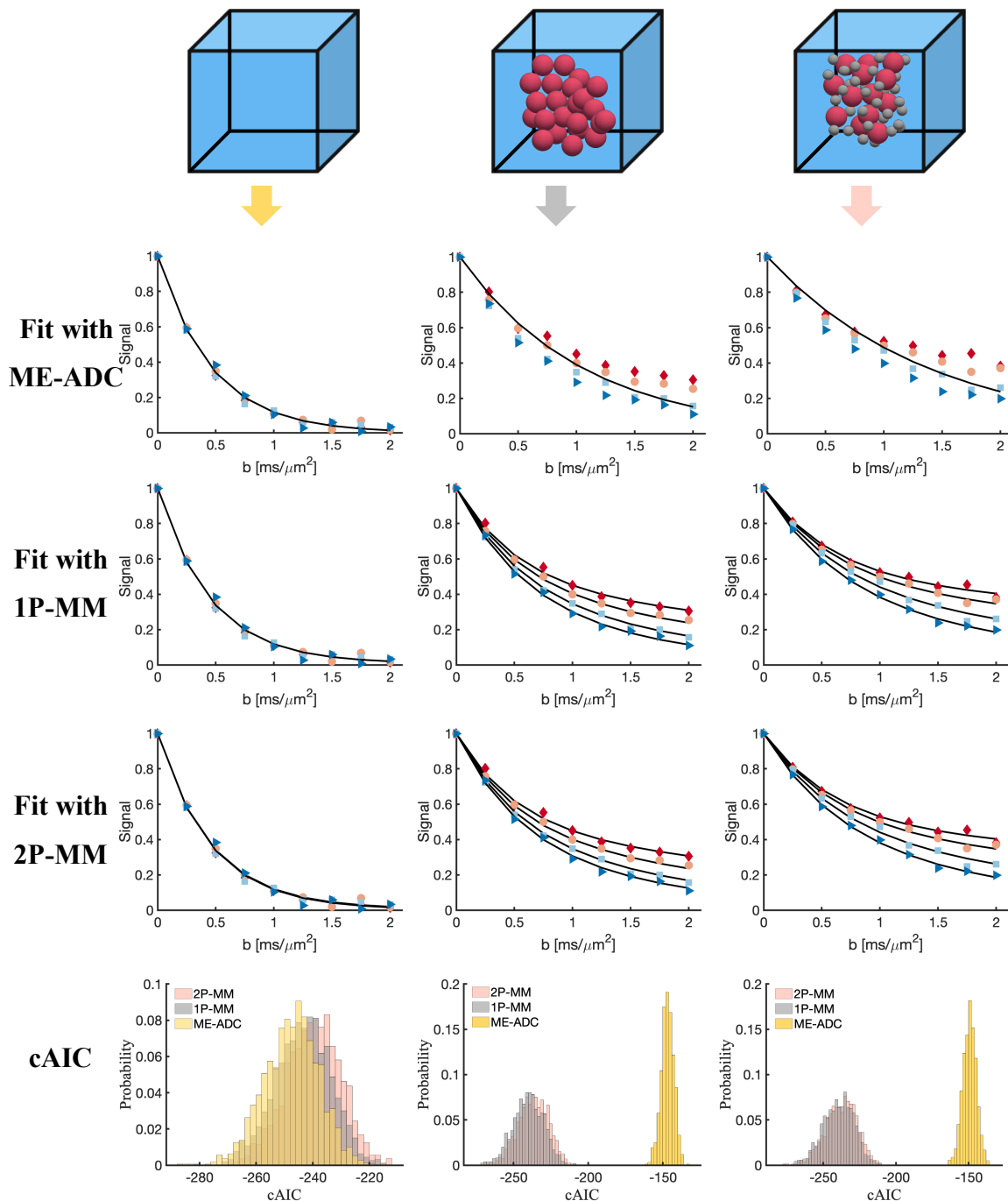


Figure 6.3 Model selection based on the corrected Akaike information criterion (cAIC) allows the distinction between necrotic and cellular tissue. Example fits of three diffusion models, ME-ADC, 1P-MM and 2P-MM (row 2-4), to diffusion signals from three scenarios simulating tumor microstructures are demonstrated. The noisy signals (SNR=50) were simulated at four diffusion times ($\Delta_{\text{eff}} = 5.7, 16.7, 36.7, 66.7 \text{ms}$), normalized to signal at $b = 0 \text{ ms}/\mu\text{m}^2$. The cAIC distributions are plotted over 1600 fits to noisy data.

Separating tissue with one-cell population from tissue with two cell populations

The tissue microstructure with a single cell population was distinguished from the tissue microstructure with two cell populations based on the estimated radii. When both 1P-MM and 2P-MM were fitted to signal from tissue microstructure with one cell population, the estimated radii were approximately equal, *i.e.* $R_{app} \approx R_l \approx R_s$ (Figure 6.4, top row). All three estimated radii followed the ground truth values closely (Figure 6.4, top row, dash-dotted lines). For signal from tissue microstructure with two cell populations, the fits returned $R_s < R_{app} < R_l$ (Figure 6.4, bottom row). The estimated R_l and R_s from the 2P-MM followed the true radii values used in simulation (Figure 6.4, bottom row, dashed and dotted lines), whereas the estimated R_{app} lay between the the true radii values of R_l and R_s .

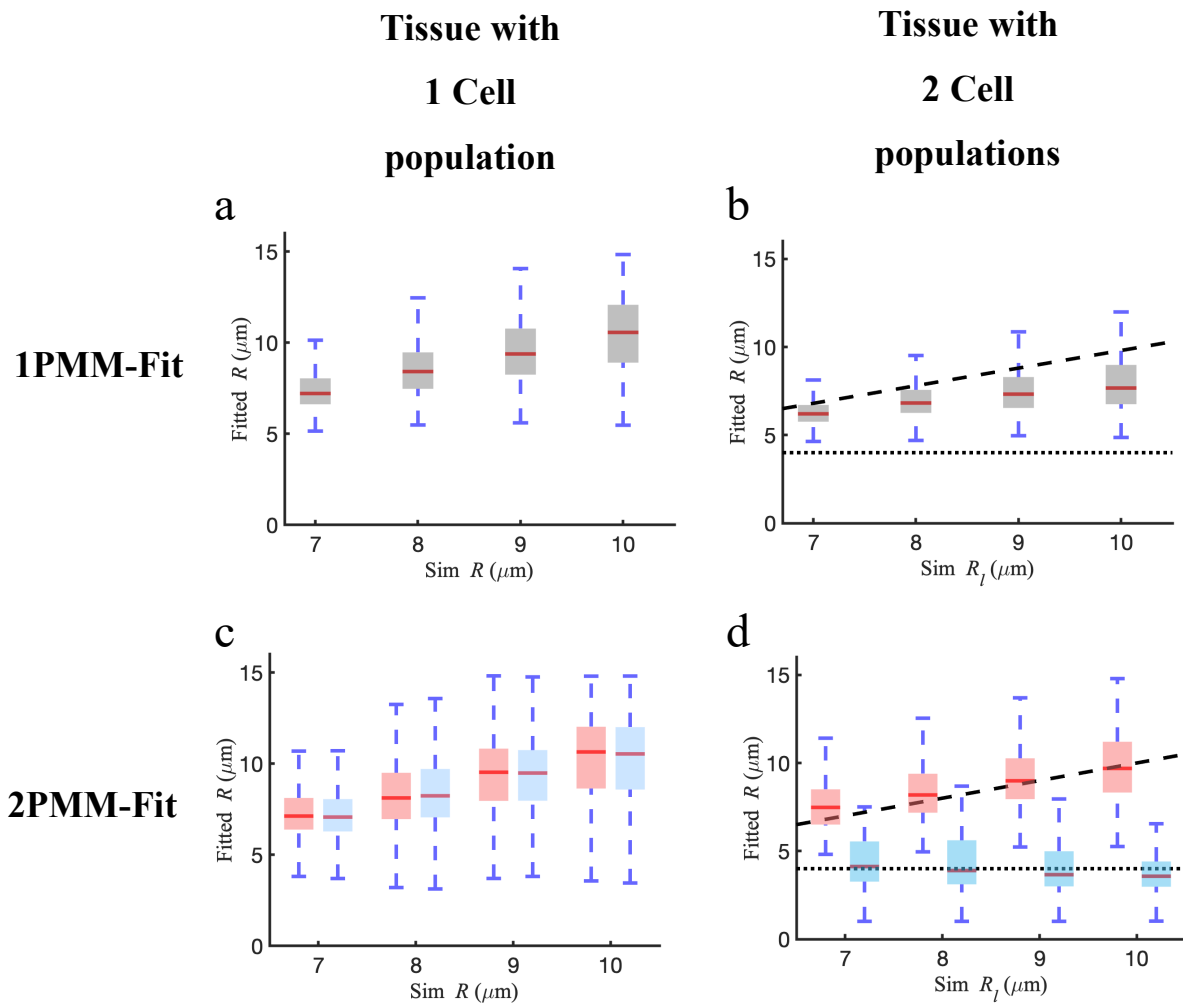


Figure 6.4 A representative example of model selection based on the fitted radii to differentiate cellular tissue with one cell population from tissue (a,c) with two cell populations (b,d). Both 1P-MM and 2P-MM were fitted to the noisy signals (SNR=50) of tissue microstructure with one cell population ($R = 7,8,9,10\mu\text{m}$, $v_{in} = 45\%$) and microstructure with two cell populations ($R_l = 7,8,9,10\mu\text{m}$, $R_s = 4\mu\text{m}$, $v_{in,l} = 45\%$, $v_{in,s} = 15\%$), where R_{app} (gray), R_l (pink) and R_s (blue) were estimated. The dashed and dotted black lines represent the ground truth values for R_l and R_s respectively. For each box, the central red line indicates the median and the edge of the box indicates the 25th and 75th percentiles over 1600 noisy simulations.

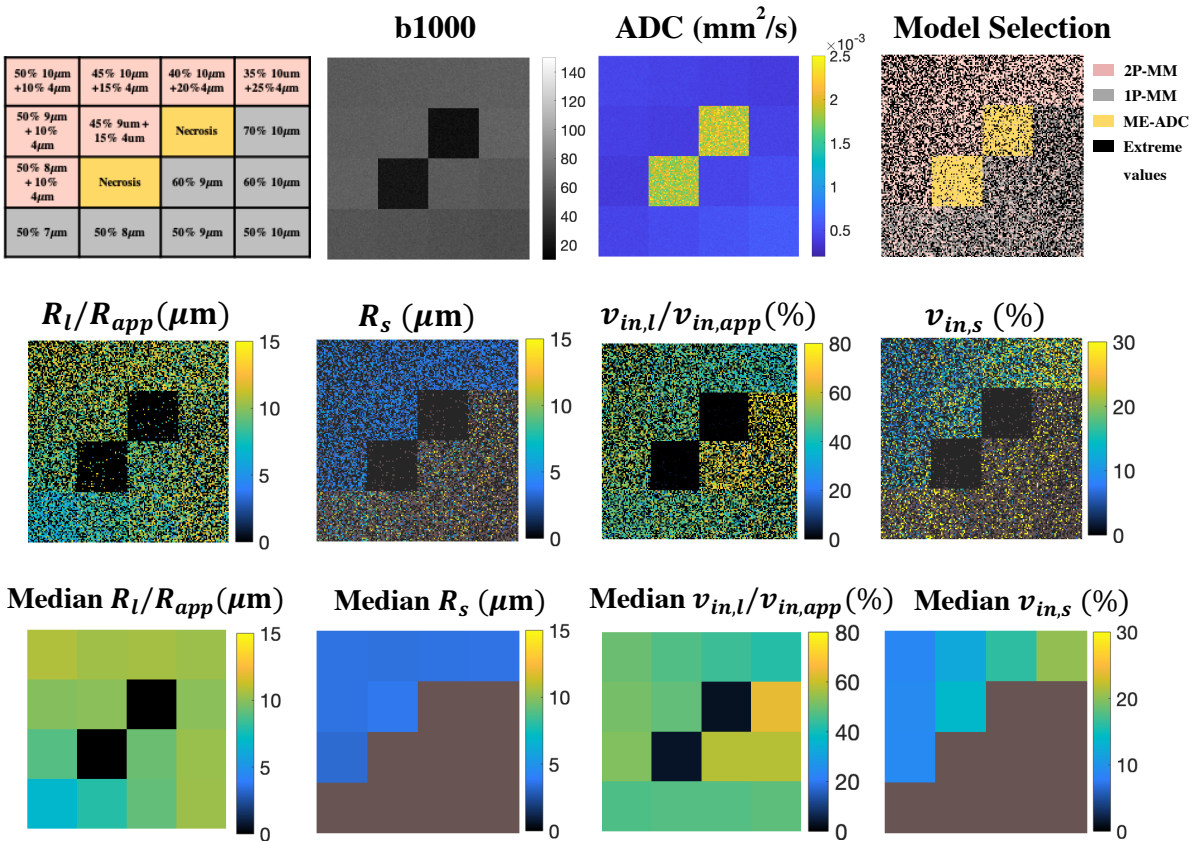


Figure 6.5 Simulations from the digital “tumor” object mimicking three clinical scenarios over a range of radii and volume fractions. ADC values are similar for multiple regions. The 1P-MM, 2P-MM and ME-ADC are correctly selected for $(72 \pm 5) \%$, $(86 \pm 7) \%$, and $(82 \pm 8) \%$ of the noisy iterations after removal of extreme fit values. The parameter maps (middle row) show results from individual fits and demonstrate the overall viability of the technique in spite of the variability of the parameter estimates. The median parameter maps (bottom row) computed as the median of 1600 noisy fits of $\text{SNR} = 50$ showed intra-tumoral heterogeneity in regions identified as cellular tissue. The R_{app} , $v_{in,app}$ estimated from 1P-MM are displayed in the R_l and $v_{in,l}$ maps. The R_s and $v_{in,s}$ not applicable for the one cell population voxels, are displayed in brown.

Analysis of the simulated tumor mimicking the three tissue scenarios covering a range of radii and volume fractions showed similar ADC values for multiple “voxels”. The parameter maps demonstrated the expected intra-tumoral heterogeneity, with contrast in R_l/R_{app} , $v_{in,l}/v_{in,l}$ and $v_{in,s}$ maps in regions identified as cellular tissue (Figure 6.5). The mean % accepted fits were

approximately (60 ± 6) % across 14 tissue microstructures with varying radii and volume fractions. Excluding the extreme values, the (mean \pm standard deviation) percentage of noisy iterations correctly classified by the model selection method was (72 ± 5) %, (86 ± 7) %, and (82 ± 8) % for the microstructures of one-cell populations, two-cell populations and necrosis, respectively. For the tissue microstructure with two cell populations, the model selection accuracy reduced from 86% to 73% as the radius of the large cells decreased from $10\mu\text{m}$ to $8\mu\text{m}$. Model selection accuracy appears to be independent of varying volume fractions. The parameter maps demonstrated considerable variability in the estimated parameters. Despite the variability, intra-tumoral heterogeneity for the cellular tissue was observed. The median parameter maps illustrated that the radii and volume fractions can be accurately estimated within $\pm 1\mu\text{m}$ and $\pm 5\%$ respectively.

6.6 Discussion

This manuscript introduced a voxel-wise model selection technique, allowing the classification of three different tissue microstructures including acellular and cellular tissue with one or two cell populations. Our proposed technique builds on the existing cAIC based model selection method [20] and further differentiates cellular tissue into tissue with one cell population and tissue with two cell populations, based on the estimated radii. This development may be beneficial for the qualitative characterization of tumor heterogeneity and the assessment of treatment induced changes. For example, immune system stimulation with T-cell recruitment to the tumor site after radiation therapy has been found to associate with positive clinical outcomes[25]. Understanding the tumor microenvironment could help determine the success of therapy at an early stage[26]. As emerging immunotherapy becomes a potent treatment for multiple cancers [27]–[29], efforts have been made to quantify immune cells *in vivo*. Fluorine-19 MRI paired with cell labeling has enabled T-cell imaging and quantification up to 3 weeks post-transfer [30]. While Fluorine-19 MRI is a technique with much merit, it requires specialized hardware not commonly available in most MRI centres [31]. Our proposed method based on diffusion-weighted MRI and microstructure modeling is both non-invasive and uses proton MRI, more suitable for clinical translation.

The proposed model selection method demonstrates decent classification accuracy, for the scenarios of one-cell populations, two-cell populations and necrosis. The classification accuracy for necrotic tissue is consistent with published results[20]. In addition, the accuracy of the model selection method depends on the underlying microstructure properties. For tissue microstructure with two underlying cell populations, the selection accuracy improved as the difference in radii ΔR between R_l and R_s increased from 4 μm to 6 μm (Result section, Figure 6.5). This observation is caused by the resolution limit of the 2P-MM. Our previous study has shown that the ability to distinguish two cell populations is SNR dependent. At a SNR of 50, a minimal radii difference of 3 μm is required to resolve the two cell populations. As a result, when ΔR approaches the resolution limit, an increased number of cases would be misclassified as one-cell population. Higher SNRs could be considered to further improve the classification accuracy.

Aside from the classification accuracy, the median parameter maps demonstrated that model parameters can be accurately estimated. A considerable amount of variability in the parameter estimates were observed (Figure 6.5 middle row), as well as extreme fits (within 1% of the fitting constraints). A similar degree of variability and percentage extreme fits were reported in previous simulation studies with the 1P-MM at similar SNR [12], [20], [32]. The median value of estimated parameters over noisy iterations were usually used to evaluate accuracy. The variability and extreme values in the estimates could present a potential challenge in voxel-wise parameter mapping. The extreme values tend to occur, when the magnitudes of the diffusion signals do not follow a descending order as the diffusion time decreases, for a given b -value. This behavior violates the premise of the diffusion signal model, thus leading to poor fitting results. Under experimental condition, three main techniques could be used to address this limitation. The simplest one would be to filter out voxels that do not exhibit the desired signal order, which is similar to our approach of removing extreme values. Secondly, signal averaging could be applied to improve the SNR of the measurement at the cost of scanning time. Lastly, one could also increase voxel size to improve the SNR[33].

This simulation study provides the initial step in developing a novel tissue classification method for three different clinical scenarios, based on the comparison of different diffusion models. *In vitro* and *in vivo* experimental validations are necessary before this can become a robust tool in the

research or clinical setting. As high-powered gradient systems (> 300 mT/m) are readily available for most pre-clinical MR scanners[33], [34], the current protocol can be directly used for experimental validations in these systems. Appropriate cell phantoms, capable of representing the three scenarios, will be developed for future *in vitro* validations. For example, established animal models and histological analysis of tumor specimen could be used for *in vivo* validations[35].

6.7 Conclusion

The combination of cAIC and estimated radii was able differentiate among models of acellular tissue, cellular tissue with one cell population, and cellular tissue with two cell populations. This could be used to characterize tumors on a voxel level. The relative cell volume fractions can be accurately estimated. This technique potentially allows the differentiation of a variety of clinical outcomes during therapy including necrosis, T-cell infiltration, and tumor advancement (failure of therapy). In addition, the percentage volume fraction of T-cells at the tumor site could potentially be quantified, thus allowing clinicians to monitor T-cell infiltration after administration.

Acknowledgement

The authors acknowledge Dr. Junzhong Xu, Zaki Ahmed, and Véronique Fortier for valuable discussions. This work is supported by Medical Physics Research Training Network Grant of the Natural sciences and Engineering Research Council (Grant number: 432290), and the *Fonds de Recherche en Santé du Québec*.

References

- [1] J. W. Prescott, “Quantitative imaging biomarkers: The application of advanced image processing and analysis to clinical and preclinical decision making,” *Journal of Digital Imaging*, vol. 26, no. 1. Springer, pp. 97–108, 14-Feb-2013.
- [2] A. Shukla-Dave *et al.*, “Quantitative imaging biomarkers alliance (QIBA) recommendations for improved precision of DWI and DCE-MRI derived biomarkers in multicenter oncology trials,” *J. Magn. Reson. Imaging*, vol. 49, no. 7, pp. e101–e121, Jun. 2019.
- [3] P. E. Kinahan *et al.*, “The QIBA profile for FDG PET/CT as an imaging biomarker measuring response to cancer therapy,” *Radiology*, vol. 294, no. 2, pp. 647–657, Jan. 2020.
- [4] A. R. Padhani *et al.*, “Diffusion-weighted magnetic resonance imaging as a cancer biomarker: consensus and recommendations.,” *Neoplasia*, vol. 11, no. 2, pp. 102–125, 2009.
- [5] M. Vallières *et al.*, “Investigating the role of functional imaging in the management of soft-tissue sarcomas of the extremities,” 2018.
- [6] O. Dudeck *et al.*, “Diffusion-weighted magnetic resonance imaging allows monitoring of anticancer treatment effects in patients with soft-tissue sarcomas,” *J. Magn. Reson. Imaging*, vol. 27, no. 5, pp. 1109–1113, 2008.
- [7] L. Qin *et al.*, “Advanced MRI assessment to predict benefit of anti-programmed cell death 1 protein immunotherapy response in patients with recurrent glioblastoma,” *Neuroradiology*, vol. 59, no. 2, pp. 135–145, Feb. 2017.
- [8] M. Regier *et al.*, “Diffusion weighted MRI and 18F-FDG PET/CT in non-small cell lung cancer (NSCLC): Does the apparent diffusion coefficient (ADC) correlate with tracer uptake (SUV)?,” *Eur. J. Radiol.*, vol. 81, no. 10, pp. 2913–2918, 2012.
- [9] X. Jiang *et al.*, “A Gamma-Knife-Enabled Mouse Model of Cerebral Single-Hemisphere Delayed Radiation Necrosis,” *PLoS One*, vol. 10, no. 10, p. e0139596, Oct. 2015.
- [10] G. Lemberskiy, E. Fieremans, J. Veraart, F.-M. Deng, A. B. Rosenkrantz, and D. S. Novikov, “Characterization of Prostate Microstructure Using Water Diffusion and NMR

- Relaxation,” *Front. Phys.*, vol. 6, p. 91, Sep. 2018.
- [11] O. Reynaud, “Time-Dependent Diffusion MRI in Cancer: Tissue Modeling and Applications,” *Front. Phys.*, vol. 5, p. 58, Nov. 2017.
- [12] D. J. McHugh, P. L. Hubbard Cristinacce, J. H. Naish, and G. J. M. Parker, “Towards a ‘resolution limit’ for DW-MRI tumor microstructural models: A simulation study investigating the feasibility of distinguishing between microstructural changes,” *Magn. Reson. Med.*, Oct. 2018.
- [13] F. Chapelin, C. M. Capitini, and E. T. Ahrens, “Fluorine-19 MRI for detection and quantification of immune cell therapy for cancer,” *J. Immunother. Cancer*, vol. 6, no. 1, p. 105, Dec. 2018.
- [14] N. S. White *et al.*, “Diffusion-Weighted Imaging in Cancer: Physical Foundations and Applications of Restriction Spectrum Imaging,” *Cancer Res.*, vol. 74, no. 17, pp. 4638–4652, Sep. 2014.
- [15] X. Jiang *et al.*, “In vivo imaging of cancer cell size and cellularity using temporal diffusion spectroscopy,” *Magn. Reson. Med.*, vol. 00, no. June, pp. 1–9, 2016.
- [16] E. Panagiotaki *et al.*, “Noninvasive Quantification of Solid Tumor Microstructure Using VERDICT MRI,” *Cancer Res.*, vol. 74, no. 7, pp. 1902–1912, Apr. 2014.
- [17] O. Reynaud, K. V. Winters, D. M. Hoang, Y. Z. Wadghiri, D. S. Novikov, and S. G. Kim, “Pulsed and oscillating gradient MRI for assessment of cell size and extracellular space (POMACE) in mouse gliomas,” *NMR Biomed.*, no. January, 2016.
- [18] S. Xing and I. R. Levesque, “Modeling the microstructure of tissue with two cell populations of different sizes using diffusion-weighted MRI,” *ISMRM*, vol. 3540, 2019 May 11-16.
- [19] X. Jiang, J. Xu, and J. C. Gore, “Quantitative temporal diffusion spectroscopy as an early imaging biomarker of radiation therapeutic response in gliomas: A preclinical proof of concept,” *Adv. Radiat. Oncol.*, vol. 4, no. 2, pp. 367–376, Apr. 2019.
- [20] D. J. Mchugh *et al.*, “Diffusion model comparison identifies distinct tumor sub-regions and tracks treatment response,” no. October 2019, pp. 1–14, 2020.
- [21] A. S. Ianu, “Advanced Diffusion MRI for Microstructure Imaging : Theoretical Developments,” 2016.
- [22] H. Li, X. Jiang, J. Xie, J. C. Gore, and J. Xu, “Impact of transcytolemmal water exchange

- on estimates of tissue microstructural properties derived from diffusion MRI,” *Magn. Reson. Med.*, Jun. 2016.
- [23] J. C. Gore, J. Xu, D. C. Colvin, T. E. Yankeelov, E. C. Parsons, and M. D. Does, “Characterization of tissue structure at varying length scales using temporal diffusion spectroscopy.,” *NMR Biomed.*, vol. 23, no. 7, pp. 745–56, Aug. 2010.
- [24] C. M. Hurvich and C.-L. Tsai, “A CORRECTED AKAIKE INFORMATION CRITERION FOR VECTOR AUTOREGRESSIVE MODEL SELECTION,” *J. Time Ser. Anal.*, vol. 14, no. 3, pp. 271–279, May 1993.
- [25] H. de A. Carvalho and R. C. Villar, “Radiotherapy and immune response: the systemic effects of a local treatment,” *Clinics*, vol. 73, no. Suppl 1, 2018.
- [26] H. E. Barker, J. T. E. Paget, A. A. Khan, and K. J. Harrington, “The tumor microenvironment after radiotherapy: Mechanisms of resistance and recurrence,” *Nature Reviews Cancer*, vol. 15, no. 7. Nature Publishing Group, pp. 409–425, 26-Jul-2015.
- [27] W. Wang *et al.*, “CD8+ T cells regulate tumor ferroptosis during cancer immunotherapy,” *Nature*, vol. 569, no. 7755, pp. 270–274, May 2019.
- [28] R. S. Riley, C. H. June, R. Langer, and M. J. Mitchell, “Delivery technologies for cancer immunotherapy.,” *Nat. Rev. Drug Discov.*, vol. 18, no. 3, pp. 175–196, 2019.
- [29] S. K. Wculek, F. J. Cueto, A. M. Mujal, I. Melero, M. F. Krummel, and D. Sancho, “Dendritic cells in cancer immunology and immunotherapy,” *Nat. Rev. Immunol.*, vol. 20, no. 1, pp. 7–24, Jan. 2020.
- [30] M. Srinivas, M. S. Turner, J. M. Janjic, P. A. Morel, D. H. Laidlaw, and E. T. Ahrens, “In vivo cytometry of antigen-specific t cells using ¹⁹F MRI,” *Magn. Reson. Med.*, vol. 62, no. 3, pp. 747–753, Sep. 2009.
- [31] U. Flogel, E. Ahrens, and E. Ahrens, *Fluorine Magnetic Resonance Imaging*. Jenny Stanford Publishing, 2016.
- [32] J. Xu *et al.*, “Magnetic resonance imaging of mean cell size in human breast tumors,” *Magn. Reson. Med.*, p. mrm.28056, Nov. 2019.
- [33] C. Eichner *et al.*, “Real diffusion-weighted MRI enabling true signal averaging and increased diffusion contrast,” *Neuroimage*, vol. 122, pp. 373–384, 2015.
- [34] H. Li, X. Jiang, F. Wang, J. Xu, and J. C. Gore, “Structural information revealed by the dispersion of ADC with frequency,” *Magn. Reson. Imaging*, vol. 33, no. 9, pp. 1083–

- 1090, Nov. 2015.
- [35] C. Bailey *et al.*, “Microstructure Characterization of Bone Metastases from Prostate Cancer with Diffusion MRI: Preliminary Findings,” *Front. Oncol.*, vol. 8, p. 26, Feb. 2018.
- [36] Z. S. Buchwald *et al.*, “Radiation, Immune Checkpoint Blockade and the Abscopal Effect: A Critical Review on Timing, Dose and Fractionation,” *Front. Oncol.*, vol. 8, no. DEC, p. 612, Dec. 2018.

Chapter 7

Conclusion and Future work

7.1 Summary

Most cancerous tumors are heterogenous in their cellular composition and morphology [1]. As the cancer therapy paradigm shifts towards personalized medicine, personalized approaches such as targeted chemotherapy and dose painting in radiotherapy are developed to provide tailored treatments for each tumor and its habitats [2]. This requires us to have a thorough understanding of tumor microenvironment, *i.e.* of tumor habitats and their underlying biophysical structures at a cellular level. This thesis presents work on developing novel diffusion MRI analysis and modelling frameworks to characterize tumor microenvironment.

The first part of this work focused on the characterization of tumor habitats (Chapter 3). Using maps of the apparent diffusion coefficient (ADC), T_2 relaxation, and a calculated map representing high- b -value diffusion-weighted MRI, we developed a novel reference-tissue-based method for

probabilistic classification of up to five tumor habitats. These habitats included hypercellularity, high T_2 proteinaceous fluid, necrosis, collagenous stroma, and fibrosis. This technique was demonstrated in seven patients with biopsy-confirmed soft tissue sarcoma. The classification results were qualitatively consistent with histopathology. The identified necrotic regions demonstrated quantitative agreement with low FDG uptake regions in FDG-PET. This technique allowed us to capture the heterogeneity in the complex tumor microenvironment and to monitor their progression during the course of radiotherapy.

While studying treatment induced changes in tumor habitats, we observed a biphasic response in ADC values for certain soft tissue sarcoma, with reduced ADC at mid-point of the radiotherapy treatment course (week 3), followed by a near doubling after the completion of treatment. The decreased ADC could be the result of the swelling of the cells, which is the pre-phase for cell apoptosis, or by increasing cellular density, indicating progression of disease [3]. This observation inspired us to look beyond the habitats and to further investigate the microenvironment on a cellular level. Quantifying microstructural parameters far below the nominal resolution of MR was a difficult task. We have demonstrated through computer simulations, in-vitro and in-vivo experiments that microstructural parameters, such as cell size and volume fraction, can be reliably estimated using the IMPULSED method (Chapter 4). The estimated cell radius and volume fraction demonstrated agreement with the ground truth values during the simulation experiment. The preliminary results of estimated cell diameters from in-vitro and in-vivo experiments were comparable to literature values.

Once we ensured that the microstructural parameters could be accurately and robustly estimated, we built on the current technique and developed microstructure mapping with two cell populations co-existing in the same space (Chapter 5). This work was motivated by recent clinical development in immunotherapy, where infiltrating t-cells ($\sim 4\mu m$) and cancer cells ($\sim 8-12\mu m$) could be seen in the same MR voxel. In this computational proof-of-concept study, we proposed a two-cell population microstructure model which allowed voxel-wise estimation of cell radii and volume fractions of a mixture of two cell populations. It was found that for a minimum difference of $3\mu m$ in radius between the large and small cell populations and an SNR of 50, the radii and volume fractions of both cell populations could be accurately estimated. Three techniques were proposed

to improve the stability of the fit, including the *constrained*-2P-MM, *2-step*-2P-MM and 2P-MM with fixed D_{in} .

The ability to reliably estimate cell radii and volume fractions for tissue with two cell populations opens exciting avenues of potential applications in treatment monitoring. For example, cancer therapy could lead to several clinical scenarios including 1) therapy induced necrosis, 2) increased number of cancerous cells due to ineffective therapy, and 3) infiltration of modified T-cells to the cancerous cells in immunotherapy or radiation induced immune-response [4]. Since the underlying tissue microenvironment was usually unknown at the time of data acquisition, a method capable of differentiating these clinical scenarios was necessary. To this end, we developed a model selection method, based on the combination of cAIC and estimated radii, to differentiate tumor microenvironment with acellular tissue, cellular tissue with one cell or two cell populations without a priori knowledge. This method was tested with simulated diffusion data. A classification accuracy of $(72\pm 5)\%$, $(86\pm 7)\%$, and $(82\pm 8)\%$ for the scenarios of one-cell populations, two-cell populations and necrosis was achieved.

7.2 Future directions

The first part of future work would be focused on the pathological validation of tumor habitats. The habitat classification work discussed in Chapter 3, demonstrated qualitative agreement between tumor histopathology and identified habitats. Due to the lack of exact spatial information of the biopsy location, we were unable to provide a direct validation of our classification method. To implement this method in the clinic, the next reasonable step would be to develop an imaging-tumor pathology pipeline to validate the classification algorithm with pathology findings at known location of biopsy. This could potentially be achieved by acquiring the same set of MR-DWI and FSE scans before and after the tumor biopsy (Figure 7.1), where biopsy markers could be left at the biopsy locations [5]. Overlaying the two sets of images would allow the identification of the biopsy locations. The habitat classification at the biopsy location could then be compared with pathological findings. The validation process would involve close collaborations with the surgeon (who performs the biopsy), the pathologist (who examines the findings), the MR technologist (who

performs the scans), and a small cohort of patients. However, after pathological validation, this classification algorithm could become a valuable tool for image-guided biopsy. In addition, the classification technique could be used to develop alternative radiotherapy treatment plans, where each habitat would be given a different amount of radiation. A systematic study on how habitat-based treatment plans would differ from conventional plans would be worthwhile.

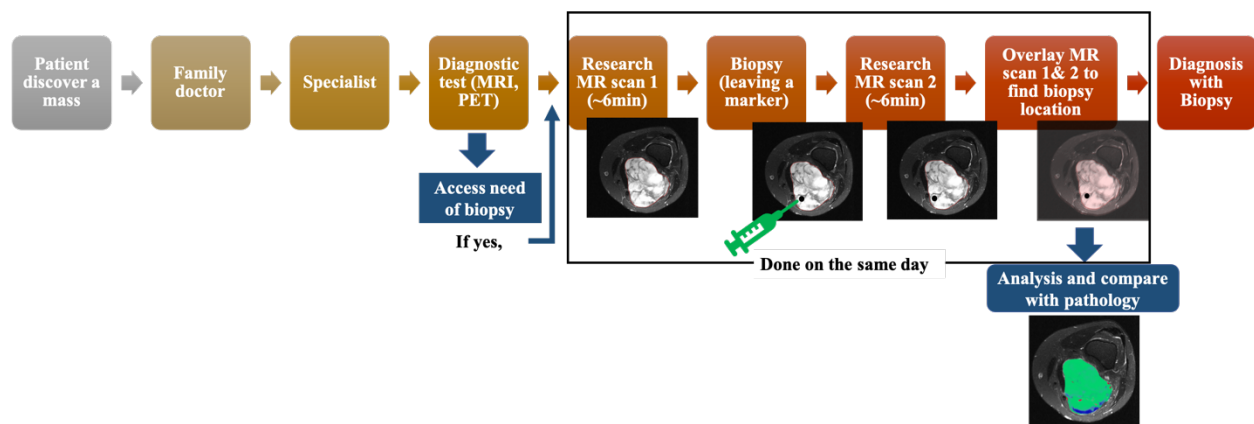


Figure 7.1 Pipeline of the proposed validation study.

The microstructure mapping technique with two cell populations co-existing in the same space (Chapter 5) would also require *in vitro* and *in vivo* validation before it could become a robust tool in the research or clinical setting. *In vitro* validation could be performed with a cell phantom, where two cell populations of different cell sizes and volume fractions are mixed together. The cells would then be centrifuged to create a cell pellet and imaged with a preclinical MR scanner. Alternatively, McHugh et al. has also proposed a biomimetic tumor tissue phantom, composed of micron-scale hollow polymer spheres, which could be modified to include two spheres of different sizes [6]. *In vivo* validation could be performed by irradiating an animal model with implanted tumor. Radiation could lead to the recruitment of T-cells to the tumor site [7]. T-cells could be labeled with perfluorocarbon (PFC) to be visible on Fluorine-19 MR images [4]. The percentage volume fraction of T-cells estimated from microstructure imaging with DWI could be compared with the percentage volume fractions estimated from Fluorine-19 MR images.

Aside from *in vitro* and *in vivo* validations, the microstructure mapping technique could be expanded to differentiate two cell populations based on their cell shapes. This could be used to

characterize biphasic tumors such as biphasic synovial sarcoma, where spindle cells and glandular epithelia cells co-exist in the same tumor [8]. The spindle cells would likely be modeled as cylinders, and the glandular cells as spheres. Differentiating cells with different shapes would likely involve diffusion tensor imaging, which would add another layer of complexity to the existing model. Existing microstructure mapping techniques for neurological applications, such as AxCaliber or ActiveAx would be a good starting point to learn to incorporate diffusion directionality into the model [9], [10].

References

- [1] G. H. Heppner and B. E. Miller, "Tumor heterogeneity: biological implications and therapeutic consequences," 1983.
- [2] F. Meric-Bernstam, C. Farhangfar, J. Mendelsohn, and G. B. Mills, "Building a personalized medicine infrastructure at a major cancer center," *Journal of Clinical Oncology*, vol. 31, no. 15. American Society of Clinical Oncology, pp. 1849–1857, 20-May-2013.
- [3] D. M. Patterson, A. R. Padhani, and D. J. Collins, "Technology insight: water diffusion MRI--a potential new biomarker of response to cancer therapy.," *Nat. Clin. Pract. Oncol.*, vol. 5, no. 4, pp. 220–233, 2008.
- [4] F. Chapelin, C. M. Capitini, and E. T. Ahrens, "Fluorine-19 MRI for detection and quantification of immune cell therapy for cancer," *J. Immunother. Cancer*, vol. 6, no. 1, p. 105, Dec. 2018.
- [5] K. Kubota, N. Gomi, T. Wakita, H. Shibuya, M. Kakimoto, and T. Osanai, "Magnetic resonance imaging of the metal clip in a breast: safety and its availability as a negative marker," *Breast Cancer*, vol. 11, no. 1, pp. 55–59, Jan. 2004.
- [6] D. J. McHugh *et al.*, "A biomimetic tumor tissue phantom for validating diffusion-weighted MRI measurements," *Magn. Reson. Med.*, vol. 80, no. 1, pp. 147–158, Jul. 2018.
- [7] H. de A. Carvalho and R. C. Villar, "Radiotherapy and immune response: the systemic effects of a local treatment," *Clinics*, vol. 73, no. Suppl 1, 2018.
- [8] C. Fisher, "Synovial sarcoma," *Annals of Diagnostic Pathology*, vol. 2, no. 6. W.B. Saunders, pp. 401–421, 01-Dec-1998.
- [9] Y. Assaf, T. Blumenfeld-Katzir, Y. Yovel, and P. J. Basser, "AxCaliber: A method for measuring axon diameter distribution from diffusion MRI," *Magn. Reson. Med.*, vol. 59, no. 6, pp. 1347–1354, 2008.
- [10] E. Panagiotaki, T. Schneider, B. Siow, M. G. Hall, M. F. Lythgoe, and D. C. Alexander, "Compartment models of the diffusion MR signal in brain white matter: A taxonomy and comparison," *Neuroimage*, vol. 59, no. 3, pp. 2241–2254, 2012.

Appendix A

Approval for in-vivo MRI studies

Studies involving human subjects require review and approval by the appropriate board. Ethics approval for the habitat classification of soft-tissue sarcoma, involving patients has been approved by the Research Ethics Board of the McGill University Health Center. The letter of approval is reproduced on the next page.



Centre universitaire de santé McGill
McGill University Health Centre

Les meilleurs soins pour la vie
The Best Care for Life

Comité d'éthique Génétique et populations / Biomedicale D
a/s Mme Esther Boyle
Genetics/Population Research
Investigator Initiated Studies
Research Ethics Board

CUSM - Hôpital général de Montréal
1650 Avenue Cedar/Bureau Ls1-509
Montréal (Québec) H3G 1A4
(514) 934-1934 local 43174
Fax: (514) 934-8202
esther.boyle@mail.mcgill.ca

January 7, 2013

JAN 07 2013

Dr. Carolyn Freeman
Department of Radiation Oncology
Montreal General Hospital
McGill University Health Centre

DATE OF APPROVAL

RE: 12-294 GEN entitled "The role of FDG-PET and F-MISO PET in the Management of Soft-Tissue Sarcomas of the Extremities with Pre-operative Radiotherapy and Surgery."

Dear Dr. Freeman:

The research proposal entitled above received Full Board review at the convened meeting of the GEN Research Ethics Board on November 27, 2012, and was found ethically acceptable for conduct at the McGill University Health Centre, and was entered accordingly into the minutes of the Research Ethics Board (REB) meeting.

We are pleased to provide you with final approval for the following documents, via review by the Co-Chairman on January 7, 2013.

- o Clinical trial protocol, version dated October 15, 2012
- o Main Informed Consent Form, English and French versions dated December 27, 2012

At the MUHC, sponsored research activities that require US federal assurance are conducted under Federal Wide Assurance (FWA) 00000840.

All research involving human subjects requires review at a recurring interval. It is the responsibility of the principal investigator to submit an Application for Continuing Review to the REB prior to the expiration of approval to comply with the regulation for continuing review of "at least once per year".

APPROVAL JANUARY 7, 2013
EXPIRATION JANUARY 6, 2014

The Research Ethics Boards (REBs) of the McGill University Health Centre are registered REBs working under the published guidelines of the Tri-Council Policy Statement, in compliance with the "Plan d'action ministériel en éthique de la recherche et en intégrité scientifique" (MSSS, 1998) and the Food and Drugs Act (7 June, 2001), acting in conformity with standards set forth in the (US) Code of Federal Regulations governing human subjects research, and functioning in a manner consistent with internationally accepted principles of good clinical practice.

We wish to advise you that this document completely satisfies the requirement for Research Ethics Board Attestation as stipulated by Health Canada.

It is important to note that validation for the translated version of the consent document has been certified by an MUHC translator. Any further modification to the REB approved consent document must be identified by a revised date in the document footer, and re-submitted for review prior to its use.